Diss. ETH No. 20701

DC, Microwave and Optical Measurement Schemes for Nano-Scale Devices

A dissertation submitted to
ETH ZURICH

for the degree of
Doctor of Sciences

presented by

GABRIEL FERNANDO PUEBLA-HELLMANN

Dipl.-Phys., ETH Zurich
born 30.12.1980
citizen of Germany

accepted on the recommendation of

Prof. Dr. Andreas Wallraff, examiner
Prof. Dr. Christian Schönenberger, co-examiner

2012

DC, Microwave and Optical Measurement Schemes for Nano-Scale Devices

—

Gabriel F. Puebla-Hellmann

To my parents

Contents

Abstract

In this thesis, we investigate the radio-frequency (RF) and photo-induced transport properties of devices based on single nanometer-sized objects, such as molecules, colloidal quantum dots and carbon nanotubes. Such devices not only offer a decrease in size compared to the current semiconductor-based electronics, but may also allow for new functionality, tailored to the specific needs by chemical synthesis [Fu04, Cuniberti05, Joachim05, Tao06]. Here, we focus on three-terminal devices, which have been previously used to investigate physical phenomena such as the Kondo Effect [Liang02, Parks06, Roch08], single nuclear spin effects in molecules [Grose08, Vincent12] and orbital gating [Song09]. While most experiments with devices based on nanometer sized objects involve measuring their DC transport properties, we expand our focus to the RF and photo-induced transport properties. Not only are these important for the long-term goal of creating integrated circuits with such devices, but they additionally allow access to time and energy scales not realizable in DC transport measurements.

We have implemented single nano-object devices, based on C_{60} molecules and colloidal quantum dots, in a three-terminal geometry using the feedback controlled breaking of a small gold wire, the so-called break-junction technique. Such break-junctions are subsequently integrated into superconducting impedance matching circuits based on transmission line elements. By measuring the microwave properties of the combined single nano-object/impedance transformer device, the RF properties of the nano-object device at GHz frequencies can be extracted. Furthermore, this technique allows for a high measurement bandwidth, on the order of 5 to 80 MHz, enabling time-resolved measurements with a resolution of 10 ns to 100 ns at high signal-to-noise ratios.

We demonstrate this approach first using a gold break-junction as a variable load and obtain good agreement between an electrical equivalent circuit model and the measured microwave properties. This method is then extended to the measurement of a single carbon nanotube device, where we observe a fivefold decrease in the RF impedance at 4.8 GHz compared to the MΩ DC resistance. The RF measurement can further simultaneously extract the reactive part of the nanotube impedance with a sensitivity on the Attofarad level.

Investigations into photo-induced transport are enabled by a custom-designed, pulse-tube cooler based cryostat with a base temperature of 2.9 K, developed and imple-

mented in this research work. This setup integrates the necessary RF and DC components with a wideband fiber-based confocal microscope allowing for a characterization of photo-induced effects as a function of intensity, position and wavelength. Utilizing this setup, we have investigated photo-enhanced conductance in gold atomic point contacts, measuring a qualitatively different behavior for 405 nm and 532 nm illumination. We then examine the wavelength dependence of the photo current in a C_{60} based device, observing a photo current for 532 nm but not for 405 nm nor for 635 nm illumination. We further demonstrate the combination of the two developed measurement techniques, investigating the photo induced conductance changes in a carbon nanotube RF device in a time-resolved measurement. The extracted response rise-time in the 100 ns range is in agreement with rise-time expected from the device bandwidth and laser pulse rise time.

Zusammenfassung

Das Thema dieser Dissertation ist die Untersuchung von Einzel-Nano-Objekt Bauelementen bezüglich ihrer Radio-Frequenz (RF) und photo-induzierten Transport Eigenschaften. Solche Bauelemente erlauben nicht nur die Verkleinerung bestehender Logikelemente, sondern könnten auch die Massschneiderung neuer elektronischen Funktionalitäten mittels chemischer Synthese ermöglichen. Motiviert durch die grossen Fortschritte im letzten Jahrzent untersuchen wir solche Nano-Objekt Bauelementen in einer Transistor Geometrie. Diese erfolgreich benutzt um eine Reihe physikalische Phänomene zu untersuchen, zum Beispiel den Kondo-Effekt [Liang02, Parks06, Roch08], einzelne nukleare Spins in Molekülen [Grose08, Vincent12] und die elektrische Beinflussung von Orbitalen [Song09]. Während in solchen Experimenten typischerweise der Gleichstrom Transport gemessen wird, untersuchen wir in dieser Arbeit den RF und photo-induzierten Transport, da diese Zugang zu Zeit- und Energie-Skalen ermöglichen welche mit Gleistrom Experimenten nicht erreicht werden können.

In einem ersten Schritt entwickeln wir die Herstellung von Nano-Objekt Transistoren mittels Bruchkontakten. Bei diesem Verfahren wird ein dünner Golddraht kontrolliert mittels Strom-induzierter Migration, auch bekannt als Elektromigration, gebrochen. Durch die Verwendung eines Rückkoppel Algorithmus erreichen wir ein kontrolliertes Brechen des Drahtes, wodurch die Herstellung von Bauelementen mit einzelnen C_{60} Molekülen and einzelnen kolloiden Quantenpunken ermöglicht wird. Solche Bruchkontakte werden in einem nächsten Schritt in supraleitende Impedanz Transformatoren eingebettet, welche es erlauben die RF Transport Eigenschaften der Nano-Objekt Bauelemente aus der RF Messung der kombinierten Bauelement/Impedanz Transformator Schaltung zu bestimmen. Durch Einsatz dieser RF Messtechnik sind desweiteren Messbandbreiten von 5 MHz bis 80 MHz möglich, welche zeitabhängige Messungen mit einer Auflösung von 10 ns bis 100 ns erlauben bei einem hohem Signal-zu-Rausch Verhältniss.

Wir untersuchen diese RF Messtechnik erst anhand eines sauberen Gold Bruchkontaktes, der durch kontrollierte Elektromigration eine variable Last darstellt. Das RF Verhalten der kombinierten Schaltung lässt sich gut durch eine äquivalente elektrische Schaltung beschreiben, welche es weiterhin erlaubt, die komplexe Impedanz der zu untersuchenden Last zu bestimmen. In einem nächsten Schritt wird diese Verfahren auf eine einzelne Carbon Nanotube angewandt, bei der die gemessen elektrische Impedanz

bei 4.8 GHz ein Faktor fünf kleiner ist als der bei Gleichstrom gemessene Widerstand im MΩ Bereich. Gleichzeitig erlaubt diese Messung die Bestimmung einer kapazitiven Laständerung mit Attofarad Auflösung.

Um photo-induzierte Transport Phänomene zu untersuchen wurde ein anwendungs-spezifischer, Pulsröhren basierter Kryostat entwickelt, in dem die nötigen Komponenten für RF- und Gleichstrommessungen kombiniert werden mit einem Faser-basierten Konfokalen Mikroskop. Dieses System mit einer Basis Temperatur von 2.9 K erlaubt die Intensitäts-, Wellenlängen- und Positionsabhängige Untersuchung von Photo-Effekten. Mit Hilfe dieses Aufbaus wurde die photo-induzierte Leitfähigkeitsänderung in Gold Quantenpunktkontakten untersucht, welche ein unterschiedliches Verhalten als Funktion der Wellenlänge aufweisst. Weiterhin war es mögliche einen wellenlängen-abhängigen Photostrom in einem C_{60} Molekül Bauelement zu messen, welcher nur bei grünem Licht detektiert wurde, nicht aber bei blauem oder rotem Licht. In einem letzten Experiment verbinden wir die beiden Messtechniken um zeitaufgel öste Messungen der photo-induzierten Impedanzänderungen in einer Carbon Nanotube durchzuführen. Die ermittelte Anstiegszeit im 100 ns Bereich stimmt mit den Anstiegszeiten des verwendeten Laserpulses und der Schaltungsbandbreite überein.

1 Introduction

Computers are today an integral part of life and the key element in a range of technologies e.g. mobile access to the Internet in form of a smart phone, or controlling key safety features in a car. This proliferation of computers to all aspects of modern life has been enabled, to a large extent, by the ongoing miniaturization of transistors, the basic building block at the heart of every digital device. As a consequence, each generation of microprocessors has seen a decrease in cost combined with an increase in computational power. Although transistors have decreased in size from several 100 microns at the inception of integrated circuits to 22 nm at the current fabrication node, the underlying complementary metal oxide semiconductor (CMOS) technology has not changed significantly. This technology is approaching its fundamental size limit, given by a minimum volume of semiconductor necessary to achieve transistor behavior, and new technologies are required to enable a further decrease in size.

The progressive miniaturization of integrated circuits was already recognized in the 1960s [Moore65], initiating research into technologies capable of replacing CMOS. One promising technology is single-molecule electronics, where a single molecule connected to two electrodes constitutes the active part of an electronic component, schematically illustrated in Fig. 1.1. The proposal of a single molecule diode by Aviram and Ratner in 1974 marks the birth of this field [Aviram74], after which it took two decades to realize such an experiment [Joachim95, Reed97]. Single-molecule based electronics are not only expected to be able to replace conventional electronics at a smaller size scale, but may also offer tailored electric responses not possible in silicon devices, enabled by the atom level precision of chemical synthesis [Joachim05, Tao06].

Initially, single-molecule electronics was restricted to theoretical investigations due to a lack of the technology to realize such devices. With the invention of the scanning tunneling microscopy (STM) [Binnig82] and the well-known demonstration of xenon atom manipulation [Eigler90], single-molecule devices became experimentally accessible and were first demonstrated by STM measurements in 1995 [Joachim95]. At the same time, an alternative method for attaining contact to single molecules was developed, the mechanically controlled break-junction [Muller92b, Zhou95, vanRuitenbeek96], allowing for an independent demonstration of a two-terminal single molecule device in 1997 [Reed97]. Following these break-throughs, three-terminal devices, single-molecule

transistors, where first demonstrated in 2000 [Park00]. In the past decade, the field of single-molecule electronics has seen appreciable growth and significant knowledge was gained in understanding the fundamental mechanism governing such devices.

1.1 Transport in Single Molecule and Single Nanocrystal Devices

More than a decade after the first realizations of single-molecule devices, device fabrication remains one of the main challenges in the field. The two most widely adopted methods to create contact to a single molecule are the use of an STM [Joachim95, Joachim97,Bumm99,Donhauser01,Lu03] and the controlled breaking of a thin wire, the so-called break-junction technique [Reed97,Kergueris99,Reichert02,Liang02,Bolotin04, Parks06,Bohler07]. Various alternative methods have been both proposed and demonstrated, ranging from magnetic beads [Blum05], where a magnetic bead connecting source and drain electrodes provides for two interfaces, crossed wires [Kushmerick02], in which two wires crossed perpendicularly are placed in a magnetic field, allowing a tuning of the separation via the Lorentz force. Further techniques involve creating junctions by shadow evaporation [Zhitenev02,Lee03], utilizing the molecular level growth control of Molecular Beam Epitaxy to achieve allowing nm sized junctions on cleaved surfaces [Luber05] and assembling gold nano-particle dimers connected by the molecule of interest on larger electrodes [Dadosh05]. Nevertheless, these techniques have not seen widespread use.

While the use of an STM allows for the identification of the molecule of interest by imaging, three-terminal measurements using an electric gate, which enable a more accurate characterization, are not possible with this setup. Further disadvantages of STM are difficulties in attaining mechanical stability and the significant technical effort required for STM-based measurements. Break-junction based devices, in contrast, offer mechanical stability, three-terminal device topology and a comparatively simple
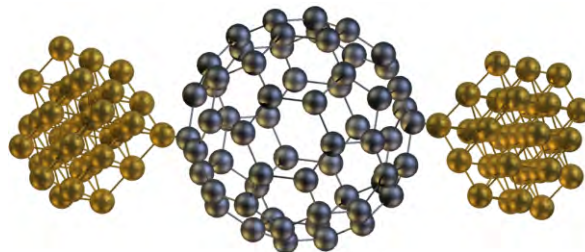

Figure 1.1: Schematic model a single molecule device.

experimental setup at the price of reduced flexibility and stochastic device formation. In particular, the identification of the molecule between the electrodes represents one of the main challenges.

A number of interesting physical phenomena have been investigated in the past decade using break-junction-based three-terminal single-molecule devices. A significant amount of research has focused on the Kondo Effect, where the exchange interaction between a localized spin and the electrons in the metallic electrodes provides for an additional transport channel at zero bias [Park02, Liang02, Yu04, Parks06, Roch08]. Other experiments have demonstrated the modulation of molecular orbits in single-molecule devices using an electric gate [Song09], creating the single-molecule analog of a field-effect transistor. Single nuclear spins in molecules are of interest for quantum computation, offering lifetimes on the order of tens of seconds [Vincent12]. A significant step toward the coherent control and readout of such a spin has been the extraction of the spin orientation from transport measurements [Grose08, Vincent12].

While optical methods, such as absorption or Raman spectroscopy, are routinely applied to characterize and identify molecule ensembles, few optical investigations of single-molecule devices have been performed so far. One demonstrated approach is Raman spectroscopy on single-molecule devices [Ward08, Ward11], where the field enhancement due to collective electron oscillation resonances, also known as plasmon resonances, allows for single-molecule sensitivity. With this technique, correlations between the measured Raman spectrum and the conductance of the device has been established [Ward08]. Photo current measurements of break-junction-based devices have so far focused on demonstrating conductance enhancement in atomic point contacts [Guhr07, Ittah09], with only recent investigations into the photo current in single molecule devices [Ward11]. Further studies involving optical probes have mainly focused on photochromic switching [Dulić03, He05, vanderMolen06, Katsonis06].

An important aspect of single molecule-electronics which has not been investigated so far, but has a large relevance for future applications, are the RF properties of such devices. Similarly, the closely related aspect of time-resolved measurements in such devices has received little attention to date. The main challenge in both cases is the high impedance of the investigated devices, typically in the 100 kΩ to 100 MΩ range. In case of time-resolved measurements, this impedance leads to a reduction of the measurement bandwidth due to the formation of a low pass RC filter together with the unavoidable stray capacitance of the wiring in cryogenic setups. This bandwidth limit can be circumvented by integrating the device of interest into a radio-frequency (RF) tank circuit and measuring the microwave properties of the combined device, which also allows deducing the microwave properties. This approach, first demonstrated for a single electron transistor [Schoelkopf98], has been successfully applied to a number

of devices, such as quantum point contacts [Qin06, Cassidy07, Reilly07], semiconductor quantum dots [Barthel10] and displacement sensors based on atomic point contacts [Flowers-Jacobs07], but, so far, has not been applied to single molecule devices.

1.2 This Thesis

The goal of this thesis was the development of a measurement setup capable of investigating devices formed by single nano-scale objects, such as molecules, colloidal quantum dots or even carbon nanotubes, using optical and RF measurement techniques. To this end, impedance transformers for GHz-range frequencies using transmission-line based circuits have been developed and investigated in a self-designed cryostat, combining DC and RF circuitry with a confocal microscope setup.

The presented thesis is structured into four parts: theoretical aspects of transport in nano-scale object based devices, chip fabrication, experimental setup and scientific results. In the first part, Chapter 2, the basic framework for transport in nanostructures is described. We discuss DC transport, light-induced effects and the expected behavior of the different nano-objects used for the devices in this thesis. This is followed by a review of the break-junction technique and a presentation of the working principles of the RF circuits for microwave-based transport measurements.

In Chapter 3 the implementation of break-junctions and transmission line based impedance matching circuits using microfabrication techniques is presented. We develop a process for 20 x 20 nm^2 cross-section break-junctions using EBL as well as a multiple lithography step process integrating MCBJs into superconducting waveguide resonant circuits. The appropriate fabrication recipes are given in Appendix A, as well as a guideline to designing microfabricated airbridges in Appendix B.

Chapter 4 is devoted to a description of the experimental setup, a custom designed cryostat enabling DC, microwave and optical studies of single nano-scale object devices. Here we first discuss the experimental principles underlying the individual aspects of the different measurement technique. We then present the design and successful implementation of a pulse-tube based cryostat, integrating a fiber-based confocal microscope.

In Chapter 5 a number of experimental results obtained using the microfabricated samples and measurement setup are presented. We demonstrate control over break-junctions, both using electromigration and mechanical bending, which have been subsequently used to create and characterize single molecule and single colloidal quantum dot devices. RF measurements of break-junctions integrated into impedance transformers have been performed, showing good agreement between the electrical model and measurement results. This method is then extended to investigate the RF proper-

ties of molecular devices and single carbon nanotube devices at GHz frequencies. In a further set of experiments, the photo current is investigated, both in gold atomic point contacts and in a molecular device. We observe photo-induced conductance changes in APCs, as well as a wavelength-dependence of the photo current for a molecular device. Finally, we locate a carbon nanotube using scanning photo current microscopy and perform time-resolved measurements of the photo response using RF reflectometry, demonstrating the combination of all three measurement techniques developed in the course of this thesis.

2 Theoretical Aspects of Transport in Nano-Structures

Since the first realization of single-molecule devices in the late 1990's, much progress has been made in understanding the properties of single molecules coupled to two electrodes. Such a device can often be described as a zero- or one-dimensional system coupled to source and drain electrodes, which allows a description using ideas developed in the context of semiconductor nanostructures. One such idea is that the molecule, or other nano-size object, provides for a number of transport channels, each contributing a fixed conductance value. The total device conductance is then the sum over all accessible channels. This framework also allows for describing the effect of light, allowing electrons to access further channels by absorbing photons.

In a similar fashion, the use of RF resonant circuits to circumvent the bandwidth limit in cryogenic transport measurements is motivated by the so called RF single electron transistor (RF SET), where an SET is embedded in a tank circuit [Schoelkopf98]. The resulting device not only displayed a bandwidth of 100 MHz but also an increase in sensitivity by an order of magnitude due to reduced $1/f$ noise, allowing for new experiments, such as determining the counting statistics of electrons tunneling onto and off an quantum dot [Gustavsson06].

This chapter first introduces the framework of transport in single-molecule devices and the effect of light on such transport. It then discusses the theoretical aspects of electrode fabrication before finishing with a discussion of RF resonant circuits.

2.1 Transport in Nano-Structures

Due to the fact that the main interest in single nano-object devices is their potential use for electronic circuits, the transport characteristics are the main property of interest. These depend both on the energy level structure of the device and the realized coupling. The framework for understanding transport properties in such devices is introduced by considering an atomic point contact, where a single atom bridges two electrodes, and goes on to describe the case of a molecule inserted between the electrodes, which is
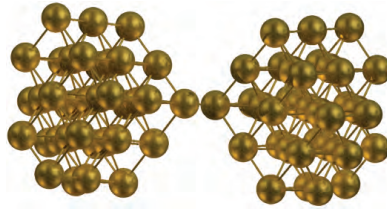
Figure 2.1: A wire frame model of an atomic point contact. The two electrodes meet at a point with a cross-section of a single atom.

typically investigated using tunneling spectroscopy. A second model for transport, the single electron transistor model, is also discussed and the section concludes with a discussion of the influence of light on transport through nano-devices.

2.1.1 Atomic Point Contacts

When using break-junctions to create atomically sharp tips for contacting nano-objects, the junctions are thinned from a cross-section of 20 nm by 40 nm, corresponding to ≈ 2700 atom diameters, down to a neck of one atom cross-section, an atomic point contact (APC), before they break and form the electrodes. As the junctions approach the few atom cross-section, the resistance of the wire is no longer dominated by the bulk properties of the metal, but instead by the intrinsic properties of the metal atoms themselves, which are most dominant in an APC. Such single atom device attracted a large amount of attention in the 1990s and their interaction with light is a current research topic. The realization and investigation of break-junctions is an essential part of this thesis and the theoretical framework used to describe transport in APCs will later be used to describe transport in nano-object devices. We will therefore use break-junctions to introduce the basic concepts of transport, starting with the different transport regimes and going on to describe the observed quantization of the conductance using the Landauer-Büttiker formalism.

Diffusive and Ballistic Transport

For a bulk metal, the flow of current is governed by Ohm's law, linking the electric field **E** to the current density **J** via the conductivity σ:

$$\mathbf{J} = \sigma \mathbf{E} \ . \tag{2.1}$$

In a microscopic picture, the electrons diffuse through the metal as they scatter at impurities and, at finite temperature, at phonons, giving rise to the finite conductivity.

This process is described by the following Boltzmann equation [Ibach01]

$$\frac{\partial f}{\partial t} + \mathbf{v}\nabla_{\mathbf{r}}f - \frac{e}{h}\mathbf{E}\nabla_{\mathbf{k}}f = \left(\frac{\partial f}{\partial t}\right)_{\text{scattering}} \quad , \tag{2.2}$$

where $f(\mathbf{r},\mathbf{k},t)$ is the distribution function, the left-hand side of the equation describes the electron diffusion and the right-hand side describes scattering. By assuming that a non-equilibrium electron state distribution will relax to the equilibrium distribution in a time $\tau(E)$, the so-called relaxation time approximation, the conductivity can be expressed as:

$$\sigma = -\frac{e^2\tau(E_F)}{m^*}n \quad , \tag{2.3}$$

where E_{F} is the Fermi energy, m^* the effective mass of the electrons and n the electron density. The relaxation time can be interpreted as the time between scattering events, leading to the mean-free path λ_{mfp} using the Fermi-velocity v_{F}:

$$\lambda_{\text{mfp}} = v_{\text{F}}\tau \quad . \tag{2.4}$$

Comparing the length of a conducting wire l to the mean free-path allows the distinction between the diffusive regime ($l \gg \lambda_{\text{mfp}}$), where the conductivity is governed by scattering, and the ballistic regime ($l < \lambda_{\text{mfp}}$), where the electrons can pass the wire without energy loss and the conductivity is determined by other effects.

Quantized Conductance

In a ballistic wire with a cross-section on the order of the fermi-wavelength $\lambda_F = 2\pi/k_F$, the conductance does not vary smoothly as a function of the cross-section, as it does for a macroscopic wire, but instead shows a step-like behavior, which was first observed in quantum point contacts (QPCs) in two dimensional electron gases (2DEG) [Wharam88, vanWees88], but can also be observed in break-junctions [Agraït93]. In a simple picture, the narrow constriction only allows for a finite number of transverse modes, or channels, of the electron wave-function, each of which contributes a fixed conductance value. As the cross-section decreases, the number of channels is reduced, leading to a step-like decrease in the total conductance. A proper description of this behavior is given by the Landauer-Büttiker formalism, the following summary is based on [Agrait03].

One can model the break-junction or ballistic wire as a scatterer connected to two leads L_1 and L_2, as depicted in Fig. 2.2(a). These leads support a number of electron modes moving in the longitudinal direction, with the total number of modes N_α given by the quantization of the transverse momentum due to the lateral confinement. At
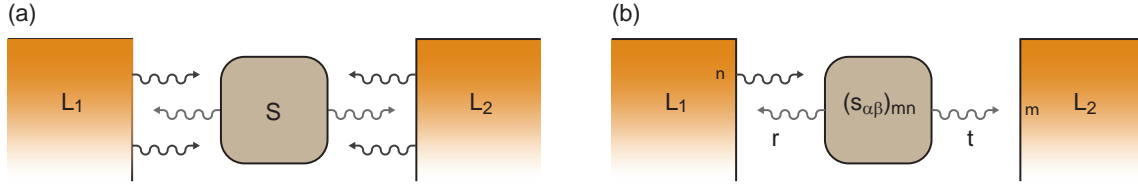
Figure 2.2: (a) Schematic of two leads connected by a scatterer. The electrons are emitted in different modes and are either transmitted or reflected. (b) For a single mode, the amplitude of the transmitted electron wave is given by t and the amplitude of the reflected mode by r.

the scatterer, electrons from the different modes are emitted toward the scatterer and may either be transmitted or reflected.

The scattering matrix $\hat{S}$ relates the amplitudes of incoming and outgoing electron modes and is given by

$$\hat{S} = \begin{pmatrix} \hat{s}_{11} & \hat{s}_{12} \\ \hat{s}_{21} & \hat{s}_{22} \end{pmatrix} = \begin{pmatrix} \hat{r} & \hat{t}' \\ \hat{t} & \hat{r} \end{pmatrix} \quad , \tag{2.5}$$

where $\hat{s}_{\alpha\beta}$ is an $N_\alpha \times N_\beta$ matrix, whose components $(\hat{s}_{\alpha\beta})_{nm}$ relate the outgoing mode n of electrode α with to the incoming mode m of lead β.

For a single perfect channel, the current is given by the difference in the number of electrons moving from electrode L_1 to electrode L_2 and the number of those traveling in the opposite direction:

$$I = \frac{2e}{\pi} \int dk \; v_k \left(f_1(\epsilon_k) - f_2(\epsilon_k) \right) \quad , \tag{2.6}$$

where $f_\alpha(\epsilon)$ is the Fermi distribution function of lead α and spin degeneracy adds the factor of two. Rewriting Eq. 2.6 as an energy integral leads to a cancellation of the group velocity v_k by the density of states, which for the one-dimensional problem is given by $1/v_k\hbar$, leading to

$$I = \frac{2e}{h} \int \mathrm{d}E \left(f_1(E) - f_2(E) \right) \quad . \tag{2.7}$$

At low temperatures, this reduces to $I = 2e^2/h \; V = G_0 \; V$, where $G_0 \approx 1/(12.9\mathrm{k}\Omega)$ is the *conductance quantum*. A perfect one-dimensional conductor with a single mode thus has a finite conductance of $1 \; G_0$.

In case of a scatterer with more channels, the same calculation leads to

$$I_{m\alpha} = \frac{2e}{h} \int_\infty^\infty \mathrm{d}\epsilon \left[\left(1 - \sum_n |\hat{r}_{mn}|^2 \right) f_\alpha - \sum_{\beta \neq \alpha} \sum_n |\hat{t}_{mn}|^2 f_\beta \right] \quad . \tag{2.8}$$

By adding all modes together and using the relationship $T_{12} + R_{11} = N_1$, the current is found to be

$$I_1 = \frac{2e}{h} \int_{-\infty}^{\infty} d\epsilon T_{12}(f_1 - f_2) \ . \tag{2.9}$$

This expression can be simplified for small source-drain voltages V_{SD} by utilizing the approximation $f_1 - f_2 \approx -\partial f/\partial E |e| V_{SD}$. The linear conductance is then given by:

$$G = \frac{2e^2}{h} \int_{\infty}^{\infty} d\epsilon \left(-\frac{\partial f}{\partial E} \right) T_{12} \ , \tag{2.10}$$

which for low temperatures reduces to the Landauer formula

$$G = \frac{2e}{h} \sum_i t_i = G_0 \sum_i t_i \ . \tag{2.11}$$

The conductance of the scatterer is now the sum over all transmission channels, where each transmission channel adds a conductance of $t_i G_0$.

In a 2DEG QPC, the number of available transmission channels is determined by the transverse quantization of the electron wave-function and each mode has a transmission coefficient close to one. While the cross-section in such a system can be smoothly varied, the situation is different in a break-junction, where the atomic nature of the contact does not allow an arbitrary variation of the cross-section, potentially also resulting in "quantization" of the conductance. Nevertheless, the observed conductance quantization is the result of the fact that each individual atom provides a number of conductance channels. Both the dynamical behavior [Krans96] and force measurements [Rubio96] correlated steps in the conductance with atomic rearrangements, the proof for this picture, however, was found by an investigation of the sub-gap structure in superconducting APCs [Scheer97].

In the superconducting case, it is possible to calculate the sub-gap structure of an APC $I-V$ curve for a given set of transmission channels and amplitudes t_i, which allows the decomposition of a measured $I - V$ curve into a set of transmission coefficients. It was found that an aluminum APC with a conductance close to G_0 did not show the sub-harmonic structure of one channel with close to unity transmission, but rather three channels with different coefficients adding up to G_0. From a quantum chemistry point of view, each valence orbital of the aluminum atom adds a transport channel [Cuevas98], a model which shows good agreement with experimental data for a number of metals, including lead (4 channels), niobium (5 channels) and, most important, a single channel with close to unity transmission for a single gold atom [Scheer98]. As in this thesis gold break-junctions are used to measure nano-objects, this result can be used to determine when a single atom is left between the electrodes as well as the point at which the junction is broken and the nano-object dominates transport. In more

detail, a conductance close to G_0 indicates a contact formed by a single gold atom or a one-dimensional chain of gold atoms [Tavazza11], and a conductance below $\approx 0.9\ G_0$ indicates a broken junction.

2.1.2 Tunneling

Once the nanowire forming the break-junction has been broken, transport through the junction takes place by tunneling through vacuum, in case of an empty gap, or tunneling through an object inside the gap. By using a similar transmission matrix approach, the relationship between the measured current and properties of the object inside the gap can be derived. In the following, we discuss a short derivation, which can be found in more detail in Ref. [Ihn10].

If we again assume a scatterer between two leads supporting different electron modes, then the elastic tunneling current through the scatterer is given as the sum of the contributions of the different modes

$$I = \frac{e}{h} \sum_{m,n} |t_{mn}|^2 \delta(E_m - E_n)\big(f_1(E_m) - f_2(E_n)\big) \ , \tag{2.12}$$

where t_{mn} is the transmission probability from mode n to mode m with energies E_m and E_n. Rewriting this expression as an integral over energy yields

$$I = \frac{e}{h} \int_{-\infty}^{\infty} \mathrm{d}E \ \underbrace{(2\pi)^2 \sum_{m,n} |t_{mn}|^2 \delta(E - E_m)\delta(E - E_n)}_{\mathcal{D}_T(E)} \ \big(f_1(E) - f_2(E)\big) \ , \tag{2.13}$$

where $\mathcal{D}_T(E)$ is the tunneling density of states (DOS). One can further simplify the expression for the DOS if the transmission probability of all pairs of states (m, n) at an energy E is about the same and given by $\mathcal{T}(E) = |t_{mn}|^2$, leading to

$$\mathcal{D}_T(E) = (2\pi)^2 \mathcal{T}(E)\mathcal{D}_1(E)\mathcal{D}_2(E) \ , \tag{2.14}$$

where $\mathcal{D}_1$ and $\mathcal{D}_2$ are the DOS of the electrodes. The current through the nano-device is thus determined by both the transmission function $\mathcal{T}(E)$ of the object, and the DOS $\mathcal{D}_{1,2}(E)$ of the electrodes.

Tunneling Spectroscopy

The goal of a nano-object transport measurement is the determination of the transmission function $\mathcal{T}(E)$ using the measured current-voltage characteristics, which are

acquired by applying a bias voltage $V_{SD} = (\mu_2 - \mu_1)/e$ to the leads L_1 and L_2, usually termed source and drain. For bias voltages larger than $k_B T/e$, the measured current is given integrating over the bias-window V_{SD}:

$$I = \frac{(2\pi)^2 e}{h} \int_{\mu_1}^{\mu_2} \mathrm{d}E \ \mathcal{T}(E)\mathcal{D}_1(E)\mathcal{D}_2(E) \ . \tag{2.15}$$

Calculating the derivative with respect to V_{SD} leads to the *differential conductance*:

$$\frac{\mathrm{d}I}{\mathrm{d}V_{SD}} = \frac{(2\pi)^2 e}{h}\mathcal{T}(\mu_\alpha + |e|V_{SD})\mathcal{D}_\alpha(\mu_\alpha + |e|V_{SD})\mathcal{D}_\beta(\mu_\alpha + |e|V_{SD}) \ . \tag{2.16}$$

In case of electrodes with a constant density of states, the differential conductance is therefore proportional to the tunneling density of states of the object of interest. Two methods can be utilized to determine the differential conductance, either numerical derivation of the measured $I - V$-curve, which is comparatively easy but prone to noise and numerical artifacts, or by adding a small sinusoidally modulated voltage to the bias, and measuring the response using a lock-in technique, as discussed in Section 4.2.2.

So far, only elastic tunneling has been considered, but especially for molecules, inelastic processes, revealed by inelastic electron tunneling spectroscopy (IETS), yield additional information about the device under test. An electron tunneling from the source electrode through a molecule can either emerge at the drain electrode without losing energy, which is the case for elastic tunneling, or it may exchange energy with the molecule, for example by exciting a vibrational state, which adds a further transport channel, as shown in Fig. 2.3(a). Due to the fact that inelastic transport channels have transmission coefficients much smaller than elastic ones, they may not be visible in the $I - V$ or $\mathrm{d}I/\mathrm{d}V$ curve, as shown in Fig. 2.3(b) and (c), but can be discerned by measuring the second derivative $\mathrm{d}I^2/\mathrm{d}V^2$, as indicated in Fig. 2.3(d). Due to the fact that IETS is sensitive to vibrational states, which for a given molecule can also be extracted by optical spectroscopy, it allows an identification of the molecule in the gap via it's vibrational "fingerprint" [Wang04], a survey on IETS is given in Ref. [Hipps02].

2.1.3 The Single Electron Transistor

Single molecule electronics is not only interesting due to the single nanometer size-scale of the molecules, but also due to the fact that the tunneling density of states depends on the chemical structure of the molecule itself. This should allow for an almost arbitrary tailoring of the device properties [Joachim05,Tao06], creating new possibilities for circuit design. Both the modeling and calculation of these properties is a complex task which was not performed in this thesis. In contrast, colloidal quantum dots and
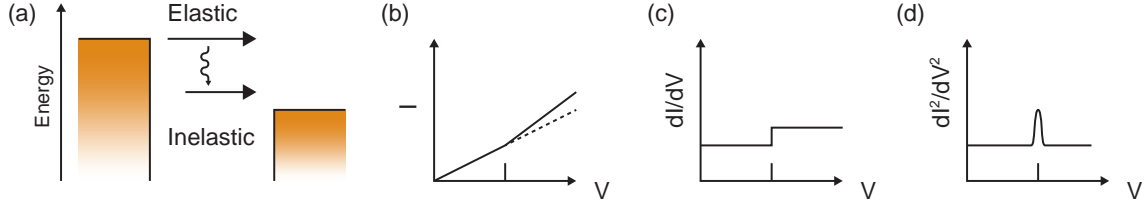
Figure 2.3: (a) Schematic of inelastic tunneling. (b)-(d) The correspoding $I - V$, dI/dV and dI^2/dV^2 curves.

molecules weakly coupled to both electrodes display a behavior similar to the single electron transistor (SET), namely a suppression of the current for low bias voltages, which can be described by a comparatively simple model. A detailed discussion of transport in semiconductor quantum dots can be found in ref. [Ihn10].

An SET consists of an island, for example a metallic grain, a nano-crystal or a molecule, which is coupled to three electrodes, source, drain and gate, as shown in Fig. 2.4(a). Tunnel barriers between the island and the source/drain electrodes allow electrons to tunnel onto and off of the island, while the gate electrode couples capacitively and allows a change in the potential of the island.
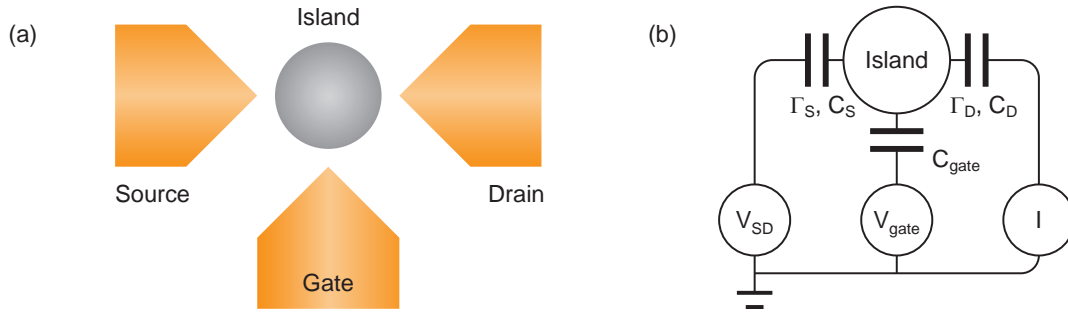
Figure 2.4: (a) Schematic layout of an SET. (b) Equivalent circuit model.

If the tunnel barrier resistances are larger than $h/2e^2$ and the barrier capacitances small, then the number of electrons on the island becomes a well defined quantity, associated with the addition energy Δ_{N+1} required to add an electron to the island. This energy is determined on the one hand by the charging energy U, which is due to the Coloumb interaction between the electrons on the island, and on the other hand by a level spacing ΔE due to the confinement of the electrons. The addition energy is therefore dependent on the degeneracy and filling of the level spacing, yielding $\Delta_{N+1} = U$ for adding an electron to an unfilled level state ($\Delta E = 0$) and $\Delta_{N+1} = U + \Delta E$ otherwise.
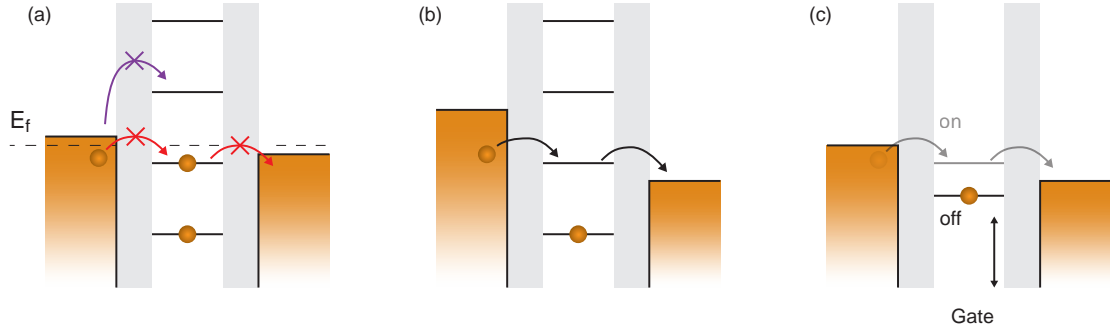
Figure 2.5: Working principle of an SET: (a) Coulomb Blockade: no energy level is
in the bias window. (b) At larger bias, electrons tunnel sequentially onto
and out of the dot. (c) The gate allows shifting an energy level into and
out of the bias window, turning the transistor "on" or "off".

The discrete level spacing influences the transport in the following way (assuming
$\Delta_{N+1} > k_B T$): If we apply a small bias and no energy level is in the bias-window,
then the electrons in the leads do not have enough energy to change the number of
electrons on the island. This is depicted in Fig. 2.5(a), where an electron from the
source cannot tunnel onto the dot as the lower level is occupied (red paths) and the
higher state is energetically not accessible (purple path). As a result, electrons can only
flow from source to drain by direct tunneling through the island, a process which is
strongly suppressed due to exponential dependence of the tunnel current on the barrier
length. Since the energy level spacing is dominated by charging for laterally confined
dots in 2DEGs, this suppression of current is called Coloumb blockade. By increasing
the bias voltage, an energy-level will eventually enter the bias window, allowing single
electrons to tunnel onto and off of the dot one by one, resulting in a current. The
energy levels on the island can be shifted by changing the gate-voltage, allowing a
transistor like-behavior between "on" and "off", as shown in Fig.2.5(c), by shifting an
energy level into and out of the bias-window. This gate dependence, in combination
with the fact that the electrons sequentially tunnel onto and off of the island, gives the
single-electron transistor it's name [Ihn10].

As each additional energy-level in the bias-window adds another "current channel",
the $I - V$ curve displays characteristic current steps, the "Coloumb staircase", depicted
in Fig. 2.6(a). Furthermore, by sweeping both the bias and the gate voltage while
measuring the current, characteristic diamond-shaped regions of current suppression are
obtained in a density plot, referred to as "Coloumb diamonds", as shown in Fig 2.6(b).
The plotted diagram corresponds to the ideal case where the coupling of both source
and drain are equal and the level-spacing is given by the height of the diamond. In the

asymmetric case, the diamonds become "tilted", shown schematically in Fig. 2.7(a).
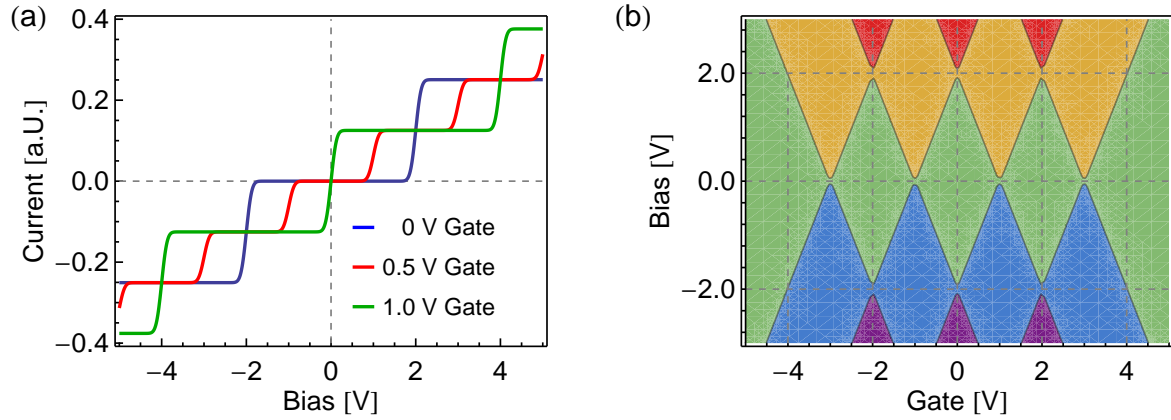
Figure 2.6: (a) Schematic I-V curves for different gate voltages. (b) Schematic density plot of the current vs. bias and gate voltage.

Important parameters of an SET are not only the level spacing, but also the different coupling of the source, drain and gate electrodes to the dot. These parameters influence the slopes of the diamond, thus allowing them to be extracted from a diamond measurement, as shown in Fig. 2.7, a detailed derivation is given in [Averin91].
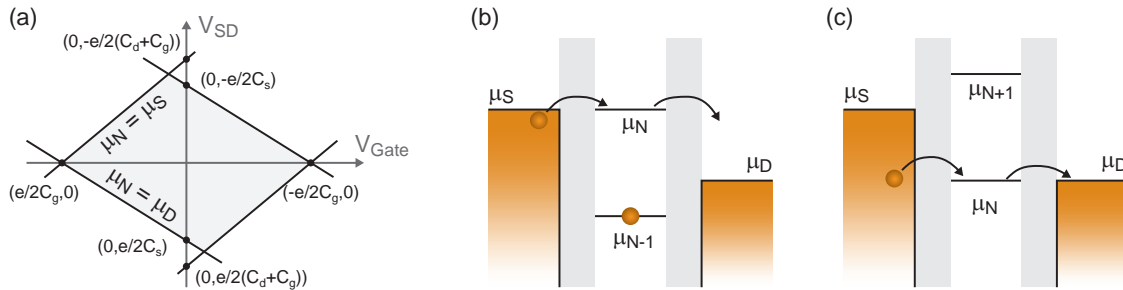
Figure 2.7: (a) Dependence of the a Coloumb diamond on the coupling capacitances. Two example boundaries of the coloumb diamond are given by the conditions $\mu_N = \mu_S$, illustrated in (b) and $\mu_N = \mu_D$, illustrated in (c).

2.1.4 Light-Induced Transport

A major issue facing investigations of break-junction-based nano-object devices is the inherent uncertainty in what type of molecule or object is present in the gap. The single nanometer size-scale of both the gap and the molecule does not allow for microscopy. Furthermore, transport is dependent on the atom-scale geometry of the electrodes and

the orientation of the object, such that two similar devices with the same object may show drastically different transport properties [Böhler04]. This motivates the search for techniques to identify the object in the gap, one example, IETS has already been mentioned.

A further possibility is illuminating the device of interest with monochromatic light and measuring the resulting photo-current. Performing this measurement at different wavelengths should, in principle, facilitate the identification of the molecule by using a combination of photo-current spectroscopy and transport spectroscopy. Additionally, depending on the involved photo-transport mechanism, it is possible to optically probe the DOS at an equivalent bias of several volts, a level at which typical devices become unstable. The implementation of such measurements is one of the main objectives of this thesis.

Other types of measurements involving the combination of single-molecule devices with a source of illumination have been demonstrated, for example, photo switching of a single molecule [Dulić03] and the correlation between Raman spectroscopy and electric conductance [Ward08]. Furthermore, a wavelength dependent study of conductance enhancement in APCs was performed by in Ref. [Guhr07].

Photo-induced transport in devices formed by break-junctions faces several difficulties, the main being heating induced by photon absorption, which may cause an expansion of the electrodes and thus changes the electrode/molecule coupling [Würfel05, Natelson12]. A successful experiment therefore is required to verify that the measured photo current is not due to heating. Heating issues are further aggravated by the small size of the nano-object, typically on the order of 0.5 nm for molecules and five nm for colloidal Quantum Dots, compared to a illumination spot size of several hundred nm, requiring intensities of 1-100 kW/cm^2 to achieve a measurable photo current. Fortunately, this issue is mitigated by a field enhancement in the nano-gaps due to collective electron oscillations, also known as plasmon resonances [Ward07], by factors which can exceed 1000 [Ward10, García-Martín11].

The observed photo current itself can have several origins: enhanced tunneling by photon absorption or emission [Tien63, Ward11], excited electron tunneling [Ittah09] and exciton creation. These three different mechanism will be examined in more detail in the following.

Photon-Assisted Tunneling

Early investigations of tunneling in microwave irradiated superconducting diodes showed evidence of absorption or emission of photons by the tunneling electrons, called photon-assisted tunneling (PAT). A quantitative description of this phenomena was given by

Tien [Tien63], which is now known as Tien-Gordon theory. Although originally derived for microwave frequencies, the theory can also be applied to the optical regime where it has been used to describe the photo-current in APCs [Viljas07, Ittah08] and nano-gaps [Ward10, García-Martín11].

Irradiating a tunnel junction with light leads to the creation of a time-dependent potential difference between the two leads of the form $V_l \cos(\omega t)$. If we assume the Hamiltonian of an electron in one of the leads to be given by H_0, then the light field simply adds the potential difference, leading to $H = H_0 + V_l \cos(\omega t)$. If the wave-function of an electron in the absence of illumination is

$$\psi(x, y, z, t) = f(x, y, z)e^{-iEt/\hbar} \ , \tag{2.17}$$

then the time dependent potential difference will not influence the spatial distribution of the wave-function. The time dependent part can then be developed in Bessel functions J_n, leading to the wave-function:

$$\psi(x, y, z, t) = f(x, y, z)e^{-iEt/\hbar} \sum_{n=-\infty}^{\infty} J_n(eV_l/\hbar\omega)e^{-in\omega t} \tag{2.18}$$

and the current is found to be

$$I(V) = C \sum_n J_n^2(eV_l/\hbar\omega) \int \left(f_1(E - eV) - f_2(E + n\hbar\omega)\right) \rho_1(E - eV)\rho_2(E + n\hbar\omega) \ \mathrm{d}E \ , \tag{2.19}$$

where $\rho_\alpha(E)$ is the density of states of electrode α and C is a proportionality constant. This result can be rewritten using the transmission function $\mathcal{T}(E)$. The low temperature linear conductance, assuming a constant DOS in the leads, is then given by [Viljas07]:

$$G(\omega) = G_0 \sum_n \left(J_n^2(eV_l/2\hbar\omega)\right) \mathcal{T}(E + n\hbar\omega) \ . \tag{2.20}$$

In this picture, electrons can tunnel through the device by absorbing or emitting a photon, thus allowing them to access $\mathcal{T}(E \pm n\hbar\omega)$, as shown in the schematic in Fig. 2.8(a). For single-molecule devices and optical frequencies, this corresponds to probing the density of states at the equivalent bias voltages of several volts. Such large bias voltages typically cannot be applied, as the large electric field leads to device instability or even device destruction.

For an APC, the expected change in conductance due to laser illumination has been calculated for several different metals using a quantum chemistry approach [Viljas07]. The calculations predict an increase in the conductance for an aluminum APC at wavelengths shorter than 800 nm, while for a platinum APC a decrease in the conductance is expected in the optical range.
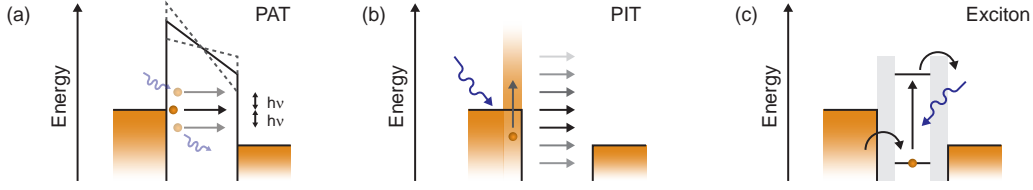
Figure 2.8: (a) Photo-assisted tunneling: electrons can access additional states by absorbing or emitting photons. (b) Photo-induced transport: The energy distribution of the electrons is modified by the impinging photons. (c) Photo-excitation: an electron-hole pair is created by the absorbed photon, which decays into the leads.

The results for a gold APC are illustrated in Fig. 2.9, where the transmission function of the APC and it's decomposition into different channels as a function of energy is shown in the upper plot. The transmission is flat around $\pm$ 1 eV, with an increase in transmission close to -2 eV due to the d-orbital. The expected change in conductance due to illumination with light is plotted in Fig. 2.9 (a)-(c) as a function of wavelength and for different approximations. Plot (a) and (c) assume a step-like light field profile, with (c) additionally assuming a "wide-band" approximation for the leads, while a linear profile is assumed for plot (b). Qualitatively, all three plots show an increase in conductance for red light and a decrease for blue light with the transition in the green range, which is due to the influence of the d-orbital. The exact energy dependence is strongly influenced by the choice of the voltage profile.

Photo-Induced Transport

When illuminating an APC with light, the power dependence of the conductance enhancement due to PAT is expected to follow a Bessel curve. This was investigated by Ittah [Ittah09], showing evidence for the bessel-like power dependence at 635 nm and 781 nm illumination wavelength. At 532 nm, however, the power dependence was found to be linear. To explain this deviation, a different transport mechanism, named photo-induced transport (PIT), was proposed, based on the fact that gold absorbs 30% of the incident radiation at 532 nm, but less than 5% at the other two wavelengths. This frequency dependence is caused by the $5d$ to $6s$ transition, which, for gold, absorbs light below 500 nm. Green light can thus generate hot electrons, which leads to a modified electron distribution function, schematically shown in Fig. 2.8(b), with a reduced electron population in the interval $[E_F - \hbar\omega, E_F]$ by a fraction θ, which is shifted
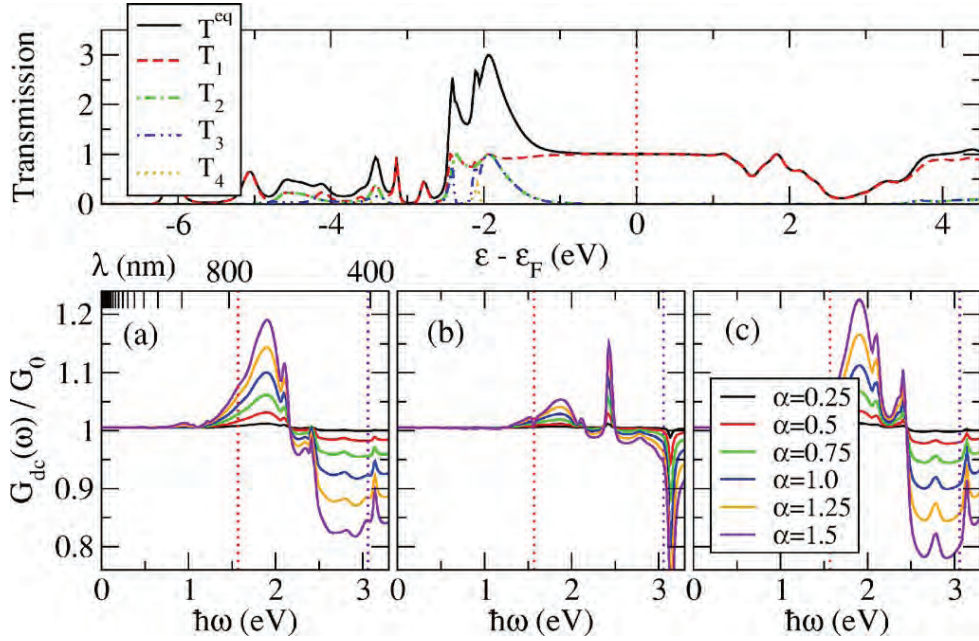
Figure 2.9: Transmission function and expected photo responce of a gold APC. The different responses correspond to different voltage drop profiles. Taken from [Viljas07].

upward into the interval $[E_F, E_F + \hbar\omega]$. The photo-current can then be expressed as

$$
\begin{aligned}
I_{PIT} &= \frac{2e}{h} \left(\int_{E_F - \hbar\omega}^{E_F} \mathcal{T}(E) \left[f_1(E)(1-\theta) - f_2(E) \right] \mathrm{d}E \right. \\
&+ \left. \int_{E_F}^{E_F + \hbar\omega} \mathcal{T}(E) \left[f_1(E) + \theta f_1(E - \hbar\omega) - f_2(E) \right] \mathrm{d}E \right) .
\end{aligned}
\tag{2.21}
$$

The shifted fraction of electrons depends linearly on the photon flux, giving rise to a linear relationship between illumination intensity and conductance change. Furthermore, the magnitude of the photo current in gold is expected to be negligible in the red and infrared compared to PAT, but dominant for green and blue, as the shifted fraction of electrons θ depends on the reflectivity of the material at the considered wavelength. Thus, PIT may be either enhanced or suppressed by the choice of electrode material used in the investigations.

Photo Excitation

A last mechanism for photo-induced transport is the excitation of an electron in the molecule or quantum dot, as illustrated in Fig. 2.8(c). For allowed optical transitions, a

photon is absorbed by an electron, shifting it to an excited state, leaving a hole behind. Both the electron and hole then decay into the electrodes, leading to a photo current, which depends linearly on the quantum efficiency of the molecule, the incident power and the coupling of the nano-object to the electrodes.

2.1.5 Nanometer-scale Objects

Three different types of nanometer-scale objects where used to form the devices investigated in this thesis, C_{60}-molecules, CdSe colloidal quantum dots and single-walled carbon nanotubes (CNT). The devices formed by each of these objects are expected to exhibit different types of behavior, such as tunneling for C_{60}-based devices and Coloumb blockade for CdSe quantum dots and CNTs, which will be discussed in the following.

C_{60} Molecules

The C_{60} molecule is a spherical molecule of roughly 1 nm diameter, consisting of 60 carbon atoms arranged in 12 pentagons and 20 hexagons. A 3-dimensional model is shown in Fig. 2.10 (a). Due to the high symmetry of the molecule only a small number of different molecular orientations with respect to the electrodes are possible. As a result, C_{60} is well suited for single-molecule experiments, ranging from the basic transport properties in vacuum [Bohler07] and liquid [Grüter05], over the demonstration of single molecule transistors [Park00,Yu04,Champagne05], to investigations of the Kondo effect [Liang02,Park02,Yu04,Parks06,Roch08] and endohedral nitrogen spins [Grose08]. The C_{60} molecule can therefore serve as a benchmark, providing investigations into the radio-frequency and optical behavior with a number of reference measurements on the same system.

For single C_{60} devices, two regimes are possible. In the low coupling regime, the molecule is weakly coupled to both electrodes and exhibits Coloumb blockade, leading to 1-100 MΩ device resistances even in the conducting case [Champagne05]. In the high coupling case, where the molecule couples well to both electrodes, the conductance can reach 0.1 G_0 [Bohler07] and the dI/dV spectrum shows several peaks spaced by roughly 50 meV.

For photo-current measurements, the absorbance spectrum is of interest, shown for C_{60} in toluene in in Fig. 2.10(b). A sharp peak is situated at 404 nm, as well as two broad peaks around 540 nm and 600 nm [Hare91]. The origin of these features is attributed to the transition between ground and first excited state in case of the 404 nm feature and a number of orbitally forbidden electronic transitions accessible via vibronic coupling in case of the larger feature [Leach92].
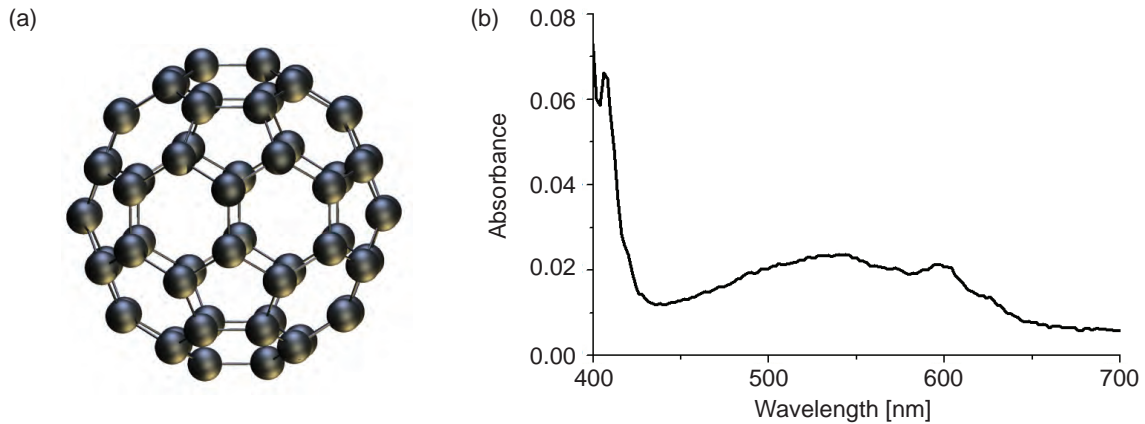
Figure 2.10: (a) CAD model of a C_{60}-molecule. (b) Optical absorbance spectrum of C_{60} in toluene [Topliuchao].

Colloidal Quantum Dots

Utilizing chemical synthesis it is possible to grow semiconductor nanocrystals from precursors with a size control on the order of 0.1 nm [Zlateva07], which allows tuning the bandgap via the crystal size [Alivisatos96]. This tunability makes nanocrystals interesting, both for electronic devices, as their charging energy in an SET configuration is on the order of 10s of meV [Klein96], as well as from an optical point of view, where they can be used for a variety of devices, ranging from LEDs [Colvin94, Dabbousi95, Wood09] to solar cells [Huynh02, Ginger99]. A TEM image of 5 nm CdSe nanocrystals is shown in Fig. 2.11(a).

To create single-quantum dot devices, the electrodes are coated with a linker molecule, for example hexanedithiol, which forms chemical bonds to both the electrodes and the nano-crystal and provides for tunnel barriers to the source and drain. Transport through such devices shows Coloumb diamonds, where larger diamonds alternate with smaller ones, consistent with a shell-filling model. This is due to the similar energy scale of the charging energy U and confinement-induced level spacing ΔE. As each confinement level can be filled with two electrons, the diamond heights alternate between U and $U + \Delta E$ [Klein96].

Colloidal quantum dots absorb light above their bandgap, illustrated by the blue curve in Fig. 2.11(b), which can be re-emitted at a wavelength corresponding to the lowest optically allowed transition (red curve). Both tunneling and optical spectroscopy of semiconductor nanocrystals are discussed in Ref. [Banin03].

(a)

(b)
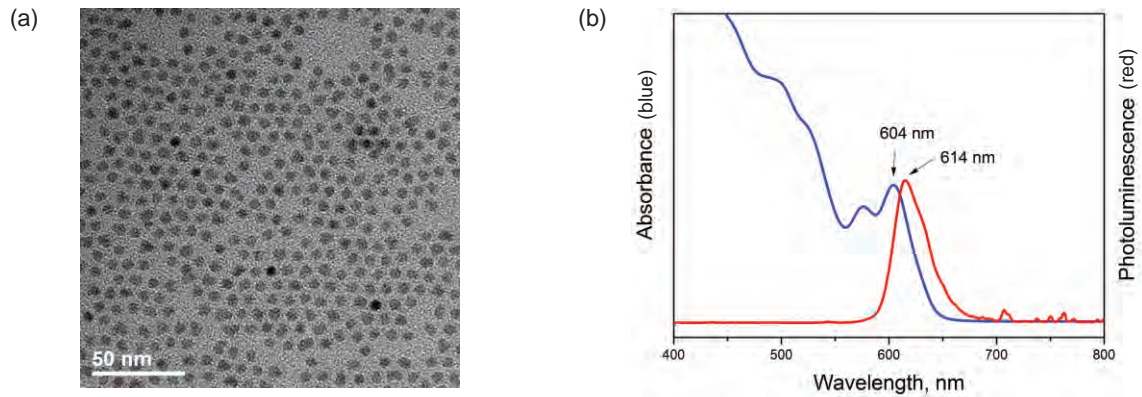
Figure 2.11: (a) TEM image of 5 nm CdSe colloidal quantum dots dispersed on a substrate [Yarema]. (b) Absorption and fluorescence spectrum of the dots shown in (a) [Yarema].

Carbon Nanotubes

Single-walled carbon nanotubes (CNTs) consist of a single sheet of carbon atoms, also known as graphene, rolled into a tube. A 3 dimensional model is shown in Fig. 2.12(a). These tubes can exhibit either metallic or semiconducting behavior, depending on how the sheet is rolled up with regard to the lattice [Ilani10]. Their small size makes semiconducting CNTs a candidate for replacing silicon based transistors, motivating a number of studies on RF properties of CNTs. The operation of single CNT transistors has been demonstrated in the GHz range [Chaste08, Li04] and the parameters of the small signal equivalent circuit were extracted from such measurements [Nougaret10]. Furthermore, the AC and DC properties have been shown to be similar for well coupled devices [Yu05b, Yu06].

(a)

(b)
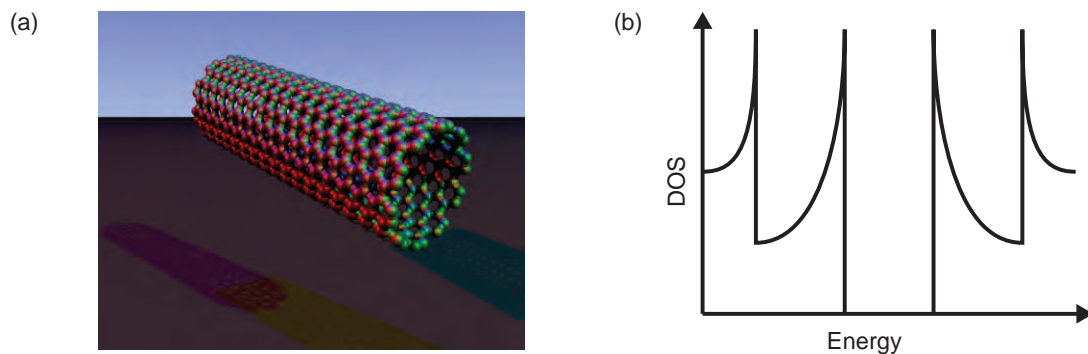
Figure 2.12: (a) CAD image of a single-walled CNT [Arnero]. (b) Schematic of the DOS for a semiconducting CNT [Biercuk08].

Single-walled carbon nanotubes are furthermore interesting for the study the physics of one-dimensional systems, which, for example, manifests itself in the DOS as the van Hove singularities [Van Hove53], sketched in Fig. 2.12(b) for a semiconducting tube [R.98]. CNT devices have been used to investigate quantum capacitance [Ilani06, Dai09], and microwave photon-assisted transport [Meyer07]. An overview of transport phenomena in CNTs is given in [Biercuk08, Ilani10].

CNT devices are attractive for the fabrication of SETs due to the typical charging energies in the range of $5 - 20$ meV$/L[\mu m]$ [Ilani10], allowing for SET behavior to be observed at 4 K, for example by RF reflectometry [Roschier04, Lechner10, Tang07]. Furthermore, suspended CNTs are good mechanical resonators, showing resonance frequencies up to several GHz [Chaste11] with quality factors up to 10^5 [Hüttel09]. These properties have been utilized to demonstrate yoctogram mass-sensing [Chaste12]. Typically, resonance frequency measurements are performed using a frequency modulation measurement technique [Gouttenoire10], but the mechanical motion also couples to charge transport [Steele09, Lassagne09]. This should allow RF investigations of mechanical motion using an RF CNT SET with suspended nanotube. In addition, CNTs absorb light in the optical frequency range, generating photo-current if voltage-biased and allowing for scanning photo-current microscopy [Buchs11].

2.2 Break-Junctions

Creating a single-molecule or nano-object device requires a pair of electrodes separated by a nanometer sized gap for the object of interest, a size scale beyond the reach of state-of-the-art electron beam lithography. A different fabrication approach is therefore necessary, which is discussed in this section. Many strategies have been proposed and implemented to address this issue, one flexible and widely used approach is the use of a scanning tunneling microscope (STM) to contact the object of interest, which is placed on a conducting substrate [Joachim97]. Other approaches involve, for example, crossed wires, which are coated with the molecules of interest and then brought into contact [Kushmerick02].

A different approach is the use of so called break-junctions, consisting of a small metal wire, which is broken in a controlled manner to create a nanometer sized gap. While this method is less flexible than using an STM, break-junctions require a significantly less complex setup by eliminating the need for moving stages and feedback circuits, while at the same time offering a much larger mechanical stability, due to which a vibration isolation is not paramount. Furthermore, an electrostatic gate can be added, allowing a better characterization of the devices under investigation.

Two different kinds of break-junctions were investigated in this thesis, mechanically controlled break-junctions (MCBJs), where the wire is mechanically stretched until it breaks, and electromigrated break-junctions (EMBJs), where current induced atom migration is used to form the gap. The details, merits and drawbacks of the two techniques are explained in the following.

2.2.1 Mechanically Controlled Break-Junctions

Although MCBJs are often used to create single molecule devices and to study their properties, they were originally developed to study supercurrents arising between two superconductors separated by a tunnel junction, also known as the Josephson effect [Josephson62]. While the Josephson effect is observable by using the native oxide of, for example, aluminum as the tunnel barrier between two overlapping electrodes, a better system to systematically study the effect involves a vacuum tunnel barrier with controllable width. A significant step toward this goal was the invention of the STM in 1982 [Binnig82], where the working principle is based on maintaining a tunnel barrier of specific width using a feedback loop. The first STMs, without the feedback loop, were not mechanically stable enough to allow for a rigorous investigation of the Josephson effect in a vacuum gap. Inspired by the STM, a method was developed which utilizes the surface strain of a bending beam to break the brittle superconductor deposited on the surface [Moreland85], creating a tunable and mechanically stable gap at the expense of losing the lateral scanning ability. This technique was then extended to non-brittle materials by gluing a notched metal wire to a flexible substrate at two points [Muller92a], the mechanically controlled break-junction (MCBJ). To improve stability, the attached metal wire was replaced by a micro-fabricated gold bridge [Zhou95, vanRuitenbeek96], which now is the typical MCBJ design.

The working principle of an MCBJ, illustrated in Fig. 2.13, is based on the fact that the top surface of a beam expands as as the beam is bent. By placing a partly suspended wire on the beam, this expansion is translated by the anchor points into a stretching δu of the wire. The amount of stretching is related to the distance between the anchor points u and the surface expansion, which in turn depends on the bending radius and beam thickness t. If the beam is pressed against two counter-supports separated by a distance L, as shown in Fig. 2.13, the relationship between the bridge elongation δu and the displacement δz is linear and can be expressed as $\delta u = r\delta z$. The displacement ratio r can be calculated using elastic beam theory and is given by [vanRuitenbeek96]:

$$r = \frac{6tu}{L^2}. \tag{2.22}$$

Vibrations in the setup cause noise on the displacement δz and thus on δu, which can

be suppressed by a small displacement ratio r. Since the practical implementation imposes both an upper limit on the counter support separation L and a lower limit on the substrate thickness t, vibration suppression is mainly achieved by using the small bridge span u achieved in a miniaturized MCBJ.
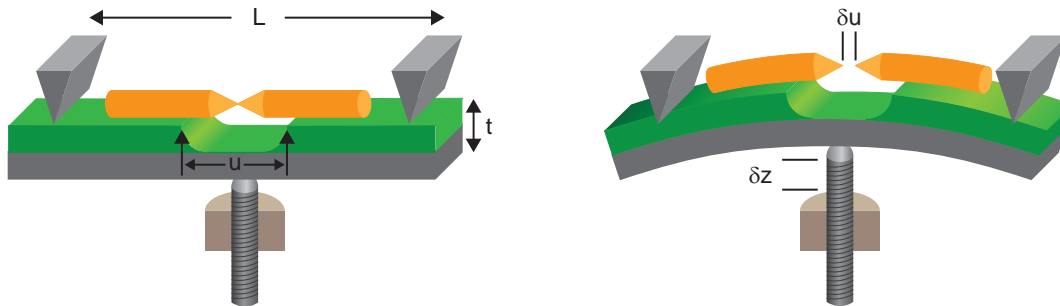
Figure 2.13: Working principle of an MCBJ: A substrate with a suspended bridge is placed against two counter supports (a) and bent by a screw or other actuator (b). The lateral displacement δu can be tuned by varying the amount of bending δz.

The MCBJs used in this thesis are fabricated either on 275 μm thick silicon or 500 μm sapphire substrates. These two substrates were chosen due to the fact that silicon is a standard substrate for micro-fabrication, whereas sapphire is used for RF devices due to the very low dielectric loss (see also Section 2.3.4). Furthermore, sapphire is optically transparent, which mitigates heating issues in optical investigations. We use a countersupport separation of $L = 10$ mm, which, together with a typical bridge span of 500 nm, results in a displacement ratio of 8.25 10^{-6} and 15 10^{-6} respectively. The implemented setup (see Section 4.1) has a vertical step size of 33 nm, which translates into an electrode separation resolution of 0.27 and 0.5 pm per step.

Both silicon and sapphire will break if a maximum bending radius is exceeded, limiting the maximum vertical displacement to between 100 μm and 150 μm. As a consequence, the maximum achievable elongation is between 1.3 nm and 1.5 nm. In contrast to MCBJs fabricated on flexible metal substrates [vanRuitenbeek96], this not only limits the amount of opening/closing cycles, but also precludes a pure mechanical breaking of even a 20 x 20 nm^2 cross-section gold wire, which needs be thinned by other means, such as electromigration, to a cross-section on the order of ten atoms before mechanical breaking is feasible.

2.2.2 Theoretical Aspects of Electromigration

The first demonstrations of single-molecule devices in the late 1990's [Joachim97, Reed97] initiated the search for a scalable method to create nm spaced electrodes, envisioning integrated circuits based on molecular electronics. During this search, it was discovered that nm and sub-nm gaps can be formed by using current induced mass flow, also called electromigration, to break thin gold wires. This method creates electrodes that are mechanically very stable and the breaking process only requires the voltage source already present for device characterization [Park99]. Due to their simplicity and stability, electromigrated break-junctions are often utilized, although device fabrication is a one-way stochastic process with an often very low yield, requiring tens to hundreds of junctions to be broken and measured before a small set of working devices is attained.

In this subsection a brief summary of electromigration theory is first given and the details of electromigrating a junction is discussed. Different types of feedback methods to achieve controlled breaking are discussed and a short overview of gated break-junctions ends this section.

Electromigration Theory

Electromigration is the process of directed metal ion diffusion, caused by momentum transfer from the scattered electrons to the metal ions at large current densities. Although discovered in 1861 [Gerardin61], electromigration did not attract much interest until the advent of integrated circuits in the 1960s, when it was discovered to cause failure of integrated circuit conductor lines [Black67]. The small dimensions of these lines and their high thermal contact to the substrate allow current densities large enough to induce electromigration, forming voids or hillocks and thus causing failure of the circuits.

The process of electromigration can be described by considering the behavior of the atoms constituting a metal [Pierce97]. Individual atoms may leave their lattice site and jump to an adjacent empty site due to their thermal energy, but without a driving force, the jumps happen in a random direction and do not lead to a mass flow. Since a vacancy is required for the atom to change sites, the atom flux can be derived by instead analyzing the vacancy flux, which is equal to the atom flux but in the opposite direction. The vacancy flux J for a conductor with an applied field is given by [Pierce97]:

$$J = -D\frac{\partial c}{\partial x} + \frac{Dc}{kT}Z^*eE = -D\frac{\partial c}{\partial x} + \frac{Dc}{kT}Z^*e\rho j \ , \qquad (2.23)$$

where D is the diffusivity, c the vacancy concentration, T the temperature, k the Boltzmann constant, e the electric charge, E the applied electric field, ρ the resistivity

and j the current density. The effective charge Z^* is a material parameter consisting of two terms

$$Z^* = Z_{ew} + Z_{el} \ ,$$

where Z_{ew} denotes the momentum transfer from the electrons to the atoms ("electron wind") and Z_{el} the electrostatic force of the applied field. The effective charge is dominated by the electron wind, leading to an atom diffusion in the direction of the electron flow.

Both the directed and undirected diffusion are strongly temperature dependent, with the diffusivity D given by:

$$D = D_0 e^{-\frac{E_0}{kT}} \ , \tag{2.24}$$

where E_0 is the activation energy (e.g. $E_0 = 0.12$ eV for gold surface diffusion [Wilson00]). As a consequence, electromigration is promoted by temperature and will more likely occur at sites with lower activation energy, for example at grain boundaries.

Simply speaking, the ions will preferably diffuse if their own energy is higher (higher temperature), the barrier is lower (less activation energy) or the "wind" is stronger (higher current density). The main goal for conventional integrated circuits is to design and fabricate small interconnects in which electromigration is suppressed to ensure reliable devices with long lifetimes. In this case grain boundaries play an important role, constrictions with high current densities are avoided by proper design rules and the temperature dependence is used to extrapolate expected lifetimes from high temperature stress tests. During the fabrication of nanoscale devices, in contrast, electromigration is induced on a time scale of minutes, where grain boundaries play a subordinate role while the interplay of current density and temperature determines the result of the electrode and device formation.

Gap Formation by Voltage Ramping

A simple procedure for the electromigration of a break-junction is to apply a voltage ramp of a several mV/s. This bias increase not only induces a rise in the current density through the constriction, but also an increase in the constriction temperature via Joule heating. At some voltage V^* the combination of heating and current density is large enough to induce electromigration, leading to a narrowing of the constriction. Due to the strong temperature dependence of the diffusivity (Eq. 2.24), this onset is mainly determined by the temperature of the junction [Strachan05, Trouwborst06], where measurements have shown that the initiation temperature is in the range of 340-400 K, independent of the starting temperature of the junction [Trouwborst06]. Hence, the migration process of a given junction is characterized by the critical power P^*

necessary to reach this temperature, which depends both on the ambient temperature and the geometry of the break-junction [Esen05].

Early migration methods simply applied a bias-ramp to the break-junction until a given resistance threshold was reached, for example the conductance quantum (12.9 kΩ). While this method is viable, the results depend critically on the lead resistances of the junction, as is shown in the following.

If we consider the case where a bias of V_{tot} is applied at the leads, the voltage V_j dropped over the junction is given by

$$V_j = \frac{R_j}{R_j + R_l} V_{tot} \ , \tag{2.25}$$

where R_j is the resistance of the junction and R_l the lead resistance. The voltage V^* and current I^* associated with the critical power P^* can then be expressed as a function of the junction resistance R_j:

$$V^* \ = \ \frac{R_l + R_j}{R_j} \sqrt{P^* R_j} \ , \tag{2.26}$$

$$I^* \ = \ \sqrt{\frac{P^*}{R_j}} \ . \tag{2.27}$$

Depending on R_l, the migration of the break-junction will show three different types of behavior: a monotonic resistance increase, a jump in resistance followed by a monotonic increase or an uncontrolled breaking resulting in a gap larger than 10 nm, also called thermal runaway. The behavior of the critical voltage and current for a critical power of $P^* = 110\ \mu$W and different lead resistances is plotted in Fig. 2.14 as a function of increasing junction resistance, starting with $R_j = 0.9\ \Omega$, a typical value, at the top of each plot and ending at $R_j = 37\ \Omega$ at the bottom right, the points indicate $R_j = 1,5,10$ and $30\ \Omega$. The starting value of R_j is chosen such that the initial values of V^* and I^* are similar to experimentally obtained values. The red dashed line in (b) and (c) indicates the $I - V$ curve of a voltage ramp applied to the un-migrated junction, which, for better visibility, is not shown in (a).

In the case of no lead resistance, the critical voltage V^* increases with increasing resistance, as shown in Fig. 2.14(a). Once the electromigration threshold has been reached, the increasing resistance of the junction limits the dissipated power thus stopping the electromigration until the bias is further increased.

Introducing a lead resistance changes the behavior of the critical voltage V^* significantly. As shown in Fig. 2.14(b) and (c), the critical voltage first decreases with increasing junction resistance, as an increase in R_j leads to an increase in the voltage V_j dropped over the junction. As a consequence, the dissipated power also increases,
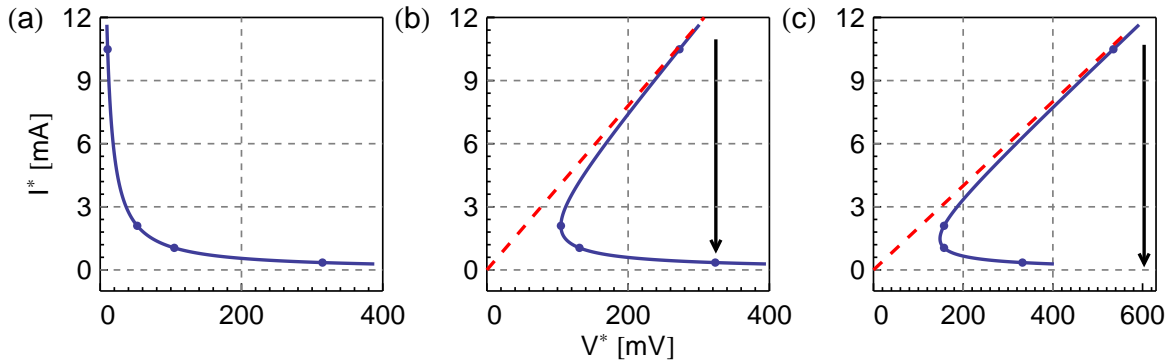
Figure 2.14: Critical voltage and current as a function of increasing junction resistance R_j, the points indicate 1,5,10 and 30 Ω respectively. (a) No lead resistance, (b) $R_l = 25\ \Omega$, (c) $R_l = 100\ \Omega$.

migrating the junction even further. Since there is no self-limiting, this part of the critical voltage curve is called the unstable branch [Hoffmann08]. At $R_l = R_j$ the behavior changes to an increase in U^* for increasing R_j, which is termed the stable branch due to presence of the self-limiting effect.

For non-zero lead resistances, a voltage ramp (red dashed line) will therefore lead to a jump in resistance once the first threshold is reached, from the unstable branch to the stable branch, as indicated by the arrows in Fig. 2.14(b) and (c). In case of intermediate lead resistances, this is not critical, as indicated in Fig. 2.14(b). For large lead resistances, in contrast, the voltage required to initially trigger the migration on the unstable branch may have a corresponding resistance on the stable branch which is larger than the conductance quantum, leading to thermal runaway and a resulting gap larger than 10 nm [Esen05]. This case is illustrated in Fig. 2.14(c), where the stable branch ends at a lower value of V^* than required to initiate the electromigration on the unstable branch.

In summary, the successful electromigration of a break-junction using a simple voltage ramp requires the minimization of the lead resistance R_l. This may be achieved by optimizing the wiring and sample design or by making use of a four-point resistance measurement [Wu07].

Feedback Algorithms for Controlled Electromigration

In practice, setup or sample constraints may prohibit lowering the lead resistance R_l sufficiently for stable electromigration to be possible with a simple voltage ramp. In this case, thermal runaway can, however, still be avoided by augmenting the voltage ramp with a feedback method, which decreases the applied voltage below V^* once

electromigration has been detected. The ramp is then restarted again, subsequently migrating the junction in a number of iterations. Due to the fact that electromigration is a comparatively slow (100 ms timescale) process, feedback algorithms can easily be implemented in a setup consisting of a computer controlling a source-measure unit.

A generic feedback algorithm applies a bias voltage, measures the current and either increases or decreases the bias depending on the outcome of the electromigration detection routine. This detection method is vital to ensure a successful migration and three different detection methods were utilized in this work, which are explained in detail in the following. Additional control measures include voltage and current limitations as well as a target resistance above which the algorithm sets the bias to zero and stops.

The first migration detection method utilizes the fact that upon migration, the resistance of the junction changes in time. At each voltage increment, the normalized change in resistance $1/R \, \partial R/\partial t$ is numerically calculated and once a given threshold is exceeded, the voltage is reduced and the ramp started again. While this method works well for junction resistances below 100 Ω, the time differential is increasingly noisy for larger junction resistances, making the detection method unreliable. Furthermore, in an experiment utilizing a similar algorithm, Coloumb blockade was observed in clean junctions, suggesting the formation of gold nano-particles in the gap [Houck04]. Such a background signal makes it difficult to distinguish the signal originating from nano-particles placed on the junction on purpose from that of residual gold particles, making this breaking algorithm ill-suited for most nano-device applications. Other methods typically do not display Coloumb blockade behavior for empty junctions and are therefore more suited.

The second method compares the measured resistance of the junction at each voltage increment to a reference resistance and triggers the voltage reduction once a given deviation percentage is reached [Strachan05]. This reference resistance is initially set to the resistance of the junction at the beginning of the ramp and updated after each reduction of the voltage to the current junction resistance measured at the ramp beginning. For low lead resistances ($R_l \approx 10\Omega$) this method works well, but requires adjustment of the threshold as the junction is migrated, from typically 5% at the beginning to more than 50% for junction resistances above 300 Ω. For lead resistances larger than 20 Ω, the detection method is not reliable due to Joule heating of the leads. This causes a substantial increase in the total resistance as the ramp increases, leading either to a premature reduction in voltage without migration, or a failure in detection and thermal runaway.

The third migration detection method is based on the idea that electromigration causes an irreversible change in the resistance of the junction which is manifested in the $I - V$ characteristic as negative differential conductance. Therefore, the voltage

at which the differential conductance changes sign can be interpreted as the critical voltage U^* at which electromigration starts. Based on this observation, the detection method calculates the differential conductance using a finite difference method at each voltage step V_i:

$$\frac{dI}{dV}\bigg|_{V_i} = \frac{I_i - I_{i-1}}{V_i - V_{i-1}} \ , \tag{2.28}$$

and reduces the applied voltage as soon as $dI/dV < 0$, restarting the voltage ramp. For the initial migration with lead resistances on the order of 200 Ω, a slow ramp (1mV per step) and a small positive threshold, typically 0.01, may be chosen to account for the finite response time of the feedback method. Later, at a junction resistance of $R_j > 50$ Ω, a negative threshold value and larger steps can be used to induce larger resistance changes per feedback iteration. A similar approach is applied in Ref. [Saha11], but only came to notice during the preparation of this thesis.

Once the resistance of the junction is larger than the resistance of the leads, electromigration becomes self-limiting and a feedback algorithm is no longer necessary. For junction resistances approaching 1 kΩ, however, the time-scale on which electromigration takes place changes, as the junction has a cross-section on the order of 10 atoms and the resistance evolution is dominated by removing single atoms. As the time-scale is typically several orders of magnitude faster (sub ms to 10 ms timescale), a different approach is necessary to ensure a controllable migration.

The Final Atoms

In the final stages of breaking a clean junction using electromigration, the size of the junction is comparable to the mean free path of the electrons in the metal, such that electron transport through the junction is no longer diffusive, but quasi-ballistic [Wu07]. Therefore, scattering is reduced, which requires an increased bias to induce migration. Furthermore, the critical power is no longer constant but rather decreases with increasing resistance.

Transmission Electron Microscope (TEM) studies suggest that in this regime the junction narrowing proceeds according to an "unzipping" model along the crystal facets [Strachan08]. In this model, illustrated in Fig. 2.15, an edge atom is thermally excited and carried away from the junction by electromigration, leading to a vacancy. This facilitates the migration of neighboring atoms, leading to the rapid migration of the entire edge layer.

Due to the fact that electromigration is dependent on single atom excitation in the quasi-ballistic regime, the reduction of the bias voltage needs to happen on a much faster time scale than in the diffusive regime, preferably on the sub-ms timescale. This can be
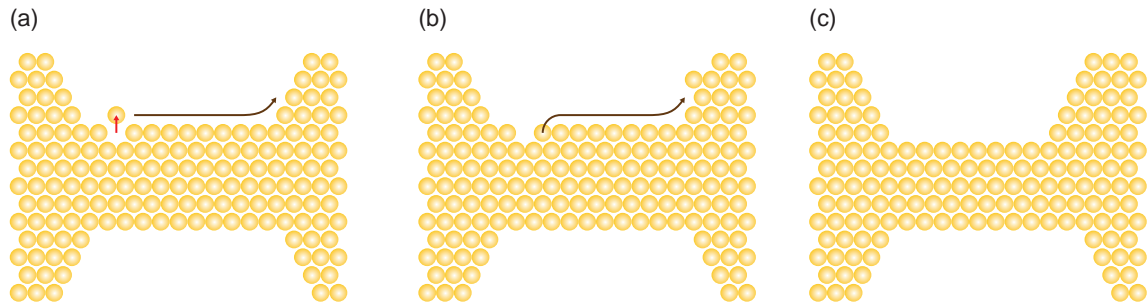
Figure 2.15: Unzipping model of breaking a break-junction (a) Thermal excitation allows an edge atom to be electromigrated. (b) The resulting vacancy facilitates the migration of neighboring atoms leading to the migration of the entire edge layer (c).

achieved using fast electronics, for example based on field-programmable gate arrays (FPGA) [Roch08]. A second possibility is the use of voltage pulses [Hayashi08,Ittah08], where a short (μs to ms) voltage pulse with large amplitude (500-900 mV) is alternated with a longer low amplitude (typically 10-20 mV) pulse to determine the resistance. Electromigration is started at the beginning of the large amplitude pulse, but is limited in time by the pulse duration, while the probe pulse amplitude is chosen low enough not to induce any migration. This method is comparatively easy to implement, a simple algorithm consists of performing a pulse sequence, comparing the resistance to a target resistance and either stopping the procedure or repeating the pulse scheme, with the option of increasing the short pulse amplitude.

A third possibility to break the junction in the final phase is the use of mechanical breaking, requiring the device to have been fabricated as a suspended bridge. For MCBJs on sapphire or silicon substrates, electromigration is necessary to allow a mechanical breaking due to the limited flexibility of the substrate. In this case, the junctions are migrated to a resistance on the order of 1 kΩ using a feedback algorithm, and are then broken mechanically, thus circumventing the issue of fast response times in the final migration stage.

Breaking Molecule Decorated Break-junctions

So far, electromigration was discussed for clean gold break-junctions, but for investigations of single-molecule devices, the break-junctions are typically coated with a sub-mono-layer or mono-layer of the molecule of interest. While this layer does not have an influence on the behavior of the junction in the first migration stage, it typically modifies the final phase of the the breaking. This is not surprising, as many molecules form

chemical bonds to the gold, for example the thiol groups in benzene-edithiol, leading to a more stable junction and requiring an increased voltage for breaking. Fortunately, the chemical bonds favor the formation of molecular device, not necessarily requiring an atom by atom migration in the final stage. In many cases, a simple voltage ramp, stopping at a specified resistance threshold, is sufficient to form a single molecule device in the final breaking phase. Once the device has been formed, the $I - V$ characteristics can be measured, for example as a function of an electric field applied via a gate. The implementation of such a gate is discussed in the next section.

2.2.3 Gated Break-Junctions

By adding an electrostatic gate to the break-junction, a three-terminal device is formed, which offers better insight into the transport properties of nano-object devices compared to a two-terminal device. In two-terminal devices, the experimental accessible quantities are the elastic and inelastic tunneling spectra derived from the $I - V$ curve, which depend on the coupling between the nano-object and each of the two electrodes [Bakkers00] and often do not allow for a straight-forward interpretation, even in the simple case of Coloumb blockade (see also Section 2.1.3). While MCBJs offer the possibility to tune the coupling between the object and the electrodes, application of an external electric field allows for the extraction of the individual coupling parameters and thus a better characterization of the device of interest. Application of an electric field requires a gate electrode, which can be implemented in a variety of geometries, both for electromigrated and mechanically controlled break-junctions.

The most common implementation of a gate is the back gate, where the source and drain electrodes are placed on the gate electrode, electrically isolated by a thin dielectric film. The nanometer control over film thicknesses can be leveraged to create a device-gate spacing on the order of a few nanometers. A simple version shown in Fig. 2.16(a), uses a doped silicon substrate (gray) as the gate electrode and a layer of silicon oxide (green) as the dielectric [Klein97, Yu04]. While easy to fabricate, both the maximum gate voltage and minimum oxide thickness are limited by dielectric breakdown, which in this geometry is aggravated by the large overlap between source-, drain-, and gate-electrode. This overlap can be significantly reduced by using a finger backgate, shown in Fig. 2.16(b), where the break-junction is placed on a small aluminum gate electrode (light gray) which is oxidized to provide the insulating layer [Houck04, Roch08, Song09]. In this geometry, the oxide thickness can be reduced to a few nanometers.

Back gates have also been realized for MCBJs [Champagne05], suspending the junction 40 nm above a doped silicon backgate. While this allows both a tuning of the electrode spacing and the electric field, the fabrication process is involved and the
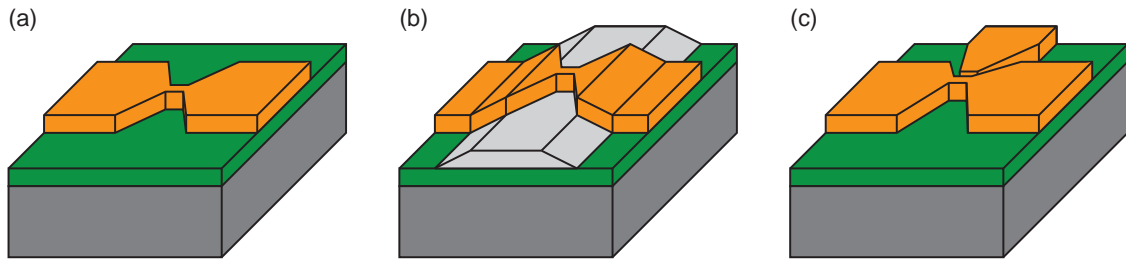
Figure 2.16: Different geometries of gate electrodes for break-junctions (a) Substrate backgate. (b) Finger backgate. (c) Side gate.

device limitations are similar to silicon/silicon oxide backgates.

A different type of geometry is the side gate, shown in Fig. 2.16(c), where the gate electrode is placed in the same plane as the source and drain electrodes, eliminating any overlap between the different electrodes. This geometry allows large gate voltages to be applied and minimizes cross coupling between the electrodes, which is important for both microwave measurements and illumination with light, while additionally being compatible with MCBJs. Fabrication requires only a single step of electron-beam lithography, but process optimization is necessary to achieve a favorable device-gate spacing. This type of gate electrode was implemented for the devices used in this thesis.

The main challenge for an electrostatic gate is the fact that the source and drain electrode size is comparatively large (20 nm x 20 nm) compared to the gap (1-5 nm). This causes significant screening of the applied electric field inside the gap where the object of interest is located and leads to a very small coupling between the device and the gate. An optimized geometry therefore requires thin electrodes to mitigate screening, a closely spaced gate to achieve maximum coupling and a gap as large as possible to allow for field penetration. A study on gate-coupling using FEM simulation [Datta09] has further shown that the nanometer scale geometry of the contacts plays a much more significant role in the gate coupling than the gate spacing or the dielectric constant. Unfortunately, the precision required for manipulation this geometry is out of range of current fabrication methods.

2.3 Radio Frequency Circuits for Reflectometry

Time-resolved measurements of the transport properties of nano-object devices are interesting not only from a fundamental research point of view, where they allow access to, for example, electron counting statistics [Gustavsson06], but also in the light of

quantum information processing, where manipulation and readout of the potential qubit needs to be performed on a time-scale smaller than the decoherence rate. In a typical DC measurement setup, where a bias is applied to the nano-object device and the resulting current is measured, the achievable time resolution is limited on the one hand by the low-pass filter formed by the device and stray wiring capacitance and on the other by the low signal-to-noise ratio due to $1/f$ noise. As a result, although the employed volt- and ammeters can achieve a time-resolution in the 10 ns to 10 μs range, the actual measurement rate is typically smaller than one kHz.

Both the low pass filter and signal-to-noise limitations can be circumvented by connecting the device to an RF resonant circuit, whose RF response is dependent on the state of the device. The combined circuit provides for a bandwidth of 10 to 100 MHz at a carrier frequency in the 100 MHz to GHz range where $1/f$ noise is significantly reduced. This concept was first demonstrated in the so called RF-SET [Schoelkopf98], where the microwave reflected at an RF tank circuit connected to a SET was measured, resulting in both a measurement bandwidth of 100 MHz and an increased sensitivity due to lowered $1/f$ noise. The measurement principle has been successfully applied to various other devices, such as QPCs [Qin06, Cassidy07, Reilly07, Muller10] and Quantum Dots [Barthel10], but mainly at frequencies below 1 GHz, where an implementation using discrete components is easily possible. The advent of cQED motivates a shift to the 4-8 GHz band to take advantage of low power, high signal-to-noise measurement techniques developed in this context, such as the use of quantum limited amplifiers. Instead of discrete components, which suffer from large parasitics in this frequency range, the RF circuits developed in this thesis are based on transmission lines, so called stub tuners, into which the device of interest is integrated on-chip, minimizing parasitics and offering significantly higher measurement frequencies.

Since the implemented devices are based on resonant circuits and transmission lines, this section will first discuss transmission line theory and the RLC resonant circuit. The RF measurement technique, which is based on impedance matching, will then first be discussed in the lumped element case, before moving on to the stub tuners themselves. At the end of the section, the properties of the implemented coplanar waveguide transmission lines will be described.

2.3.1 Transmission Line Theory

While circuit theory assumes that the size of the circuit is much smaller than the wavelength of the propagating signals, this is usually not the case when working with microwaves. Circuit theory is in this case replaced by transmission line theory, which takes variations of the voltage and phase over the length of the circuit into account.

The elements constituting a microwave circuit can be divided into two classes, *lumped elements*, whose size is smaller than $\lambda/10$ and whose behavior can be described by circuit theory, and *distributed elements*, which require transmission line theory for an accurate description. The summary of transmission line theory presented in this section follows Ref. [Pozar05].

Transmission Lines

A transmission line is a set of wires connecting two points and can be modeled as a series of lumped element units, shown in Fig. 2.17(b), consisting of the four elements R, L, C and G. The series resistor R models the resistivity of the conductor and the series inductor L the self-inductance of the line. The capacitance due to the spacing of the lines is represented by the shunt capacitor C, while any loss due to the dielectric is accounted for by the shunt conductance G. Using this model one can derive the transmission line equations for both the voltage $v(z,t)$ and current $i(z,t)$ in the line:

$$\frac{\partial v(z,t)}{\partial z} = -Ri(z,t) - L\frac{\partial i(z,t)}{\partial t} \ \ ,$$
$$\frac{\partial i(z,t)}{\partial z} = -Gi(z,t) - C\frac{\partial v(z,t)}{\partial t} \ \ .$$

From this we can derive the wave equations:

$$\frac{d^2V(z)}{dz^2} - \gamma^2 V(z) = 0 \ \ ,$$
$$\frac{d^2I(z)}{dz^2} - \gamma^2 I(z) = 0 \ \ , \tag{2.29}$$

where γ is the complex propagation constant given by

$$\gamma = \alpha + i\beta = \sqrt{(R + i\omega L)(G + i\omega C)} \ \ . \tag{2.30}$$

Here the loss in the transmission line is described by the attenuation constant α, which is function of frequency in a manner dependent on the type of transmission line. The phase constant β is related to the wavelength by

$$\beta = \frac{2\pi}{\lambda}. \tag{2.31}$$

Solving 2.29 yields traveling waves, both forward and backward, with amplitudes V_0^+, V_0^- and I_0^+, I_0^- respectively:

$$V(z) = V_0^+ e^{-\gamma z} + V_0^- e^{\gamma z} \ \ ,$$
$$I(z) = I_0^+ e^{-\gamma z} + I_0^- e^{\gamma z} \ \ .$$

Using Ohm's law, the characteristic impedance of the line is then defined as:

$$Z_0 = \frac{V_0^+}{I_0^+} = \frac{V_0^-}{I_0^-} \frac{R + i\omega L}{\gamma} \quad . \tag{2.32}$$

In the lossless case where $R = G = 0$, γ reduces to $\sqrt{LC}$ and Z_0 simplifies to $Z_0 = \sqrt{\frac{L}{C}}$.
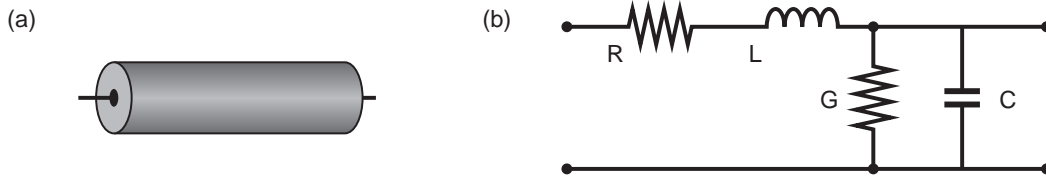
Figure 2.17: (a) Schematic representation of a transmission line. (b) Lumped-element equivalent circuit.

Terminated Transmission Lines

When a transmission line is terminated by a load with impedance $Z_{\text{Load}} \neq Z_0$ at one end, the ratio of current to voltage is fixed at this point. If a forward traveling wave of the form $V(z) = V_0^+ e^{-\gamma z}$ is applied at the input of the line, then part of the wave will be reflected at the load to satisfy the following boundary condition:

$$Z_{\text{Load}} = \frac{V(d)}{I(d)} = \frac{V_0^+ + V_0^-}{V_0^+ - V_0^-} Z_0 \quad .$$

The amplitude of the reflected wave V_0^- is

$$V_0^- = \frac{Z_{\text{Load}} - Z_0}{Z_{\text{Load}} + Z_0} V_0^+ \quad ,$$

which motivates the definition of the voltage reflection coefficient Γ as the amplitude of the reflected wave normalized by the amplitude of the incident wave:

$$\Gamma = \frac{V_0^-}{V_0^+} = \frac{Z_{\text{Load}} - Z_0}{Z_{\text{Load}} + Z_0} \quad . \tag{2.33}$$

This implies that Γ will only be zero if the load impedance is equal to the line impedance, which is also called the *matched* case. For $Z_{\text{Load}} \neq Z_0$, there will always be a finite amount of reflected wave and the load and line are *mismatched*. Furthermore, there is a one-to-one relation between the voltage reflection coefficient and the load, allowing for the determination of the load by measuring Γ.

The incident and reflected wave in the transmission line interfere with each another and create standing waves. The impedance of a terminated transmission line Z_{in} at a distance d from the load thus depends on both the load Z_{Load} and the distance d:

$$Z_{in} = Z_0 \frac{Z_{\text{Load}} + Z_0 \tanh(\gamma d)}{Z_0 + Z_{\text{Load}} \tanh(\gamma d)} \quad . \tag{2.34}$$

This shows that the impedance of the load can be transformed using a piece of transmission line. We will make use of this fact in Section 2.3.5, where two lengths of transmission line are used to transform an arbitrary load to Z_0. Note that in the lossless case, where $\gamma = i\beta = i2\pi/\lambda$, Z_{in} repeats with a period of $\lambda/2$ as the length of the transmission line is increased.

For the two special cases of the open and short termination, equation (2.34) simplifies to:

$$
\begin{aligned}
Z_{short} &= Z_0 \tanh(\gamma d) \ , & (2.35) \\
Z_{open} &= Z_0 \coth(\gamma d) \ . & (2.36)
\end{aligned}
$$

2.3.2 The Scattering Matrix

The electrical properties of a given microwave circuit can be described by considering the circuit as a network connecting the in- and output ports of the circuit. The network is then described by a matrix connecting the different ports. Depending on the type of analysis, different parameters can be used to describe voltages and currents at the ports, leading to different matrix descriptions, the most commonly used one being the scattering matrix [Pozar05].

At microwave frequencies, it is in practice comparatively easy to measure the magnitude and phase of the incident, transmitted and reflected waves, while measurement of the voltage and current are much more difficult. Since the latter quantities can be inferred from the former, the scattering matrix employs a description that is based on the directly measured quantities. Similar to the scattering matrix discussed in the framework of electron transport in Section 2.1.1, the S-parameters constituting the scattering matrix in the context of network analysis relate the incident and reflected voltage waves at each of the ports. The scattering matrix of an n-port network is hence defined as

$$
\begin{bmatrix} V_1^- \\ V_2^- \\ \vdots \\ V_n^- \end{bmatrix} = \begin{bmatrix} S_{11} & S_{12} & \dots & S_{1n} \\ S_{21} & S_{22} & \dots & S_{2n} \\ \vdots & \vdots & \ddots & \vdots \\ S_{n1} & S_{n2} & \dots & S_{nn} \end{bmatrix} \begin{bmatrix} V_1^+ \\ V_2^+ \\ \vdots \\ V_n^+ \end{bmatrix} \quad ,
$$

where V_n^+ is the amplitude of the incident wave at port n and V_n^- the amplitude of the wave reflected from port n. The individual entries of the scattering matrix are given by

$$S_{ij} = \left. \frac{V_i^-}{V_j^+} \right|_{V_k^+ = 0 \text{ for } k \neq j} \quad ,$$

where an incident wave is only applied to port j and measured at port i, with all other ports terminated in matched loads. For a one-port network, the parameter S_{11} is equal to the reflection coefficient Γ.

2.3.3 Resonant Circuits

Microwave resonant circuits are the basis for a large range of RF devices, for example different types of filters. Some of the basic concepts will be introduced in this section, which will later be employed to describe the RF circuits for reflectometry measurements in Section 2.3.4 and Section 2.3.5.

In its simplest form, a resonant circuit consists of a capacitive and an inductive element, to which a resistive element is added for modeling circuit losses, as shown in Fig. 2.18(a) in a series configuration and in (b) in a parallel configuration. We make use of the series lumped element model to introduce the concepts associated with resonant circuits, followed by a short discussion of the $\lambda/2$ transmission line resonant circuit. The presentation will focus on the main results, a detailed derivation of which can be found in [Pozar05].
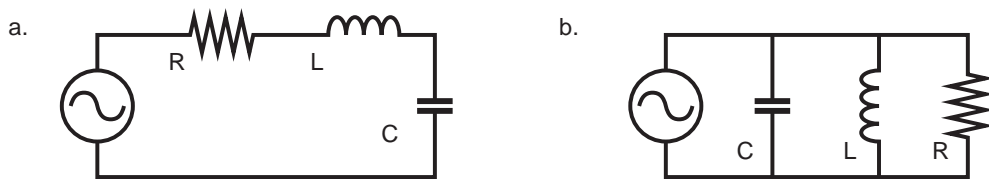

Figure 2.18: Series (a) and parallel (b) RLC lumped element resonator.

The Series RLC Circuit

Connecting a resistor, an inductor and a capacitor in series, as shown in Fig. 2.18, leads to a resonant circuit, also known as tank circuit, with a resonance frequency ω_0:

$$\omega_0 = \frac{1}{\sqrt{LC}} \quad . \tag{2.37}$$

The circuit can store energy at resonance, hence the name ''tank'', but will lose part of the energy due to dissipative effects. The quality factor of the circuit, denoted by Q, captures this loss and is defined as

$$Q = \omega_0 \frac{\text{average energy stored}}{\text{energy loss/second}} \quad . \tag{2.38}$$

A large quality factor thus indicates a resonant circuit with low loss. The expression for the quality factor of the RLC circuit is

$$Q = \frac{\omega_0 L}{R} = \frac{1}{\omega_0 R C} \quad ,$$

which yields an inverse relationship between the resistor and the quality factor. This is expected as a small value for R means low dissipative loss, which translates into a high quality factor and vice versa.

The quality factor is also related to the bandwidth $\Delta\omega$ of the resonance, which is defined as the width of the frequency interval in which the amplitude of the signal is larger than half the maximum value. Using this definition, the quality factor can be expressed as:

$$\frac{1}{Q} = \frac{\Delta\omega}{\omega_0} \quad . \tag{2.39}$$

A device with a large Q thus has small bandwidth and vice versa. Furthermore, in case of a circuit with fixed Q, the bandwidth can be enlarged by increasing the resonance frequency, assuming that Q is frequency independent.

So far, only the isolated resonant circuit has been considered and any coupling to the outside world has been neglected. In this case, derived quality factor is usually referred to as the internal quality factor Q_{int}, representing the ideal circuit behavior limited only by internal losses. When the resonant circuit is connected to other elements, additional loss channels have to be considered and the total Q is reduced by this "loading" of the resonant circuit. By attributing a quality factor to the loading elements, Q_{ext}, which for a load impedance Z_l is given by

$$Q_{\text{ext}} = \frac{\omega_0 L}{Z_L} \quad ,$$

the total or loaded Q of the combined circuit, Q_{L}, can be expressed as

$$\frac{1}{Q_{\text{L}}} = \frac{1}{Q_{\text{int}}} + \frac{1}{Q_{\text{ext}}} \quad .$$

From this definition, one can identify three different regimes for Q_{L}, the *undercoupled*, the *overcoupled* and the *critically* coupled regime. In the undercoupled case, $Q_{\text{ext}} >>$

Q_{int}, the quality factor is dominated by the internal quality factor of the circuit, while in the overcoupled case, $Q_{\mathrm{int}} >> Q_{\mathrm{ext}}$, the quality factor is given by the external quality factor. For critical coupling the two quality factors are similar, $Q_{\mathrm{int}} \approx Q_{\mathrm{ext}}$, and both contribute to Q_{L}, in which case the power transfer to the resonant circuit is maximal.

In many experiments utilizing resonant circuits, the internal quality factor needs to be determined in order to evaluate the circuit performance. While measuring an undercoupled circuit would directly provide this information, the small bandwidth and low transmission often make undercoupled resonators undesirable. In this case we can utilize the insertion loss L_0, defined as the transmission through the resonant circuit at the resonance frequency ω_0. The insertion loss relates the internal and external quality factors allowing for Q_{int} to be determined from an overcoupled resonator. By defining the coupling coefficient g as the ratio between internal and external quality factor

$$g = \frac{Q_{\mathrm{int}}}{Q_{\mathrm{ext}}} \ ,$$

the insertion loss is given by

$$L_0 = \frac{g}{g+1} \ . \tag{2.40}$$

The internal and external quality factors can then be deduced from a measurement of Q_{L} using the relations

$$Q_{int} = \frac{1}{1-L_0}Q_{\mathrm{L}} \ , \tag{2.41}$$

$$Q_{ext} = \frac{1}{L_0}Q_{\mathrm{L}}. \ . \tag{2.42}$$

The Transmission Line Half-Wave Resonator

To ensure the desired properties and allow for an accurate design of transmission line based microwave circuits, a precise characterization of the transmission line parameters, the attenuation constant α and phase constant β, is necessary. This can be achieved by using a $\lambda/2$ resonator which consists of a length l of transmission line coupled to the input and the output line via gap capacitors, as shown in Fig. 2.19.

The transmission of an applied RF tone from the input to the output port shows a resonance when the length of the line is equal to an integer multiple of half the applied wavelength:

$$n\frac{\lambda_{Res,n}}{2} = 2l \ .$$

This result can also be derived from the fact that, at resonance, the microwave acquires a phase shift of π over the length of the line. This condition can be written as $\beta l = n\pi$, where β is the phase constant, leading to the same condition.
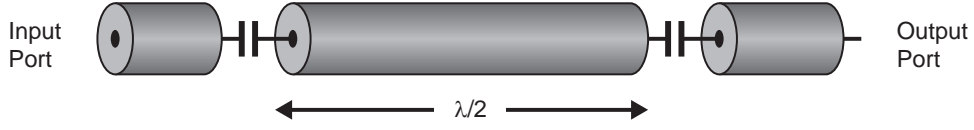
Figure 2.19: Schematic of a $\lambda/2$ transmission line resonator. The half wave line is coupled to the input and output lines via capacitors.

By measuring the center frequency f_0 and quality factor of the observed resonance, it is possible to determine the transmission line parameters α and β. The loss constant α is related to the internal quality factor of the resonator, and can be calculated using

$$Q_{\text{int}} = \frac{\beta}{2\alpha} \ . \tag{2.43}$$

The frequency dependence of the phase constant is determined by the effective dielectric constant ϵ of the transmission line by:

$$\beta = \frac{2\pi\sqrt{\epsilon\epsilon_0}}{c}f \ , \tag{2.44}$$

where ϵ_0 is the vacuum permittivity and c the speed of light in vacuum. A measurement of the resonance frequency f_0 together with the known physical length of the half-wave resonator l allows for a determination of ϵ via

$$2lf_0 = \frac{c}{\sqrt{\epsilon\epsilon_0}} \ .$$

For a single resonance, fitting a Lorentzian line shape of the form

$$S_{21}(f) = \frac{A_0}{2\pi Q f_0} \frac{1}{\left(f/f_0 - 1\right)^2 + 1/4\left(1/Q\right)^2} \tag{2.45}$$

extracts the resonance frequency f_0, the quality factor Q, and a scaling factor A_0. The insertion loss is then calculated by using $f = f_0$ and the extracted parameters. In many instances, not only the fundamental mode, but also higher harmonics can be measured, in which case an equivalent circuit based model is more appropriate for parameter extraction [Goppl08].

2.3.4 Impedance Matching Circuits

Transport measurement bandwidths in the tens of MHz range are possible by using a technique based on detecting the reflected power of a microwave applied to the object of interest. To achieve a better signal, the object of interest is embedded in an impedance

transformation circuit which converts the large resistances of the nano-object device to an impedance close to 50 Ω. This measurement technique will be discussed in more detail in this section, first in the lumped element case followed by the a discussion of the theoretical limits and finishing with the distributed element impedance transformer.

Circumventing the RC Bandwidth Limitation

Devices in which a nano-scale object dominates the transport characteristics generally have a resistance ranging from several kΩ up to tens of GΩ. To improve device stability and allow for the observation of effects such as Coloumb blockade, characterization measurements are performed at low temperatures, which introduces a large amount of stray capacitance due to required wiring. As a result, the device and wiring form a low pass RC filter, limiting the bandwidth (BW) of the measurement circuit to

$$ \mathrm{BW} = \frac{1}{2\pi RC} \ . $$

Assuming a typical value of $C = 800$ pF for wiring stray capacitance, the attainable device bandwidth is 15 kHz for a device resistance of 12.9 kΩ and 1 kHz for a 250 kΩ device, a significant reduction compared to the detection bandwidth of the instrumentation, which can easily surpass 100 MHz.

The straightforward solution approach is to minimize the stray capacitance by placing an amplifier close to the sample inside the cryostat. A setup of this type has been demonstrated for the detection of single-electron tunneling events, utilizing a QPC as the charge detector [Vink07]. In this configuration, a bandwidth of 1 MHz was determined from measurements at a QPC conductance close to G_0. The setup, however, is not optimal due to the heat dissipation of the amplifier and the presence of $1/f$ noise.

An improved approach makes use of the fact that the reflection coefficient Γ of a transmission line depends on the impedance of the attached load (Eq. 2.33). Directly connecting the device of interest to a transmission line will result in poor sensitivity, as for $Z_{\mathrm{Load}} >> Z_0$, the reflection coefficient Γ is close to unity. In contrast, by using an impedance transformation circuit, the load impedance can be transformed to the line impedance, significantly increasing the response of the circuit to load changes. Measuring the reflection coefficient not only allows for bandwidths approaching 100 MHz at loads of 50 kΩ [Schoelkopf98], but additionally offers a reduced $1/f$ noise floor, as the measurements are performed at frequencies higher than 100 MHz.

L-Networks

A simple impedance transformation circuit, transforming an arbitrary load impedance to Z_0 is given by the L section [Pozar05], which consists of two reactive components, as shown in Fig. 2.20(a). To derive an expression for the reactances, X and B, we assume an arbitrary load of the form $Z_{\text{Load}} = R_l + iX_l$, where $R_l > Z_0$. The combined impedance of the matching network and load should be Z_0, i.e.

$$Z_0 = iX + \frac{1}{xB + 1(R_l + iX_l)} \ .$$

This equation can be separated into real and imaginary parts and rearranged, returning two equations, one for X and one for B:

$$B(XR_l - X_lZ_0) = R_l - Z_0 \ , \tag{2.46}$$
$$X(1 - BX_l) = BZ_0R_l - X_l \ . \tag{2.47}$$

These can be then solved for B and X leading to the following expressions for the required reactances:

$$B = \frac{X_l \pm \sqrt{R_l/Z_0}\sqrt{R_l^2 + X_l^2 - Z_0R_l}}{R_l^2 + X_l^2} \ , \tag{2.48}$$

$$X = \frac{1}{B} + \frac{X_lZ_0}{R_l} - \frac{Z_0}{BR_l} \ . \tag{2.49}$$

The L section can be realized in two different ways, a series inductor and shunt
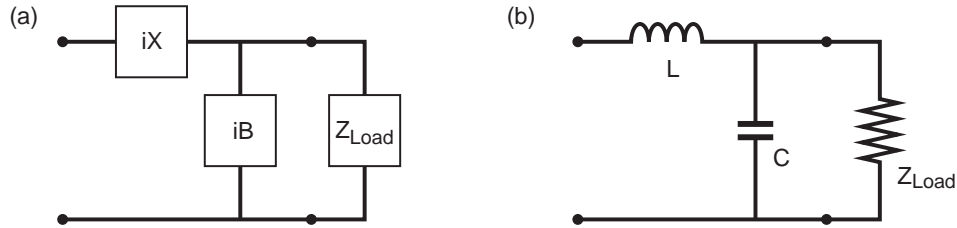
Figure 2.20: (a) Schematic of an L section with two reactances X and B for a load Z_{Load}. (b) Implementation using an inductor L and capacitor C.

capacitor or a series capacitor and shunt inductor. For transport measurements, a DC bias is required, which is why the L section is typically implemented by a series inductor and a shunt capacitor, as illustrated in Fig. 2.20(b). For a resonance frequency of ω_0, the values for L and C are given by

$$L = \frac{\sqrt{Z_{\text{Load}}/Z_0 - 1/2}}{\omega_0 Z_{\text{Load}}} \ , \tag{2.50}$$

$$C \;=\; \frac{Z_{\text{Load}}}{\omega_0 \sqrt{Z_{\text{Load}}/Z_0 - 1/2}} \;. \tag{2.51}$$

The L section itself is a resonant circuit and therefore also has a quality factor, given by

$$Q = \omega_0 Z_{\text{Load}} C \;.$$

Using the definition of the resonance frequency in (2.37) and $Z_0 = \sqrt{\frac{L}{C}}$, this can be written as [Waissman06]:

$$Q = \sqrt{\frac{Z_{\text{Load}}}{Z_0}} \;. \tag{2.52}$$

Consequently, in the lossless case, the Q factor of the L section is fixed by the load and line impedances. For a given load, an increase in bandwidth can thus be obtained either by increasing the operating frequency ω_0, or by increasing the line impedance.

The Bode-Fano Criterion

By adding a number of L-sections in series, the quality factor of the matching network can be further decreased [Teufel08]. A fundamental limit to the attainable bandwidth is given by the Bode-Fano criterion [Bode45,Fano50], which, for a lossless matching network transforming a resistance R shunted by a capacitance C, as shown in Fig. 2.21(a), is given by:

$$\int_0^\infty \ln \frac{\mathrm{d}\omega}{|\Gamma(\omega)|} \le \frac{\pi}{RC} \;. \tag{2.53}$$

The width of the band in which $\Gamma \ne 1$ is therefore limited by the load resistance and shunt capacitance, regardless of the center frequency. In case of an absorptive Lorentzian line shape, the bandwidth is given by [Teufel08]:

$$\Delta\omega \le \pi/RC \;. \tag{2.54}$$

In case of the L section, the shunting capacitance is ideally determined by the transformation circuit, whereas parasitic shunt capacitances are negligible. In this case the bandwidth of the circuit is close to the theoretical limit.

The Lossy L-Section

A real world implementation of an L-section will inherently introduce losses, which need to be taken into account in the model. This is generally done in terms of internal and external quality factors, where Q_{int} describes the matching network with losses and Q_{ext} the attached load. A series resistor is introduced in order to model the loss, as
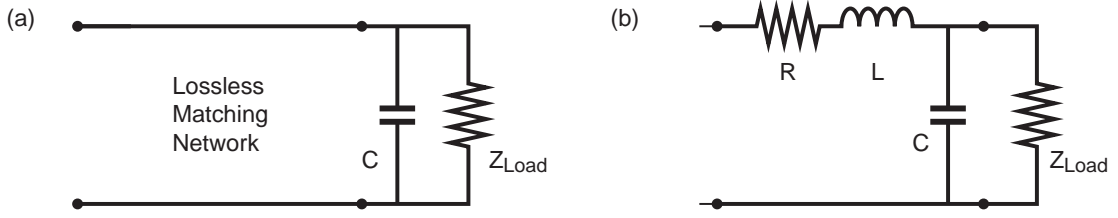
Figure 2.21: (a) Circuit considered for the Bode-Fano criterion. The load Z_{Load} is shunted by a stray capacitance. (b) Equivalent circuit of the lossy L-section. The loss is described by the resistor R.

shown in Fig. 2.21(b), forming an RLC circuit which is loaded by the device impedance Z_{Load}. The loaded quality factor can now be calculated using $Q_{\mathrm{ext}} = 1/\omega_0 C Z_{\mathrm{Load}}$:

$$\frac{1}{Q_{\mathrm{L}}} = \frac{1}{Q_{\mathrm{int}}} + \frac{1}{Q_{\mathrm{ext}}} = \omega_0 C (R + Z_{\mathrm{Load}}) \ . \tag{2.55}$$

This implies that by measuring Q_{L}, it is possible to extract Z_{Load}, with a sensitivity depending on R. To achieve optimal sensitivity to changes in the load Z_{Load}, the loss and hence R needs to be minimized, implying $Q_{\mathrm{int}} >> Q_{\mathrm{ext}}$.

Typically, the matching circuits for reflectometry measurements are implemented as L-sections [Schoelkopf98, Qin06, Flowers-Jacobs07], mostly using SMD inductors and relying on the parasitic capacitance of the chip, for example from the bond pads, to form a resonant circuit. This, however, limits the working frequency to several 100 MHz due to the comparatively large capacitances and the non-ideal behavior of SMD inductors at these frequencies. While the use of on-chip matching networks with superconducting inductors allows for an increase in the operating frequency up to 1.2 GHz [Xue07, Fong12], L-sections are difficult to implement in the 4-8 GHz frequency range.

2.3.5 Stub tuners

A different approach to matching networks utilizes the distributed element paradigm, where pieces of transmission lines are utilized to realize the reactances required for impedance transformation. In the following, matching circuits based on single shunt transmission lines, also known as stub tuners, will be discussed. The key advantages of stub tuners are that the operating frequency is only limited by the acceptable loss and that matched loads in the MΩ range are possible when integrating the device of interest on-chip.

This section will discuss the properties of stub tuners, both in the lossless and lossy

case, and analyze different measurement regimes before concluding with an outlook on future circuit design.

Stub Impedance Matching in the Lossless Case

The distributed elements equivalent of the L section is the single stub tuner which consists of two transmission lines. In this thesis, the shunt stub configuration is investigated, where the load is attached to a length d of transmission line, which is shunted by a transmission line of length l, the stub.

When matching a specific load Z_{Load} to an impedance Z_0, we make use of the fact that the impedance of a load can be transformed by a piece of transmission line, as implied by equation (2.34). We can therefore transform Z_{Load} into an admittance of the form $1/Z_0 + iB$ by using a transmission line of length d, as shown in Fig. 2.22(a). By adding an open ended transmission line in parallel, with length l such that its admittance is $-1/iB$, the two susceptances cancel and the total impedance of the circuit is Z_0, matching the line impedance.

To derive an analytical expression for l and d, let $Y = G + iB = 1/Z$ be the admittance of a transmission line of length d terminated by the load $Z_{\mathrm{Load}} = R_l + iX_l$. Using equation (2.34) and $t = \tan(\beta d)$, the real and imaginary parts of Y are given by

$$G = \frac{R_l(1 + t^2)}{R_l^2 + (X_l + Z_0 t)^2} \quad, \tag{2.56}$$

$$B = \frac{R_l^2 t - (Z_0 - X_l t)(X_l + Z_0 t)}{Z_0(R_l^2 + (X_l + Z_0 t)^2} \quad. \tag{2.57}$$

Choosing $G = 1/Z_0$ fixes both t and B, with t given by

$$t = \frac{X_l \pm \sqrt{R_l((Z_0 - R_l)^2 + X_l^2)/Z_0}}{R_l - Z_0} \quad.$$

The transmission line length d can now be calculated using

$$\frac{d}{\lambda} = \left\{ \begin{array}{ll} \frac{1}{2\pi} \tan^{-1} t & t \geq 0 \\ \frac{1}{2\pi}(\pi + \tan^{-1} t) & t < 0 \end{array} \right\} \quad. \tag{2.58}$$

Furthermore, the length of the stub l is given by

$$\frac{l}{\lambda} = -\frac{1}{2\pi} \tan^{-1} B Z_0 \quad. \tag{2.59}$$

This rather general result for the tuner lengths can be simplified by using the fact that the expected matched loads are real-valued ($X_l = 0$) and larger than Z_0. In this case

the tuner lengths can be expressed as

$$d \;=\; \frac{1}{\beta} \tan^{-1} \sqrt{\frac{Z_{\mathrm{Load}}}{Z_0}} \;,\tag{2.60}$$

$$l \;=\; \frac{\lambda}{2} - \frac{1}{\beta} \tan^{-1} \frac{Z_{\mathrm{Load}} - Z_0}{\sqrt{Z_{\mathrm{Load}} Z_0}} \;,\tag{2.61}$$

where β is the propagation constant given in equation (2.31). For large matched loads, both lengths d and l approach $\lambda/4$, with d slightly shorter and l slightly longer. This implies a capacitive behavior of the line connected to the load and an inductive behavior of the shunt stub, leading to an L-section equivalent circuit with a series capacitor and shunt inductor, as shown in Fig. 2.22(b).
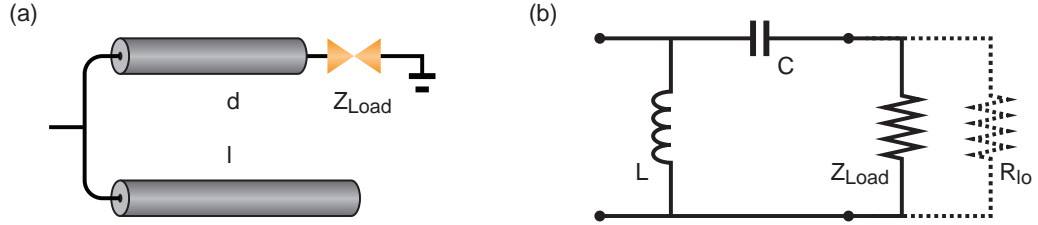

Figure 2.22: (a) Schematic of a stub tuner. The load Z_{Load} is attached to a transmission line of length d, which is shunted by an open line of length l. (b) Lumped element equivalent circuit of a stub tuner, an L-section with a series capacitance and shunt inductance. The dotted resistor R_L represents the loss in the tuner.

An alternative interpretation of the circuit is to view it as an interferometer: the microwave is split at the T-junction, one part travels to the load, where it is reflected with a load dependent amplitude and phase, while the second part is reflected at the stub with a $\pi/2$ phase shift. The two reflected waves recombine at the T-junction and will be exactly out of phase and cancel each other for the matched load. In this interpretation, adding a fixed length to both transmission lines shifts the resonance frequency, but only weakly affects the matched load, while adding a length of transmission line to only one arm shifts the matched load but not the frequency. This is illustrated in Fig. 2.23, where the dependence of the frequency on the transmission line lengths l and d is shown in (a) and the dependence of the matched load on the lengths in (b). Moving from one resonance frequency to another corresponds to moving along the diagonal, which is equivalent to adding equal lengths to both arms. Shifting the matched load, however, requires moving cross-diagonal, increasing or decreasing the difference between the two arms. It can further be seen, that the matched load increases as the two arms approach similar lengths.
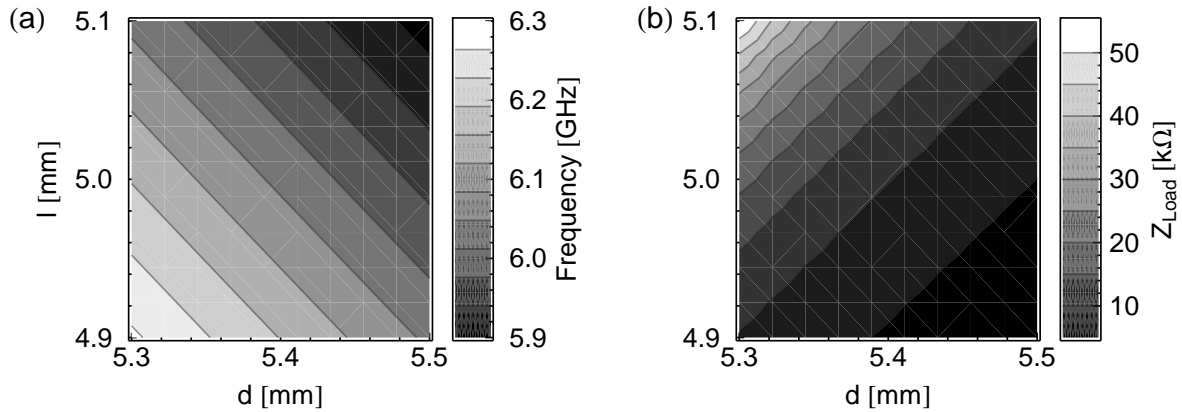
Figure 2.23: (a) Resonance frequency as a function of d and l. (b) Matched load as a function of d and l.

So far, only the matched load and the resonance frequency have been discussed, but the off-resonant characteristics are also of interest, as the are used for measuring the impedance of a device by reflectometry. To describe these characteristics we can again make use of quality factors. In the lossless case, the total quality factor is given by the external quality factor of the load, which is proportional to Z_{Load}, (see also Section 2.3.4) and therefore expected to increase as the load increases. Furthermore, we expect the reflection coefficient $\Gamma = S_{11}$ to be close to zero at resonance and approach unity for off of resonance.

This behavior is illustrated for an example device with matched load of $1/G_0$ at 6 GHz in Fig. 2.24. The frequency response for different loads is plotted in (a) and displays the expected increase in Q, starting with a broad resonance at 2 kΩ (dark red) and increasing in Q as the load approaches the matched load (blue, green and red). The minimum reflection coefficient, on the other hand, decreases as the load is approached. Above the matched load, both the quality factor and reflection coefficient increase again (dark yellow curve). The response of the reflection coefficient at resonance is plotted in Fig. 2.24(b), where both amplitude (blue) and phase (red) are shown. The amplitude decreases toward a minimum at the matched load, after which it increases again and, in the lossless case, approaches unity for large loads ($Z_{\text{Load}} >> G_0$). Moreover, a change in phase by $\pi/2$ while crossing the matched load is observed, which, together with the amplitude, establishes a one-to-one relationship between the value of the load and the complex reflection coefficient.
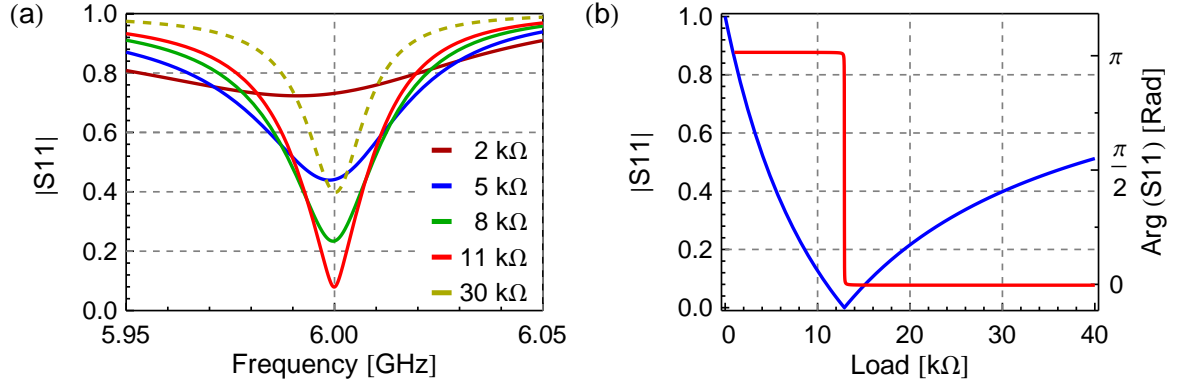
Figure 2.24: RF response of an example device, with a matched load of G_0 at 6 GHz. (a) $|S_{11}|$ vs. frequency for different loads. (b) Both magnitude (blue) and phase (red) versus load resistance at 6 GHz.

Stub Tuner Impedance Matching including Losses

The main influence of loss on the impedance transformer response is a reduced sensitivity to changes in the load, similar to the case of the L-section. Furthermore a maximum matched load value is imposed, above which changes in load no longer lead to a change in microwave response. Losses also change the behavior of the circuit, modifying the transmission line lengths compared to the lossless case.

Losses can be incorporated by using equation (2.34) with a non-zero attenuation constant ($\alpha \neq 0$), where $\gamma = \alpha + i\beta$, but the hyperbolic tangent precludes a separation of the impedance and the reactance, as in equation (2.57). This precludes an analytical solution for the lengths, which need to be found numerically.

The input impedance of the stub tuner is the sum of the two transmission line impedances connected in parallel and can be derived using equations (2.34) and (2.36):

$$Z_{\text{Tuner}} = Z_0 \left(\tanh(\gamma l) + \frac{Z_0 + Z_{\text{Load}} \tanh(\gamma d)}{Z_{\text{Load}} + Z_0 \tanh(\gamma d)} \right)^{-1} . \tag{2.62}$$

This result allows a calculation of the reflection coefficient Γ using equation (2.33), which is required to be zero at the matched load and frequency. A minimization routine can then find the correct lengths by minimizing $|\Gamma|$. Suitable starting points need to be provided, as Γ is close to unity far off of resonance, providing no gradient for the minimization routine. Furthermore, multiple solutions exist due to the periodicity of equation (2.34), where the solution with the largest bandwidth is the one with the shortest lengths.

Equation (2.62) also allows for an investigation of how the losses influence the device

response, which is illustrated in Fig. 2.25 for two devices with matched loads $1/G_0$ and $1/0.1\ G_0$, at a resonance of 6 GHz. For each value of α the matching lengths d and l are calculated and the reflection coefficient at resonance is plotted. Due to losses, the length difference between the two arms increases for increasing α, e.g. in case of the $1/G_0$ device from 415 μm to 470 μm. Furthermore, the response of the circuit changes: For loads smaller than the matched load, the response to a change in load is steeper for larger α, while close to the matched load and for larger values, the slope is diminished. Typical values for α are 0.02 for Nb at 4.2 K and 0.002 for NbTiN at 3 K. The device matching $1/G_0$ shows a reduced response for larger α, but good sensitivity can be achieved at 4.2 K. In contrast, the $1/0.1\ G_0$ device shows a very weak response to load changes at $\alpha = 0.02$, requiring lower loss to obtain sensitivity.
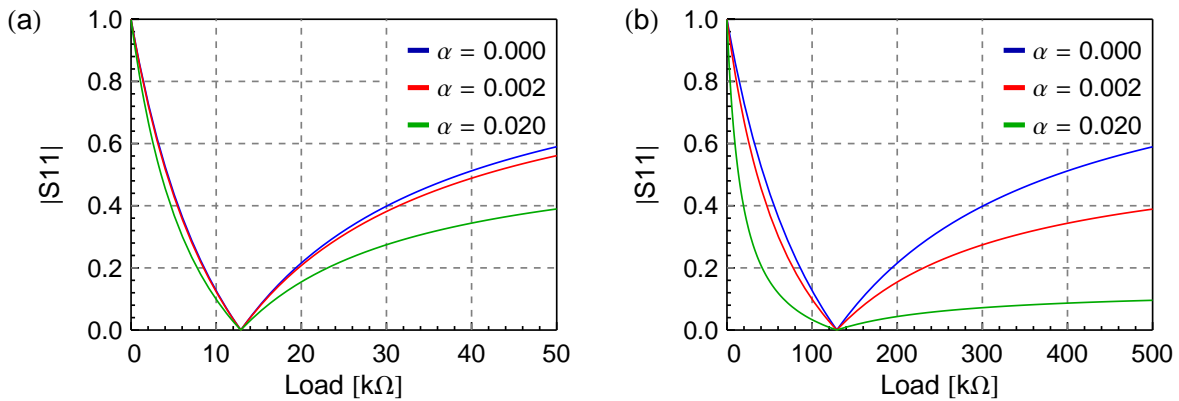

Figure 2.25: Circuit response at resonance for different loss magnitudes. (a) Design matched load $1/G_0$. (b) Design matched load $1/0.1\ G_0$.

The described behavior can be qualitatively understood by adding a parallel resistor R_{lo} to the equivalent circuit, as shown in Fig. 2.22(b), with a value $R_{\mathrm{lo}} \propto 1/\alpha$. The load is then the parallel sum of load and loss, leading, on the one hand to the modification of the lengths, due to the fact that the loss shifts the total impedance, and on the other hand to the decrease in response, as for $R_{\mathrm{lo}} > Z_{\mathrm{Load}}$ the total impedance is dominated by the loss.

In principle, two different kinds of measurements can be performed using a stub tuner: The absolute impedance of the load can be determined, or a change in impedance can be detected. In the first case, one can exploit the fact, that for fixed lengths and loss, the reflection coefficient has a one-to-one relationship to the impedance of the device under investigation. In a first approximation, the measured value is the differential impedance and thus proportional to the "RF density of states". A number of additional effects are expected, such capacitances and inductances arising from quantum effects, which will not be discussed here [Prêtre96, Wang07, Frey12]. This type of measurement

does not necessarily require large bandwidths, but rather an accurate calibration of the microwave setup and transmission line lengths.

In the second case, the load is used as a detector, for example an SET or QPC in electron counting experiments [Gustavsson06], and the measurement bandwidth is paramount. Since the bandwidth is not only given by the circuit but also by the signal-to-noise ratio (SNR) it is crucial to achieve a signal with large amplitude. The change in circuit response as a function of loss is illustrated in Fig. 2.26. In panel (a) the change in the magnitude reflection coefficient $\Delta|S_{11}|$ for a 10% change in load is plotted, showing a maximum in signal close to the matched load, while the overall change diminishes as α increases. Although $\Delta|S_{11}|$ is zero in the vicinity of the matched load, the phase signal is at a maximum at this point (not shown in the plot). An on/off type of measurement shows the same behavior, as illustrated in panel (b), with maximum sensitivity if the on-state impedance is equal to the matched load, although the measurement is still sensitive to changes at impedances five times larger than the matched load. This large sensitivity range allows measurements to be performed even if the matched load does not exactly coincide with the device load, at the cost, however, of a reduced signal amplitude. While it is possible to build tuneable impedance matching circuits, for example by placing a variable capacitance at the end of the shunt stub [Hellmüller12], this will introduce additional losses and an individual investigation is necessary to determine whether the gain in signal due to better matching justifies the reduction in signal due to loss.
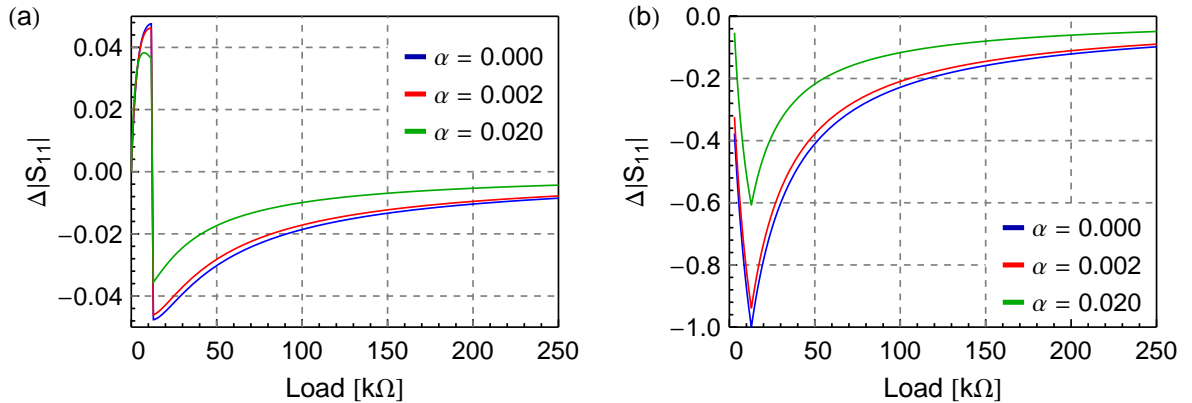

Figure 2.26: Change in reflection magnitude for a $1/G_0$ device. (a) With a 10% increase in the load. (b) With a 1 GΩ reference load.

Bandwidth Limitations

The main motivation for investigating stub tuners is their potential to increase the attainable measurement bandwidth, both by an increase in circuit bandwidth and by improving the SNR, with the former being limited by the Bode-Fano criterion (Section 2.3.4). In the following, we will address the question of how well stub tuners perform with regard to this limit and whether it is possible to further increase the bandwidth.

The Bode-Fano limit of a 6 GHZ, $1/G_0$ matched load device can be calculated by utilizing the equivalent circuit shown in Fig. 2.22(b), where the capacitance C is given by the reactance of the transmission line with attached load. By using equation (2.34) and $X = 1/\omega f C$, the equivalent capacitance is found to be 8.38 pF, leading to a theoretical bandwidth limit of 29 MHz. In contrast, the actual bandwidth of the stub tuning circuit is 17 MHz. The difference is due to the periodic nature of the transmission line impedance, which leads to matching at higher harmonics, as illustrated in Fig. 2.27(a). Simply speaking, part of the bandwidth is distributed to higher modes, reducing the bandwidth of the fundamental mode.
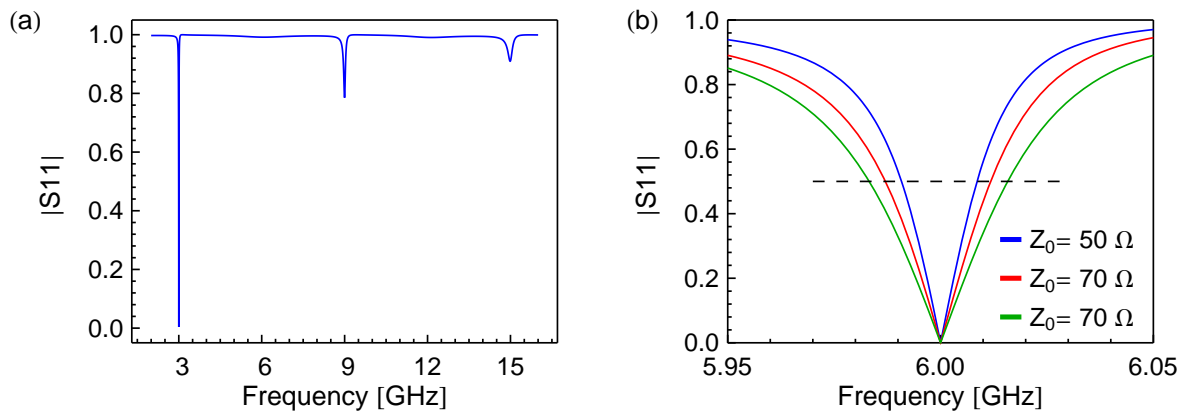

Figure 2.27: (a) Plot of $|S_{11}|$ of a G_0 device at matched load vs. frequency. (b) Spectrum of different G_0 devices at matched load: Standard geometry (red and blue) and double stub (green).

It is possible to increase the bandwidth by using a number of methods, the most simple one being an increase in the characteristic impedance of the transmission lines used for the circuit. If the lengths d and l are implemented with $Z_0 = 70$ Ω, the bandwidth increases even if the match is to a $Z_0 = 50$ Ω feedline. This is illustrated in Fig. 2.27(b), where the blue curve is the resonant response of the standard circuit, optimized for a match of $1/G_0$ at 6 GHz, while the red curve is the response of a circuit optimized for the same parameters but with Z_0 of d and l equal to 70 Ω. This increases the bandwidth from 17 MHz to 25 MHz. A further increase to 33 MHz is possible by

using two shorter shunt stubs in parallel (green curve). These changes in the circuit do not reduce the bandwidth reduction caused by the presence of higher modes, but instead lower the reactance in the circuit, thus achieving the increase in bandwidth. It may be possible, however, to suppress higher harmonics using a transmission line with a photonic bandgap structure [Yang99], which does not support higher modes, a possibility for investigation in future experiments.

2.3.6 Coplanar Waveguides

The implementation of circuits such as the discussed $\lambda/2$ resonator and the stub tuner requires a physical realization of a transmission line. One such realization, the coplanar waveguide, is well suited for both types of circuits due to its uni-planar character. For stub tuners, this facilitates electric contact and therefore fabrication, as both the signal line and ground are in the same plane, while additionally minimizing stray capacitances.

This section will cover the basic properties of coplanar waveguides followed by the details of implementing stub tuners in this geometry.

Basic Properties

A coplanar waveguide consists of a center conductor separated from a semi-infinite groundplane by two gaps, all of which is placed on a dielectric substrate, as illustrated in Fig. 2.28(a). This type of conductor was first demonstrated by Wen in 1969 [Wen69] and due to the good compatibility with microfabrication has seen widespread use in microwave integrated circuits.
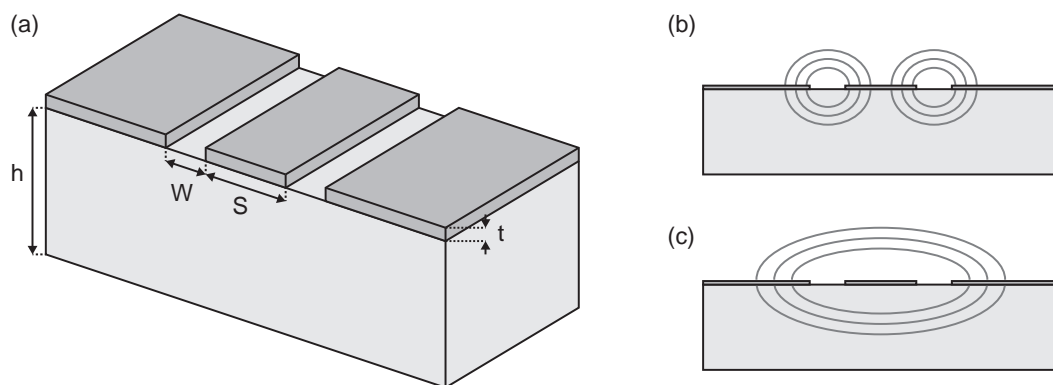

Figure 2.28: (a) Schematic of the coplanar waveguide geometry. (b) Schematic of the even mode field distribution. (c) Schematic of the odd mode field distribution.

In a coplanar waveguide the transmission line parameters are a function of the center conductor width S, the gap width W, the substrate height h and the metalization thickness t. Given these parameters, the characteristic impedance Z_0 and the effective dielectric constant ϵ_{eff} can be determined using a conformal mapping [Simons01]. Assuming that the dielectric constant of the substrate is ϵ_r, the effective dielectric constant of the coplanar waveguide is found to be

$$\epsilon_{eff} = 1 + \frac{\epsilon_r - 1}{2} \frac{K(k_1)}{K(k_1')} \frac{K(k_0')}{K(k_0)} \ , \tag{2.63}$$

where K are the complete elliptic integrals of the first kind. The moduli k_0, k_0', k_1 and k_1' are given by the relations

$$
\begin{aligned}
k_1 &= \frac{\sinh(\pi S/4h)}{\sinh[\pi(S + 2W)/4h]}, \\
k_0 &= \frac{S}{S + 2W} \ , \\
k_1' &= \sqrt{1 - k_1^2} \ , \\
k_0' &= \sqrt{1 - k_0^2} \ .
\end{aligned}
$$

Furthermore, the characteristic impedance is given by

$$Z_0 = \frac{30\pi}{\sqrt{\epsilon_{\text{eff}}}} \frac{K(k_0')}{K(k_0)} \ . \tag{2.64}$$

The derived formulas are valid for the so-called even mode of the coplanar waveguide, where the electric field of the wave is concentrated into the gaps at either side of the center conductor, as schematically drawn in Fig. 2.28(b). The waveguide is, however, capable of supporting further propagating modes [Wolff06], the most prominent of which is the so called odd mode. For this mode, the field is similar to a slotline mode, where the potential of the two groundplanes oscillates, while the center conductor is not affected, as sketched in Fig. 2.28(c). As a result, the odd mode has different transmission line characteristics and is usually considered a parasitic mode.

For a given substrate, equations (2.64) and (2.63) allow for designing a 50 Ω transmission line and calculating the expected phase constant β. Together with a $\lambda/2$ resonator measurement from which the loss constant α can be extracted, all relevant parameters for the design of an arbitrary stub tuner are known. The physical implementation of the stub tuner circuits, however, introduces several parasitic effects, which need to be taken into account and will be discussed in the following.

Parasitic Effects and Discontinuities

The implementation of a stub tuner in coplanar waveguide geometry introduces two types of waveguide discontinuities, a T-junction where the stub branches off and an open/load at the end of the transmission lines. Each discontinuity can be modeled using a lumped element equivalent circuit, allowing for an accurate determination of the expected behavior.

The discontinuity simpler to model is the open end, illustrated in Fig. 2.29(a), where the center conductor ends in a rectangular gap of length l_{gap}. While in a lumped element model this adds a stray capacitance [Simons01], the discontinuity can also be described as an additional length l_{oc}, by which the open end is shifted, illustrated in Fig. 2.29(b). The added length depends on l_{gap} and saturates to a constant value for $l_{\text{gap}} \geq S + 2W$, at which point the added length is approximately [Simons01]

$$l_{\text{oc}} = \frac{S + 2W}{4}. \tag{2.65}$$

If a break-junction is placed inside the gap, this formula no longer holds, as the junction adds a significant amount of capacitance to ground. Using an electromagnetic field simulation program [ANSYS], the stray capacitance added by the break-junction was found to be approximately 50% of the open-end capacitance (0.35 fF opposed to 0.7 fF) in our typical waveguide geometry.
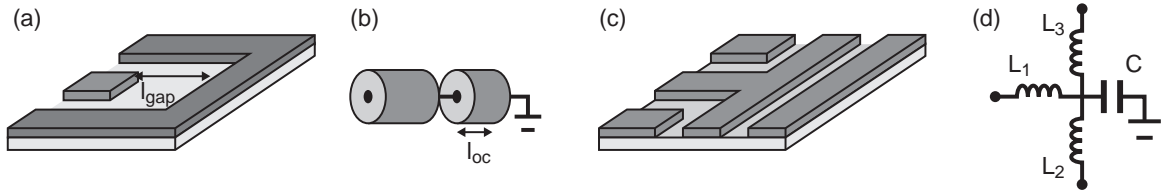

Figure 2.29: (a) Schematic of an open end. (b) Added length due to open end. (c) Schematic of a T-junction. (d) Lumped element equivalent circuit of a T-junction.

Since adding the same length of transmission line to both arms of the stub tuner leads to a shift in resonance frequency, the influence of the gap capacitance is a change in resonance frequency of approximately .1 %, which, in practice, can be neglected. In contrast, the stray capacitance of the junction is added only to one arm, leading to a shift in the matched load. For matched loads on the order of $1/G_0$, the influence is small ($\approx 20\ \Omega$), but becomes more pronounced for matched loads larger than 200 kΩ.

The T-junction, illustrated in Fig. 2.29(c), has a significant influence on the behavior of the stub tuner and subsequent design, due the fact that it not only introduces

parasitic capacitances and inductances, but also introduces mode conversion from the even mode to a number of other modes, such as the odd mode [Wolff06]. An equivalent circuit is shown in Fig. 2.29(d), consisting of three inductances L_1, L_2 and L_3 as well as a capacitance C. While the capacitance C has a negligible effect on the behavior of the stub tuner, the inductances shift the electrical lengths of the arms similar to the open ends. As a consequence of symmetry, L_2 and L_3 are identical, which can be used to reduce the effect of the inductances to a shift in resonance frequency by proper orientation of the T-junction. The resulting shift is on the order of 10 MHz, while the inductance L_1 has no influence on the matching properties of the tuner.

An important issue for obtaining repeatable and predictable device characteristics is the mode conversion taking place at the T-junction, from an incoming even mode to a superposition of even and odd mode in the two arms at the T-junction [Simons01, Wolff06]. Due to the different attenuation and phase constant of the odd mode, the microwave characteristics of the circuit are substantially altered, shifting the resonance frequency in the measured devices by more than 150 MHz. This issue can be addressed by maintaining electric continuity between the groundplanes, as illustrated in Fig. 2.30(a), which suppresses the parasitic modes. While electric continuity may be achieved via bondwires, both the suppression magnitude and the parasitic inductances associated with the T-junction will depend on the placement of the wires [Wolff06]. In order to obtain repeatable device characteristics, microfabricated airbridges are utilized, which can be placed within several μm of the T-junction with sub μm accuracy. A scanning electron microscope (SEM) image of a set of airbridges (red) at a T-junction (blue) is shown in Fig. 2.30(b).
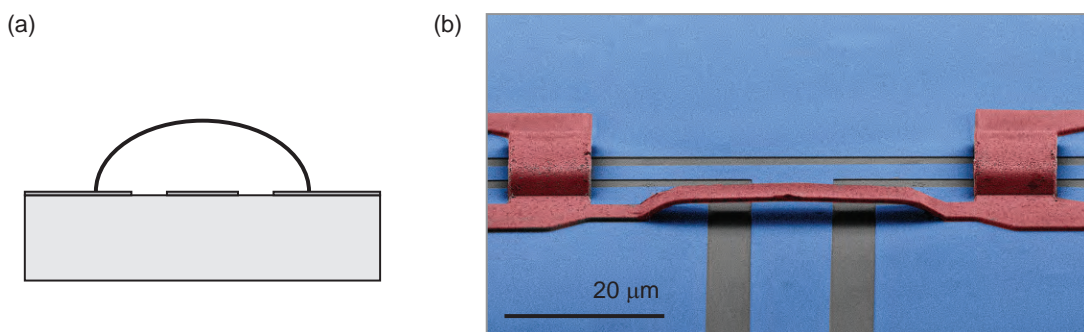

Figure 2.30: (a) An electrical connections between the groundplanes via a wire or bridge suppresses spurios modes. (b) SEM image of three airbridges (red) at the T-junction of a coplanar waveguide (blue).

2.3.7 Temperature Dependence

The properties of the utilized transmission lines are influenced by their superconducting properties in two ways: on the one hand losses are reduced, while on the other hand an extra inductance, the so called kinetic inductance, is introduced. Both of these effects are dependent on temperature and will be discussed in the following.

Kinetic Inductance

In a waveguide the current flowing through the line induces a magnetic field in which energy can be stored. This effect is determined by the geometry of the waveguide and therefore referred to as the geometric inductance, denoted by L_g. Superconducting waveguides additionally allow storage of energy in the motion of the electrons themselves, which in a normal conducting waveguide is lost due to scattering. As a result, the inductance of a superconducting transmission line is given by the sum of these inductances $L = L_\text{g} + L_\text{k}$, where the kinetic inductance L_k is temperature dependent. This leads to a temperature dependence of the phase constant β, shifting the resonance frequency of transmission line based circuits as a function of temperature.

The geometric and kinetic inductances for a coplanar waveguide are given by the following expressions [Watanabe94]:

$$L_\text{g} = \frac{\mu_0}{4} \frac{K(k_0')}{K(k_0)} \ , \tag{2.66}$$

$$L_\text{k} = \mu_0 \frac{\lambda_\text{L}^2}{Wt} g(S, W, t) \ , \tag{2.67}$$

where λ_L is the London penetration depth and g a geometric factor given by [Watanabe94]

$$g(W, S, t) = \frac{1}{2 k_0^2 K(k_0)^2} \left[-\ln \frac{t}{4S} - \frac{S}{S+2W} \ln \frac{t}{4(S+2W)} + \frac{2(W+S)}{S+2W} \ln \frac{W}{S+W} \right] \ .$$

Note that this result is valid only for film thicknesses smaller than $2\,\lambda_\text{L}$. The temperature dependence is implicitly included in the London penetration depth

$$\lambda_\text{L}(T) = \frac{\lambda_0}{\sqrt{1 - (T/T_\text{c})^4}} \ ,$$

where T_c is the critical temperature and λ_0 the penetration depth at 0 K. The kinetic inductance can now be written as

$$L_k(T) = \frac{\mu_0 g \lambda_0^2}{tW(1 - (T/T_\text{c})^4)} \ . \tag{2.68}$$

After obtaining the critical temperature T_c from a DC measurement and calculating g from the waveguide geometry, λ_0 can be determined by measuring the temperature dependence of the kinetic inductance. This is typically achieved by a of the uncoupled resonance frequency $f_0(T)$ of a $\lambda/2$ resonator with length l_r as a function of temperature. The resonance frequency depends on the inductances through:

$$f_0(T) = \frac{1}{2l_r\sqrt{C(L_g + L_k(T))}} = \frac{1}{2l_r\sqrt{CL_g}\sqrt{1 + L_k(T)/L_g}} \ , \qquad (2.69)$$

where C is the capacitance per length of the transmission line. Since the uncoupled resonance frequency cannot be directly measured, it needs to be inferred using

$$f_0 = f_m\left(1 - \frac{1}{2Q_{int}}\right)^{-1} \ , \qquad (2.70)$$

where Q_{int} is obtained using equation (2.41).

RF Losses in Superconducting Waveguides

Several mechanisms lead to losses in a waveguide, the most important of which are conductor losses caused by the resistivity of the metal and dielectric losses caused by absorption of the microwave in the dielectric. In this thesis, superconducting circuits on low loss sapphire substrates are investigated in a temperature range of 2.9 K to 4.2 K, where the conductor loss is dominant, even though the devices are superconducting.

While the DC resistance vanishes for a superconducting line, this is not the case for an AC field. This effect can be modeled using the two-fluid model [Booth99], where a fluid of quasiparticles coexists with a superfluid of Cooper pairs. Here, the quasiparticles lead to a real valued impedance, while the superfluid only has a reactance. The conductance σ of the superconductor can then be written as [Schuster07]:

$$\sigma = \sigma_n + i\frac{A}{\omega L_k} \ , \qquad (2.71)$$

where the normal conductivity is given by $\sigma_n = n_n e^2 \tau_n/m$, A is the conductor cross-section and τ_n the quasiparticle scattering time. The resistance per unit length is then found to be [Yoshida95, Schuster07]:

$$R_l = L_k^2\omega^2\sigma_n = \frac{n_n}{n_s}L_k\omega^2\tau_n g(W, S, t) \ , \qquad (2.72)$$

where n_n is the density of quasiparticles and n_s that of Cooper pairs. BCS theory predicts a temperature dependence of $n_n/n_s = \exp(-1.76\,T_C/T)$, while the temperature

dependence of L_k is given by Eq. 2.68. One can thus expect the loss to display an an exponential decay as a function of the reduced temperature T/T_C.

This dependence implies that, at a fixed temperature, the loss will be smaller for a superconductor with larger critical temperature, motivating the use of NbTiN as the superconductor for impedance matching devices. Alternatively, the loss can be reduced by further decreasing the temperature, for example by utilizing a dilution refrigerator.

2.3.8 Calibration Procedures

Microwave reflectometry in a cryostat requires a number of connected microwave components, which introduce a background signal that is superimposed on the spectrum of the impedance matching device. In the following, we discuss different procedures for removing this background from the measurements.

The reflection measurement setup can be considered as a three-port network, where a microwave tone is applied to port 1, which is reflected at the device connected to port 3 and detected at port 2, as shown schematically in Fig. 2.31(a). The resulting transmission coefficient S_{tr} from port 1 to port 2 is given by [Schoon93]:

$$S_{tr} = S_{21} + \frac{S_{23}S_{31}\Gamma}{1 - S_{33}\Gamma} \ ,$$ (2.73)

where S_{ij} are the scattering parameters from port j to port i, illustrated in Fig. 2.31(b), and Γ is the reflection coefficient of the device. This model will be used to investigate different calibration procedures.
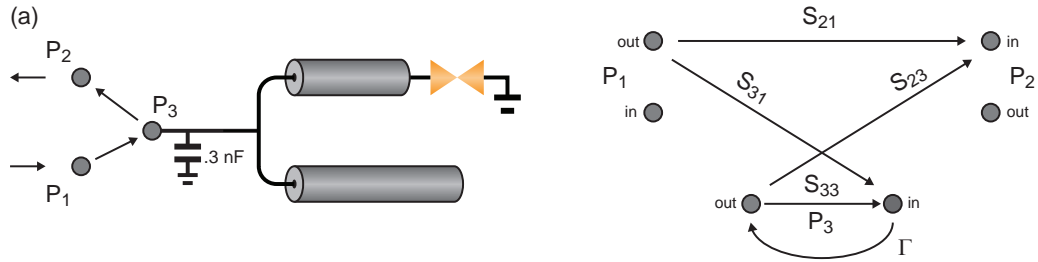

Figure 2.31: (a) Schematic of a reflection measurement. (b) The associated scattering parameters.

The "full" calibration method requires three devices with known reflection coefficient Γ to calculate the scattering parameters in equation 2.73, where the product $S_{23}S_{31}$ can be viewed as a single parameter. By assuming a small value (10^{-3}) for S_{21}, which is justified from the measurement setup, this can be further reduced to two measurements. For this type of calibration to be accurate, a setup with static microwave properties

is required as well as a set of reflection standards with known properties at cryogenic temperatures, both of which are typically not viable.

In RF break-junction experiments, the junction is typically closed at the beginning of the experiment, with a resistance close to 10 Ω, leading to a device reflection coefficient close to unity. The measured spectrum therefore closely resembles the background and can be used for an approximate calibration. In this case, the background is removed by division and the expected tuner response at 10 Ω can be used to further improve the accuracy of the procedure. We obtain the calibrated reflection coefficient Γ_{cal} the measured reflection coefficient Γ_{measured} using

$$\Gamma_{\text{cal}} = \frac{\Gamma_{\text{Theory},R_{BJ}=10~\Omega}}{\Gamma_{R_{BJ}=10~\Omega}} \, \Gamma_{\text{measured}} \quad . \tag{2.74}$$

While this method is easy to implement, it is only accurate for an ideal setup with no back-reflections due to connector mismatches. To investigate the limits of this method, we utilize a simulated dataset, generated using the expected stub tuner response together with equation (2.73) and calibrated using the proposed method. Realistic values of $S_{21} = 10^{-3}$, $S_{31} = 10^{-1}$ and $S_{23} = 1$ are used and the non-perfect setup is simulated by a 0.3 nF shunt capacitor, as shown in Fig. 2.31(a). This capacitor creates a mismatch on the order of typical SMA specifications (20 dB return loss at 18 GHz). The deviation between the actual reflection coefficient and the one obtained using the calibration procedure is shown in Fig. 2.32, where the calibrated curve (red) does not match the expected response (blue). In particular, the peak amplitude changes by 1 dB and the matched load is shifted by 200 Ω. Furthermore, the spectrum is tilted, an effect which has also been observed in the case of resonators [Khalil12], where it was shown that the extracted quality factor in the presence of tilt is an overestimation of the actual value. As such, fitting the stub tuner parameters to the extracted response will include a systematic error. Furthermore, the deviation in this example is small, but as the experimental setup includes a number of connectors and components, each with a small impedance mismatch, a larger deviation between the actual tuner response and the calibrated curve can be expected in the experiment even when all components and connectors are in specifications.

The influence of impedance mismatches on the measurement depends on the bandwidth of the device. For bandwidths in the MHz range, which is the case for matched loads in the 100 kΩ range, one only observes a small tilt, whereas devices with matched loads in the kΩ range and bandwidths close to 100 MHz show periodic oscillations in the spectrum caused by standing waves in the coaxial lines. Tilting can be corrected using the diameter correction method described in [Khalil12], while, for large bandwidth devices, a full calibration is necessary to completely remove the background.

An *in-situ* full calibration of the measurement setup should be possible by using
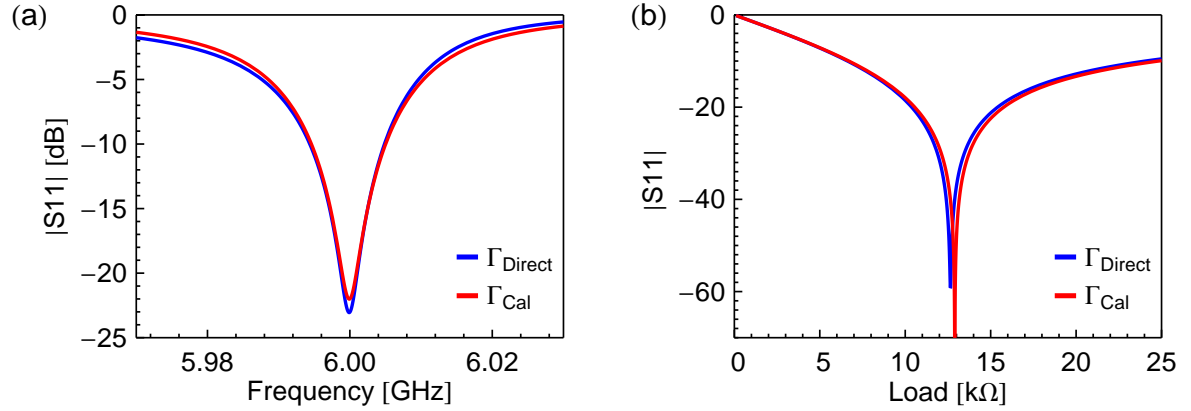
Figure 2.32: Comparison of the stub tuner reflection coefficient Γ_{Direct} and the reflection coefficient calibrated using Eq. 2.74.(a) At a load of 11 kΩ. (b) At 6 GHz.

the temperature dependence of the reflection coefficient of a stub tuner loaded by an unmigrated break-junction. At low temperatures, the tuner reflects the microwave, but as the losses increase, more of the microwave is absorbed in the transmission line, leading to a variable load. This temperature dependence for a small fixed load is illustrated in Fig. 2.33, showing both a change in (a) amplitude and (b) phase. By extracting the temperature dependence of the devices from resonator measurements, the tuner response is known, allowing for an extraction of the parameters $S_{21}, S_{23}S_{31}$ and S_{33} from a measurement of the temperature dependency of the setup/device using equation (2.73). This method has been tested using simulated data, where the setup parameters where successfully recovered from a simulated measurement with added noise, but so far this method has not been applied to a real experiment.
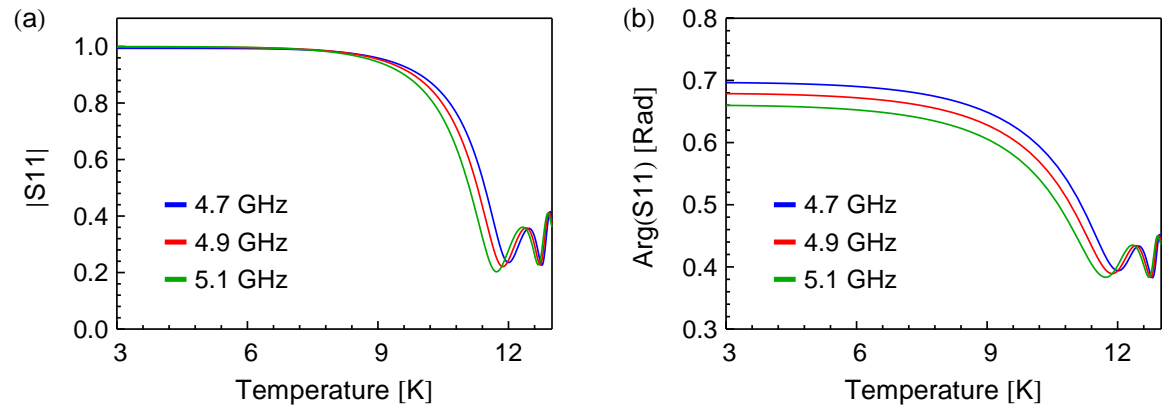

Figure 2.33: Magnitude (a) and phase (b) of S_{11} as a function of temperature.

3 Micro-Chip Design and Fabrication

The physical implementation of break-junctions and stub tuners requires the use of micro- and nanofabrication techniques such as photo- and electron beam lithography. The devices are fabricated on a substrate, which is subsequently diced into individual chips which are then placed in the experimental setup. Two different types of circuit were investigated, a simple design for the DC measurement of side-gated break-junctions and a more involved design in which the break-junction is integrated into a superconducting stub tuner. Each type of chip requires a number of lithography steps for fabrication, utilizing photo- and electron beam lithography as well as metal deposition and etching to define the structures on-chip. Finally, a deposition method for the investigated objects themselves is necessary. The details of the fabrication process and the practical aspects of the sample design will be discussed in the following chapter.

3.1 Sample Design

3.1.1 DC Samples

Single molecule and single nanocrystal devices cannot be deterministically fabricated using current standard fabrication methods. Even when utilizing break-junctions, the success rate for correct device formation is typically less than 50%. Moreover several working devices are necessary to demonstrate systematic effects. It is thus an advantage to have samples with as many break-junctions as possible per cooldown run.

By dividing the structure of the DC samples into two parts, the nanometer scale break-junction and the μm-scale electrodes, chips accommodating a number of break-junctions can be fabricated efficiently and even on a wafer scale, minimizing the time spent on fabrication. The different lithography methods, electron beam lithography (EBL) for the nano-scale structure and photolithography (PL) for the μm-scale, impose different constraints on the design.

Photolithography Mask Design

Following the philosophy of a large number of break-junctions per chip, the photolithography (PL) mask for MCBJ chips, shown in Fig. 3.1, was designed to maximizes the number of available sites per chip. The electrode design is mainly constrained by the counter supports in the MCBJ setup. To provide for positioning tolerance both with regard to mounting the chip in the printed circuit board (see Section 3.2.6) and mounting the board in the experimental setup, a chip size of $10{\times}20$ mm^2 was chosen. We place the electrodes close to one another along the middle of the chip to avoid short circuits at the counter-supports, subsequently fanning the electrodes outwards toward bond pads at the left and right hand sides of the chip.
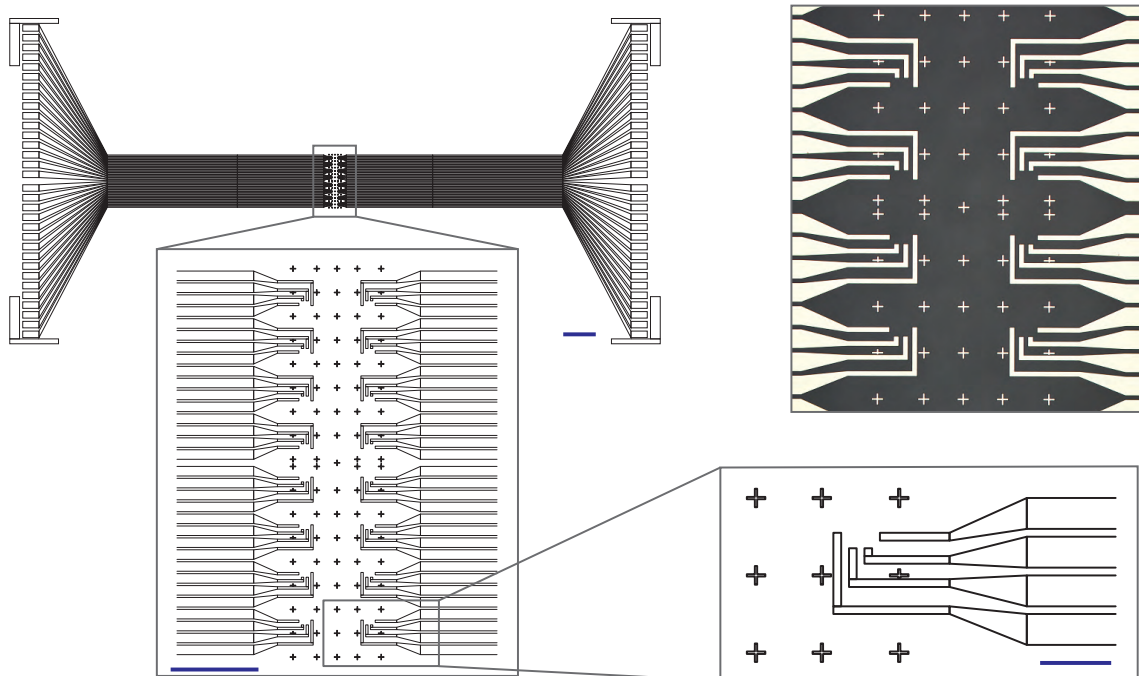

Figure 3.1: PL electrode layout in successing enlargements. The blue scale bars are 1 mm, 500 μm and 100 μm respectively. An optical image is shown in the upper right.

A total of 64 electrodes are placed on the chip, 32 per side, allowing for 16 break-junctions in a four-point, or 32 break-junctions in a two-point measurement configuration. Since a dedicated gate line was not provided for in this design, the total number is reduced when utilizing a number of electrodes as gate lines. Alignment markers are placed on a 100 μm grid at the center of the chip, enabling both manual and automatic alignment of the subsequent EBL layer to the PL layer.
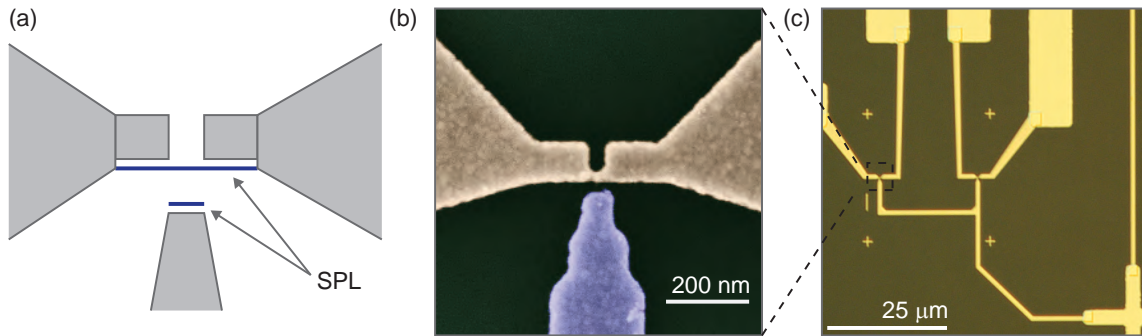
Figure 3.2: (a) EBL design of a break-junction, the thinnest part is defined by a SPL. (b) False color SEM image of a break-junction (yellow) with gate (blue). (c) Optical image of two break-junctions, including the gate-line, alignment markers and numbering.

The size of the chips can be shrunk in future mask designs to an RF chip compatible size of 4.3×14.3 mm², providing more chips per wafer run. Further improvements would include a large groundplane, dedicated gate lines and photolithography based markers for confocal microscope navigation.

EBL Layout

The break-junctions themselves consist of a gold wire with variable width, ranging from one to two μm in the leads down to 20 nm at the designated breaking point. This small width is necessary to minimize screening of the gate electric field and is achieved in the design by the use of a single pixel line (SPL), a line with the best EBL resolution, as illustrated in Fig. 3.2(a). A second single pixel line at the end of the gate electrode allows precise control over the electrode-gate spacing. In case of MCBJs, the break-junctions are suspended by isotropically etching 60-80 nm into the substrate, leading to a suspension of any structure with a width smaller than 120-160 nm. The suspension length can therefore be controlled by choosing an electrode width smaller than twice the etch depth for the suspended part and tapering outward to μm width at the bridge anchors. A false-color SEM image of a break-junction (yellow) with side-gate (blue) is shown in Fig. 3.2(b).

Since the original layout of the PL mask did not include a dedicated gate line, a number of connecting gate lines are added in the EBL step, part of which is visible in Fig. 3.2(c) on the right-hand side. We further use automatic line scans for write-field alignment to allow placement of the EBL pattern with an accuracy on the order of 50 nm, reducing the necessary overlap between the EBL and PL layer and thus exposure time. Furthermore, the patterns are overexposed at the overlap to ensure complete

removal of the resist and good contact between the layers.

For optical identification of the individual sites using the confocal microscope in the measurement setup, a small number is added within the scan range of the confocal microscope. Smaller alignment markers are further added to aid further processing such as ion beam milling, see also Section 3.2.4. An optical image showing two break-junctions with gate line, numbering and alignment markers is shown in Fig. 3.2(c).

3.1.2 RF Circuits with Integrated Break-Junctions

The design of stub tuners with break-junctions combines the EBL design of the DC samples with a circuit consisting of transmission lines, whose lengths are determined by the desired microwave response. In contrast to DC electrodes, the layout of the transmission lines can influence the behavior of the circuit due to parasitic effects (see also Section 2.3.6). Furthermore, these devices require additional fabrication steps to provide electric contact between the transmission lines and the break-junction, a sacrificial layer to allow suspension of the break-junction, as well as airbridges to suppress parasitic modes. The constraints and layout of these elements will be discussed in the following.

Transmission Line Layout

A superconducting stub tuner is a comparatively simple device, consisting of an input port, two transmission lines and the integrated break-junction at one end. The main constraints are the length of the lines, which are determined by the matched load, leaving considerable freedom in the actual layout, which can be used to minimize the influence of parasitic effects.

The standard layout places four stub tuners on a 4.3 x 14.3 mm^2 chip, as illustrated in Fig 3.3(a). This size is large enough to allow for mechanical bending. We further add a coplanar gate line to each of the break-junctions, allowing for both DC and RF gate fields.

The transmission lines are realized in a nominal 50 Ω coplanar waveguide geometry with a 10 μm center conductor and 5.5 μm gap on a 500 μm sapphire substrate. To allow bonding of the center conductor, a launcher with a 150 μm center conductor width and 75 μm gap is necessary at the input port, as shown in Fig. 3.3(b). The transmission line then tapers to the smaller geometry over a distance of 500 μm.

For a given matched load, the transmission line lengths can be calculated by numerically minimizing the reflection coefficient of the circuit shown in Fig. 3.3(d), which takes the stray inductances at the T-junction and parasitic capacitances at the open
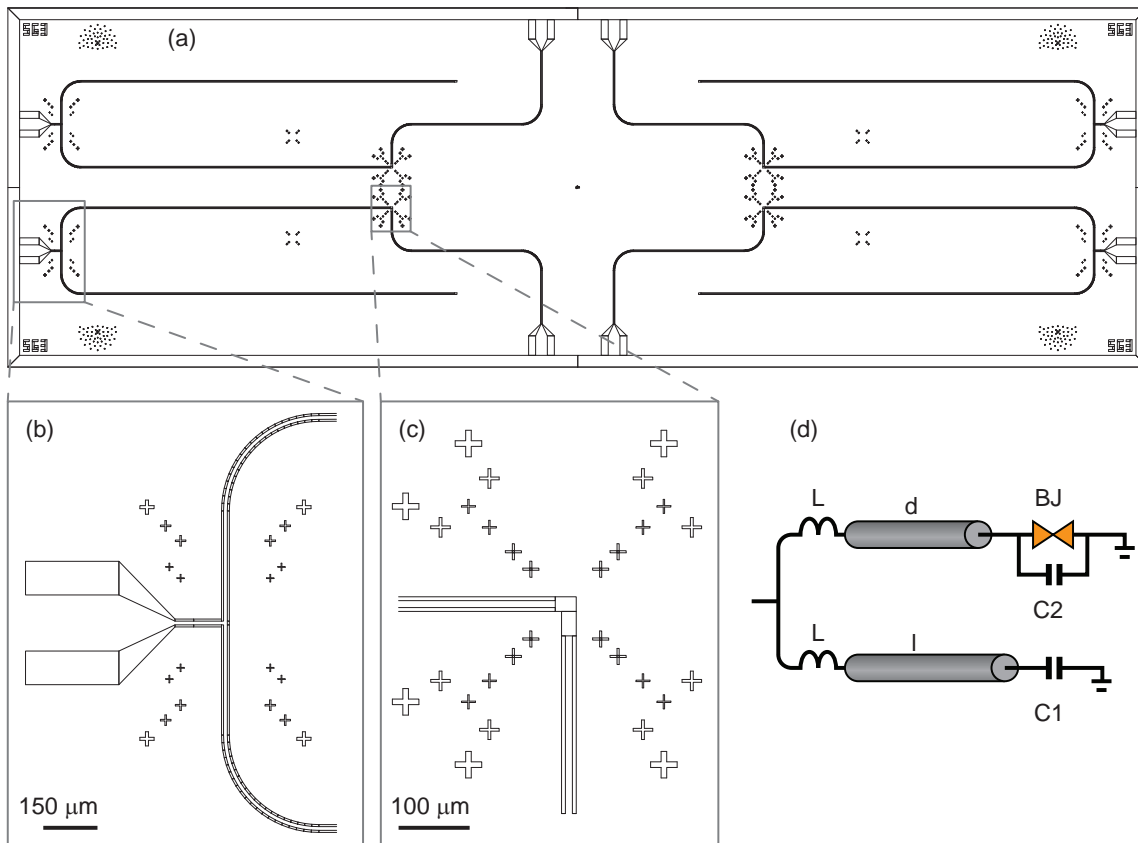
Figure 3.3: Layout of a four-device chip. (a) The entire layout. (b) Launcher and T-junction. (c) Gap for placement of the break-junction, including RF gate line. (d) Equivalent circuit including stray capacitances.

ends into account. Typical values for the stray capacitances are $C1 = 0.7$ fF and $C2 = 1fF$, calculated using an finite element electrostatic simulation [ANSYS], and $L = 2$ pH, extracted from measurements.

We use a symmetric design to take advantage of the fact that parasitic effects affecting both transmission lines will mainly change the resonance frequency but not the matched load. Therefore the gaps at the end of the transmission lines have identical dimensions. We choose the gap length of 30 μm to be 50% larger than $S + 2W$ such that the stray capacitance is saturated. To further minimize the impact of stray capacitance by the break-junction, the leads are designed with a width of 1-2 μm. As described in Section 2.3.6, the T-junction introduces stray inductances, two of which are identical due to symmetry. This fixes the orientation of the T-junction in our design. The layout is illustrated in 3.3.

Bending the transmission lines 90 degrees creates a "tuning fork" shape, which allows placement of four tuners on a single chip. The bending radius is 100 μm to avoid introducing further stray effects, in accordance with established design rules [Simons01]. A remaining constraint is placement of the break-junctions within the field of view of the confocal microscope, a 5×5 mm^2 square centered on the middle of the chip. Here, alignment tolerances of at least 200 μm should be taken into account.

Contact and Sacrificial Pads, Airbridges

Suspended break-junctions in RF matching circuits require a sacrificial layer to allow underetching, as the low-loss sapphire substrate is etch resistant to most chemicals. Furthermore, contact pads are necessary to ensure electric contact between the vertical sidewalls of the coplanar waveguide and the thin gold layer of the break-junction. The position of these structures is fixed with regard to the transmission lines and the design accounts for the μm resolution and 500 nm alignment accuracy of subsequent masks. An illustration is given in Fig. 3.4(a). The contact pads (yellow), with a size of 8×6 μm^2, are placed at the end of the coplanar waveguides (grey), while the sacrificial pad (green), a 10×4 μm^2 square, is placed in the middle. The outline of the side-gated break-junction is indicated by the dashed lines.

The airbridge design accounts for the same alignment accuracy, but otherwise places short bridges as close as possible to the T-junction, electrically connecting all three groundplanes as illustrated in Fig. 3.4(b). Due to their fabrication process, airbridges require two photolithography steps, one with a positive and one with a negative mask, and care needs to be taken that the masks for the typically 10 μm wide and 25-30 μm long bridges are correct. A general guide to airbridge design is given in Appendix B.

Performing a number of subsequent lithography steps on a wafer requires successive
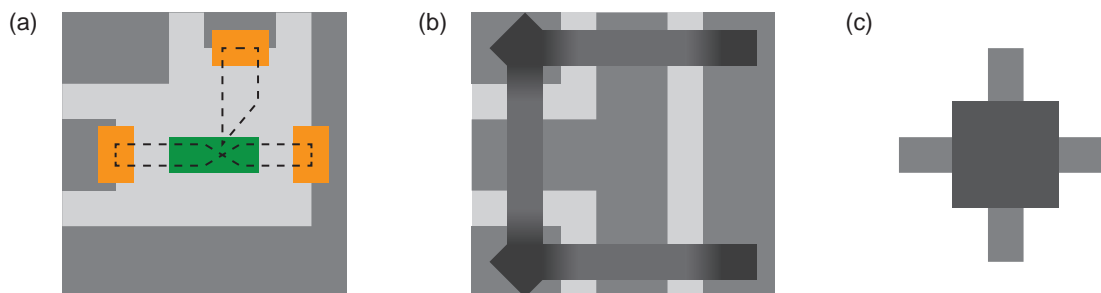
Figure 3.4: (a) Sketch of the contact pads (yellow) and sacrificial layer (green) at the end of a coplanar waveguide (grey), with an outline of the break-junction (black). (b) Schematic of the airbridge layout (dark grey). (c) Alignment marker combination.

alignment of the lithography masks to structures already present. This is typically done using alignment markers, which come in a large variety of shapes. The implemented markers and alignment structures, illustrated in Fig. 3.4(c), follow the idea that humans excel at lining up the centers of two structures. The box (dark grey) on the mask is thus aligned to the cross (gray) on the chip. Each photolithography and EBL step requires a number of alignment marks leading to several sites of markers on the chip.

In the implemented design, some of the markers for the contact pads and the sacrificial layer were placed close to the break-junction gap (visible in Fig: 3.3(c)), where the resulting deposited material can influence the resist thickness. This should be avoided in future designs. Furthermore, no test structures exist to independently verify contact between the niobium and the contact pads and airbridges, a necessary feature for a multiple step fabrication process.

3.2 Sample Fabrication

Once the masks for a given design are finished, the samples are fabricated in FIRST, the ETH cleanroom. For efficiency, fabrication is on a wafer-scale, often with several wafers, which are subsequently diced into the individual chips. In the following, the fabrication process of the two sample types is presented, starting with a discussion on the limits of electron beam lithography, followed by a step-by-step explanation of the fabrication process and finishing with nano-object deposition. Fabrication recipes can be found in Appendix A.2.

3.2.1 Electron Beam Lithography

While it is possible to migrate gold wires with a width of hundreds of nanometers, two constraints require a smaller wire. The first constraint is given by the fact that the source and drain electrodes will shield an applied electric field, as discussed in Section 2.2.3. To mitigate this effect, the two electrodes are fabricated be as thin as possible, which applies to both DC and RF type samples. The second constraint is only imposed on RF devices, namely that the critical current for migrating the junction is smaller than the critical current of the superconducting center conductor. We typically observe a critical current in the superconductor of 25-30 mA for a 10 μm wide center conductor. The critical current necessary for migration is proportional to the cross section of the wire, leading to a maximum junction cross-section of ≈ 2000 nm^2.

Electron beam lithography (EBL) is the tool of choice for fabricating structures with a feature size smaller than 300 nm. In EBL, an appropriate resist, for example polymethylmetharcrylat (PMMA), is exposed by a focused electron beam steered by a pattern generator, with a resolution given by the beam size and pattern generator. The electron beam itself can be focused to a diameter of 2-5 nm and interacts with the resist, creating secondary electrons with energies in the range of 2 to 50 eV. These secondary electrons are responsible for most of the resist exposure and can travel several nm in the resist, which effectively widens the beam to the order of 10-20 nm [Levinson97].

Unfortunately, the range of secondary electrons cannot be influenced, but two further parameters which determine the beam spot size can be optimized, namely forward scattering and resist contrast. Forward scattering is the increase in line width due to scattering of the electrons on the resist and thus dependent both on the resist height and the acceleration voltage. As a rule of thumb, the increase in beam size is roughly 10% of the resist height at 30 kV acceleration voltage. Higher acceleration voltages lead to less interaction of the electron beam with the resist and hence less foward scattering. Since the samples are written using the maximum acceleration voltage available, 30 kV, the optimization of forward scattering is limited to using a thin (60 nm) resist.

Even with a 60 nm resist, the minimal line width reproducibly writable over several chips on a 2" wafer is on the order of 40 nm, with more than 10 nm fluctuations. To further improve the line-width, the resist contrast needs to be increased. This is possible by either moving to a different resist system or by reducing the temperature at which development is performed. Simply speaking, the electron beam cuts the polymer chains of the resist to smaller pieces and the maximum solvable chain length decreases with temperature, yielding better contrast between the exposed and unexposed areas. Good results can be obtained by placing the developer and stopper beakers in an ice bath, thus developing at 0° C. Not only is the line width reduced, width fluctuations

are also reduced to less than 5 nm, significantly improving the process stability. While research indicates that the optimal contrast is achieved at $-15°$ C [Cord07], a further reduction in temperature was not pursued due to the associated increase in technical effort.

The minimal line-width achievable with this process using single-pixel lines spaced far apart is on the order of 10 nm, as illustrated in Fig. 3.5(a), with a metalization of 20 nm gold. For break-junctions, the minimal line-width is closer to 15 nm, the smallest gate spacing less than 20 nm. By slightly increasing the line width ≈ 20 nm and placing the gate 35-40 nm away from the gate, a device yield larger than 99% for fabrication on succesive 2" wafers can be obtained. An example break-junction using these parameters is as shown in Fig. 3.5(b).
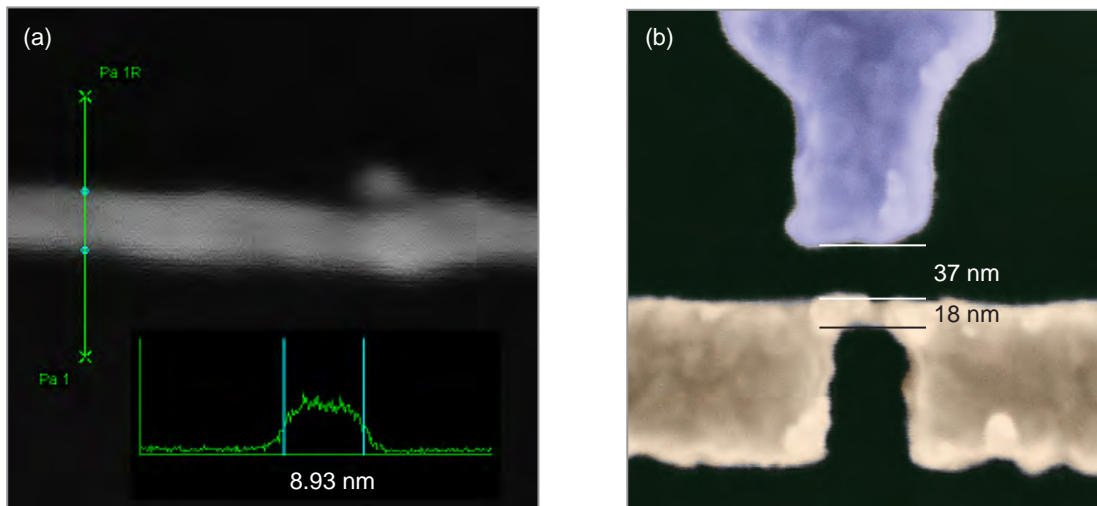
Figure 3.5: (a) SPL with a width smaller than 10 nm. (b) 18 nm wide break-junction with 36 nm gate spacing.

3.2.2 DC Sample Fabrication

The fabrication of DC samples requires two lithography steps, a photolithography step for the large electrodes and an EBL step for the break-junctions. A more detailed description of the fabrication process is given in this subsection.

Starting point is a 2" diameter substrate, either a 275 μm silicon wafer or a 500 μm sapphire wafer. Both types of substrates are coated with a layer of silicon oxide, which acts as a sacrificial layer to obtain free-standing break-junctions. In case of silicon, the wafers are bought with a 50 nm to 300 nm thick layer of thermal oxide from a

commercial supplier, while in case of sapphire wafers, the sacrificial layer is deposited using plasma-enhanced chemical vapor deposition (PECVD).

To reduce the number of fabrication steps performed after defining the break-junction, the large electrodes are fabricated first on the wafer using photolithography. In the first step, a double-layer resist stack consisting of a LOR 5B layer and a positive tone AZ1505 resist layer is spun onto the sample (Fig. 3.6(a)). This double-layer structure is necessary to create a resist profile with large undercut for the subsequent metalization step. Following the exposure of the top layer through a contact mask with a broadband UV light source (Fig. 3.6(b)), photochemically altering the solubility of the exposed resist, the sample is developed (Fig. 3.6(c)). Not only the exposed areas of the top resist layer are dissolved by the developer, but also the sacrificial LOR 5B layer independent of illumination. As a result, the undercut can be controlled by the time the sample is immersed in the developer, allowing for a value on the order of 1-2 μm. The sample is then placed in an physical vapor deposition (PVD) system, where a sticking layer of 5 nm titanium followed by a 50 nm gold layer is evaporated onto the sample (Fig. 3.6(d)). During the evaporation the sample is rotated at a rate of 20°/second and tilted 75° to 82° with respect to the incident metal vapor. This procedure creates sloped electrode sidewalls which ensure good electrical contact to the following metal layer. By subsequently placing the sample in acetone the resist is dissolved, releasing the metal film on top of the resist ("lift-off") and leaving only the patterned electrodes and undercut layer (Fig. 3.6(d)). The undercut layer is removed in the last step with developer and O$_2$ plasma(Fig. 3.6(e)).
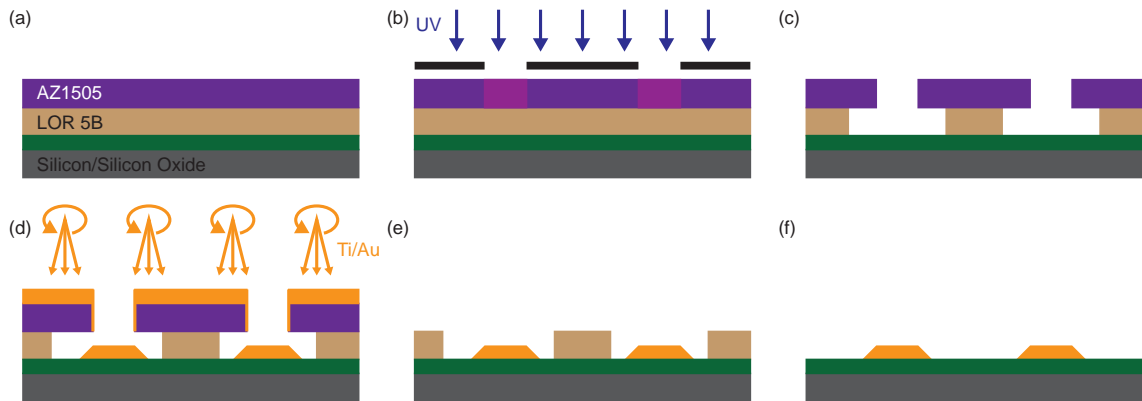

Figure 3.6: Electrode fabrication process. (a) Double layer resist stack LOR 5B/AZ1505. (b) Exposure. (c) Development. (d) Metalization using angled evaporation on a rotating substrate. (e) Lift-off. (f) Cleaning.

The break-junctions are fabricated by EBL (3.2.1), using a two-layer resist stack consisting of PMMA 50K followed by PMMA 950K (Fig. 3.6(a)). Resist exposure

is achieved by moving a focused electron beam over the chip in the required pattern (Fig. 3.6(b)). Afterwards, the structure is developed in cold developer (Fig. 3.6(b))) and placed in the PVD system. Prior to the metal film deposition, an argon-ion etching step is performed to remove residual resist (Fig. 3.6(d)), after which a one nm titanium sticking layer is deposited. This is followed by a 30-80 nm gold layer (Fig. 3.6(e)). After lift-off (Fig. 3.6(f)), the wafer is covered in resist and diced into individual chips using a rotary saw.
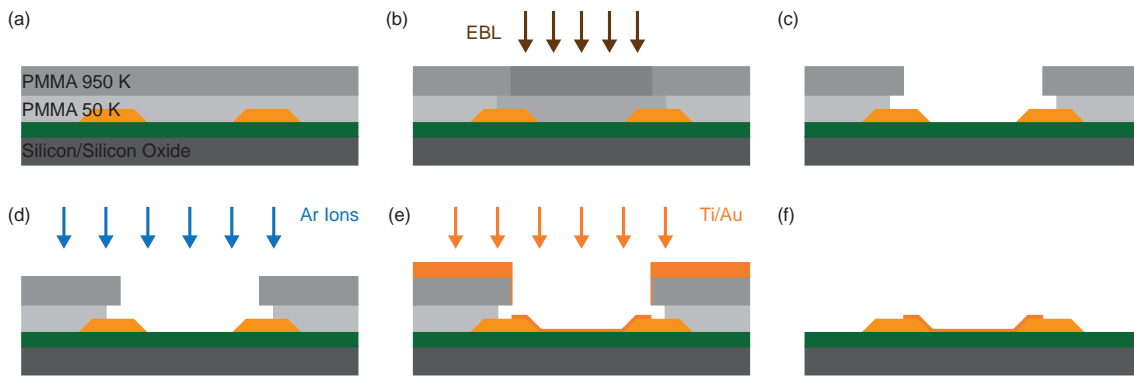

Figure 3.7: Break-junction fabrication process. a. Double layer resist stack PMMA 50K/PMMA 950K. b. Exposure. c. Development. d. Removal of residual resist via argon-ion etching. e. Metalization. f. Lift-off.

To create suspended break-junctions which can be mechanically controlled, the sacrificial silicon oxide layer is isotropically etched using a solution of hydrofluoric acid (HF) buffered with ammonium fluoride (Fig 3.8(b)). By etching 80-100 nm into the oxide layer, only the break-junction is completely underetched, as the metalization acts as an etch mask. This way the length of the suspended bridge can be controlled through the design of the break-junction. To achieve clean junctions, the chips are afterwards cleaned with Dimethyl sulfoxid (DMSO), acetone and IPA. Any remaining contamination is then removed with an O_2 plasma.

For sapphire wafers, the release process was modified, replacing the buffered HF wet etch by an argon/SF6 reactive-ion etch (RIE). The comparatively bad quality of the PECVD silicon oxide, with respect thermally grown silicon oxide, allows for an isotropic etch in the RIE, which additionally removes any residue from the structure, thus eliminating further cleaning steps. The samples are then ready for deposition of the nano-objects.

Figure 3.8: Break-junction suspension process: (a) Starting structure. (b) Removal of sacrificial layer, the break-junction acts as an etch mask. (c) Cleaning with O_2 plasma.

3.2.3 RF Sample Fabrication

The fabrication of RF impedance matching circuits with integrated break-junctions uses a similar EBL step to define the break-junction but requires a number of additional photolithography steps compared to the DC samples. These can be roughly grouped into fabrication of the transmission lines, steps associated with the break-junction and fabrication of the airbridges, all of which will be discussed in the following. The detailed fabrication recipe is given in Appendix A.3.

Transmission Lines

Starting point for the RF Devices are 500 μm thick 2" sapphire wafers, which have been coated with a 150 nm thick niobium or niobium-titanium-nitride film. The wafer is spin-coated with either a AZ1505 positive tone resist layer or a PMMA 950K layer. Both resists were used, with the AZ resist providing better selectivity and allowing longer etch times, necessary for NbTiN films, whereas PMMA provides a better resolution due to the use of 220 nm deep ultra-violet light (DUV). Following exposure and development, residual resist at the exposed metal surfaces is removed using O_2 plasma and the pattern is etched into the metal film using a mixture of argon and SF6 for RIE. After the etching step, the remaining resist mask is stripped with acetone.

Break-Junctions

For MCBJs in RF samples, several process steps are necessary: contact pads, a sacrificial layer and the break-junctions themselves. In the first step, contact pads with sloped side-walls are manufactured, ensuring electrical contact between the vertical sidewalls of the transmission line and the subsequently defined break-junctions. This process is similar to the electrode fabrication of the DC samples in Section 3.2.2. A double-layer of LOR 5B/AZ1505 is spun onto the wafer and exposed (Fig. 3.10(a) and(b)). Using standard developer, both the exposed resist and the UV-insensitive LOR layer are developed away, with an undercut in the micron range (Fig. 3.10(c)). After a O_2
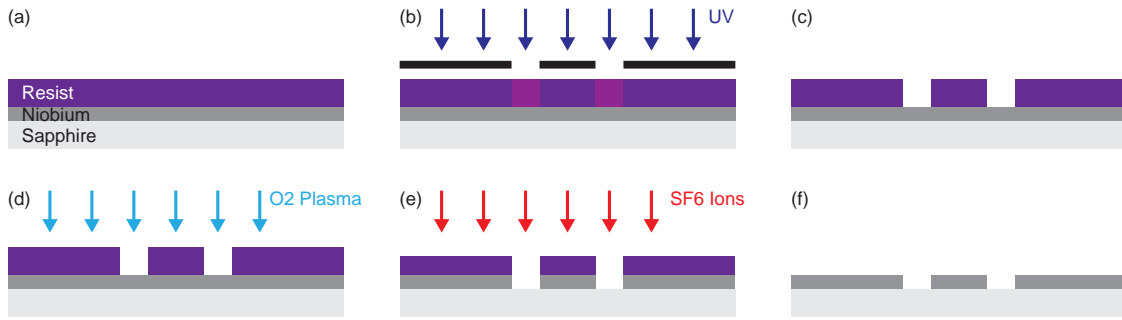
Figure 3.9: Transmission line etch process: (a) Resist layer: PMMA 950K or AZ1505. (b) Pattern exposure. (c) Development. (d) O$_2$ plasma clean. (e) Reactive-ion etching. (f) Resist mask removal.

plasma cleaning step, the sample is loaded into the PVD system and argon-ion etched to remove the native oxide on the niobium surface (Fig. 3.10(d)). A sticking layer of 5 nm titanium, followed by a 20-80 nm gold contact layer is then evaporated onto the sample, which is tilted at 82° with respect to the incident metal vapor and rotating at a rate of 20°/s (Fig. 3.10(e)). This is necessary to achieve continuous gold pads at the edge of the transmission line and also yields pads with sloped sidewalls, allowing good contact to the subsequent electron beam step. The excess metal film is then lifted off in acetone (Fig. 3.10(f)).

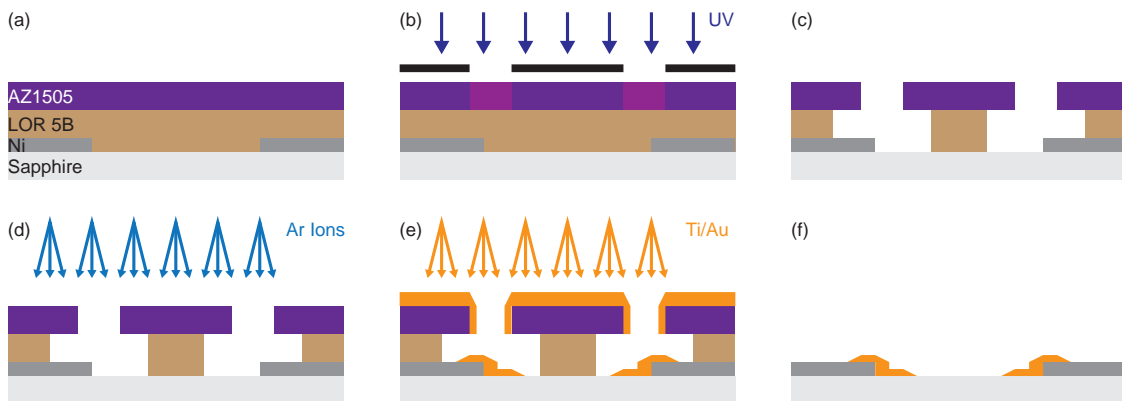**Figure 3.10:** Contact Pad deposition: (a) Double resist stack: LOR 5B/AZ1505. (b) Exposure. (c). Development. (d) Argon-Ion etch. (e) Metalization Ti/Au. (f) Lift-off.

To create a suspended break-junction, necessary for mechanical control, the substrate is typically etched in an isotropic manner. The low loss sapphire substrate, however, is very etch resistant [Williams03] and although it is possible to wet etch sapphire

using phosphoric and sulfuric acid at temperatures exceeding 200° C, the etchant will also attack the other metals present on the chip and most photo resists, prohibiting this process. A second possibility is reactive-ion etching, but possible issues with both selectivity and anisotropy of such a process precluded further investigation. The third possibility and chosen solution is the deposition of a sacrificial layer in a small area, which can subsequently be isotropically etched at the end of the process. Silicon oxide, deposited using PECVD, was chosen as the material due to compatibility with the DC sample process. Furthermore, the PECVD process yields sacrificial pads with sloped edges, which mitigates issues with film continuity of the break-junction leads.

Chemical vapor deposition is a conformal process and as such requires a significant amount of undercut, in the range of 2-4 μm, to achieve deposition of a pad without "ears", as well as a clean lift-off. Due to the good undercut tunability of the LOR 5B/AZ1505 double layer, the process is almost identical with the contact pad deposition (Fig. 3.11 a-c). A longer development time yields an undercut of 3-4 μm (Fig. 3.11(c)), after which a 50-100 nm thick silicon oxide film is deposited via PECVD (Fig. 3.11(d)). After lift-off in acetone (Fig. 3.11(e)), a final strip with developer removes the LOR 5B layer (Fig. 3.11(f)), and a cleaning step with O$_2$ plasma ensures a contamination free wafer.
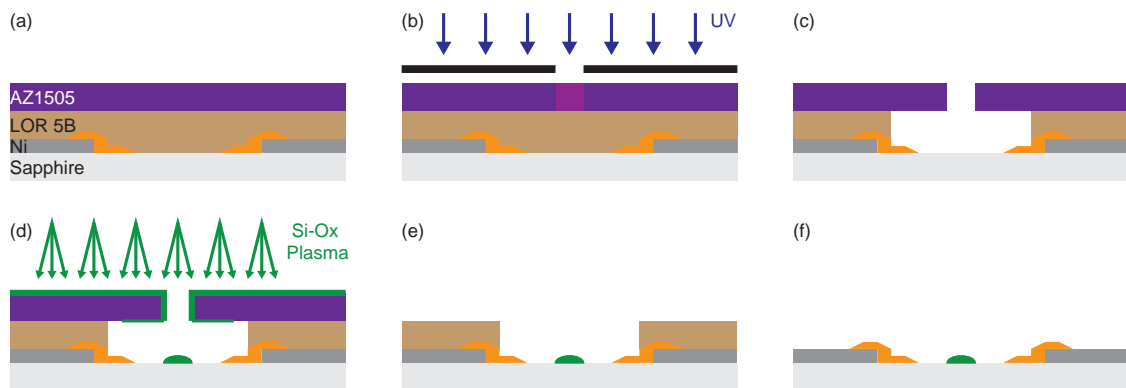
Figure 3.11: Sacrificial Pad deposition: (a) Double resist stack: LOR 5B/AZ1505. (b) Exposure. (c). Development. (d) PECVD of silicon oxide. (e) Lift-off.(f) Removal of LOR layer.

With both the contact pads and the sacrificial layer in place, the last step is the fabrication of the break-junctions themselves. This process is identical to the process for DC break-junctions described in 3.2.2. Starting with a double-layer resist stack of PMMA 50K and PMMA 950K (Fig. 3.12(a)), the break-junctions are patterned using EBL (Fig. 3.12(b)) and developed using cold developer (Fig. 3.12(c)). The exposed surface of the wafer is ozone-cleaned and argon-ion-etched to remove residual resist

(Fig. 3.12(d)), followed by a metalization step, depositing 1 nm titanium and 30-80 nm gold (Fig. 3.12(e)). Lift-off in acetone concludes fabrication of the break-junctions (Fig. 3.12(f)).

Figure 3.12: Break-junction fabrication process. a. Double layer resist stack PMMA 50K/PMMA 950K. b. Exposure. c. Development. d. Removal of residual resist via argon-ion etching. e. Metalization. f. Lift-off.

Airbridges

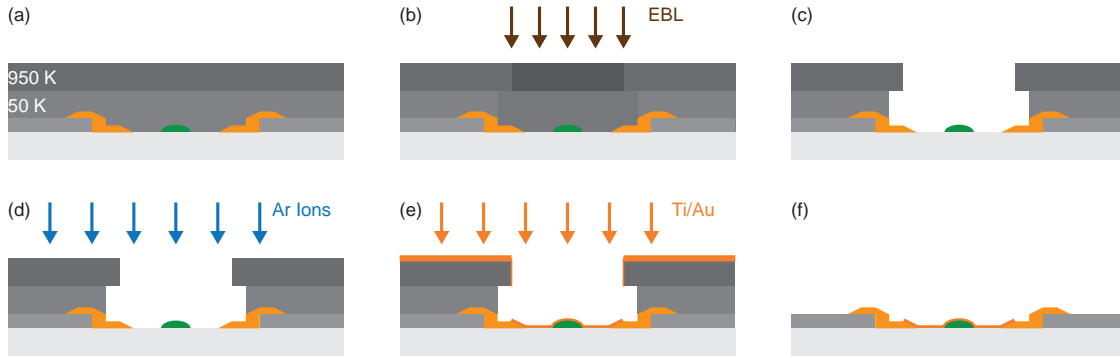To suppress spurious modes in coplanar waveguides, the two ground planes on either side of the center conductor need to be electrically connected. This can either be achieved by using bond wires, or, to ensure repeatable characteristics of the device, with airbridges. These are fabricated using a three-dimensional process where a patterned PMMA layer is used to create the vertical profile of the bridges. The presented process was adapted from a recipe supplied by the group of Prof. Bolognesi at ETH Zurich.

Starting from a two to three μm thick PMMA 950K layer (Fig. 3.13(a)), the bridge contact points are patterned using 220 nm UV light (Fig. 3.13(b)). After development (Fig. 3.13(c)), the wafer is heated to 180° C for a several minutes, causing the PMMA to reflow, which results in rounded edges and creates the bridge-like vertical profile (Fig. 3.13(d)). The planar outline of the bridge is then defined using a layer of AZ5214E image reversal resist ((Fig. 3.13(e)), which is patterned using a negative mask (Fig. 3.13(f)). In this process the 360-410 nm UV light used does not further expose the PMMA layer. A reversal-bake step cross-links the exposed resist, making it insoluble to the developer and insensitive to UV light. The wafer is then flood exposed and developed (Fig. 3.13(g)), the negative mask/reversal bake/flood exposure procedure creating a resist profile with undercut, while the water-based developer does not affect the PMMA layer. Afterwards the sample is loaded into the PVD system where an argon-ion etch step removes native oxide on the niobium contact areas. Using a series

of evaporation steps at different angles, all with a rotating substrate, a metalization profile of 250 nm titanium and 250 nm aluminum, encased in 10-30 nm gold is created. The gold outer layer is necessary to render the airbridge metalization inert to the break-junction release step. Lift-off in acetone and release in N-Methyl-2-Pyrrolidon (NMP) or DMSO concludes fabrication of the airbridges.
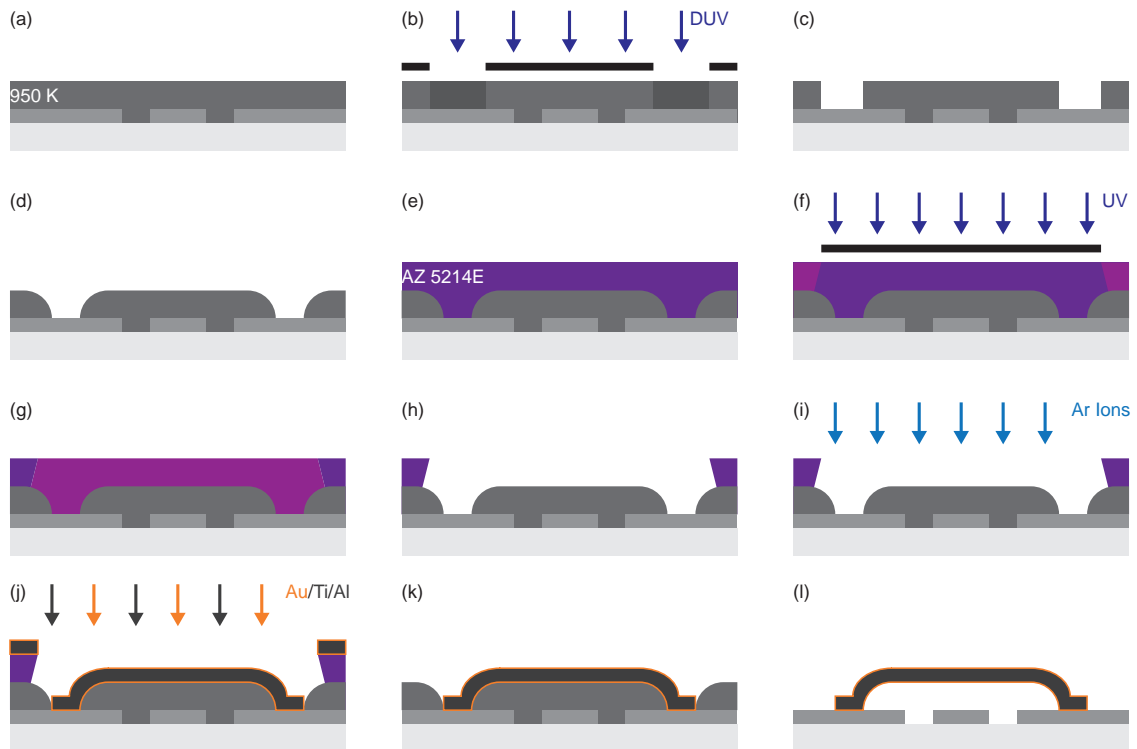
Figure 3.13: Airbridge fabrication process: (a) PMMA 950K layer. (b) Patterning of bridge contact points. (c) Development. (d) Reflow. (e) AZ5214E layer. (f) Patterning of bridge outlines. (g) Reversal bake and flood exposure. (h) Development. (i). Argon-ion etching. (j) Metalization with gold/titanium/aluminium/gold (k) Lift-off. (l) Bridge release.

Post-Processing

The finishing steps of the RF device fabrication are dicing and release of the break-junctions, an optical image of a finished wafer is shown in Fig. 3.14(a). After deposition of a protective resist layer, the wafer is diced using a rotary saw. The protective layer is then stripped in several consecutive baths of acetone and the individual chips are now ready for release of the break-junctions. In contrast to thermal silicon oxide, the PECVD oxide is not very etch resistant to buffered HF and shows varying etch rates,

requiring care to avoid over-etching. Alternatively, RIE etching can be used, but a photo-resist mask is necessary to avoid etching the RF circuit. The sacrificial pad is visible in the zoom in shown in Fig. 3.14(b) as a dark rectangle. The final cleaning step is identical to that of the DC samples, using DMSO/Acetone/IPA followed by O_2 plasma cleaning. The chips are now ready for coating with the nano-objects of interest.
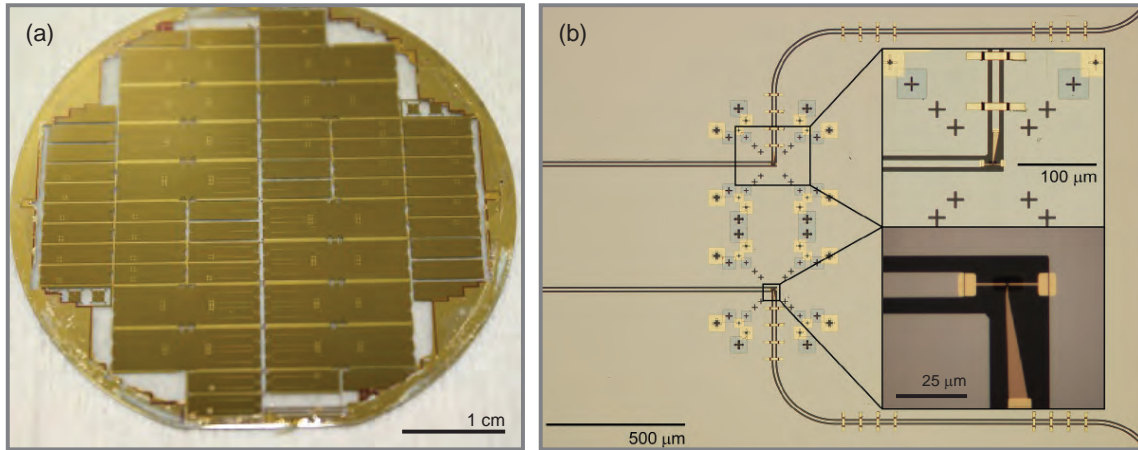

Figure 3.14: (a) Photograph of a finished wafer prior to dicing. (b) Optical image of the break-junctions integrated into transmission line circuits, showing the niobium transmission line, contact pads (bright gold), break-junction (orange gold) and a number of gold-plated airbridges.

3.2.4 Focused Ion Beam Milling

While break-junctions are well suited for the formation of single molecule devices, the resulting gap, typically smaller than 1 nm, is too small to achieve the ideal axial geometry in case of 5 nm diameter colloidal quantum dots. While a gap of 5 nm can be achieved using EBL [Klein96], the sample yield is expected to be low. In contrast, technical advances in focused ion beam (FIB) milling provide for feature sizes on this size scale with high fidelity. FIB milling utilizes an ion beam to remove material in a given pattern, much like an electron beam is used to expose resist in EBL. By using helium instead of gallium it is possible to achieve cutting widths on the order of 5 nm. In particular, by cutting a break-junction, electrodes with a 5 nm gap can be deterministically fabricated, which should lead to higher device yield and more stable devices when working with colloidal quantum dots. An example device is shown in Fig. 3.15, before FIB (a) and afterward (b), the cut can be clearly distinguished, for better comparison a 10 nm scale bar is placed beneath the cut. The milling was performed by Dr. Shorubalko at EMPA.
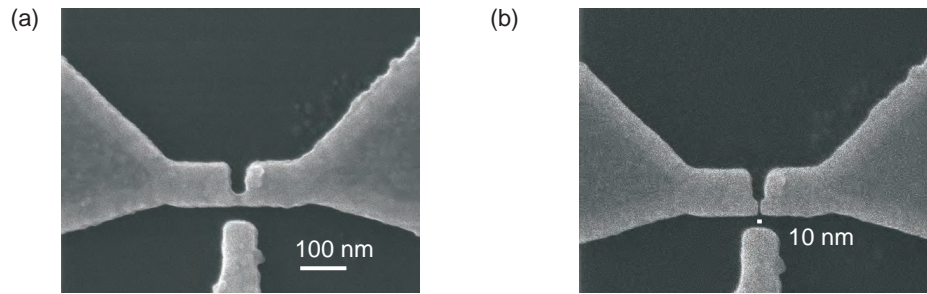
Figure 3.15: (a) A break-junction sample before FIB milling. (b) The same sample after FIB milling, the cut is visible.

3.2.5 Nano-Object Deposition

Three different types of nano-objects were investigated in this thesis: C_{60} molecules, colloidal quantum dots and carbon nanotubes. The first two require break-junctions to form a device, in which case the objects are deposited from solution onto the break-junctions which is subsequently broken to form the device. Carbon nanotubes, on the other hand, are large enough to be directly deposited on the device. The specifics of the deposition process will be presented in the following.

C_{60} Molecules

C_{60} molecules can be bought in dry, purified form from commercial supplier and are subsequently diluted in toluene to a concentration of .14 mMol/mL using a precision scale and several dilution steps. For deposition, the chips are placed in a dedicated beaker containing 1 mL of solution for 30 seconds. Afterwards, the chips are removed and immediately blown dry with nitrogen. This is important to avoid "coffee-stains", aggregations of molecules which can short-circuit the electrodes on the chips and is especially critical for RF devices.

Colloidal Quantum Dots

Although colloidal quantum dots can also be bought from commercial suppliers, the manufacturers typically do not disclose the exact composition and dimensions of the dots. For this reason, CdSe and ZnCdSe colloidal quantum dots with a diameter of 5 nm where synthesized by O. Yarema (Nanoelectronics group, Prof. Wood, ETH Zurich). To ensure that the dots stick to the gold electrodes, different types of linker molecules where used to bind the dots to the electrodes. These linkers consist of two thiol endgroups, which stick both to gold and CdSe, connected either by a 6 carbon

atom chain (hexanedithiol or HDT) or by a benzene ring (benzenedithiol or BDT).

A monolayer of these linker molecules is first assembled on the gold surface by immersing the chip in a solution for several hours. The samples are then rinsed and placed in a solution of quantum dots, where they also remain for several hours. Afterwards, the samples are rinsed in IPA and blown dry with nitrogen. An SEM image of a break-junction with deposited dots is shown in Fig. 3.16(a), where the dots are visible as white round spheres, several dots are indicated the white arrows.
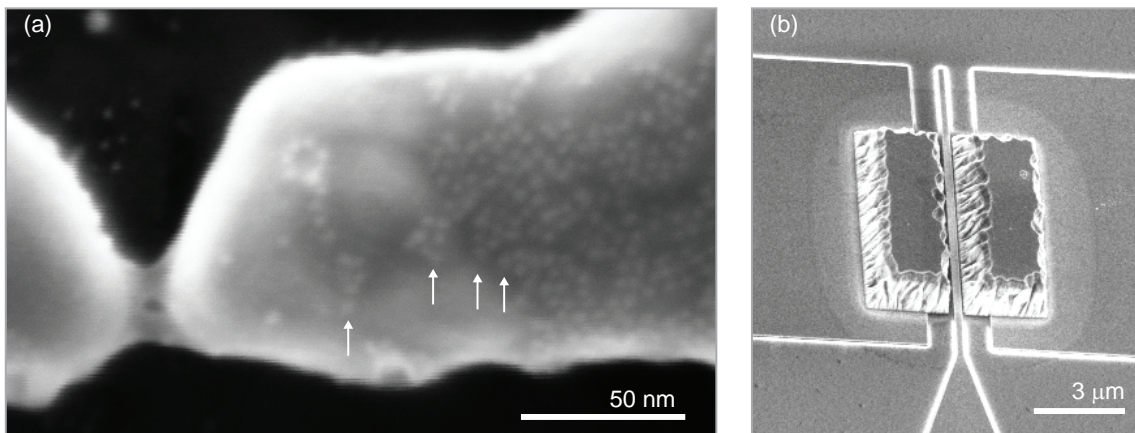
Figure 3.16: (a) Colloidal quantum dots (white spheres) on a gold break-junction. (b) Source and drain contacts for a CNT. The 1.7 μm high contacts are separated by a 1 μm gap into which a back gate is placed.

Carbon Nanotubes

While the focus of this thesis is on nano-object devices formed using break-junctions, a series of measurements was performed using single-walled carbon nanotube (SW CNT) devices. Deterministic CNT device fabrication is possible by CNT growth, location by atomic force microscopy (AFM) and contacting via EBL, but the resulting devices are contaminated by resist residue, which influences the behavior of the devices. Clean nanotubes can be grown after device fabrication from patterned catalyst, but device yield is typically below 10% and the growth temperatures exceed 700° C, which leads to superconducting waveguides with large loss. In this thesis a transfer method is used, which deterministically yields clean nanotube devices and is achieved by segregating growth and device fabrication. This method, first demonstrated in Ref. [Wu10], was adapted by M. Muoth [Muoth12] of Prof. Hierolds group, who performed CNT growth and transfer.

In a first step, CNT are grown across fork structures on a silicon chip at growth

conditions favoring single tubes that span the 8-10 μm gap between the fork tines. At
the same time, source and drain contacts for the CNT are fabricated at the load end of
an RF stub tuner. These contacts are palladium and elevated by 1.6 μm with respect
to the chip surface, as can be discerned in the SEM image shown in Fig. 3.16(b). The
stub tuner is then mounted into a printed circuit board, wire bonded and finally argon-
ion etched to remove contamination and possible oxide from the palladium contacts.
In the second step, the RF device is placed in a micro-manipulator setup and the
silicon chip with the fork structures is mounted on the micro-manipulator arm. The
following deposition of the nanotube is illustrated in Fig. 3.17 and proceeds as follows:
the fork is moved to the vicinity of the source/drain contacts and aligned using an
optical microscope (Fig. 3.17(a)), after which it is lowered onto the chip (Fig. 3.17(b).
During this procedure, a bias of 200 mV is applied to the electrodes and the current is
monitored. If a CNT is present and bridges the electrodes, a current is detected and
the bias is increased to 2.4 V for several seconds to anneal the contact. The fork is then
retracted sideways (Fig. 3.17(c)), ideally leaving the CNT in place. Due to the fact
that the current is monitored, the successful formation of a device can be confirmed
and in case of an empty fork or non-sticking CNT, the procedure is repeated until a
working device is formed. The resulting clean CNT device is then ready for placement
in the measurement setup.
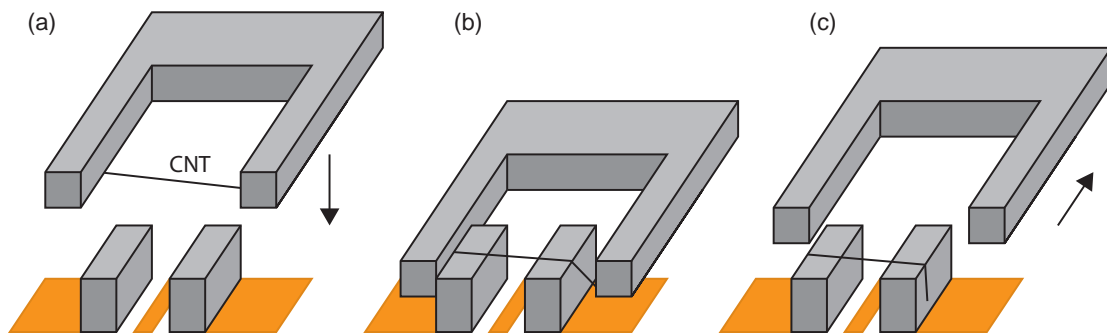
Figure 3.17: (a) Approach and alignment of the CNT/fork with the sample elec-
trodes. (b) Placement. (c) Retraction of the fork.

3.2.6 Printed Circuit Boards for Sample Mounting

The last steps before the finished devices can be measured in the experimental setup
are mounting in a printed circuit board (PCB) and wire bonding the electrical contacts.
This is necessary to allow the transition from the mm-scale electrical connectors present
in the experimental setup, to the 100 μm scale electric contacts of the devices.

In case of DC samples, the PCB features 48 copper connects and pins for electric contact to the break-junctions as well as four SMP connectors to connect to the RF gate lines of the measurement setup, a picture is shown in Fig. 3.18(a). The chip is placed in a recess in the middle of the home-made FR4/copper PCB and held in place using double-sided tape, while a hole in the center allows access to the rear of the chip for the MCBJ setup. After mounting, the contacts are wire-bonded using aluminum bonds.
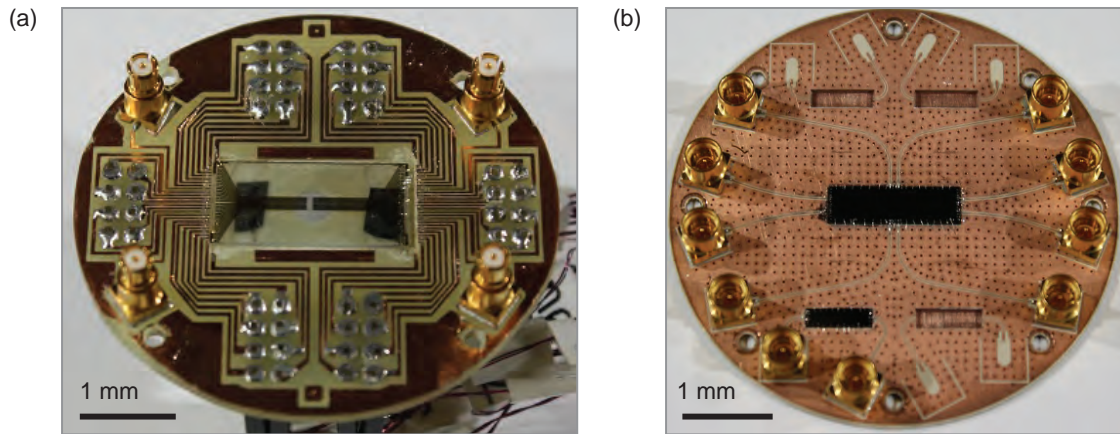
Figure 3.18: (a) DC sample with PCB. (b) RF sample with PCB

In contrast, the RF PCBs require 50 Ω transmission lines, implemented as ground-backed coplanar waveguides, to connect the devices, as shown in Fig. 3.18(b). A large number of vias connect the top and bottom copper groundplane to suppress spurious modes in the 500 μm thick Arlon dielectric, while SMP connectors are used to connect the RF lines to the measurement setup. The sample is glued into a recess using PMMA and also wire-bonded with aluminum bonds. A large number of bonds connecting the groundplanes is necessary to suppress slotline modes along the PCB/chip gap. Similar to the DC devices, a hole is present in the copper bottom plane to allow bending the chip. In addition to the recess and connections for the stub tuner, a number of slots for $\lambda/2$ resonators is provided.

Mounting and bonding concludes the fabrication of the samples, which are subsequently placed in the experimental setup to perform experiments.

4 Measurement Principles and Experimental Setup

Optical and RF investigations of MCBJ based nano-object devices requires a combination of the different elements necessary for these investigations in one cryogenic setup. To enable these measurements, we develop a pulse-tube based cryostat in which an MCBJ setup, a confocal microscope and the necessary RF reflectometry components are combined. This setup opens the possibility of a number of different experiments combining optical excitation with time-resolved transport measurements.

This chapter discusses the individual experimental principles underlying the different components of the experimental setup, such as MCBJs, RF reflectometry and confocal microscopy in the first part. In a second part a detailed discussion of the implemented cryostat, including the vacuum and thermal design, is given.

4.1 Mechanical Control of Break-Junctions

Electrodes with tunable nanometer separation can be implemented by breaking a suspended break-junction in an MCBJ setup via bending the supporting chip, as explained in Section 2.2.1. In a typical setup the chip is pressed against two counter-supports by a fine-thread screw, as shown in Fig. 4.1, which offers the advantage of a large range of travel in comparison to, for example, piezo-electric actuators. This allows the screw to be retracted during cooldown to avoid breaking the chip by mechanical stress due to thermal contraction. Fortunately, the small translation factor between the z-axis displacement and electrode separation allows for picometer control over the electrode gap with a displacement resolution in the 100 nm range.

The implemented setup utilizes a fine-thread screw at base temperature to bend the sample, actuated by a stepper motor at room temperature via a drive shaft and vacuum-feedthrough. A 200 μm/revolution screw, together with a 400 steps/revolution stepper motor yields a z-axis control of 500 nm per step, which can be increased to 33 nm per step by use of an additional 15:1 gear-box.
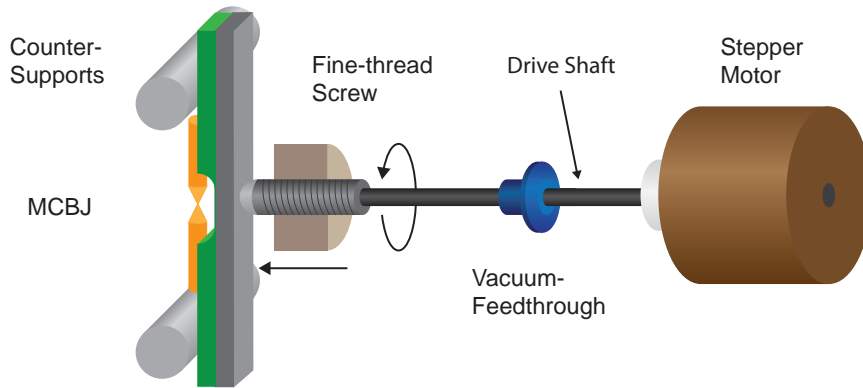
Figure 4.1: Schematic of the mechanical setup. The MCBJ chip is bent by pressing it against two counter supports via a fine-threaded screw. A stepper motor is used to rotate the screw via a vacuum-feedthrough and drive shaft.

4.2 DC Measurements

To record the DC and low-frequency $I - V$ characteristics of the investigated devices, two different types of setups were utilized. One setup is based on an integrated source-measure unit, which allows DC measurements in a four-point configuration, while the second one is based on a current-to-voltage $(I - V)$ converter, allowing both DC and low-frequency lock-in measurements.

4.2.1 Four-Point Measurement Setup

To eliminate the additional resistance introduced by the wiring and leads, which dominates the resistance for an unbroken break-junction and strongly influences the electromigration (see also Section 2.2.2), a measurement configuration known as four-point measurement is adopted. As illustrated in Fig. 4.2(a), the device under test (DUT) is biased through one set of leads, either by a voltage or a current source and the resulting current is measured with an ammeter. A second pair of leads is then utilized to measure the voltage drop over the DUT. As the voltmeter ideally has an infinite input resistance, no current will flow through the second pair of leads, and therefore no voltage will drop over these "sense" leads. This results in an accurate measurement of the voltage drop over the DUT, eliminating the influence of the leads on the resulting measurement.

To perform a four-point measurement, a voltage or current source, an ammeter and a voltmeter are necessary. As this type of measurement setup is common, source-measure units (SMUs) which integrating these components into a single instrument are
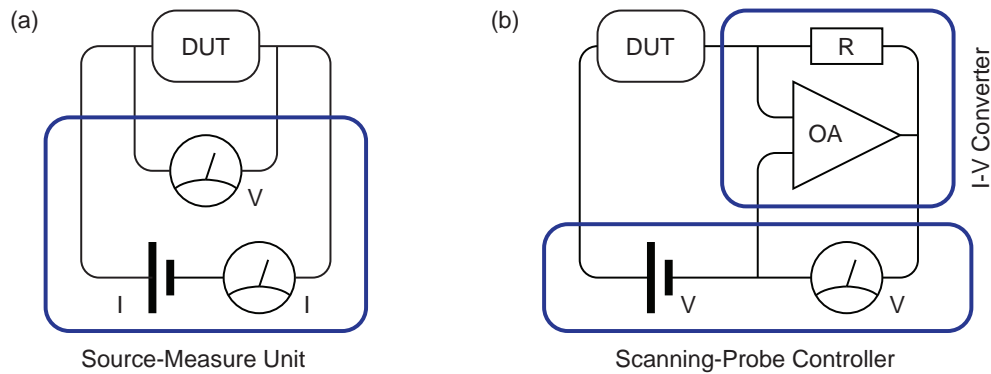
Figure 4.2: (a) Schematic of a four point measurement. (b) Schematic of the $I - V$ converter setup.

commercially available. In this thesis a SMU with two independent differential outputs and both two- and four-point measurement modes was used [Keithley].

This SMU can act both as a current or a voltage source, depending on the measurement requirements. Internally, both modes source a current, but in "voltage source mode", a feedback loop is used to apply a current such that the required voltage drop is achieved. This can be an issue when using the four-point mode and measuring a device with large parasitic capacitances, as introduced, for example, by a bias-tee, leading to unstable operation.

4.2.2 I-V Converter Measurement Setup

Although a SMU offers a large range of functionality, it does not allow for lock-in measurements, which are useful both to determine the DOS of the device and to measure a photo current.

To perform these types of measurements, a second setup was used, consisting of a voltage source, an $I-V$ converter and a voltmeter, as shown in Fig. 4.2(b). The DUT is biased by the voltage source and the resulting current is converted into a voltage using an $I - V$ converter. A voltmeter is then used to measure the resulting voltage. Two types of FPGA-based instruments were utilized, both of which integrate the voltage source and voltmeter. One is the scanning-probe controller (SPC) used for the confocal microscope [attocube GmbHe], the second a dedicated lock-in detection unit [Zurich Instruments]. The $I - V$ converter is based on a standard operational amplifier (OA) design, with the conversion factor of current to voltage given by the feedback resistor R.

This setup can be used both to measure the current or to perform a lock-in measure-

ment. While typically applied to record $I-V$ or $\mathrm{d}I/\mathrm{d}V$ curves, the confocal microscope controller further allows for position dependent measurements, where a number of input channels can be measured per pixel, allowing for a spatial map of, for example, the photo current.

In case of a DOS measurement, a small a.c. voltage with frequency f_0 is added to the bias voltage V_{dc}, resulting in a time-dependent current

$$I(t) \approx I(V_{\mathrm{dc}}) + \frac{\partial I}{\partial V}\Big|_{V_{\mathrm{dc}}} V_{\mathrm{ac}} \cos(f_0 t). \tag{4.1}$$

The differential conductance can therefore be extracted by measuring the frequency component of $I(t)$ at f_0. In case of the light-dependent transport, the illumination source is intensity modulated with a frequency f_0, resulting in a photo current at frequency f_0. In both cases, the modulation is provided by the instrument, which then extracts the correct frequency component using a homodyne detection method, discussed in Section 4.3.

4.2.3 Electrostatic Discharge

The controlled breaking of a thin gold wire, either by electromigration or mechanical means, requires the gold wire to be susceptive to the breaking. Unfortunately, this renders the break-junctions prone to electrostatic discharge (ESD) and can result in broken junctions, as shown in Fig. 4.3. Several safety precautions are therefore required to avoid premature and uncontrolled breaking.
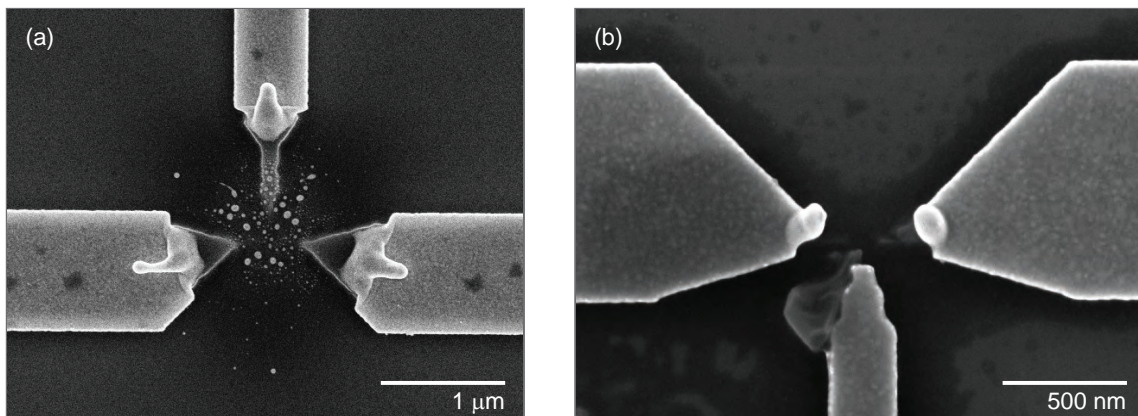

Figure 4.3: SEM images of two different break-junctions destroyed by ESD.

In general, devices with large lead resistances, such as stub tuners in the normal conducting state, suffer much less from ESD issues, as the leads act as current limiters.

Furthermore, the substrate is an important factor, where DC devices on sapphire are prone to ESD damage even during fabrication and SEM imaging, while devices on silicon are not affected at all during these steps.

As a general principle, the devices should be shorted whenever possible, especially when connecting the devices to the experimental setup. In this case, both the devices and the setup wiring are required to be shorted and ideally an ionization fan should be running.

When bonding the chips, the PCB connections should be shorted, either by appropriate connectors for the DC devices, or by a shorting bondwire connecting center conductor and groundplane on the RF PCBs. One should use the ionization fan and wear a grounding strap, which should also be worn when mounting the samples in the cryostat.

Due to the reduced resistance of the leads at low temperatures, precautions are necessary when connecting or disconnecting instrumentation, especially in case of stub tuners. While the break-out box is fitted with shorting switches and a multimeter can be used to check the resistances of both of cold and warm samples without any preamble, the SMU will break the junctions at low temperatures if precautions are not taken. This may be avoided by turning the SMU on and off again while having the SMU connected to the correct site at the break-out box and the shorting switch closed. Afterwards, the shorting switch can be opened and the measurements started.

When connecting or disconnecting RF components, such as the network analyzer, it is advisable to heat the sample to a temperature above the critical temperature of the tuning circuits. This precaution is prompted by the destruction of several devices while connecting equipment, even though the devices were shorted and DC blocks used.

4.3 Microwave Measurements

Reflectometry measurements of impedance matching circuits with integrated nano-object devices require both a room temperature setup which generates and analyzes the microwave tones as well as microwave circuitry in the cryostat. Both of these setups will be discussed separately in the following.

4.3.1 Cryogenic Setup

The components placed in the cryostat fulfill several purposes: they provide a mechanical mount for PCB and sample, shielding it from stray radiation. Furthermore, the incoming and reflected microwave signals are separated as well as the RF signal path

from the DC bias path.

To provide mounting and shielding, we use a two part sample holder. The top part is permanently installed in the setup and contains the semi-rigid (SR) coaxial transmission lines which lead to the rest of the RF circuit. The PCB itself is mounted on the bottom part of the sample holder, SMP bullets provide for the connection between the SR lines and the SMP connectors on the PCB.

Although the detection of the microwave signal reflected from the sample in principle requires only a single line leading from the sample to the room temperature setup, using a setup with two lines and a directional coupler close to the sample reduces the influence of impedance mismatches in the setup. The directional coupler itself consists of two weakly (-10 dB to -20 dB) coupled lines, where one end of the input line is terminated by a matched load. Most of the input signal is therefore absorbed by the termination, with a small part coupling to the sample port. Any reflected signal entering at the sample port will weakly couple to the input line, but mainly exit at the output port. The coupling between the lines is therefore a trade-off between signal loss and input power efficiency. A circulator can also be used, but typically has a larger impedance mismatch on the sample input line, leading to difficulties in the calibration procedure.

To enable simultaneous RF and DC measurements, a bias-tee is necessary to combine/split the individual RF and DC signals applied to the sample. It consists of a low-pass DC port, a high-pass RF port and the combined port. Ideally, the bias-tee is placed as close as possible to the sample to reduces the systematic measurement error.

The cryogenic part of the setup thus consists of the sample in a sample holder, a directional coupler, a bias-tee and the DC and RF cables leading to room-temperature, as illustrated in Fig. 4.4. Ideally, the bias-tee should be placed at the output port of the directional coupler, reducing any unwanted effects introduced by the non-perfect impedance matching of the bias-tee connectors and internal circuit. For unknown reasons, the utilized directional coupler increase in resistance at cryogenic temperatures, thus requiring the bias-tees to be placed at the sample port of the directional couplers.
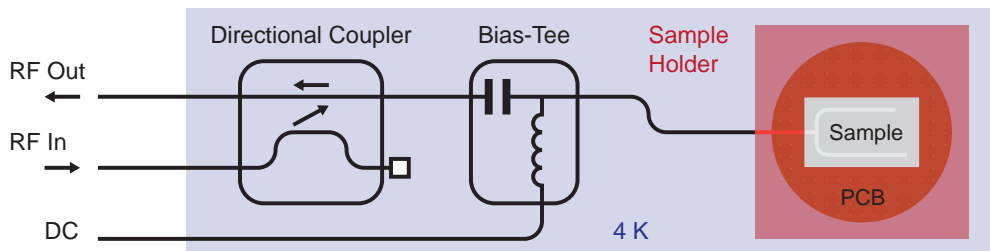

Figure 4.4: Schematic of the microwave setup at cryogenic temperatures.

4.3.2 Room-Temperature Setup

Measurements of stub tuners with integrated break-junctions at microwave frequencies fall into two categories, frequency dependent and time-resolved measurements. In both cases, the S-parameters of the tuner are measured using a heterodyne detection method, implemented either by a vector network analyzer (VNA) or an FPGA-based setup. Both setups are based on the same principle, with the FPGA-based setup additionally allowing time-resolved measurements and the VNA, as an integrated instrument, offering easier handling.

Heterodyne detection is based on the non-linear mixing of two frequencies, the signal frequency f_{Sig} and the local oscillator frequency f_{LO}, which generates signals at the sum and difference $f_{Sig} \pm f_{LO}$ of the two frequencies. As signals in the GHz range are hard to digitize, the heterodyne method can be used to shift the signal of interest into the MHz range, the intermediate frequency (IF) $f_{Sig} - f_{LO}$, here 25 MHz, while the sum frequency is filtered out. At this frequency, the signal is then amplified and digitized. In a final stage, the digitized signal is down-converted to DC by multiplication with the IF, allowing for digital filtering and avoiding issues such as DC offsets in the mixer. Although possible, an IF frequency of 0 Hz (homodyne detection) is typically avoided due to mixer offsets as well as the better noise performance and bandwidth of amplifiers in the MHz range. An exception is the lock-in amplifier, which is a homodyne detector, but is built specifically for low frequencies and small bandwidths.

The used heterodyne measurement setup is sketched in Fig. 4.5. The measurement tone is generated by a signal generator and applied to the input port of the cryostat, where it is applied to the sample. The resulting output signal exits the cryostat at the output port, where it is first amplified by a low-noise amplifier and low-pass filtered to remove harmonics introduced by the amplifier. Multiplication with the LO signal, phase-locked to the signal via a reference clock, is achieved by a mixer, after which the signal is low pass filtered to remove the sum frequency component, amplified and filtered again before being digitized in the ADC at a sampling rate of 10 ns. Finally, digital downconversion is performed by multiplication with the IF frequency. This results in a signal with 10 ns time resolution but which is the moving average of four points, requiring 40 ns to rise to full amplitude after a step. The phase-lock of the measurement tone and LO signal allows both the amplitude and phase of the reflected signal to be extracted.

Several measurements require precise timing between an applied stimulus and the measurement window of the ADC. In this case, the waveform of the stimulus is generated by an arbitrary waveform generator (AWG). The pattern is then output together with a rising edge on the external channel, triggering the acquisition of data in the
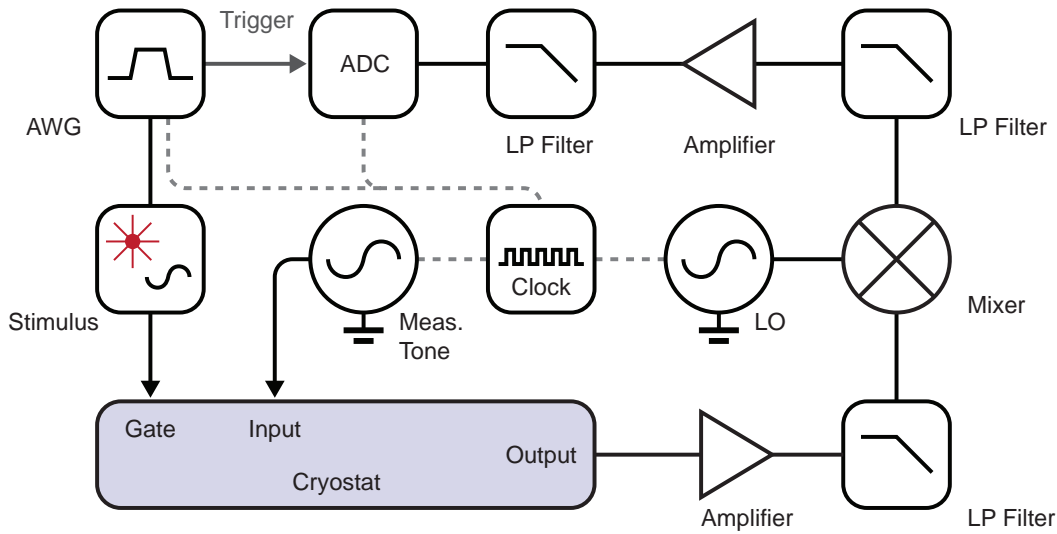
Figure 4.5: Schematic of the time-resolved heterodyne measurement setup.

ADC for a fixed time-window and allowing for a repetition of the measurement with a timing jitter between stimulus and acquisition smaller than 10 ns.

4.4 Optical Setup

To investigate the transport properties of single nano-object devices in dependence of laser irradiation, an optical setup is needed to illuminate the sample inside the cryostat. The basic requirements for such a setup are a controllable intensity and polarization as well as a degree of spatial confinement of the light, in addition to compatibility with a MCBJ setup and a broad range of excitation wavelengths. To fulfill these requirements, a fiber-based confocal microscope setup with a movable objective was implemented. The setup consists of three parts, one part generating and regulating the excitation laser, another distributing the laser into the fiber and detecting reflection and possible emission and finally the low-temperature part, consisting of the moving stage and the objective, all of which will be discussed in the following.

4.4.1 Confocal Microscopy and Setup Constraints

In a confocal microscope (CFM), a light source illuminates a small spot of the sample through a focus lens, as sketched in Fig. 4.6. Fluorescent light emitted by the sample (red lines) is collected by the same lens and spatially filtered by an aperture situated in the *con*jugate *focal* plane, hence the name confocal microscope, before being detected.

The advantage of this setup, compared to standard microscopy, is that only a very small part of the sample is illuminated and any emission is spatially filtered, as light emerging from points other than the focal point (green lines) is blocked by the aperture. Developed and patented by Marvin Minsky in 1957, the emergence of lasers and computer-based analysis led to the development of laser-scanning confocal microscopy, a powerful tool widely used for investigating optical phenomena.
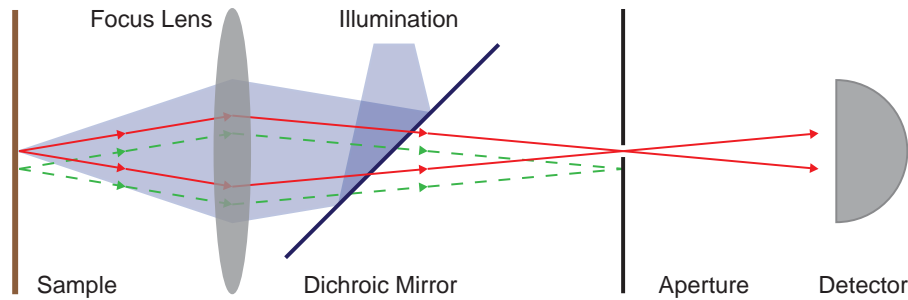
Figure 4.6: Schematic of a confocal microscope.

CFM setups for cryogenic applications can be divided into three basic designs:

a. Room-temperature setups, where all optical elements are at room temperature and the sample is placed on a cold finger behind a window.

b. Free-space setups, where the lens or objective is at cryogenic temperatures, with a free-space optical path from the room temperature ocular to the objective through a vacuum window.

c. Fiber-based setups, similar to free-space setups, where the optical path from room temperature to base temperature takes the form of an optical fiber.

Although the room-temperature setup allows the biggest flexibility as well as using an apochromatic objective, it was not considered as a possible design because the sample must be placed very close to the room-temperature window, therefore introducing significant space constraints and possible issues with thermal radiation.

The CFM design needs to address several issues, leading to a preference of a fiber based setup over a free-space one:

Compatibility with MCBJ Setup The screw actuation of the MCBJ setup requires scanning the laser over the sample, as opposed to moving the sample with regard to a stationary focal spot.

Field of View (FOV) A large FOV is crucial, as it allows for probing multiple sites and relaxes assembly and mounting tolerances. In a fiber based setup with movable objective the FOV is limited by the range of the positioning stage (here 5×5 mm^2), with constant performance over the entire range. In a free-space

setup, the clear aperture of the fixed objective limits the FOV to roughly the same range, but the optical performance decreases as the beam is moved off-axis.

Mechanical Stability Due to its compact nature and short optical paths, the fiber-based setup is expected to be significantly more stable than a free-space setup, which requires a stable optical path from the room-temperature ocular to the base temperature objective.

Polarization and Bandwidth Free-space setups are limited in bandwidth by the anti-reflection coating of the optics, while allowing arbitrary polarizations to be applied. A similar bandwidth limit may be obtained in a fiber-based system by the use of polarization-maintaining large-mode-area photonic crystal fibers [Birks97]. The polarization maintaining property allows for application of two different polarizations, although a calibration of the birefringence allows for arbitrary polarization angles at the sample.

Practical Issues Free-space setups allow direct imaging of the sample using a CCD, while fiber-based setups are limited to scanning point-by-point and require some amount of time to determine the position of the microscope with respect to the sample. Furthermore, free-space setups allow trading off spatial resolution for signal by changing the aperture, while the aperture is fixed for fiber-based systems.

Based on the presented arguments, it was decided to implement a fiber-based setup using a scanning objective and a photonic crystal fiber. The main arguments for this setup are a less complicated implementation with larger tolerances regarding vibrations and an easy adaptation of the implemented design for use in a dilution refrigerator.

4.4.2 Laser Generation and Intensity Regulation

The ideal light source to investigate the interaction of nano-object devices with light at a defined wavelength is a laser. Although a tunable laser would be optimal for spectroscopic investigations, the unknown wavelength range combined with the cost and complexity of a tunable laser led to a preliminary setup based on laser diodes. Modulation and stabilization of the laser power is achieved via an acousto-optical modulator (AOM) for all three currently integrated wavelengths.

Solid-state laser diodes are available at a large number of wavelengths and offer an economic and maintenance free source of laser light. Three wavelengths were selected based on the availability of laser diodes in the bandwidth of the setup, a blue 405 nm laser, a green 532 nm diode-pumped solid state (DPSS) laser and a red 635 nm laser, with powers ranging from 5 mW for the green and red laser to 120 mW for the blue

laser.

An acousto-optic modulator (AOM) is used to control the laser intensity, allowing the laser diodes to run at a constant current and leading to a stable output spectrum, as the diodes are not frequency locked and the laser frequency and width depend on the current. The AOM is based on the acousto-optic effect, a scattering process between phonons and photons in an optical crystal. Here, the passing photons can alter their momentum by absorbing or emitting a phonon, as schematically shown in Fig. 4.7(a). The acoustic wave is induced in the crystal by applying an 50 MHz to 100 MHz RF frequency signal to the attached piezo-electric transducer, which leads to a diffraction of the photons for a specific incident angle of the light. Momentum and energy conservation lead to a Bragg-type criterion for this angle, which depends on the wavelength of the light and the phonon frequency, as illustrated in Fig. 4.7(b).
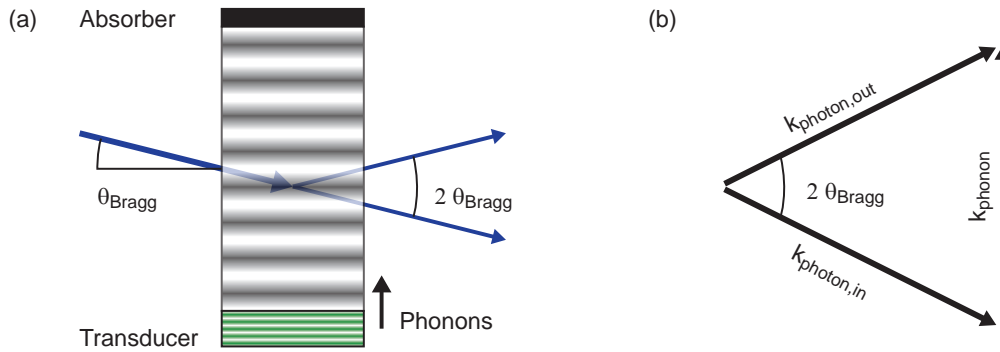
Figure 4.7: (a) Schematic of an acousto-optical modulator. (b) Bragg criterion for phonon scattering. Axes are not to scale.

Generation and modulation of the RF signal controlling the light intensity is realized by the driving circuit schematically shown in Fig. 4.8. A voltage-controlled oscillator (VCO) with an output power of 10 dBm is tuned to the resonance frequency of the AOM, here 80 MHz. This base signal is then multiplied with the control signal using a mixer and amplified using a power amplifier with a gain of 30 dB. To protect the AOM, which has a maximum power input of 34 dBm, an attenuator is placed between mixer and amplifier, limiting the maximum signal to powers below the damage threshold.

The AOM-based intensity control has two modes of operation, a feedback mode for constant intensity or low-frequency modulation up to 10 kHz and a fast mode utilizing the full bandwidth of the setup, but without absolute intensity control.

For most applications, a constant laser intensity at the fiber input of the confocal microscope is required. The feedback loop eliminates laser intensity drift and also allows modulation of the intensity with stable and defined amplitude at frequencies up
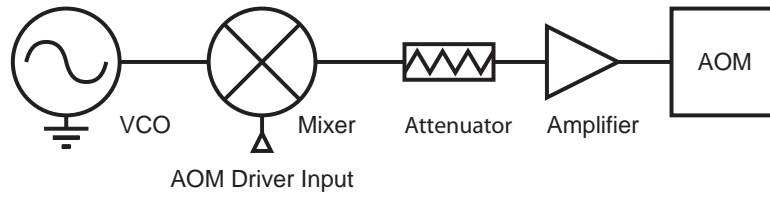
Figure 4.8: Schematic of the AOM driving circuit.

to the kHz range for lock-in measurements. The feedback loop is shown in Fig. 4.9 and operates as follows: The laser is passed through the AOM, where part of the beam is diffracted and coupled into a photonic crystal fiber (PCF) using two high reflectivity (HR) mirrors. This allows intensity control from zero to the maximum diffraction efficiency, 30% in case of blue light. In principle, the undiffracted beam could also be used, allowing the power to be regulated from 100% minus the diffraction efficiency to full power. At the fiber output, the light is split into two beams, one entering the fiber of the CFM, the second being used to determine the intensity of the arriving light via a photo-detector. The intensity signal is then fed into a PID controller connected to the AOM driver, creating a feedback loop.
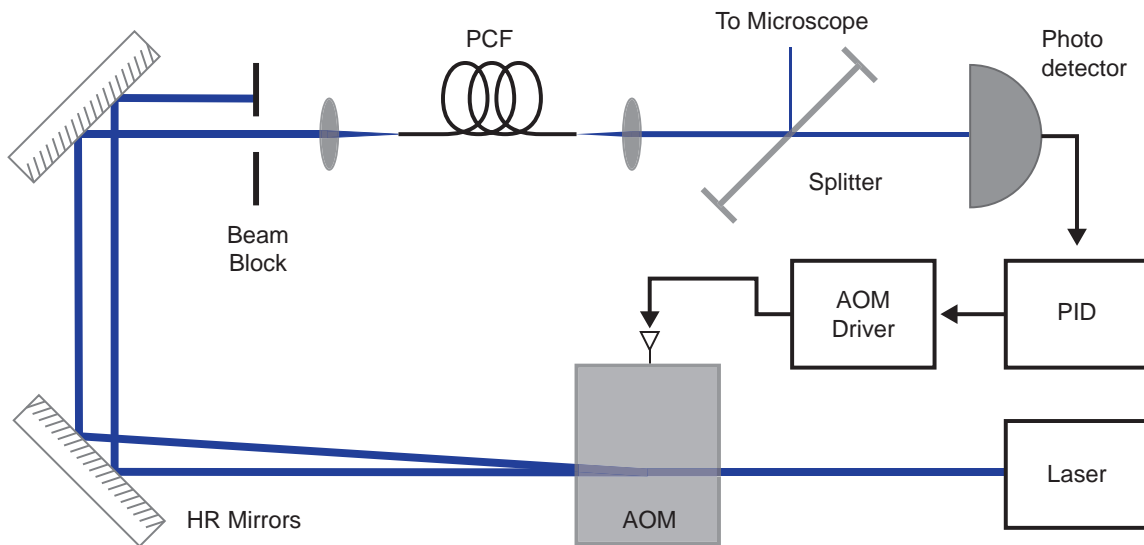
Figure 4.9: Schematic of the stabilization loop.

The control signal S_{Out} applied at the input of the AOM driver is determined by the PID controller using the control law:

$$S_{\mathrm{Out}} = P \times (\epsilon + I \int \epsilon dt) + C$$

where P and I are the constants for the proportional and integral gain, ϵ is the error signal and C a constant offset. Values for P and I found using the Ziegler-Nichols method [Aström95], after determining C using the manual output of the controller.

Using the feedback mode for stabilization virtually eliminates drift in laser intensity at the input of the CFM, as illustrated by the red curve in Fig. 4.10(a). In contrast, the power drifts by more than 5% over time without stabilization (blue curve).
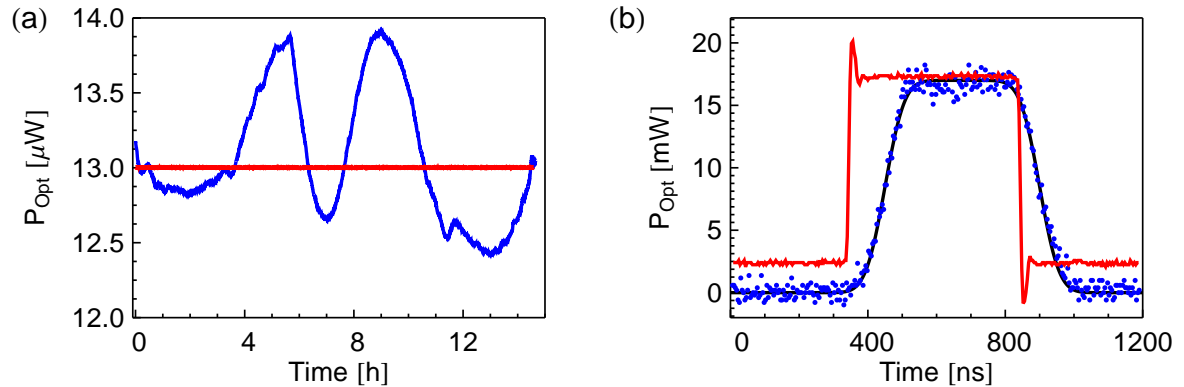
Figure 4.10: (a) Optical power versus time with (red) and without (blue) stabilization recorded at the photodetector. (b) Open loop response (blue) to a 500 ns square wave reference signal (red), the black line is a square wave with 150 ns rise-time.

By removing the feedback loop, the full bandwidth of the AOM and AOM driver circuit can be utilized at the expense of a drifting intensity. The rise-time of a square pulse is then limited by the time required for the sound wave to transverse the beam diameter. A characterization measurement is shown in Fig. 4.10(b), where a 500 ns square pulse was generated by an AWG and sent to the AOM driver (red curve). The resulting photo-signal (blue points) shows a rise time of ≈ 150 ns (black curve), consistent with a specified rise-time of 108 ns per mm beam diameter and a beam diameter of ≈ 1.5 mm.

To allow for intensity control of all three lasers, they each need to pass the AOM at their specific Bragg angle before being coupled into the photonic crystal fiber. In principle, several AOMs or an acousto-optic filter could be used, but since a simultaneous illumination is not required, a setup utilizing only one AOM was implemented. The working principle is sketched in Fig. 4.11 for two lasers, but can be adapted to three. Using a high reflectivity and a dichroic mirror, the two laser beams are brought close enough to enter the aperture of the AOM at their specific Bragg angle. After the AOM, the spatial separation allows for deflecting the two beams using two separate mirrors, after which an HR and a dichroic mirror recombine the two beams and fiber-couple

them into the same fiber. The set of mirrors for each individual beam after the AOM is necessary to achieve the 2 μm spatial positioning accuracy of the focused laser with regard to the fiber tip that is necessary to achieve efficient fiber coupling. Together, the set of mirrors provides the four degrees of freedom for beam adjustment in both position and angle. In the fiber coupler itself, an apochromatic lens is used to ensure that the light is focused to the same spot regardless of wavelength, allowing for efficient coupling in the entire 400-700 nm band.
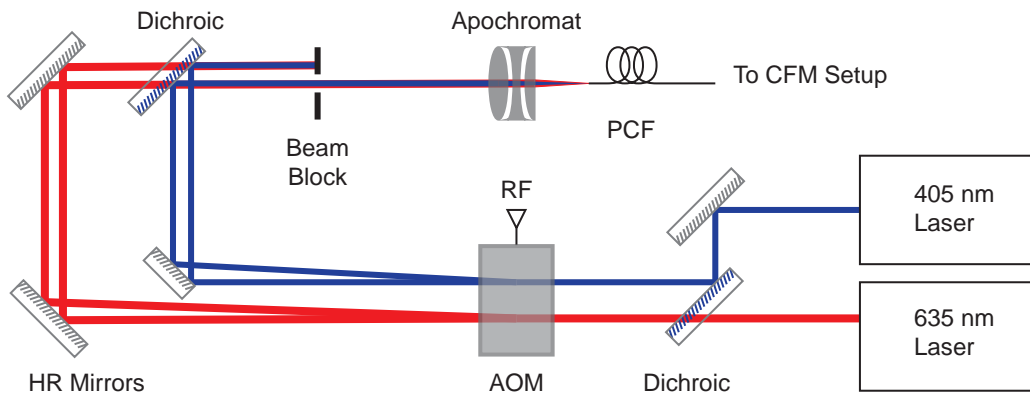
Figure 4.11: Schematic of the multi-color laser setup.

4.4.3 Objective and Moving Stage

A confocal microscope needs to both focus the light to a very small spot and to collect any emitted light originating from the point of interest, while blocking the light emitted from other points. In a fiber based setup, these task are performed by the objective, consisting of two lenses, a collimation and a focus lens. The light emanating from the fiber is first collimated and then focused to a spot, while the emitted light is collected by the focus lens and coupled into the fiber by the collimation lens. The fiber itself acts as the confocal aperture, a schematic is shown in Fig. 4.12(a). As a CFM will only return information about the focal spot, the objective needs to be scanned over the sample to collect information about an area. In the presented setup, this is achieved by mounting the objective on a three-dimensional positioning stage, consisting of a coarse and a fine positioning stage.

The main goals of a minimal spot size and maximal collection efficiency of the objective both depend on the numerical aperture (NA) of the objective, which is dominated by the NA of the focus lens. Ideally, this lens should be chromatically corrected, but the composite nature of commercially available achromatic lenses prohibit their use at cryogenic temperatures due to a mismatch in the thermal contraction coefficients of

the used glasses. Alternatively, air/vacuum spaced lenses can be used, but require extensive optical design and custom made lenses. For simplicity and first investigations, an objective design based on Ref. [Hogele08] was used, consisting of two aspheric lenses and offering diffraction limited performance, but with a wavelength-dependent focal plane.
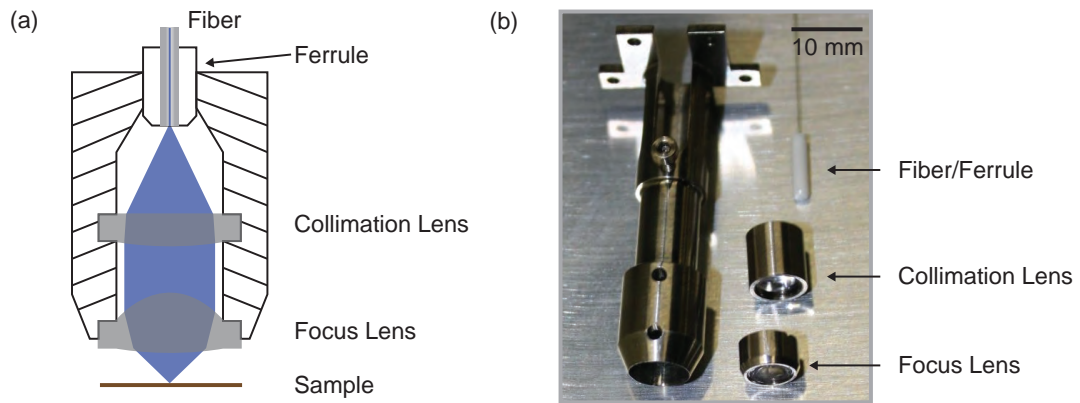
Figure 4.12: (a) Schematic and (b) image of the objective. The lenses and fiber/ferrule are placed beside the objective housing.

We choose focus lens according to the largest NA available for diffraction limited performance in the chosen wavelength range, with the added constraint of a working distance larger than 1.5 mm. Criteria for the collimation lens are a match between the NA of the lens and of the optical fiber as well as a similar clear aperture as the focus lens. The collimation lens should also offer diffraction limited performance, but this is typically not an issue for low NA lenses. In particular, a 0.15 NA aspheric collimation lens is used to match the approximately 0.12 NA photonic crystal fiber, providing a clear aperture of 5 mm. A low-cost molded lens developed for *BlueRay* drives serves as the focus lens with an NA of 0.6 and diffraction limited performance in the blue region. The clear aperture of 4.8 mm matches the collimation lens, while an effective working distance of 2.73 mm yields enough clearance to the sample to avoid accidental damage.

To facilitate assembly, the lenses are glued into titanium tubes using *Stycast* epoxy, which are subsequently inserted into the objective housing and fixed with glue. The fiber ends in a ceramic ferrule, which is also mounted into the housing and fixed by a screw, allowing adjustment of the on-axis position. We designed the objective housing be light and stiff to minimize vibrations. A picture is show in Fig. 4.12(b), where the housing, lens tubes and the fiber with ferrule are visible.

A combination of a coarse positioner and fine piezo scanner is used to achieve a total scanning range of 5 x 5 x 5 mm^3 together with a fine scanning range of 40 x 40 x 15

μm^3. The coarse scanners are based on a stick-slip travel mechanism, illustrated in
4.13(a)-(c). A piezo is used to actuate a guiding rod, which is clamped to the moving
part, or stage, of the positioner with a defined force (a). Accelerating the piezo at
a high rate overcomes the friction between the guiding rod and clamp, allowing the
rod to slip further into the clamp without moving the stage (b). A slow retraction of
the piezo will now allow the rod to move the stage, achieving a step (c). With this
mechanism, the stage can be moved along the entire travel range in steps of typically 50
nm. To ensure repeatable positioning and to compensate for the variable step size due
to the nature of the slip-stick mechanism, the steppers are equipped with a resistive
position encoder, yielding a positioning accuracy of $\approx$ 1 μm. Two linear [attocube
GmbHa] and a vertical positioner [attocube GmbHb] are mounted in a stack to allow
three-dimensional positioning. Faster scanning of a small area is made possible by a
three axis piezo scanner [attocube GmbHc] mounted on top of the coarse positioners.
A image of the assembled positioning stack is given in Fig. 4.13(d).
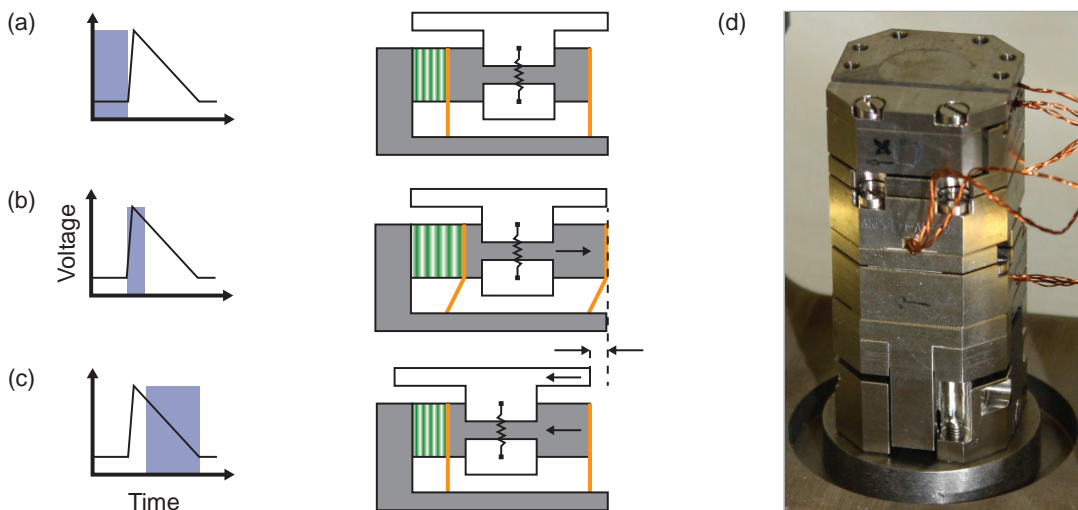
Figure 4.13: (a)-(c) Schematic of the slip-stick working principle. (d) Image of the
positioning stack.

The necessary voltages for the three stepper units and three piezo scanners are gener-
ated by a control unit [attocube GmbHd], which in turn is controlled by an FPGA-based
scanning probe controller [attocube GmbHe], allowing spatial mapping of up to 13 ar-
bitrary input responses, such as reflection, current, or counts, as a function of objective
position.

4.4.4 Beam Splitting and Detection

A confocal microscope can perform two tasks: illuminate the sample at a specific spot and collect the emitted light from a specific spot. These tasks can be expanded to illumination with a specific intensity and polarization and detection of the emitted light according to wavelength, which is typically performed simultaneously and leads to the setup show in Fig. 4.14.
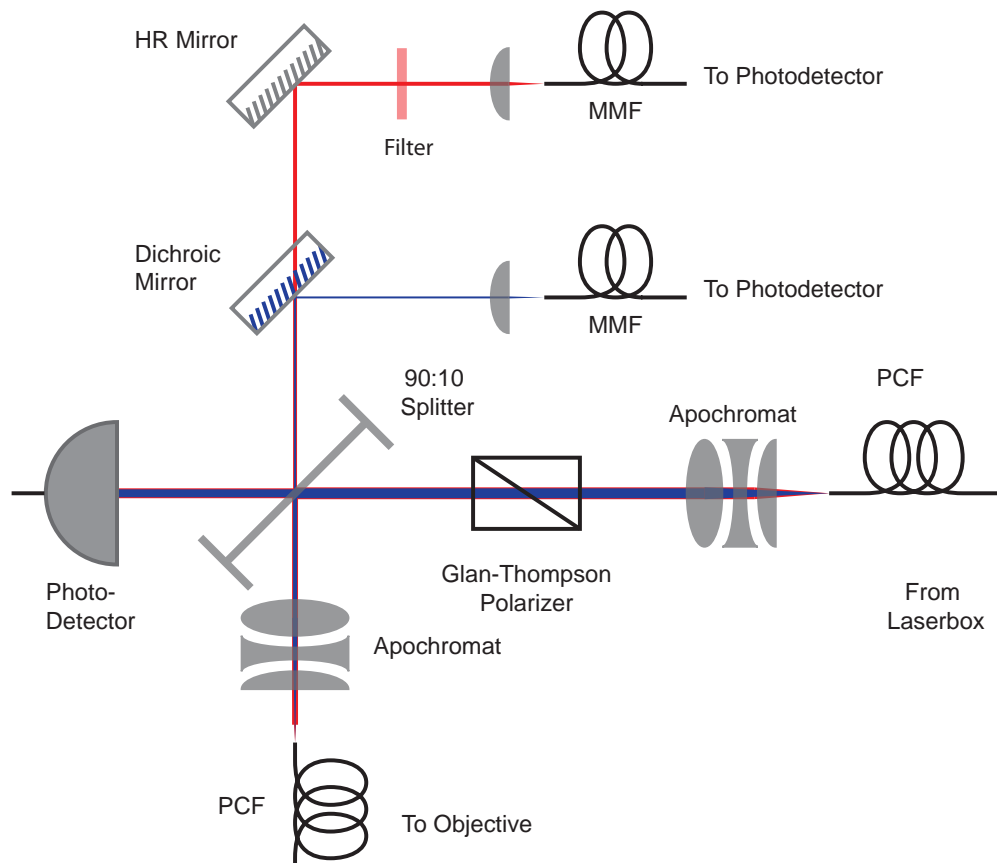
Figure 4.14: Schematic of the splitting and detection unit.

Starting with the laser source, the photonic crystal fiber coming from the laser generation unit (4.4.2), the laser is first collimated, again with an apochromat. We use a Glan-Thompson polarizer to define the polarization, oriented such that it reflects in-plane polarization and transmits out-of-plane polarization with respect to the optical table top. Afterwards, the beam is coupled into the fiber leading to the objective. As any light collected by the objective will follow the same path as the illumination laser in reverse, an element is needed to separate the incoming and outgoing light. This is accomplished using a 90:10 beam splitter, in a fashion similar to the RF directional

coupler. The main part of the illumination laser passes the splitter and is detected by a photodiode, yielding the feedback signal for the intensity stabilization (see also Section 4.4.2), while the deflected 10% are coupled into the photonic crystal fiber and illuminate the sample. For the collected light exiting the fiber, the situation is reversed: The main part of the light passes the splitter and enters the detection setup, while 10% is reflected toward the laser source. This setup is thus a trade-off between the maximum power available at the sample and the detection efficiency of the collected light.

Depending on the sample, the collected light can have two different origins. It is either light reflected from the sample at same wavelength as the illumination, or redshifted light due to absorption and subsequent reemission in case of a fluorescent sample. To distinguish these two signals, the light exiting the fiber is separated into two beams using a dichroic mirror, reflecting light below 450 nm and transmitting longer wavelengths. The blue light is attenuated, spatially filtered by coupling into a 10 μm multimode-fiber (MMF) and detected by an amplified photodetector [Thorlabs]. In contrast, the red light is filtered in several stages to remove the illumination wavelength and other unwanted signals, also spatially filtered by a multimode fiber and detected by an avalanche photodetector [Laser Components GmbH].

4.5 Prototype Setups

We aim to investigate mechanically-controlled break-junctions integrated into superconducting RF impedance matching circuit, which requires an experimental setup capable of mechanically bending the chip while performing RF measurements at temperatures below 5 K in vacuum. The implementation of such a setup required several prototypes, each testing specific solutions to a given sub-problem. The MCBJ setup was developed with the help of a master student, first as a room-temperature setup, followed by a prototype allowing measurements in vacuum at 4.2 K [Burch09]. A separate setup for RF measurements at 4.2 K was also implemented before the gained experience was applied to the design of a cryostat integrating all the required features.

To achieve the required low temperatures, the two prototypes were implemented as so-called dipsticks, where the samples are placed at the end of a stainless-steel tube, which is subsequently immersed into a dewar filled with liquid helium, reaching a sample temperature of 4.2 K. The implementation of these two prototypes will be discussed in the following.

Vacuum Dipstick for DC Measurements of MCBJs

Due to the fact that helium adsorbed on the chip surface may interfere with the measurements of nano-object devices formed by MCBJs at cryogenic temperatures, the samples themselves cannot be placed directly in liquid helium. A setup was thus developed in which the sample is in vacuum, with part of the vacuum chamber placed in liquid helium.

In essence, the setup is an evacuated stainless steel tube, where the sample is placed inside at the cold end and electric and mechanical access made available by room temperature vacuum-feedthroughs. A schematic is shown in Fig. 4.15(a). A removable cap with conical seal allows access to the sample and provides a vacuum tight seal even when immersed into liquid helium. The sample is connected to the room-temperature instruments via a set of 14 copper twisted pairs, while a step motor actuates the screw to bend the chip via a shaft and a vacuum feedthrough. Due to the limited sample space - the dipstick needs to fit through the KF 50 flange of a liquid helium dewar - the PCB carrying the chip and connectors is implemented as a flexible PCB and mounted in a U shape. A picture of the lower end of the dipstick with the cap removed is shown in Fig. 4.15(b).
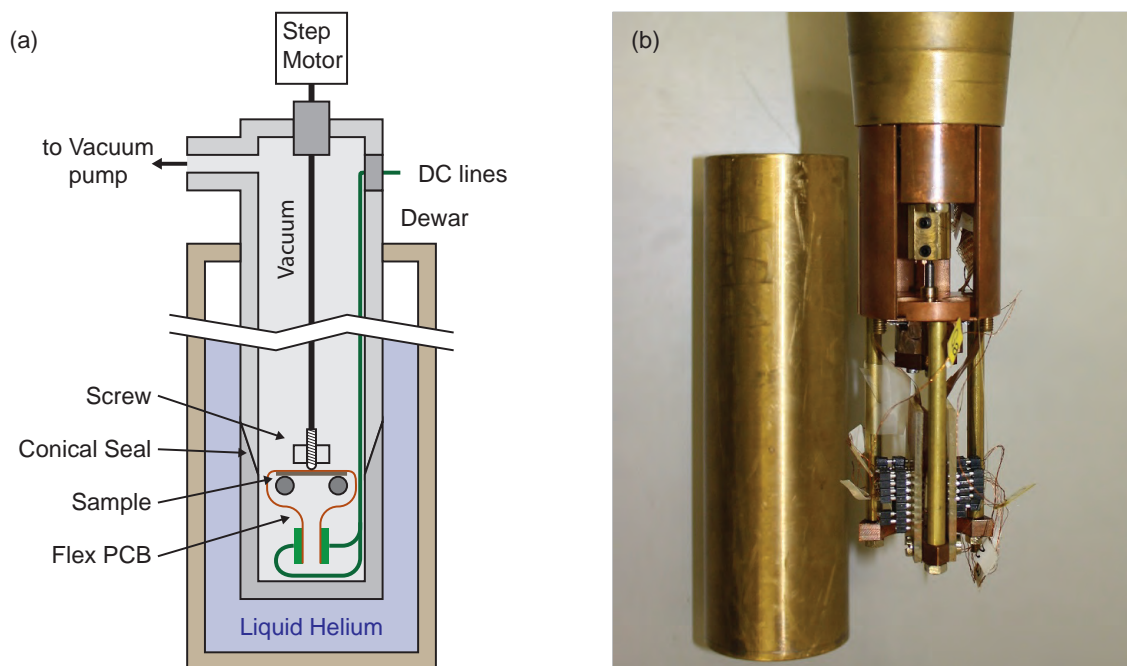
Figure 4.15: (a) Schematic of the vacuum DC dipstick. (b) Image of the lower end of the dipstick with mounted sample and and removed cap.

RF Dipstick for Stub Tuners with Integrated Break-Junctions

The characterization of impedance transformation circuits with integrated break-junctions requires a low temperature setup, which can be kept simple if only electromigration is used to change the impedance of the break-junction. Thus, solely RF and DC lines are required, together with the microwave components discussed in Section 4.3.1. Furthermore, by investigating only bare junctions, a vacuum vessel is not required.

The setup consists of two parallel measurement circuits, each consisting of a bias-tee [Mini Circuits], a directional coupler [Krytar] and the associated DC and RF lines, mounted at the end of a stainless steel tube. A schematic of one measurement circuit is shown in Fig. 4.16. The sample PCB is mounted in a small copper sample holder, electrically connected to the input semi-rigid coaxial cables via SMP bullets. The individual circuits are then connected to a bias-tee (BT) followed by a directional coupler (Dir. Coup.). Two semi-rigid coaxial lines provide for a connection between the input and output port of the directional coupler and the vacuum-feedthrough at the room-temperature end of the dipstick. A DC feedthrough and twisted pairs provide for DC access to the bias-tees in a four-point configuration.
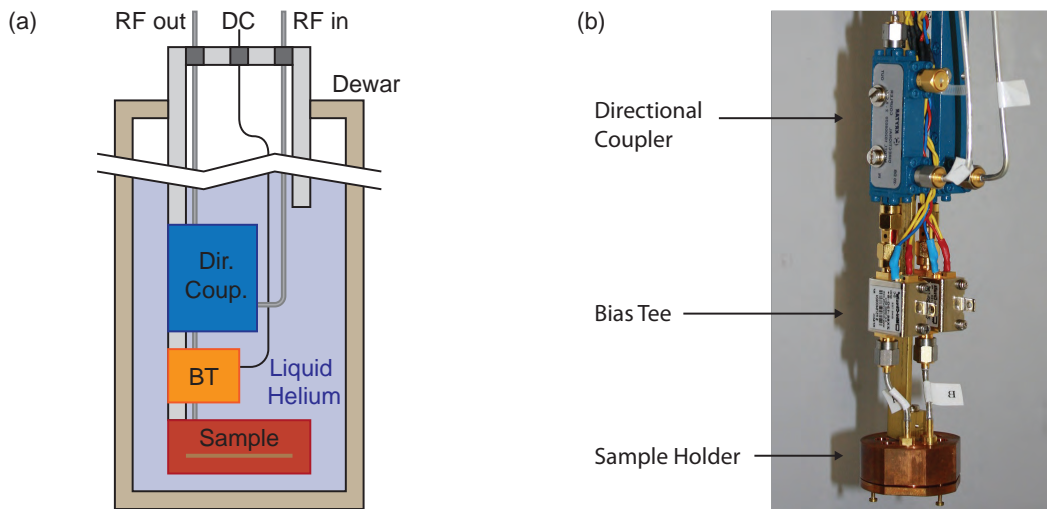

Figure 4.16: (a) Schematic of the RF dipstick. (b) Image of the lower end of the dipstick.

4.6 Arctic Cryostat

In order to perform combined optical, RF and MCBJ measurements, a cryogenic setup is required which can house the necessary components, and due to the statistical na-

ture of single molecule device formation, allows the measurement of several devices in each cooldown run. Furthermore, the setup should feature fast cycle times and simple operation to allow a high sample throughput. The energy scale of the investigated systems, typically 20 meV to 100 meV, allows for a base temperatures in the range of three to five Kelvin, which greatly simplifies the design and shortens cycling times. In this range, losses in the RF devices are small enough to investigate matched loads up to one MΩ.

To fulfill these requirements a cryostat based on a pulse-tube cooler (PTC) was designed and built from scratch, using the flexibility of a custom system to implement a low-vibration setup referenced to an optical table. The name is inspired by its intended use: trAnsport, Rf and optiCal Three kelvIn Cryostat (Arctic), although it is not a true acronym.

This section discusses the various aspects of the cryostat, starting with vacuum chamber and structural layout then describing thermometry and the thermal design aspects and finally discussing the implementation of the experimental setup.

4.6.1 Vacuum Chamber and Structural Design

Design and construction of the Arctic cryostat pursue the goal of a low-vibration system in which the cold stage is referenced to an optical table. While this reference is not necessary for a fiber-based confocal microscope, the setup also serves as a test bed for experiments involving the coupling of Rydberg atoms to superconducting resonators, which do require such a reference. This design constraint has a profound impact on the entire layout and leads to a deviation from the standard "hanging" design, where all parts of the cryostat are fixed to a top-flange.

Most aspects of a cryostat design are given by the need to isolate the cold stage from the three sources of heat transfer: conduction, convection and radiation. The easiest source to eliminate is convection, which can be suppressed by placing the cold stage in a vacuum chamber. Choosing low heat-conductivity materials, such as stainless steel or glass-fiber reinforced plastic, minimizes heat conduction. The last source, radiation, is minimized by means of high reflectivity radiation shields attached to each stage and enclosing the subsequent stage. These shields absorb or reflect the thermal radiation emitted from the warmer stage, while themselves only emitting thermal radiation at the stage temperature toward the colder stages.

An important design constraint is therefore given by the radiation shields, as they need to be removed to access the sample. This is typically solved by utilizing a "hanging" cryostat, where the flanges, heat shields and vacuum chamber are attached from below to a room-temperature top flange. Sample access is then possible by sequentially
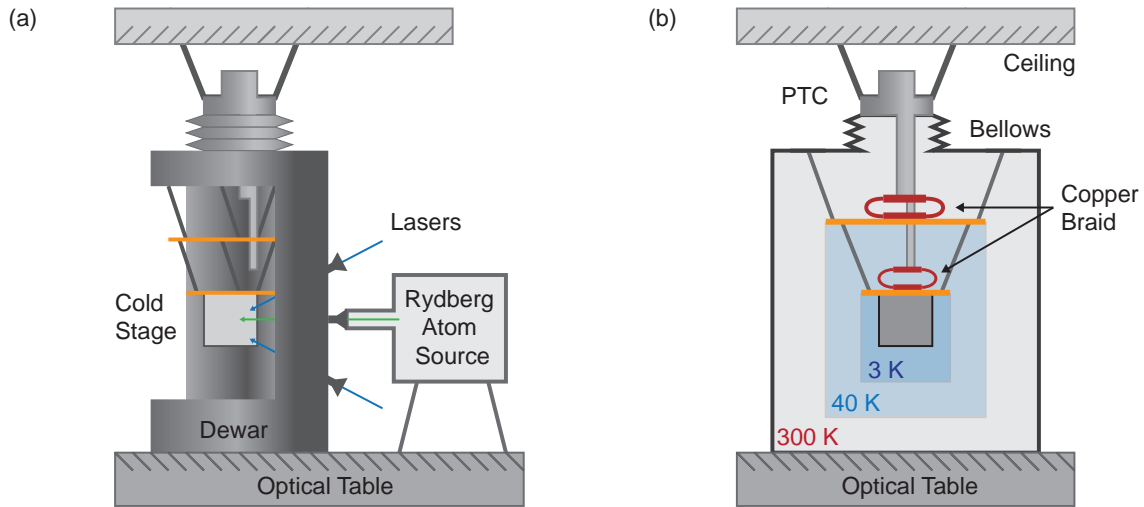
Figure 4.17: (a) Design schematic of a cryogenic experiment involving Rydberg atoms. (b) Schematic of the vibrational decoupling.

lowering and removing the chamber and shields.

Compatibility with Rydberg atom experiments adds a number of significant constraints. Such experiments require an atom source sharing the same vacuum chamber as the cryogenic sample stage as well as requiring optical access to this stage for the excitation, cooling, trapping or manipulation of the atoms. Thus the cold stage should be referenced to an optical table for beam alignment and be accessible without disassembling the cryostat chamber/atom source vacuum system. These requirements are solved by using the vacuum chamber itself as the support for the top flange of the cryostat, creating the optical reference by placing the chamber on an optical table, as shown in Fig 4.17(a). Large cutouts in the chamber allow the removal of the radiation shields and access to the sample without disconnecting the chamber from other vacuum assemblies or disturbing any optical or atom beam alignment. Note, however, that at the current stage the flange supports are not compensated for thermal contraction.

A general advantage of placing the cryostat on an optical table is the inherent decoupling from vibrational sources propagating either through the floor or the ceiling. To vibrationally isolate the PTC from the cryostat, the PTC itself is fixed to the ceiling. The connection to the vacuum chamber is formed via a flexible bellows, while inside the cryostat, the flanges are coupled to the cold heads of the PTC using flexible copper braids, which are discussed in more detail in Section 4.6.4. A schematic of this setup is shown in Fig. 4.17(b).

The cryostat is based on a two-stage PTC with a specified cooling power of 45 W at 40 K on the first stage and 1.5 W at 4.2 K on the second stage, with an unloaded base

temperature below 2.8 K. We therefore utilize two cold flanges, the 3 K flange mounted beneath the 40 K flange, which in turn is mounted beneath the third room temperature flange, also referred to as the top flange. Mechanical support for each flange consists of 6 struts, constraining the 6 degrees of freedom of the connected flange and creating a stiff kinematic mount. Due to the large amount of available cooling power, the dimensions of the flanges and the volume available for experiments was chosen to be much larger than required for the implemented experiment, allowing both for good access and the possibility of additional experiments. A picture of the flanges with supporting struts is shown in Fig. 4.18(a).
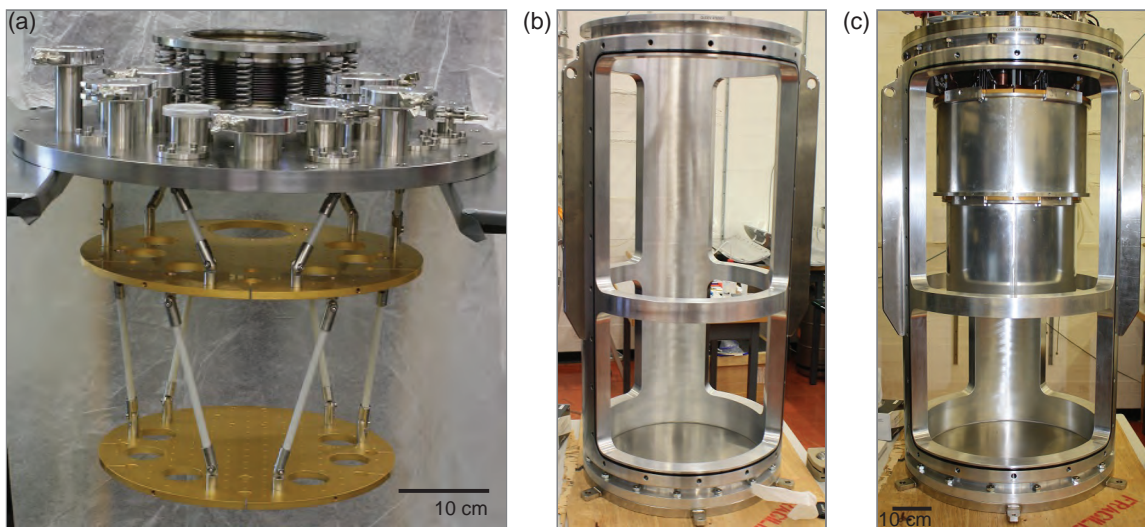
Figure 4.18: (a) Image of the 300 K, 40 K and 4 K flanges. The white struts supporting the individual flanges are visible. (b) Image of the empty vacuum chamber with all cutouts open. (c) Image of the open vacuum chamber with mounted inner assembly. The 4 K shield and the upper half of the 40 K shield are mounted.

The vacuum chamber features three cutouts, one large and two small ones, providing as much access as possible to the flanges when removing the covers. An image of the empty chamber with open cutouts is shown in Fig. 4.18(b). As the cold flanges are attached to the top flange, the cold assembly of the cryostat can be removed from the chamber by lifting the top flange upward, which also allows the current design to be easily converted into a standard "hanging" type of cryostat. For the same reason, the feedthroughs for mechanical, optical and electric experimental access are placed on the top flange. Four 40 mm line-of-sight ports, as well as a number of KF 40, KF 25, KF 16 and custom made flanges are available. Flanges for direct optical access parallel to the optical table can be added to the covers of the chamber. With the exception

of a single KF 40 flange to evacuate the chamber, these were not implemented in the current stage.

A major constraint on the design is imposed by the radiation shields on the two stages, which should be removable through the main window of the vacuum chamber without opening the other windows. This calls for a mounting mechanism which does not require access to the rear of the flanges and additional space in the chamber to lower the shields below the experiment. To minimize the required space, the 40 K shield is split into two parts. An image of the cryostat with the 4 K shield and half of the upper 40 K shield mounted is shown in Fig. 4.18(c). A further reduction would be possible by splitting the shield into more than two parts, at the expense of increased handling and decreased thermal contact between each part.

The mounting mechanism is based on four c-clamps, two at the front and two at the rear of the flange, and uses inclined planes on the clamps and the shield to induce pressure between the shield and flange in order to achieve good thermal coupling. Only the two front clamps require disassembly to remove the shield while the inaccessible rear clamps remain fixed. A schematic of the mechanism is shown in Fig. 4.19(a)-(c). To mount the shield, it is lifted upward toward the flange (a) and then pushed into the rear c-clamps (b). The front c-clamps are then mounted (c) and fixed using screws from the side.
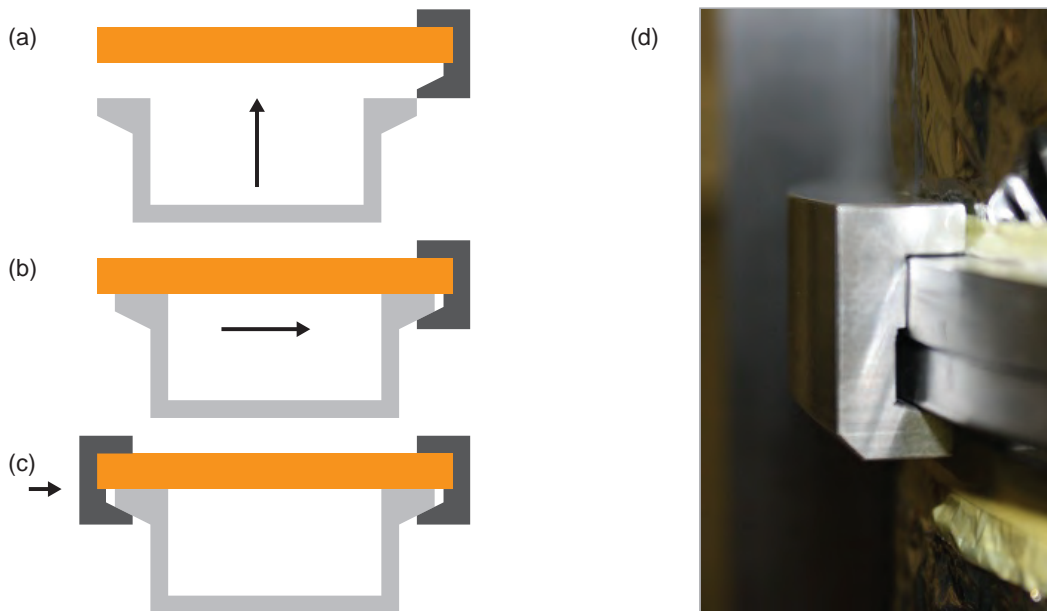
Figure 4.19: (a)-(c) Schematic of the shield clamping mechanism. (d) A c-clamp connecting the two 40 K shields.

An initial design implementing the discussed ideas and constraints is shown in Fig. 4.20(a), including dimensions, placement of ports and the general features, but excluding the detailed dimensioning of the chamber. As the forces acting on the evacuated chamber due to the ambient pressure are large and its cylindrical symmetry is broken by the cutouts, a suitable mechanical design is critical in order to avoid a failure of the vacuum vessel. Accordingly, the final plans was made together with the physics department engineering office, drawing on their expertise in vacuum design and FEM calculations to ensure structural safety. The resulting design has wall strengths of 40 mm for the chamber and a ring in the cutouts to improve the structural integrity of the chamber. A CAD model is shown in Fig. 4.20(b).
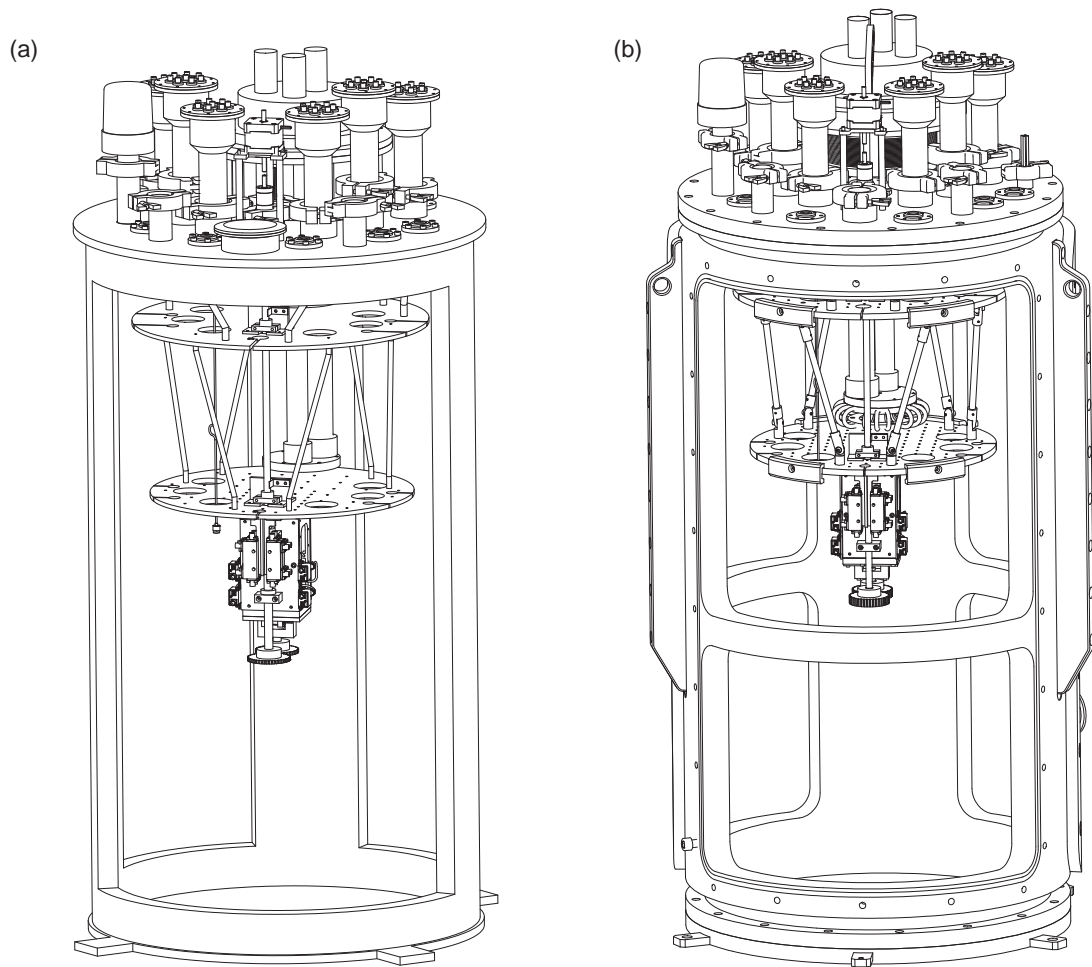
Figure 4.20: (a) Initial design of the cryostat. (b) CAD model of the finished cryostat. The chamber dimensions have been changed to accommodate the pressure forces and a reinforcement ring has been added for structural integrity.

4.6.2 Thermometry

Experiments involving RF measurements of superconducting devices require a temperature stabilization to achieve repeatable results, as the properties of the devices are sensitive to temperature variations. In addition, a detailed knowledge of the temperatures at different points in the cryostat is crucial for the optimization of the design. To this end, six temperature sensors are placed at different points in the cryostat, monitoring the two cold stages of the PTC, the two flanges, the bottom of the 40 K radiation shield and the bottom of the sample holder. A schematic is shown in Fig. 4.21. These sensors are silicon diodes, which offer a calibrated accuracy of 12 mK in the range of 1 to 10 K at an economic price. The forward voltage drop of the diodes is temperature dependent and follows a standard temperature-voltage curve, achieving an uncalibrated accuracy of 0.5 K over the 3 K to 300 K range, with a repeatability of 10 mK at 4.2 K. A factory calibrated sensor was used to determine the calibration curves of the other five sensors.

A loom consisting of 12 constantan twisted pairs is used to connect the different sensors to a 24-pin vacuum feedthrough and is thermalized at both stages with the three 40 K stage sensors branching off at the 40 K flange. Read out of the individual sensors is performed in a four-point measurement by the temperature controller. The combined accuracy of a calibrated diode with the temperature controller is specified at 25 mK.

We use a room-temperature vacuum gauge to monitor the pressure inside the chamber at ambient temperature, with a 30% accuracy and 5% repeatability over the entire range of 10^{-8} to 1000 mbar. To protect against overpressure, a pressure relief valve is installed. A custom software logs the cryostat temperatures, sensor voltages and pressure for analysis and optimization of the cryostat performance.

Three heaters are installed in the cryostat, a 50 W cartridge heater on the 40 K flange, a 25 W cartridge heater on the 3 K flange and a homebuilt constantan wire heater on the sample holder. While the nominal rating on the cartridge heaters can be exceeded if the heaters are properly heat sunk, the available heating power is limited by the maximum current which can be applied to the wiring. We use cooper wiring to connect the heaters, which introduces extra heat load on the flanges and are therefore not dimensioned for the full heating range. Currents larger than 700 mA will burn the isolation and short circuit the heaters. By using the heaters on the flanges, the warmup time can be significantly reduced, see also section 4.6.4 for more details.

The controller used to read out the temperature sensors is also used to stabilize and sweep the temperature of the sample. It offers two independent PID loops with different output ratings and is specified to provide a maximum deviation of 1.6 mK in the range

of 1K to 10K using a calibrated silicon sensor and a 100 Ω heater. The accessible range for temperature sweeps is from base temperature to 25 K. The controller further offers up to 10 temperature ranges, each with different PID parameters, to allow for efficient temperature control.
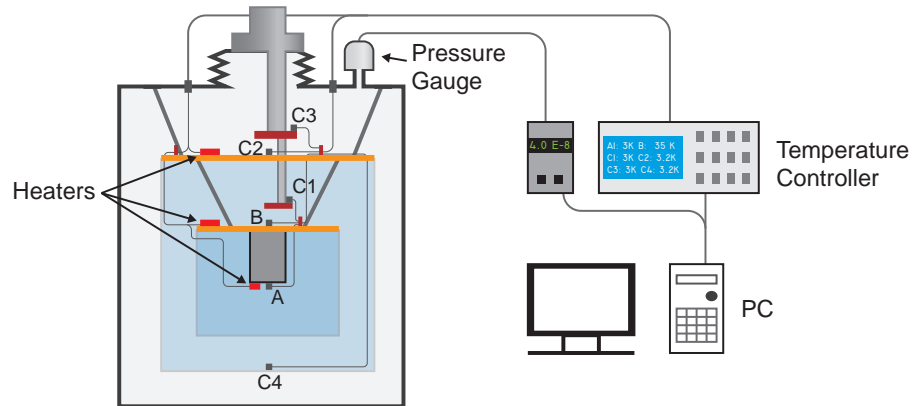
Figure 4.21: Placement of sensors and heaters in the cryostat. The six sensors are placed at different points in the cryostat, denoted by A,B,C1 etc. These sensors and three heaters are connected to the temperature controller. A room-temperature vacuum gauge is used to monitor the pressure inside the chamber and all sensor values are logged by a computer.

4.6.3 Cryogenic Experimental Setup

The heart of the experiment is a micro-fabricated chip (see also Section 3) accommodating the devices of interest. To probe the devices using RF and optical fields, a combination of a sample holder, RF circuitry, DC circuitry, a screw-based bending mechanism and a confocal microscope is implemented inside the cryostat.

Mechanical Design

The design goals for the experimental setup are not only a mechanically stable combination of the different probes but also to allow flexibility to accommodate future changes, together with a simple way of exchanging the sample. We achieve these goals by taking a modular approach, separating the microscope and its cage from the two sample holder components, the top part housing the RF wiring and connectors, and the easily detachable bottom part serving as PCB mount. The modularity of the design allows to easily accomodate changes in sample holder geometry and/or wiring, as this does not require a redesign or even a disassembly of the microscope.

The most critical design task is the combination of a confocal microscope with an MCBJ setup, as this requires access to both the top and bottom of the chip. We achieve this by implementing a fiber-based confocal microscope with a moving objective to scan the fixed sample mounted in a bending mechanism, see also Section 4.4.1. The positioning stage and objective are placed in a "hanging" position above the sample, as can be seen in Fig. 4.22, while the sample holder bottom houses the fine thread screw for bending the chip. A "chip cover" provides the counter supports while the screw is actuated via a set of gears, breaking the mechanical connection and allowing for an easy removal of the sample holder bottom.

A crucial component is the microscope housing, which should be made as rigid as possible to ensure stable positioning and minimize vibrations between the microscope and sample. We choose titanium as the cage material, both for mechanical stability and low thermal contraction. To ensure good thermal contact between the sample and base plate, all other parts of the sampleholder/microscope assembly are oxygen-free high conductivity (OFHC) copper. The cage is attached to the 3K flange via a copper adapter, while copper side plates add mechanical stability as well as thermal conductivity.

The top part of the copper sample holder features space for 16 semi-rigid RF lines ending in SMP connectors, arranged equidistantly on a circle and a central hole allows optical access to the sample. This design is compatible with the sample holders and PCBs used for other experiments performed in the group, which allows sharing PCB designs and facilitates a possible investigation of chips for cQED using optical probing. A picture of the sampleholder/microscope assembly with the sample-holder bottom removed is shown in Fig. 4.23(a).

To implement the mechanical setup introduced in section 4.1, the bending screw is placed in the bottom part of the copper sample holder and actuated via a set of 50 tooth gears, visible in Fig. 4.23(b). A dry lubricant avoids immobilization of the screw at low temperatures due to frozen moisture. We further use a flexure based coupling (HeliCal) to compensate for differences in thermal contraction between the flanges and the fiber-glass driveshaft.

Electrical Setup

RF measurements can be performed using four similar circuits, each implementing the directional coupler design described in Section 4.3.1, combined with a microwave gate line. A set of 12 stainless steel outer and inner conductor SR coaxial lines connect the room temperature vacuum feedthroughs with the components at the 3 K flange. Each line is thermalized at the outer conductor on the 40 K stage and on both conductors at

the 3 K stage, either by the directional coupler or a 3 dB attenuator in case of the gate line. Copper SR coaxial lines then connect the directional couplers/attenuators with the SMP connectors mounted in the sample holder top, where SMP bullets provide the connection to the PCB.
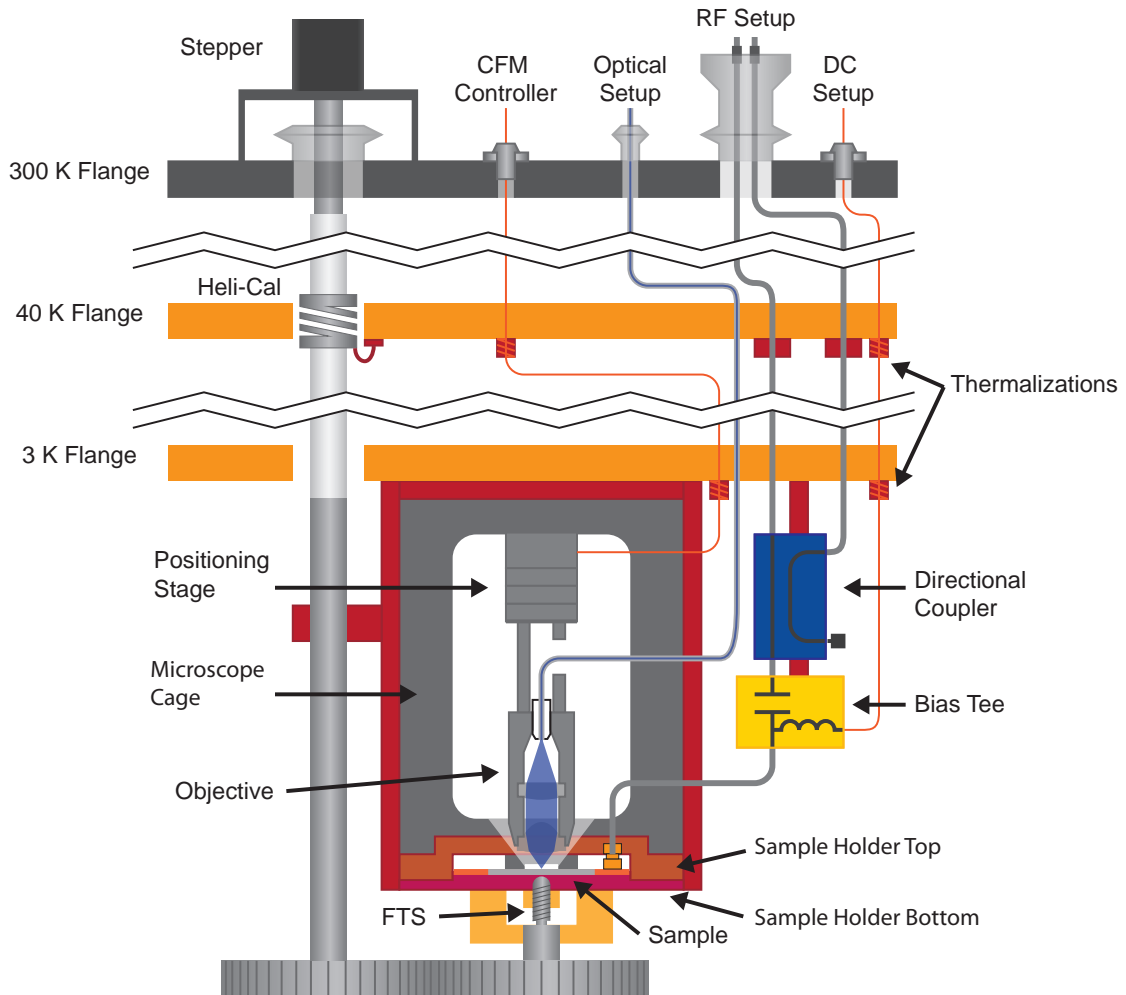
Figure 4.22: Schematic of the experimental setup inside the cryostat.

In order to keep the effect of line impedance mismatches on the reflectometry minimal, the directional coupler lines are assembled using 3.5 mm (SMA+) connectors and are attached to 2.9 mm (SMK) vacuum feedthroughs, both of which have a specified return loss of better than 30 dB at 6 GHz. The bias-tees were also chosen minimal impedance mismatch, having a specified return loss of better than 35 dB at 6 GHz. The cut-off frequency of the bias-tees is 45 MHz, in contrast to the kHz cut-off frequencies of standard bias-tees. This avoids capacitive loading of the DC measurement circuit, which leads to instability of the voltage-source feedback loop in the SMU due

to phase-lag, see also Section 4.2.1.

We further installed a set of two coaxial lines with a frequency range up to 40 GHz for resonator measurements. These lines also have stainless steel outer/inner conductors and are thermalized at the outer conductor on the 40 K stage and on both conductors via 3 dB attenuators at the 3 K stage.

DC measurements can be performed using 12 copper twisted pairs of 2.5 m length, thermalized on both stages and ending in a micro sub-D connector at the 3 K flange. This allows for a flexible reconfiguration of the connections according to the experiment. At ambient temperature, a break-out box with shorting switches distributes the pairs to four-pin connectors for individual four-point measurements.

The confocal microscope requires both a connection to the optical setup via the photonic crystal fiber as well as DC wiring for the positioning stage. The fiber is fed into the vacuum chamber by a homebuilt KF 16 feedthrough made from a blank flange and high vacuum epoxy. Standard tubing and strain relief are added at the ambient pressure side to protect the fiber, ending in an FC/APC connector. The fiber is bare inside the cryostat and ends in a 250 μm diameter ceramic ferrule. The holes of the photonic crystal structure are collapsed at both ends for a distance of 100-200 μm to allow cleaving and polishing of the end facet. This collapsing process, performed by the fiber vendor, leads to an end facet with minimal return loss while allowing cleaning and repolishing of the fiber end.

For optimal functionality of the positioning stage, the vendor states that the electrical wiring should be kept as short and conductive as the tolerable heat load allows. The 12 copper twisted pairs with a length of 1.5 m are thermalized at both cold stages and connect to the control unit via a DC feedthrough and custom shielded cables. A micro sub-D connector provides easy disconnection of the positioning stage from the wiring at the 3 K stage. For safety reasons, the stage connector and the DC measurement connector are of opposite sex.

An image of the assembled cryogenic setup is shown in Fig. 4.23(b). The positioning stage inside the titanium housing is clearly visible, the objective is hidden behind the sample holder. Two blue directional couplers followed by golden bias-tees are visible on the right side, as well as the gear set for mechanical actuation.

4.6.4 Thermal Design

The most important aspect of a cryostat is the thermal design and a large amount of development and engineering is spent on creating an optimal solution for the imposed constraints. While minimization of the heat load on the cold flanges is the central
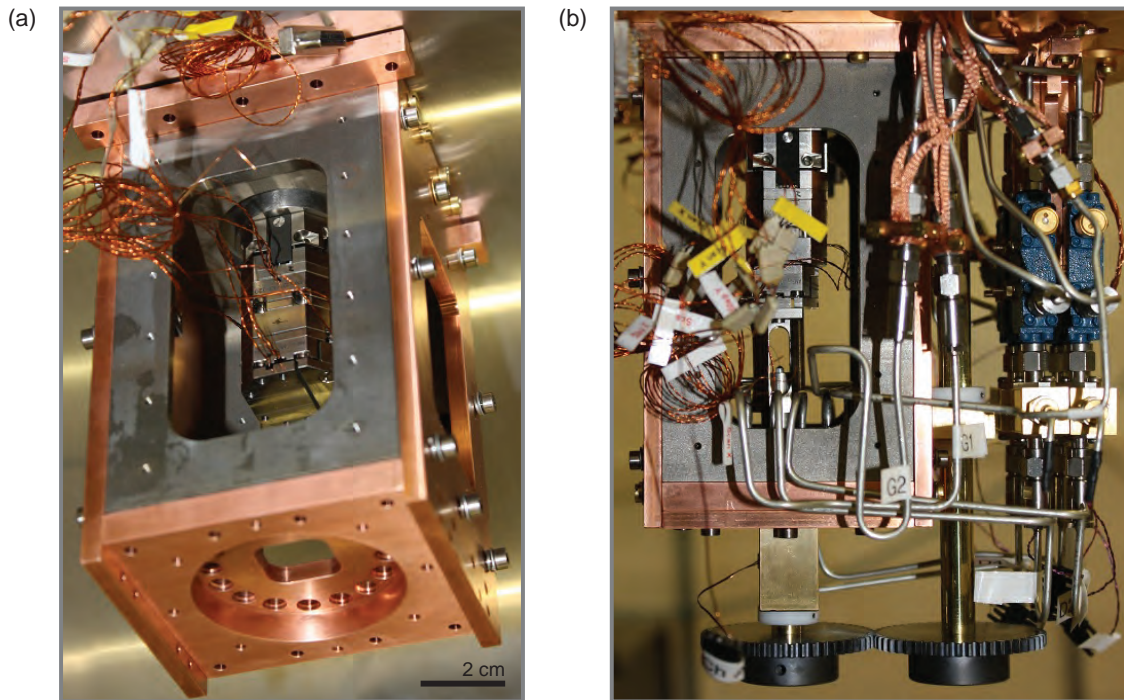
Figure 4.23: (a) Sampleholder/microscope cage assembly with sampleholder bottom removed. The positioning stage can be seen, the objective is not mounted. (b) The assembled cryogenic setup, the RF components are visible on the right-hand side, the gears for mechanical actuation on the bottom.

objective of any cryostat design, the thermal coupling between cooler, flanges and experiment requires extra attention in a dry cryostat. In contrast to immersion cryostats, the available cooling power is limited at all times and the use of a single vacuum chamber precludes the use of exchange gas as a thermal coupler. As a consequence, both optimal thermal coupling to the cooler and large thermal coupling between all parts of the experiment are required to not only achieve a low base temperature but also fast cooldown times.

The following provides a detailed analysis of the expected heat loads, discusses the thermal couplers and finally investigates the elimination of various heat load sources.

Heat Load Budget

The minimum achievable temperature at the 3 K flange is given by the heat load on the stage for a given experimental configuration and has its origin in conduction and radiation. While the part of the heat load originating from the mechanical support

and surface area of the radiation shielding is pre-determined, the amount of heat load introduced by the experimental setup, mainly by the electrical wiring, can, up to certain limits, be chosen. The load can be decreased by using materials with low thermal conductivity, but there is always a trade-off between the amount and cross-section of the wiring and the achievable base-temperature. Furthermore, the correlation between electrical and thermal conductivity also implies that there is a trade-off between wire resistance and thus signal strength and achievable base-temperature.

The thermal load $\dot{Q}$ introduced by a heat conduction path connecting two points at different temperatures is a function of the cross section, length and heat conductivity integral of the path and is given by

$$\dot{Q} = -\int_{x_1}^{x_2} \frac{dx}{A(x)} \int_{T_1}^{T_2} K(T)dT$$

where the path connects x_1 at temperature T_1 to x_2 at T_2 with a cross-section of $A(x)$ and $K(T)$ is the thermal conductivity. The thermal budget of the experimental setup is detailed in Table 4.1, listing the individual loads on both the 3 K and 40 K stage. The heat load on the 40 K stage is dominated by the RF wiring and the struts, but the total is only a small fraction of the 40 W available cooling power. The largest contribution at the 3 K stage originates from the RF wiring, with smaller contributions from the struts and DC wiring.

The capacity curve of the PTC, shown in Fig. C.1, indicates that the cooling power at the 3 K stage increases with increasing load on the 40 W stage, due to the improved gas flow inside the PTC. Consequently, the best performance may achieved by loading the 40 K stage, for example with a small heater at the 40 K cold head. The optimal loading should be achieved at a load below maximum, as the higher temperature and thus larger temperature gradient increase the heat load at the 3 K stage, negating part of the increased cooling power at the 3 K stage. Due to time constraints, the heater on the 40 K cold head was not implemented, although a preliminary test using the heater on the 40 K flange showed a 10 mK decrease in base temperature when applying 5 W of heating power.

Thermalizations

In a dry cryostat, the thermal coupling between the flanges and the cooler is a critical issue, because the thermal conductivity at the coupling point has a large influence on both cooldown time and base temperature. From a thermal viewpoint, mounting the PTC directly on the flange is the optimal configuration. Unfortunately, this requires compensation for thermal contraction and, more importantly, vibrations from the cooler

Component	40 K load [mW]	3 K load [mW]
Attocube DC wiring	100	10
Meas. DC wiring	100	5
Thermometry	4	0.1
Struts	264	8
Shaft	6	1
RF outer conductor	250	10
RF inner conductor	-	19
Total	724	53.1

Table 4.1: Heat load budget for the proposed cryostat.

couple directly to the flange. To mitigate these effects, a flexible connection with high thermal conductivity is necessary.

The initial design of such a connection was adopted from existing solutions in commercial cryogen-free cryostats, and consists of two circular anchors connected by stranded wires. To ensure good thermal contact between the strands and the anchors, the strands were soldered to the anchors. We used lead-free soldier to avoid possible heat barriers due to superconducting lead. As the solder tends to creep into the strands and make them stiff, they were made longer than necessary to keep them flexible. Both the strands and anchors are made from standard grade copper, a picture is shown in Fig. 4.24. The anchors are cut in the middle to create two half-rings, allowing disassembly of the thermalization without removal of the PTC.

Using the initial design of the thermalizations, the 40 K stage required approximately 12 hours to reach equilibrium temperature, with a maximum temperature difference between cold head and flange of about 200 K, as is shown in Fig. 4.25(a). While the equilibrium temperature is sufficiently low, the large difference between the cold head and the flange temperature during cooldown implies that the cooldown time is limited severely by the thermal conductivity of the thermalization. We therefore redesigned the thermalizations with the goal of increasing the thermal conductivity and hence improving the cooldown time.

Given that the copper stranded wires are the limiting factor for the conductivity, an improved design with changes in material, cross-section and length of the wires was implemented. OFHC copper is used both for the anchors and the wire strands, which are woven into a flexible braid. Increasing the total number of wires yields a total cross-section of 360 mm^2 compared to 162 mm^2 for the initial design. The wires are electron-beam welded to the anchors to improve the coupling between anchor and wire,

Figure 4.24: Image of the 40 K thermalization half-rings, the initial design is shown
in the back, the improved design in front.

which also allows the braids to be shortened from 13 cm to 4.5 cm.

For comparison, the performance of the improved thermalization design at the 40 K stage is also shown in Fig. 4.25(a). The graph shows that the improved design significantly changes the cooldown characteristics of the cryostat. Temperature equilibrium is reached five hours earlier, while the maximum temperature difference between flange and cold head is reduced by more than a factor of two. At equilibrium, the remaining difference between cold head and plate was reduced from 9 K to 3 K, implying an increase in thermal conductivity by a factor of three. In contrast, the cooldown curve of the 3 K flange is only slightly modified by the new design, as shown in Fig. 4.25(b), which is expected for well decoupled flanges. The slight differences between the two curves are mainly due to the internal configuration of the PTC, in which the 40 K stage cools the regenerator of the 3 K stage. Thus the differences in the 3 K cooldown curves mirror the differences between the curves of the 40 K cold head.

The same improved design was also implemented at the 3 K stage, resulting in a 30 minute reduction in cooldown and a decrease in base temperature of 100 mK. The smaller impact of the improved design on cooldown of the 3 K stage is due to the fact that the initial design of the 3 K thermalization already provided a large wire cross-
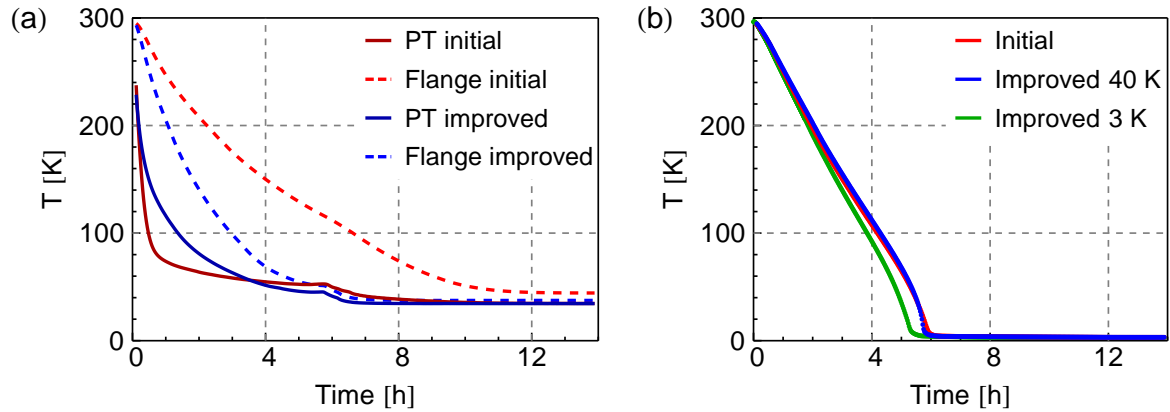
Figure 4.25: (a) 40 K stage cooldown curves of the PT head and flange (dashed)
for the initial design of the 40 K thermalization (red curves) and the
improved version (blue curves). (b) Cooldown curves of the 3 K flange
for the initial 40 K thermalization design (red), the improved 40 K
design (blue) and the improved design on both stages (green).

section, which could only be increased by 20 % using the improved design. This alone
does not account for the 100 mK decrease in base-temperature, a significant part of
which is likely caused by the change in strand material to OFHC copper.

Superisolation

With both convection and conduction accounted for in the design, a closer look at heat
transfer via radiation is merited. All surfaces emit thermal radiation with a power
proportional to the emissivity of the material and the fourth power of the temperature,
and also absorb this radiation. A warmer surface can therefore transfer energy to a
colder surface via the imbalance in absorbed and emitted radiation. The resulting heat
flow can be estimated using the Stefan-Boltzmann law, which for two long concentric
cylinders leads to [Balshaw96]:

$$\dot{Q} = A_1 \sigma \frac{T_2^4 - T_1^4}{\frac{1}{\epsilon_1} + \frac{A_1}{A_2}\left(\frac{1}{\epsilon_2} - 1\right)} \tag{4.2}$$

where σ is the Stephan-Boltzmann constant, A_1 and A_2 are the surface areas, T_1 and
T_2 the temperatures and ϵ_1 and ϵ_2 the emissivities of the inner (colder) respectively the
outer (warmer) cylinder.

By applying equation 4.2 and using emissivities of 0.1 for both the chamber and 40 K
shield, the expected heat load at the 40 K stage is calculated to be 13 W, about a third
of the available cooling power. Using the same emissivities, the expected radiation

load on the 3 K stage is 1.5 mW, smaller than the heat load introduced by the wiring. Since the surface areas and temperatures are determined by the cryostat design, the radiation heat load can only be manipulated by changing the surface emissivities, which is possible both by the choice of material and by surface treatment such as polishing. By covering the shield with a highly reflective aluminum sheet, the emissivity and thus the heat load introduced by the shield can already be substantially lowered, avoiding the cumbersome and expensive process of polishing the shield.

A further possibility to reduce the effect of thermal radiation is the use of multi-layer isolation (MLI), where a series of highly reflective and thermally isolated layers is wrapped around the shield. A single isolated layer will absorb the room-temperature radiation and re-emit it to both sides, one half to the chamber and only one half toward the cold stage. Each additional layer will thus reduce the radiation load, leading to a reduction by a factor of $\approx 1/(n+1)$ when using n layers. In practice, 5 to 10 layers will already achieve minimal load due to the non-perfect thermal isolation of the individual layers. Furthermore, each additional layer, while improving isolation, introduces a substantial amount of surface area inside the cryostat, extending the vacuum pumping period before cooldown.

As the radiation heat load on the 40 K stage is quite substantial, a reduction using MLI is expected to significantly decrease both the cooldown time and the equilibrium temperature of the 40 K stage. In contrast, the benefit of MLI on the 3 K stage is expected to be small, on the order of several 10 mK, as the radiation load is less than 2% of the total heat load. A similar decrease in base temperature is expected caused by the reduced thermal gradient to the 40 K stage. Unfortunately, we expect the reduced cooling capacity at the 3 K stage as a result of less radiation heat load on the 40 K stage to mitigate part of the expected decrease in base temperature.

We implemented a MLI on both shields, consisting of aluminum oxide fiber blankets alternating with high reflectivity aluminum sheets. Three layers were placed on the 40 K shield and two layers on the 3 K shield. As a result, the maximum temperature of the 40 K shield dropped by 13 K, from 62 K to 49 K, and the time to reach the equilibrium decreased by approximately one hour, to 7 hours, as is shown in Fig. 4.26(a). Furthermore, the 40 K flange temperature decreased by 1.2 K and on the 40 K PT head temperature by 0.4 K. We used the electric heater on the 40 K stage to quantify the reduction in radiation heat load on the 40 K stage, which required 8 W of electric power to increase the flange temperature to the pre MLI value. A similar decrease of one hour in the time to reach the thermal equilibrium was also achieved on the 3 K plate, along with a decrease in base temperature of approximately 50 mK, as shown in Fig. 4.26(b).
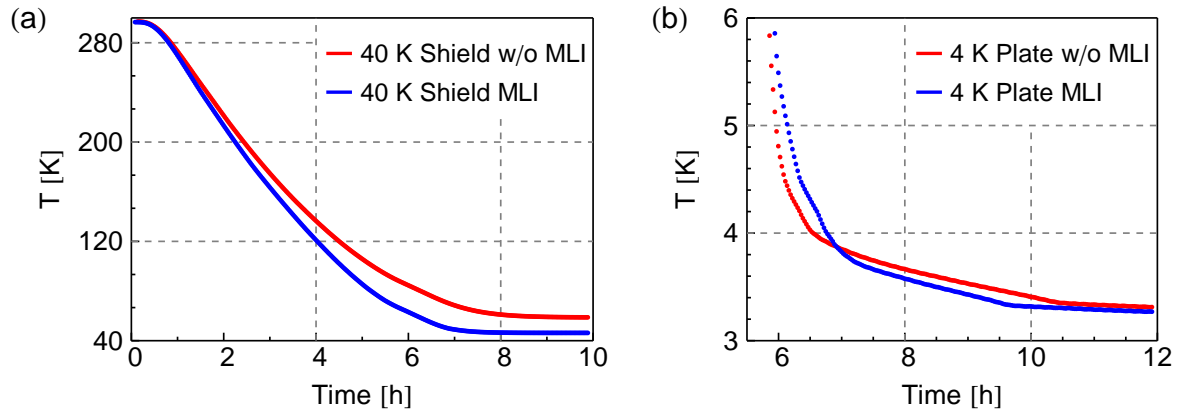
Figure 4.26: (a) Comparison of the 40 K shield temperature during cooldown with-
out MLI (red) and with MLI (blue) (b) Comparison of the 3 K plate
temperature during cooldown without MLI (red) and with MLI (blue).

Further Thermal Aspects

While the use of a single vacuum chamber facilitates the vacuum engineering issues
in a dry cryostat, more attention needs to be paid to the thermal design of the cryo-
genic experimental setup, as exchange gas cannot be used to thermalize the individual
components.

In the original design, the entire microscope assembly was made from titanium al-
loy in order to increase stability and to avoid thermal contraction issues encountered
when using different materials. Since similar experimental setups use titanium hous-
ings [Hogele08], the comparatively low thermal conductivity of titanium was not con-
sidered an issue. However, the first cooldown runs showed that the sample holder
bottom had bad thermal coupling to the base plate and would require several days
to reach base-temperature. This is caused not only by the low thermal conductivity
of titanium, but also by its hardness, making good thermal contact at the interface
between two parts difficult to achieve. Furthermore, titanium alloys can become su-
perconducting at temperatures below 5 K [Clark70], leading to a further deterioration
in thermal conductivity.

In order to achieve good thermal coupling between all parts of the assembly, all
titanium parts except the microscope cage where exchanged by OFHC copper parts, as
shown in Fig. 4.23(a). The two side plates are screwed to the base plate but only pressed
against the microscope cage and sample holder via spring washers, creating thermal
contact while allowing the plates to slide, thus compensating the approximately 100
μm thermal contraction difference between the titanium housing and the sideplates.

Warm up

While the main parameters of interest for a cryostat are usually the cooldown time and achievable base temperature, the cycling time also includes the time required to reach room temperature again at the end of an experimental run. As cryostats are inherently well isolated from the environment, it typically takes several days for a cryostat to reach room-temperature equilibrium if only the PTC is turned off. A significant speed-up can be achieved by using helium as a heat exchange gas, reducing the pressure in the vacuum chamber to a value between 0.1 and 1 mbar, and thus creating thermal coupling between the chamber and the flanges. While simple, the helium pressure is limited, as the chamber can cool below the point of condensation.

Due to the fact that the thermal flux is dependent on the temperature gradient, a fast warm-up strategy based on exchange gas requires an increase in pressure to compensate for the decreasing temperature gradient. An alternative is the use of temperature controlled electrical heaters, which not only circumvent the need for a gas-handling system but are also able to actively heat the stage when approaching room temperature. For this reason, two heaters were installed in the cryostat, which, when connected in series, achieve a significant speed-up in the time to reach room-temperature even though the wiring limits the total heater input power to 33 W. A comparison of the two discussed warm-up methods is shown in Fig. 4.27, in which the warm-up curves of the 40 K flange and the sample holder are plotted. When using 0.1 mbar of helium, approximately 20 hours are required to reach room temperature if the exchange gas pressure is increased after 15 hours. In contrast, electrical heating allows a warm-up time of only 10 hours, which can be further reduced to less than 9 hours by using a combination of both methods.

A PID loop implemented in the temperature controller is used to control the heating based on the temperature of the sample holder. The heaters can provide a maximum of 11 W on the 3 K flange and 22 W on the 40 K flange, and are not controlled independently, leading to an overshoot to 315 K on the 40 K flange. This can be eliminated using a second control loop, but is considered small enough for practical purposes.
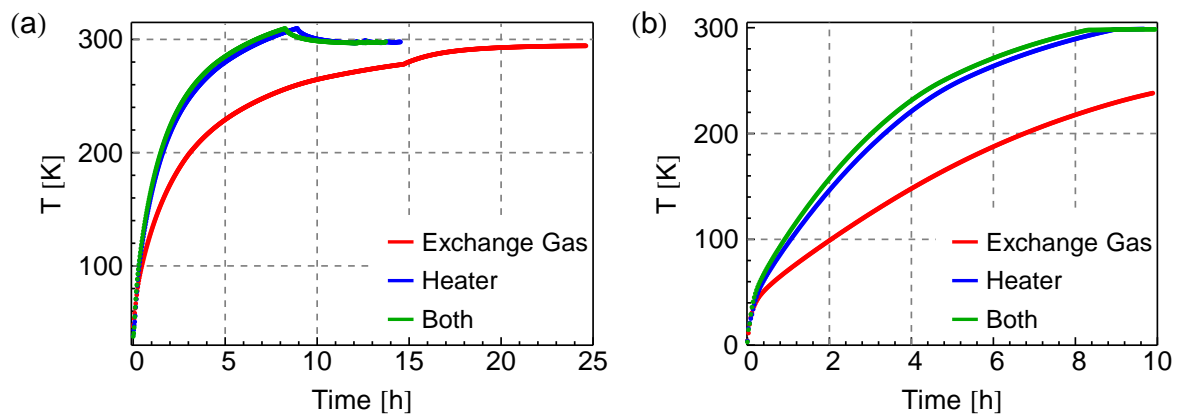
Figure 4.27: Warm-up curves for the 40 K flange (a) and sample holder (b) for 0.1
            mbar helium (red), electrical heating (blue) and a combination of 1
            mbar helium and electrical heating (green).

5 Scientific Results

The versatility of the implemented measurement setup described in the previous section allows for a number of different experiments to be performed. These include DC transport measurements, RF reflectometry and scanning photo current microscopy, as well as combinations of these experiments, for example simultaneous measurements on the DC and RF properties of the device or the time-resolved photo-response. In the following, we present characterization measurements of the different measurement techniques developed in this thesis. Starting with clean break-junctions in a DC setup, we first demonstrate control over the breaking process and then utilize these break-junctions to form and characterize single molecule and single colloidal quantum dot devices. We then shift our focus to RF devices, with which we characterize clean break-junction integrated into impedance matching circuits. The employed measurement concepts are then extended to the investigation of molecular junctions and single carbon nanotube devices. A further set of experiments involving photo-induced processes is then presented, where we study the wave length dependence of the observed photo current both for clean break-junctions and a C_{60} based molecular junction. Finally, we combine RF and optical measurements to perform time-resolved investigations of the photo-induced impedance change in a single carbon nanotube device.

5.1 Direct Current Measurements of Break-Junctions

Starting point for most of the nano-scale object devices investigated in this thesis is a the gold break-junction. The controlled breaking of such a junction is critical for the formation of single molecule devices and is achieved either entirely by electromigration or by pre-migration and mechanical means. We therefore first investigate the controlled breaking of a clean break-junction and demonstrate good control over the different breaking methods.

The controlled electromigration of a break-junction is a key component in most of the performed experiments. A successful migration depends both on the measurement configuration and on the type of feedback method applied. We tested several different

approaches for the initial migration up to a junction resistance of 1 kΩ, including both two-point and four-point measurement topologies and different feedback algorithms, see also Section 2.2.2. For migration above 1 kΩ junction resistance, an approach using short pulses is demonstrated, as well as the self-breaking of a biased break-junction at room-temperature.

5.1.1 Electromigration in Two-Point and Four-Point Measurement Configurations

When using a voltage ramp to electromigrate a break-junction, the observed migration behavior depends critically an the wiring and lead resistances, as discussed in Section 2.2.2. We investigate this behavior using clean break-junctions with different wiring resistances at cryogenic temperatures.

Initial investigations utilized a four-point measurement setup, eliminating the 200 Ω to 400 Ω lead and wiring resistance, leaving a residual resistance on the order of 10 Ω. More than 80 % of the lead/wiring resistance is due to the 1 μm by 20 μm electron-beam defined leads to the break-junction, which were kept as small as possible to achieve short writing times. We first utilized a feedback algorithm based on the junction resistance leaving a fixed resistance window to ensure successful migration. A more detailed description of the algorithm is given in Section 2.2.2.

A typical example for the resulting migration curve is plotted in Fig. 5.1, both as an $I - V$ plot in (a) and as resistance versus time plot in (b). Starting from zero bias, the bias voltage is ramped, up to 50 mV in steps of 10 mV, then at 1 mV per step with an integration time of 2 ms per point. Close to 220 mV and 9 mA, we observe an increase in resistance, the onset of electromigration. At this point the voltage is reduced by 40 mV and the ramp is started again. This procedure is then repeated, showing a decrease in the current necessary to initiate migration each iteration. The critical current follows the theoretical curve (black line) given by (2.26) and (2.27), obtained using a critical power of 750 μW and 15 Ω lead resistance.

In the resistance-time plot, a smooth increase in resistance can be observed from the initial 10 Ω up to 200 Ω. Beyond this point, the change gradually becomes step-like and erratic and does not always lead to an increase in resistance. This behavior is attributed to a measurable response of the junction resistance to the migration of atom clusters, as the cross-section at this point is less than 100 atoms, as estimated by the conductance of ≈ 70 G_0 and assuming one channel per atom.

Based on the observation that the critical power is reached at a constant or increased bias voltage each iteration, a simple voltage ramp for migration was tested in the four-
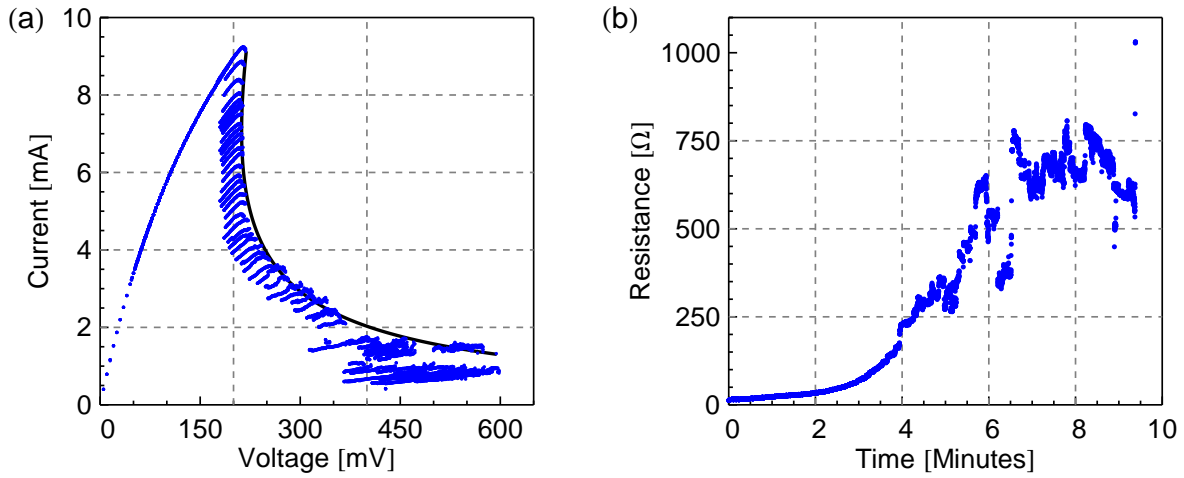
Figure 5.1: (a) $I - V$ plot of a break-junction electromigration in four-point config-
uration at 4 K. (b) Plot of the resistance versus time of the same data
set.

point measurement setup. The resulting $I - V$ and $R - t$ plots are shown in Fig. 5.2,
displaying a sharp decrease in current in the initial stage of migration and followed
by a slower decrease up to 500 mV, the signature of a self-limiting electromigration.
The $R - t$ plot is similar to the feedback case. Overall, the electromigration using a
four-point setup is qualitatively the same with and without feedback, but about five
times faster without feedback than with.
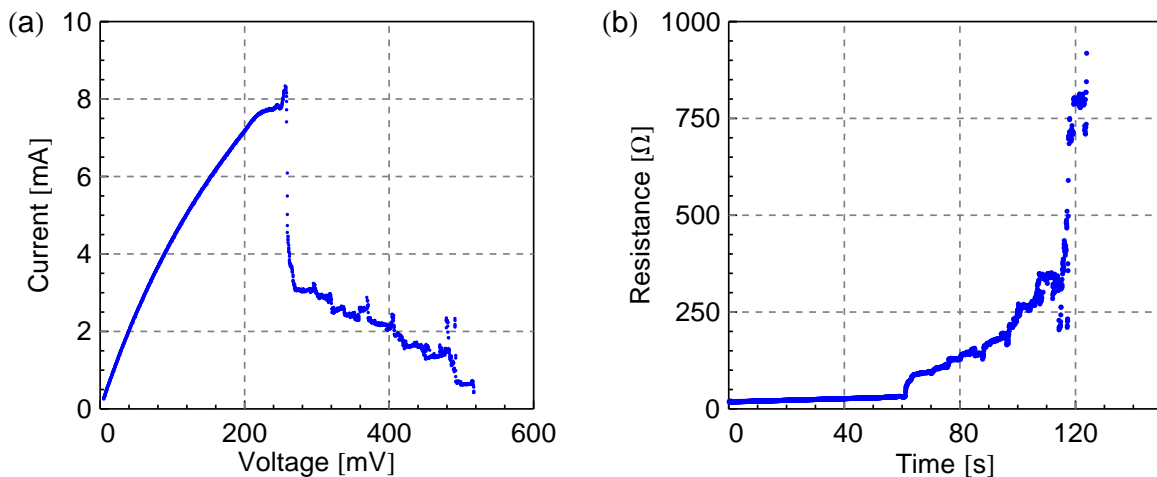
Figure 5.2: (a) $I - V$ plot of a break-junction electromigration in four-point config-
uration at 4 K, using a simple voltage ramp. (b) Plot of the resistance
vs. time of the same data set.

Due to the 100 kΩ to GΩ resistances of single-molecule devices, a four-point mea-surement setup is not strictly necessary for the measurement of the final device. In particular, the lead resistances can be determined by a measurement of the initial break-junction resistance and subsequently subtracted. By switching to a two-point measurement setup, twice the number of junctions are available per cooldown, moti-vating the investigation of feedback controlled electromigration at large lead resistances. In the current setup the additional resistance is largely due to the EBL defined leads and can be reduced by using a different chip design, but future experiments may require better filtering, typically increasing the wiring resistance by 100Ω to 200 Ω. Further-more, superconducting stub-tuners also profit from this method, as migration can be performed with the tuners in a non-superconducting state, where lead resistances on the order of 700 Ω are observed.

The $I - V$ plots in both Fig. 5.1(a) and Fig. 5.2(a) show an initial ramp that is not linear. Instead the resistance of junction increases with increasing voltage. This behavior is due to Joule-heating of the sample by several degrees, as several 10 mW are dissipated in the leads. When utilizing a feedback method based on comparing the current resistance to a reference resistance, the thermally induced resistance increase triggers a reduction in bias voltage although no migration has taken place. As increasing the window can lead to thermal runaway, this feedback method is limited to wiring/lead resistances on the order of 40 Ω to 50 Ω. We therefore require a different detection method for larger wiring/lead resistances.

The second detection method is motivated by zooming into the $I - V$ curve of the first example, shown in Fig. 5.3(a). The onset of migration is manifest as a change of sign in the differential conductance, which we utilize to determine when the migration threshold has been reached, more details are given in Section 2.2.2. This method reliably detects migration even in presence of Joule-heating and at wiring resistances of several 100 Ω, limited mainly by the maximum voltage rating of the setup.

An example migration of a break-junction with 290 Ω wiring resistance is shown in Fig. 5.3(b) and (c). The $I - V$ curve shows that the critical power in each subsequent iteration is reached at a bias voltage ≈ 400 mV below that of the previous iteration. As break-junctions typically break at bias voltages of 1-1.5 V, thermal runaway would occur without feedback in the presented case. By utilizing the differential conductance-based feedback algorithm, it is, however, possible to controllably migrate the junction to a total resistance of 1 kΩ, in a manner similar to the four-point measurement method, as can be seen in the plot of resistance versus time shown in Fig. 5.3(c). The four-point measurement setup can therefore be replaced by a two-point measurement setup, even with considerable wiring resistance, allowing for an increased number measurement sites per cooldown run.
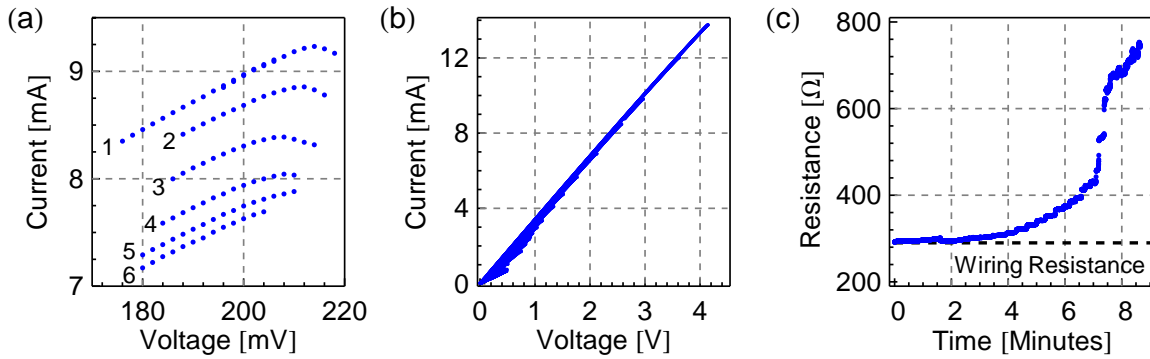
**Figure 5.3:** (a) $I-V$ plot of the initial 6 feedback steps of Fig. 5.1(a). (b) $I-V$ plot of a break-junction electromigration in two-point configuration at room temperature. (c) Plot of the resistance versus time of the same data set.

5.1.2 Pulsed Migration

For several experiments, such as laser-induced conductance changes, a clean break-junction with a conductance of a few conductance quanta is required. Such values are easily achieved using a mechanically controlled break-junction, but the use of bridge-like structures is not optimal when laser induced heating is an issue, therefore requiring the use of a planar break-junction. In the few G_0 regime, an atom by atom thinning is required, where standard computer-controlled electromigration is too slow to allow feedback control. By using a voltage-pulse method (Section 2.2.2), the response time limit can be circumvented, allowing for a controlled migration as demonstrated in the following.

We migrate a break-junction up to 750 Ω in a two-point configuration, at which point further migration was induced using a pulse sequence consisting of two pulses, a migration pulse of 1 ms length and variable amplitude, followed by a 10 mV, 20 ms measurement pulse, with a delay of 10 ms between the pulses. In Fig. 5.4(a) the migration pulse current as a function of the pulse amplitude is shown, in (b) the resistance obtained from the low amplitude measurement is plotted as a function of time. The pulse-sequence is repeatedly applied and the resistance compared to a target resistance after each iteration by a software program. The migration pulse amplitude was increased manually, starting from 100 mV. As one can see in Fig. 5.4(a), migration is induced for pulses with an amplitude larger than $\approx$ 650 mV, a similar value as observed for short pulses in Ref. [Hayashi08]. By repeatedly applying such pulses, the resistance can controllably be increased up to the target value, in this case 2 kΩ or 6.4 G_0. By using this process, good control over the target value can be achieved, as it is possible to stop the migration at each of the measured points, allowing for a precision

on the order of 100 Ω.
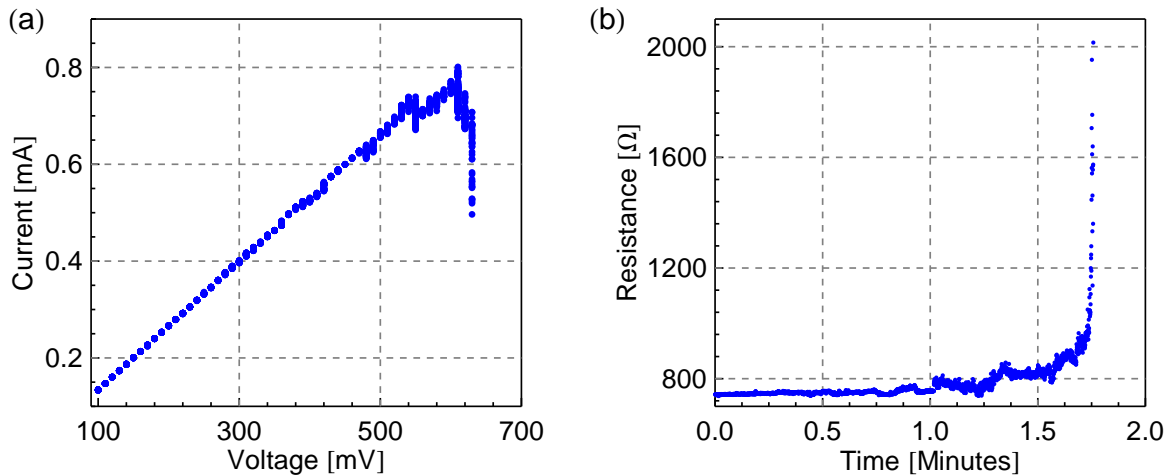
Figure 5.4: Electromigration using a 1 ms pulse of variable amplitude and a 20 ms 10
mV measurement pulse. (a) $I-V$ curve of the variable amplitude pulse,
the amplitude is slowly increased until migration starts close to 650 mV
amplitude, and stopped once the target resistance has been achieved. (b)
The junction resistance obtained from the 10 mV measurement pulse as
a function of time.

5.1.3 Room Temperature Measurements

Due to the high mobility of gold atoms at room temperature, clean break-junctions
with a resistance of 1 kΩ or more are typically not stable for more than a few minutes.
This behavior can be exploited to controllably create 0.5 to 0.8 nm gaps [Tsutsui10]. As
a demonstration, a junction was migrated to a conductance of 6 G_0 and subsequently
the conductance was monitored at a bias of 100 mV. The resulting time trace is shown
in Fig. 5.5(a). After one minute, the conductance drops rapidly from 6 G_0 to 3 G_0, a
plateau at which the junction is stable for 8 minutes. The value then decreases to 1.7
G_0 and shortly thereafter breaks via a smaller step to a conductance of 0.1 G_0. The
final value is most probably due to contamination, as the experiment was performed
at ambient pressure and temperature. This experiment highlights the high mobility of
gold, requiring cryogenic temperatures for stable gold contacts. An alternative are, for
example, graphene/graphite electrodes, which can be electro-chemically burnt in much
the same way a gold break-junction is electromigrated, but which are stable at room
temperature. It is therefore possible to fabrication and subsequently characterize an
empty junction before performing molecule deposition [Prins11].
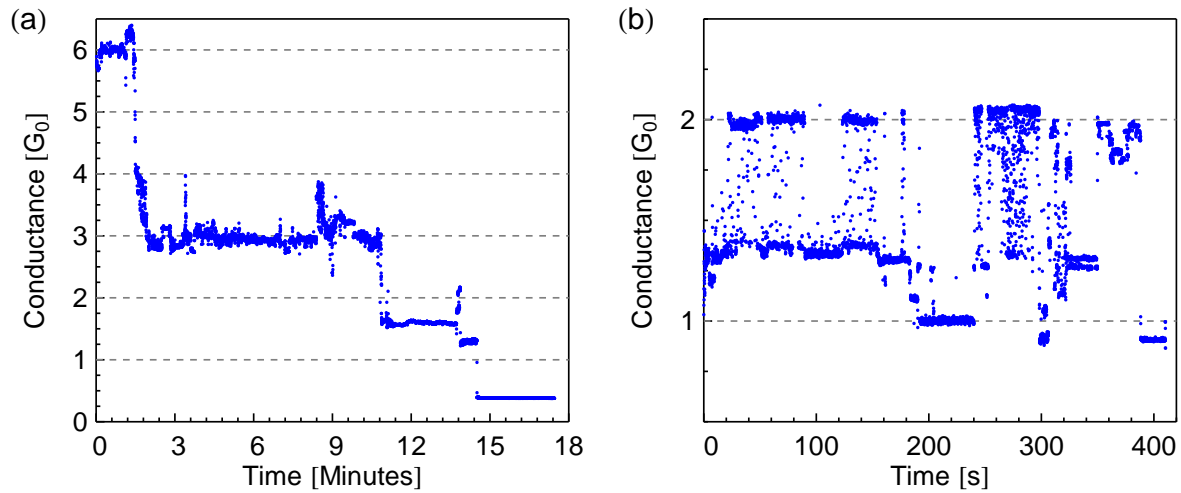
Figure 5.5: (a) Conductance versus time plot of a break-junction, measured at room temperature and a bias of 100 mV, the wiring resistance has been subtracted. (b) Time trace of fluctuating conductance in a break-junction measured in a four-point configuration at room temperature and a bias between 100 mV and 300 mV.

A further interesting effect observed at room temperature is switching between two different conductance values. In this case, two separate, meta-stable electrode configurations exist with an energy separation smaller than the thermal energy, allowing the system to jump from one state to the other [Krans96]. This type of behavior was one of the first indications that the quantized conductance observed in APCs was due to the atomic nature of the contact. A time-trace of such switching behavior is shown in Fig. 5.5(b), showing fast fluctuations between 1.3 G_0 and 2 G_0. In this measurement, the applied bias was slowly ramped from 100 mV to 300 mV. Investigating such behavior in a time-resolved fashion would be an application of the developed RF circuits. Unfortunately, the temperature dependence of the transition rate for such switching is expected to be follow an Arrhenius form with an activation energy of 0.1 to 1 eV [Agrait03]. We thus expect such switching events to be rare at the cryogenic temperatures necessary for superconducting transmission lines.

5.1.4 Mechanical Control

When using crystalline material such as silicon or sapphire as the substrate for MCBJs, it is necessary to first electromigrate the break-junctions to a conductance on the order of 8 G_0 to 10 G_0 using the methods demonstrated in the previous section. Afterwards, we can break the junctions mechanically by bending the chip. An example plot of

the conductance measured at a constant voltage of 20 mV versus the displacement of the chip at cryogenic temperatures is shown in Fig. 5.6(a). The conductance starts at 4 G_0 and decreases with increasing displacement where both gradual and abrupt steps are visible, due to the elastic and inelastic deformation of the junction [Agrait03]. Furthermore, although the conductance in general decreases with the displacement, we also observe the opposite behavior. The type of response to displacement depends on the particular arrangement of the atoms in the APC, as demonstrated by simulations [Tavazza11].
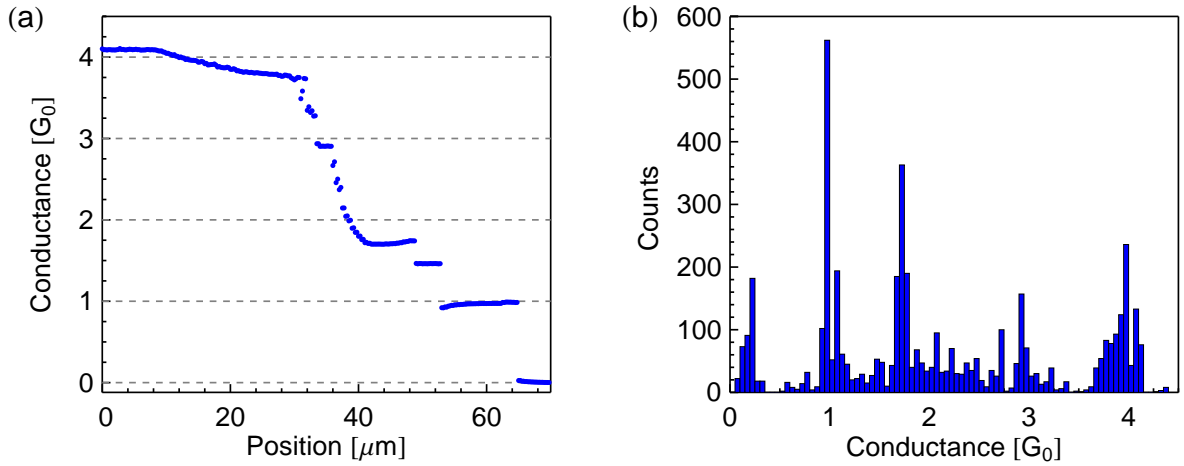
Figure 5.6: (a) Conductance of a break-junction vs. displacement at a bias of 20 mV, measured in a four-point configuration. (b) A conductance histogram of 10 opening/closing cycles, for clarity, the 0.05 G_0 bin was removed.

By opening the junction at a constant speed and binning the measured conductances, the preferred conductance values can be extracted from a histogram. To exemplify this approach, a histogram of 10 opening/closing cycles is shown in Fig. 5.6(b), where a clear peak at 1 G_0 is visible, corresponding to a single atom bridging the gap. For clarity, the bin 0-0.05 G_0 with 1602 counts is not shown. Further peaks can be distinguished close to three and four G_0, while the two G_0 peak is shifted downward to 1.8 G_0. Simulations using tight binding conductance calculations have demonstrated that such deviations are due to the detailed atomic configuration of the contact [Tavazza11]. The small peak around 0.2 G_0 is due to contamination in several opening/closing cycles.

Once a clean junction is broken, a potential barrier is formed through which electrons can tunnel with an exponential dependence of the resulting current on the tunnel barrier width. This behavior is shown in Fig. 5.7(a), where the resistance extracted from a small voltage sweep is plotted against the displacement for one opening (blue) and closing (red) cycle. After breaking the contact at 9 μm, the resistance immediately jumps to $\approx$ 500 kΩ and then increases exponentially. The integration time (20 ms)

limits the sensitivity of the measurement to resistances of several 100 MΩ. For larger resistance, a constant value is extracted. As the electrodes are moved back together, the same exponential dependence can be observed with a jump-to-contact at 1 μm. The shift between opening curve and closing curve is caused by mechanical slack in the setup which in further measurements is corrected for.
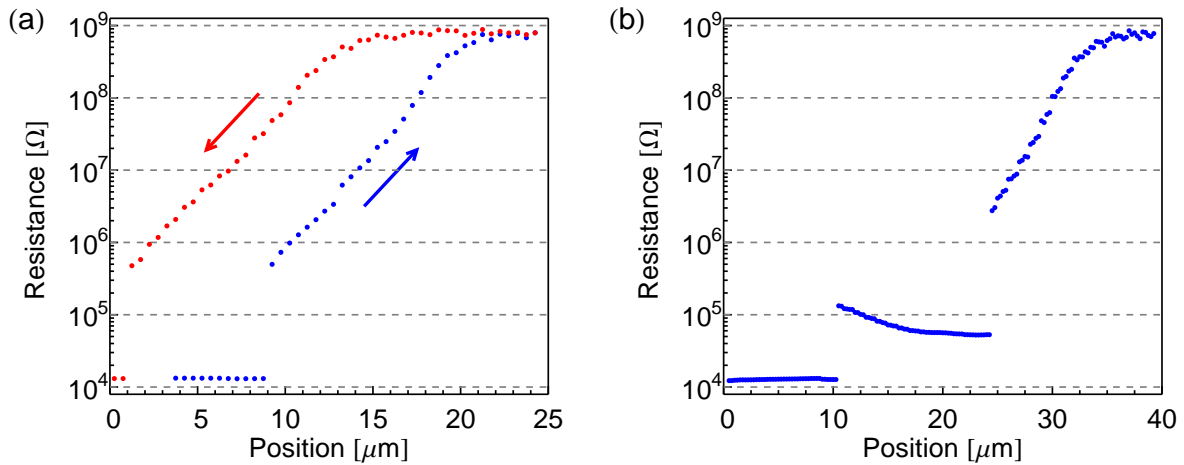
Figure 5.7: (a) Breaking (blue) and closing (red) cycle of a clean break-junction. (b) Breaking cycle in the presence of contamination.

The behavior of the resistance versus displacement changes in the presence of molecules on the surface, as show in Fig. 5.7(b), where the resistance jumps to 100 kΩ at 10 μm but decreases for rising displacement, before breaking at 25 μm, after which the exponential increase in resistance is recovered. The molecule in this measurement is of unknown origin, the break-junction showed no indication of a molecule in the previous 8 opening/closing cycles.

A calibration of the electrode motion as a function of displacement can be performed using the exponential decay of the tunneling current, which is expected to follow [Agrait03]

$$I = \exp\left(\frac{2\sqrt{2m\phi}}{\hbar}\delta\right). \tag{5.1}$$

Assuming that the work function for gold is $\phi = 5.1$ eV [Tipler99], the mechanical translation factor between the electrode separation δ and the displacement z is found to be 2.8 10^{-5}. The expected value of 1.3 10^{-5} for an 800 nm bridge is smaller by a factor of two, which can be due to several reasons, such as non-uniform bending, a larger bridge span or a deviation of the work-function value from the bulk value [Kolesnychenko99b]. A more accurate calibration can be obtained using Gundlach oscillations [Kolesnychenko99a], but was not performed. This deviation is not considered an issue, because it is reproducible between different chips manufactured in the same run.

5.1.5 SEM Imaging

SEM images of three different break-junctions after migration are shown in Fig. 5.8. The two junctions shown in (a) and (b) migrated in the middle of the nano-wire, typically observed in junctions with less than 20 nm wide wires. At such widths, the deposition of metal on the resist leads to a reduced metalization height on the order of 25-30 nm, additionally reducing the cross-section at the center of the junction. This favors migration at this point and leads to maximal gate coupling. In contrast, thicker wires lead to asymmetric migration, as shown in in (c), where the junction is well shielded from the gate field.
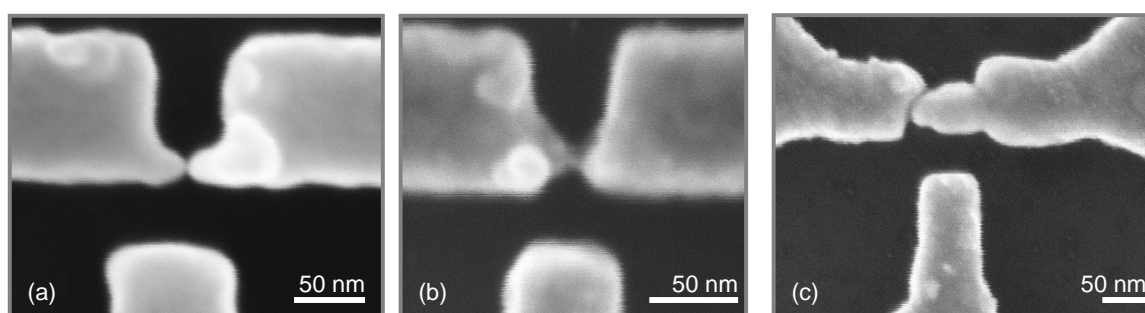
Figure 5.8: (a)-(c) SEM images of different break-junctions after electromigration and measurement, the scale bar is 50 nm.

5.2 Transport in Single Nano-Scale Object Devices

After achieving control over clean break-junctions, the next step is the fabrication of single nano-scale object devices. The main challenges here are the formation of the device itself and a verification of the type of object present in the junctions. Device formation is mainly dependent on the concentration of the objects on the break-junction surface, which can be influenced by the solution concentration and time that the chip is exposed to the molecules. To ensure that the resulting devices are formed by the molecule of interest and not by fabrication residue or metal clusters, "control" chips from the same wafer run but without any deposited molecules are measured in the same setup. If the cleaning process for the wafer run was successful, the junctions on the control chip will only show vacuum gap tunneling behavior.

In the following, measurements on C_{60} molecules and CdSe nanocrystals are presented, demonstrating the feasibility of realizing and investigating such devices in the presented setup.

5.2.1 Fullerene Molecules

We first investigate devices based on C_{60} molecules, a well studied system attracting much interest due to the high symmetry of the molecule. Once formed, the device $I - V$ characteristics are measured, which strongly depend on the molecule-electrode coupling. In case of weakly coupled molecules, the $I - V$ curves are expected to display Coloumb Blockade, whereas for intermediate to strongly coupled devices we expect a non-linear $I - V$ curve with peaks in the dI/dV curve close to ± 50 mV [Bohler07] due to the presence of inelastic channels at 34 mV and 64 mV.

An example set of $I - V$ and dI/dV curves is shown in Fig. 5.9, where the results of four different sites (#04u,#04l,#06l,#07l) from the same chip (#210) and cooldown run are presented. Each site was electromigrated in a two-point configuration using the differential conductance feedback method up to a resistance of 800-1000 Ω. Subsequently the wire is broken by ramping the voltage until a conductance smaller than G_0 is detected. We measure differential conductances in a range from larger than G_0 (green) to less than 0.2 G_0 (blue). The large measured conductances suggest that several molecules connect the electrodes, as the expected conductance at a bias of 100 mV is on the order of 0.1 G_0 [Bohler07] to 0.2 G_0 [Kiguchi08]. Although molecular concentrations similar to other experiments [Champagne05] were utilized, where the concentration yields a working device in 30 % of the junctions, the surface-to-volume ratio is significantly larger in the presented devices, most likely causing the formation of devices with several molecules.

Sites #06l and #07l show a roughly similar behavior and in general features appear at -90 mV and +100 mV bias. Combined with the fact that only linear tunneling was observed in the control chip, not shown here, we conclude that the observed behavior is likely to originate from transport through C_{60} molecules, but expect these devices to consist of several molecules, leading to the larger conductance and shifted peaks. A further set of control experiments involving only the toluene solvent is necessary, although toluene has been reported leave no contamination in break-junction experiments [Grose08].

Using the described experimental procedure, we mainly obtain intermediate and strongly coupled devices. This may be due to minute time-scale breaking process, where the break-junction is first controllably migrated to 1 kΩ and subsequently broken either by a voltage ramp or mechanical stretching, allowing the molecule to couple well to one of the electrodes. In contrast, most experiments involving Coloumb blockade [Yu04, Parks06, Grose08, Roch08] perform the migration on a time-scale of several 10 seconds, which may favor weak coupling to both electrodes. On the other hand, the cited success rate for obtaining devices which display Coloumb diamonds is less than
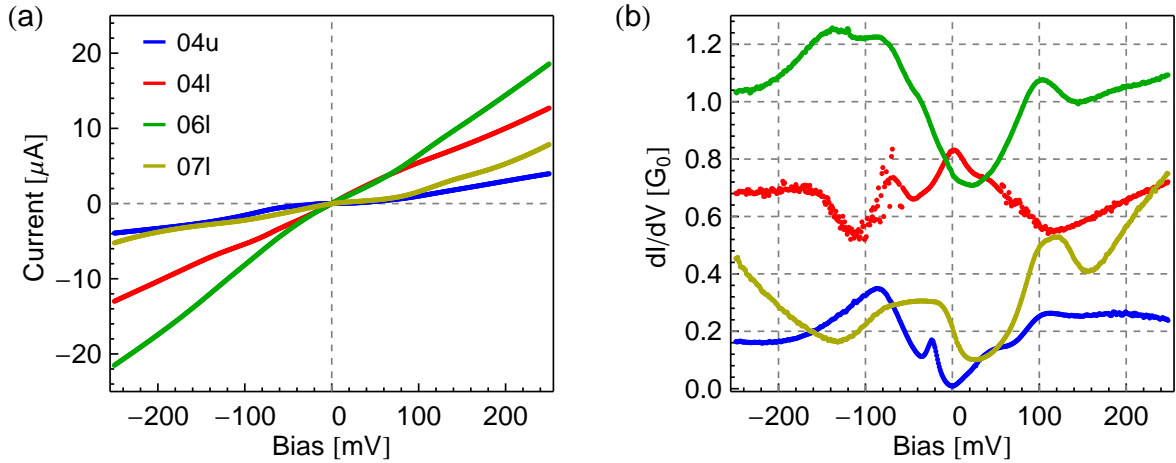
Figure 5.9: (a) $I-V$ and (b) $\mathrm{d}I/\mathrm{d}V$ curves for four C_{60} devices from the same chip.

1 %, requiring more than 100 migrated devices to obtain one weakly coupled device, in which case the migration time-scale is not important but rather the total number of devices investigated.

We only fabricated a single C_{60} device (Site 03, Chip 48) showing indications of Coloumb blockade, the results are plotted in Fig. 5.10. A suppression of current at low bias is observed, which is strongly gate dependent, as can be seen both in the individual traces in (a) and in the density plot (b). The accessible energy level is shifted by almost 150 meV, the total height of the coloumb diamond observed is comparable to references [Park00, Champagne05], and s. Unfortunately, the device was not stable, as can be seen by several jumps in $\mathrm{d}I/\mathrm{d}V$ at gate voltages around -30 V. Moreover, the cryogen in the utilized dipstick measurement was exhausted during this measurement, leading to an unstable device for gate voltages larger than 5 V (not shown) and precluding a further measurement. Nevertheless, this measurements demonstrates that single molecule devices with Coloumb Blockade behavior can be implemented in the presented setup.

5.2.2 Gate-dependence in Benzene-Edithiol Devices

To allow for a better characterization of the investigated nano-scale object devices we implemented a side gate to enable measurements as a function of electric field. In the following, the response of a molecular device to the applied DC electric field is investigated more closely. The investigated device consists of benzene-edithiol (BDT) molecules which form self-assembeld monolayers on gold and are used as a linker molecule for colloidal quantum dots. Due to the delocalized electron orbitals in the
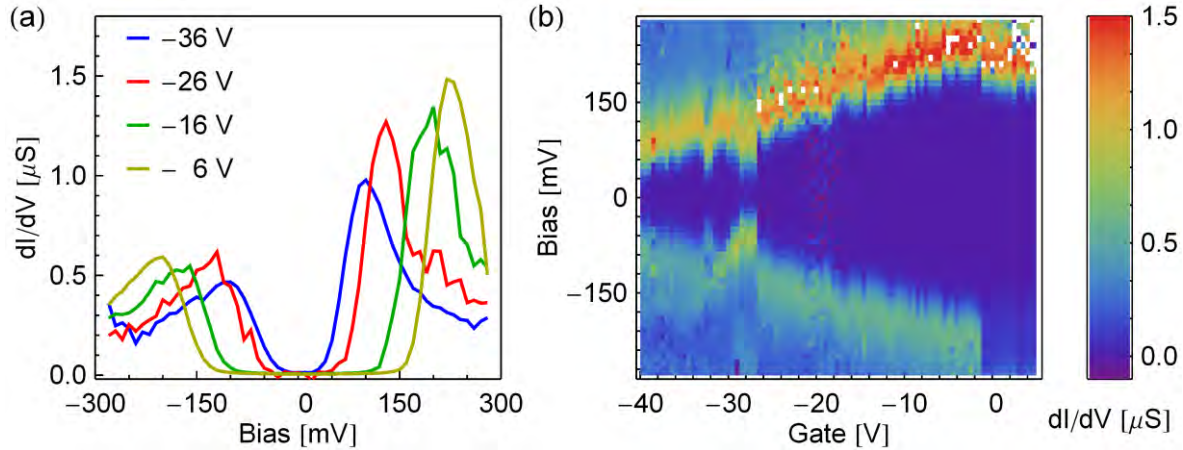
Figure 5.10: dI/dV curves for a weakly coupled C_{60} molecule. (a) Individual curves. (b) Density plot of the full range.

benzene ring, BDT is a good conductor and conductances of up to 0.5 G_0 have been measured in single BDT devices [Kim11]. In case of the presented samples, the goal was the fabrication of single colloidal quantum dot devices.

Four chips (194,195,197 and 198) where functionalized with BDT and subsequently immersed in quantum dot solution, a total of 39 break-junctions were broken and measured. A total of 33 devices showed a non-linear conductance smaller than 1 G_0. Only three devices immediately displayed Coloumb Blockade, while three further devices could be obtained with Coloumb Blockade after additional voltage ramps. Since the goal was a working quantum dot device, the resulting $I-V$ curves where not investigated in detail, save for the results shown below.

In case of the presented device (site #04u, chip #198), we assume one or several BDT molecules to couple to the electrodes. The measured dI/dV curves are shown in Fig. 5.11(a) as a density plot, and are in general agreement with the results presented in Ref. [Kim11]. The density plot shows a shift of the DOS that is symmetric about $V_{gate} = 0$ V (dotted line), with lower coupling at lower absolute gate voltages. This result is surprising, as one would expect a change in one direction due to a shift in the energy levels, but not symmetric around $V_{gate} = 0$ V.

To further investigate this behavior, traces along V_{gate} at different bias voltages are shown in Fig. 5.11(b). We observe a quadratic dependence of dI/dV on the gate voltage (dotted lines), which suggests that the gate is exerting an electrostatic force on the source and drain electrodes. The force acting on each electrode due to polarization in the metal is proportional to U_{Gate}^2, leading to a displacement $\delta y \propto F_{pol} \propto U_{Gate}^2$, assuming the electrode can be modeled as a cantilever beam. For small displacements, the change in electrode spacing δx is then proportional the electrode displacement δy.
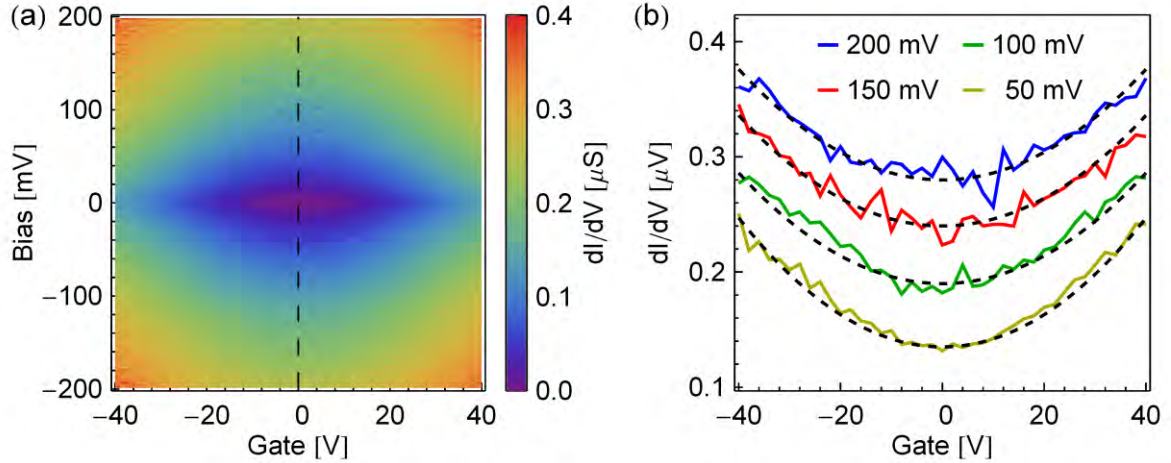
Figure 5.11: (a) dI/dV density plot for BDT device #04u, Chip #198. (b) dI/dV versus gate for the same device for the indicated bias voltages.

In case of BDT and a small change in electrode spacing, a very simple model describing the differential conductance is that of an intrinsic density of states of the molecule DOS_{in} and an electrode spacing dependent coupling $\Gamma_{electrode}(\delta x)$. Using a linear approximation for the dependence of the coupling on the electrode spacing, $\Gamma_{electrode}(\delta x) = \Gamma_0(x_0 - \delta x)$, justified by the approximation of the coupling being the proportional to the overlap of the electrode and molecule orbitals, we arrive at

$$dI/dV = \Gamma_{electrode}(\delta x)DOS_{in} = k_0 \ DOS_{in} \ (k_1 U_{Gate}^2) \ ,$$

where k_0 and k_1 are proportionality constants. The observed change in dI/dV is therefore more likely caused by a change in electrode separation, while the contribution due to the shift in the energy levels is too small to be observed. In many cases, increasing the electrode spacing leads to a reduced coupling, but for this device, mechanically opening the gap confirms an increase in differential conductance with increasing gap size, likely due to a change in conformation [Kim11].

The mechanical effect of the side gate is an important issue for the investigated devices and can be eliminated in several ways. One possibility is to mechanically strengthen the electrodes by increasing the metal thickness and the beam width in the electrode design. A second possibility is the use of a stronger second layer of metal, for example titanium, to reinforce the electrode beams, using shadow evaporation to maintain a gold break-junction. The third and favored possibility is the implementation of a dual gate, where a second side gate is placed on the other side of the break-junction. The resulting forces will cancel and an overall increase in gate efficiency is expected [Cao12].

To further demonstrate the increase in conductance with increasing electrode spac-

ing, measurements on a second BDT device (Site 04l) on the same chip are shown in Fig. 5.12. We observe a Kondo-like zero-bias anomaly with a conductance peak close to zero bias. Assuming that this feature indeed arises from the hybridization of a single unpaired electron on the molecule with the electrons in the electrode, we expect the peak-width to be dependent on the coupling of the electrodes to the molecule and further a broadening with increased coupling [Parks06]. Extracting the full-width half-maximum from each dI/dV-curve, plotted versus gate in Fig. 5.12(b), we observe a broadening with increased absolute gate voltage. This is a tentative second indication of an increase in molecule/electrode coupling due to the mechanical deformation of the electrodes.

Most experiments involving the Kondo-effect are performed with devices showing Coloumb blockade [Parks06, Roch08]. In contrast, our device does not show Coloumb blockade, but nevertheless a Kondo-like zero bias anomaly, requiring further work to understand the origin of this effect. Such features have also been observed in well coupled C_{60} devices, but no systematic investigation was performed and no a transport model given [Bohler07].
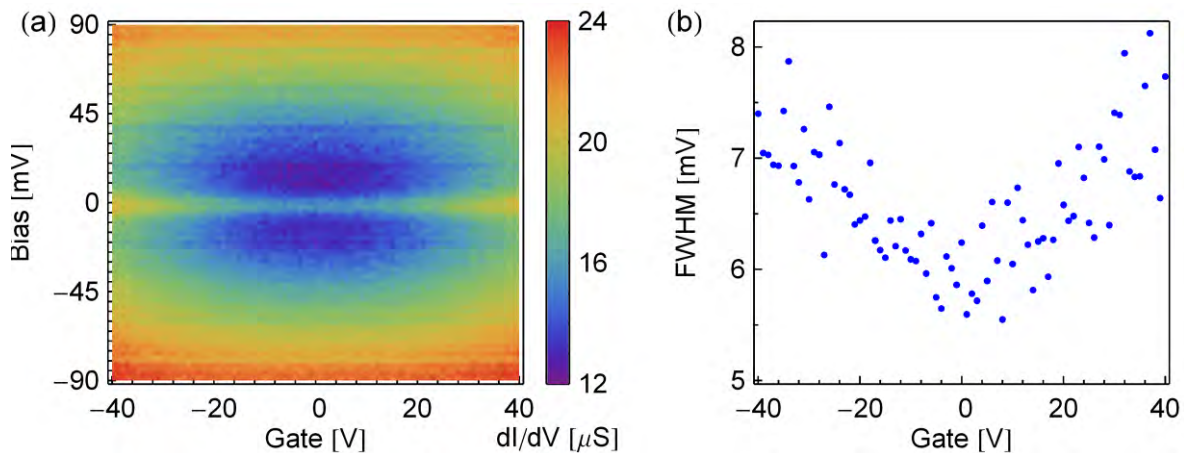
Figure 5.12: (a) dI/dV density plot of BDT device #04u, Chip #198. (b) Extracted full-width half-maximum (FWHM) of the Kondo-like peak.

5.2.3 P(MAA/MMA) Residue

During the development of a fabrication process yielding sub 20 nm thin break-junctions, an initial double-layer process using P(MAA/MMA) as the lower layer was used. While this resist structure results in a stable process and is often used in microfabrication, it was not possible to remove the resist residue from the chips fabricated using this process, although a number of harsh cleaning methods such as O_2 plasma and a mixture

of H2SO4/H2O2, commonly known as piranha etch, were utilized. Clean samples were only obtained after changing the bottom resist layer from P(MAA/MMA) to PMMA 50K. We measured a number of samples before identifying this issue, which we utilize to show the influence of changing the electrode spacing on the transport characteristics.

A comparison of the gate dependence of site #06 chip #97 at two different electrode spacings is shown in Fig. 5.13, where the differential conductance as a function of gate and bias voltage are plotted. In both cases, a pattern symmetric around $V_{\text{gate}} = 0$ V was observed, similar to the ones discussed in Section 5.2.2, but with reduced instead of increased conductance for increasing $|V_{\text{gate}}|$. As the device conductance decreases for increasing electrode spacing, this measurement further confirms the mechanical influence of the applied gate field.
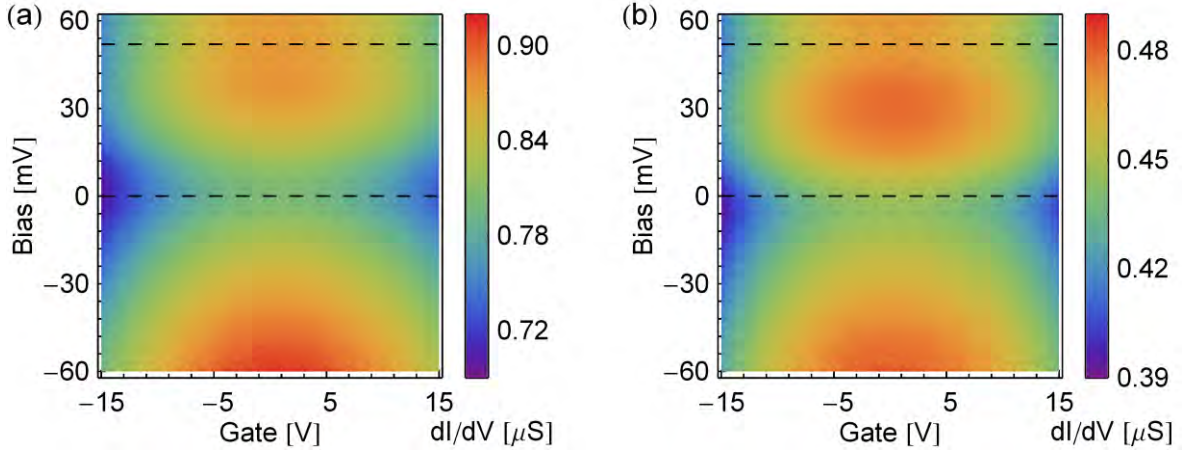
Figure 5.13: dI/dV density plots of site #06 chip #97 at the reference position (a) and with the electrodes opened by 280 pm (b). The dashed lines indicate local minima in dI/dV at zero bias and 55 mV.

Changing the electrode spacing by 280 pm not only leads to a change in the conductance of close to a factor of two, but also changes the shape of the dI/dV curve. While two local minima are visible at zero bias and 55 mV (horizontal lines) in plot (a), the second local minimum at 50 mV is not present anymore in plot (b). Furthermore, the region of low DOS around zero bias is smaller in plot (b) than in plot (a). This implies that the electrodes have large influence on the behavior of a single molecule device and the possibility to tune the molecule-electrode coupling mechanically is an advantage for investigating such devices.

5.2.4 Transport in colloidal quantum dots

Research into single colloidal quantum dots electrically contacted by electrodes is motivated by the following two factors: (i) their common usage in optical devices, both for absorbing and emitting light, in which a characterization on the single dot scale may yield a more precise understanding of photo-processes than ensemble measurements; (ii) their large optical absorption cross-section, which, together with a comparatively easy identification of quantum dot devices, makes such devices attractive for testing photo-current investigations into nano-scale object devices.

Two key parameters control the formation of colloidal quantum dots devices, the linker molecule and the concentration of the dots with the linker molecule further influencing the transport through the device. The first single colloidal quantum dots experiment utilized hexan-edithiol (HDT) [Klein96], which yields devices with resistances in the 100 MΩ to 10 GΩ range due to the large tunneling barrier formed by the 1.2 nm long linker molecule. In contrast, short linkers such as mercapto-acetic acid (MAA) and BDT are expected to lead to lower resistances, as the tunnel barrier is thinner (MAA) and due to delocalized electron systems (BDT) allowing for improved transmission [Kim11]. In particular, a resistance on the order of 50 kΩ to 1 MΩ would allow for RF measurements, motivating their use in the following experiments.

The chosen linker molecules form a self-assembled monolayer on the gold surfaces of the chip, while the concentration of the dots on the gold depends both on deposition time and solution concentration. Initial investigations with several mg/mL concentrations and several hours of deposition led to chips with high device yield, displaying Coloumb-staircase like $I - V$ curves, but did not allow gating with an electric field. SEM inspection revealed a large agglomeration of dots and linker molecules around the break-junction which most likely screens the gate field.

In order to avoid this screening effect, we reduced the concentration to 0.1 mg/mL, which did not yield a quantum dot device, although molecular devices with non-linear $I - V$ curves where formed for 15 of 16 migrated break-junctions. SEM inspection revealed a quantum dot coverage of less than 0.1 monolayers, insufficient to create devices with reasonable yield. In case of the following break-junction chip #195 the concentration was increased again to 1 mg/mL with an immersion time of 24 hours.

A device showing Coloumb Blockade behavior was attained at site #01l on this chip, the measurement results are shown in Fig. 5.14, both as current traces in panel (a) and dI/dV density plot in panel (b). The low yield is attributed to an insufficient density of quantum dots on the break-junction. The $I - V$ traces show a suppression of current at low bias, as expected for Coloumb blockade and the density plot shows a diamond-like structure between the gate voltages -30 V and 10 V. We extract a charging energy of ≈

15 meV, in agreement with the 14-29 meV charging energies observed in Ref. [Klein96]. We attribute the measured resistances in the 100 kΩ range to the use of BDT as a linker molecule, which would provide a significant decrease in resistance compared to the use of HDT as linker molecule, but further measurements are necessary to confirm this.

Instabilities in the $I-V$ and dI/dV traces are further observed, which we attribute to a conformation change of the quantum dot and/or linker molecules or a change in the electrostatic environment. Further measurements where performed on this device at a higher bias and gate resolution, but were severely affected by the device instability, which may have its origin in the 0.5 to 1 nm gap sizes produced by electromigration. As a consequence, the quantum dot is not confined between the electrodes, allowing for easier rearrangement.
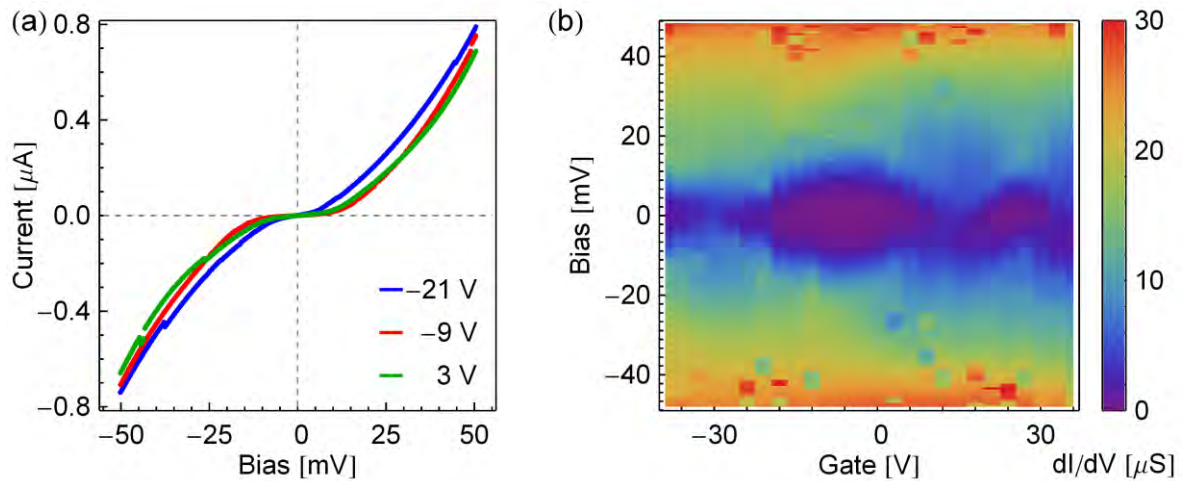
Figure 5.14: (a) $I-V$ traces, (b) dI/dV traces and (c) density plot of a colloidal quantum dot device (Site 01l Chip 195)

To address the issue of the small gap formed by electromigration, FIB milling was used to cut 5 nm gaps into the break-junctions on a test chip (chip #198), which was subsequently coated with linker molecules and quantum dots and measured in the cryostat. The individual sites yielded either empty junctions or closed junctions which had to be electromigrated at currents twice as large as necessary for the break-junctions on a chip fabricated in the same run. An SEM inspection revealed that several sites had fused shut, most probably due to ESD, creating break-junctions with reduced scattering, therefore requiring more current to migrate. In case of the closed junctions, linker molecule devices were obtained (see also Section 5.2.2) but the concentration of quantum dots was too low to yield working devices, requiring further tests to obtain the correct concentration.

5.3 Radio-Frequency Measurements using Reflectometry

A significant part of the project presented in this thesis is the implementation and characterization of transmission-line based impedance transformers for investigating break-junction-based nano-scale object devices. Such circuits allow an increase in the measurement bandwidth to the 1-100 MHz range at improved signal-to-noise, as well providing for a method to extract the impedance at GHz frequencies. We implemented a number of such circuits and characterize a device with a designed matched load of 12.9 kΩ using the break-junction as a variable load. We then utilize similar circuits to investigate both a molecular junction and a single carbon nanotube device.

In the following section, the transmission line characterization will first be presented, before results on stub tuners with integrated clean break-junctions, molecular devices and single carbon nanotubes are presented.

5.3.1 Waveguide Characterization with Half-Wave Resonators

Both the accurate design and rigorous characterization of transmission-line based circuits rely on a precise determination of the transmission line parameters. To extract these parameters, each photolithography mask with superconducting devices also includes a number of $\lambda/2$ resonators designed for the same resonance frequency as the tuners. These resonators are then measured during the same cooldown run as the investigated stub tuners. In the following, characterization and temperature dependent measurements of Nb and NbTiN coplanar waveguide resonators are presented.

Transmission Line Parameters

An accurate determination of the attenuation constant α and phase constant β for a given transmission line geometry is best performed by measuring the resonances of an undercoupled $\lambda/2$ transmission line resonators. By fitting a Lorentzian, given in (2.45), to the measured data, the quality factor and resonance frequency can be extracted, allowing for the calculation of α and β.

For each fabricated wafer, coplanar waveguide resonators with the same coplanar waveguide dimensions as the impedance matching devices and a length of $l_{res} = 10.8235$ mm where measured to characterize the waveguide. In Fig. 5.15, the transmission spectrum of (a) a Nb and (b) a NbTiN resonator are shown. In both cases, the Lorentzian (black line) fits well to the transmission spectra. Although identical in dimension, the larger kinetic inductance [T.V.81] of NbTiN significantly shifts the resonance frequency

from 6.15 GHz to close to 4.64 GHz as the geometric and kinetic inductances in the chosen coplanar waveguide geometry are comparable.
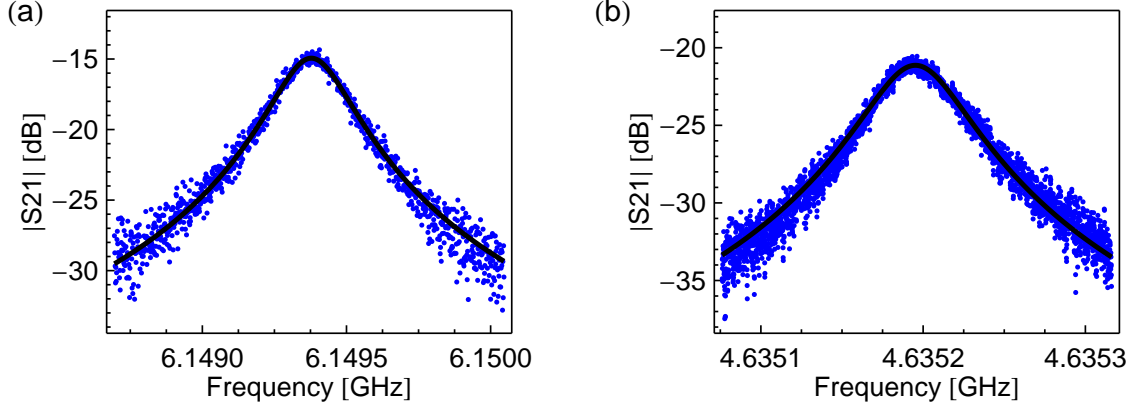
Figure 5.15: Transmission spectra of (a) Nb and (b) NbTiN undercoupled $\lambda/2$ transmission line resonators (blue) and lorentzian line fits (black) at 4.2 K.

We further performed temperature dependence measurements of the transmission spectra for both materials. The Nb resonator was investigated in a dilution refrigerator down to a temperature of 25 mK, and the NbTiN resonator in the Arctic cryostat (see Section 4.6) down to a temperature of 2.96 K.

From these measurements we obtain the temperature dependence of α, which is plotted in Fig. 5.16(a). In case of Nb (blue), the dependence is approximately exponential above 2.5 K and saturates toward a value of $3\ 10^{-4}$ at 25 mK, where dielectric loss originating from oxide on the metal and imperfections at the metal-substrate interface dominates over quasi-particle loss [Wenner11, Megrant12, Geerlings12]. The temperature dependence of NbTiN also shows an approximately exponential dependence, with a larger deviation at temperatures below 3.5 K. This has been observed previously [Frunzio05], but the origin of this deviation was not investigated. We obtain a value of α at 3 K of 0.0050 1/m for Nb and 0.0017 1/m for NbTiN, hence NbTiN is preferred for matching circuits investigated in the Arctic Cryostat, as this allows for higher matched loads and better sensitivity. Note that the two loss values are extracted at different frequencies, using the expected quadractic scaling [Booth99] the loss in Nb is expected to be 0.0028 at 4.6 GHz.

It is useful to write the phase constant in a frequency dependent form $\beta = \beta_0 f$, where β_0 is an "effective" phase constant accounting for factors influencing the propagation properties such as the dielectric constant and the inductance kinetic inductance. The temperature dependence of β_0, extracted from the resonance frequency using equation (2.44), therefore shows the expected $(1 - (T/T_c)^4)^{-1/2}$ dependence (dashed lines) due to the kinetic inductance. For comparison, both curves are shown in Fig. 5.16(b). The
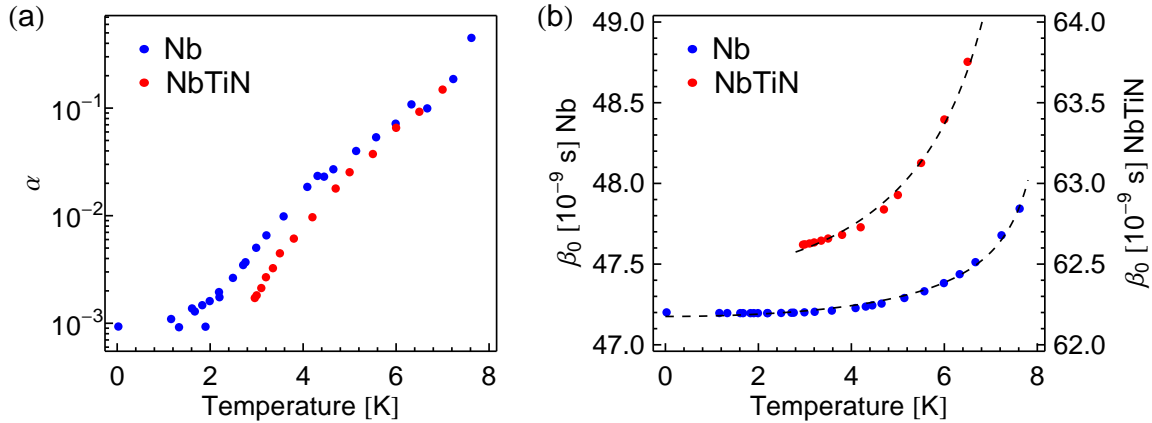
Figure 5.16: (a) The attenuation constant as a function of temperature for Nb (blue) and NbTiN (red). (b) The effective phase constant as a function of temperature for Nb (blue) and NbTiN (red).

value of β_0 for Nb at 3 K is 47.2 10^{-9}, which is 30% smaller than the value for NbTiN of 62.62 10^{-9}. As a result, NbTiN devices require less space than Nb devices at the same frequency, which can be used to either make circuits more compact or decrease the circuit resonance frequency.

Kinetic Inductance

The temperature dependence of the resonance frequency can further be used to determine λ_0, the penetration depth at zero temperature, which is material specific. Once determined, λ_0 can be used to calculate the expected kinetic inductance for different coplanar waveguide geometries, offering design flexibility for future devices.

By fitting equation (2.69) to the measured bare resonance frequencies taken at different temperatures, the 0 K penetration depth is determined to be 45 nm for Nb and 267 nm for NbTiN, the data and fits are plotted in Fig. 5.17. In case of NbTiN, the penetration depth agrees with other work (280 nm [Yu05a]). For Nb, the extracted penetration depth is close to the bulk value of 47 nm [Maxfield65], an unexpected result for a thin film device, where we would expect a penetration depth on the order of 70 nm [Sheen91, Taber90]. An independent verification using a different sample in the Arctic cryostat, not shown, yields the same value of 45 nm. We conclude that the film thickness of 150 nm for the niobium samples, on the order of three times the penetration depth, leads to the observed deviation, as the formula for extracting λ_0 is only valid for a film thickness less than twice the penetration depth.
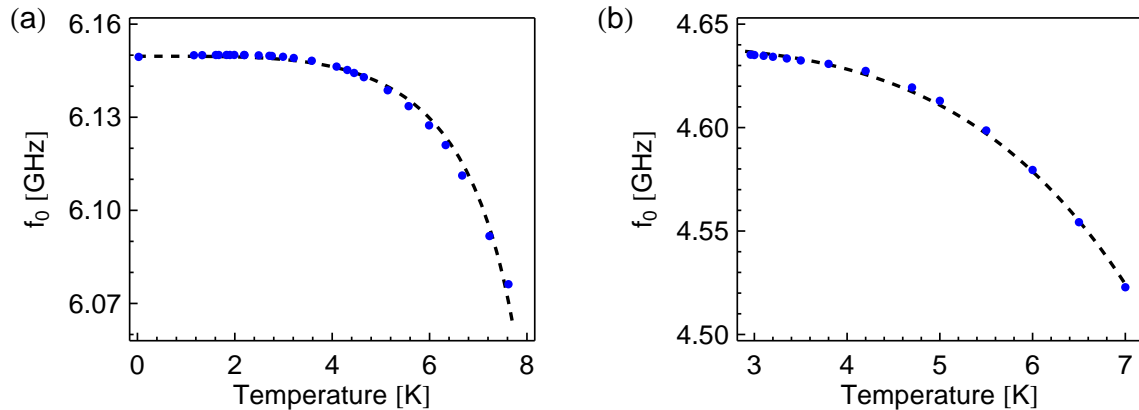
Figure 5.17: Measured resonance frequency as a function of temperature (points) and λ_0 fit (dashed line) for (a) Nb and (b) NbTiN.

5.3.2 Parasitic Modes and Groundplane Continuity

The mode conversion taking place at the T-junction in coplanar waveguide stub tuners influences the tuner properties due to the different effective dielectric constant and losses of the parasitic modes. This results in a change of both the resonance frequency and matched load of the device, requiring a suppression of the parasitic modes for predictable behavior and is achieved by ensuring ground-plane continuity. A comparison of the reflection spectrum of an example device with and without groundplane continuity is shown in Fig. 5.18. Note that this stub tuner does not include a break-junction, the observed resonance is due to internal loss. The device was first measured without any modification (a), after which groundplane continuity was established via bond wires and the device measured again (b). The resulting difference in the spectrum is twofold: first, the resonance is shifted by 153 MHz from 5.393 GHz to 5.546 GHz, which is closer to the expected resonance frequency of 5.6 GHz extracted from resonator measurements. Second, without bond wires the resonance does not follow the expected lorentzian line shape. To accurately design impedance transformers based on transmission lines, it is therefore essential to ensure groundplane continuity, ideally using microfabricated airbridges.

5.3.3 Impedance Transformers with Integrated Break-Junctions

Now that the transmission line characteristics are known, we focus our attention on impedance transformers with integrated break-junctions. We first investigate devices with clean break-junctions [Puebla-Hellmann12] in order to demonstrate the measurement concept and then go on to expand this concept to molecular junctions.
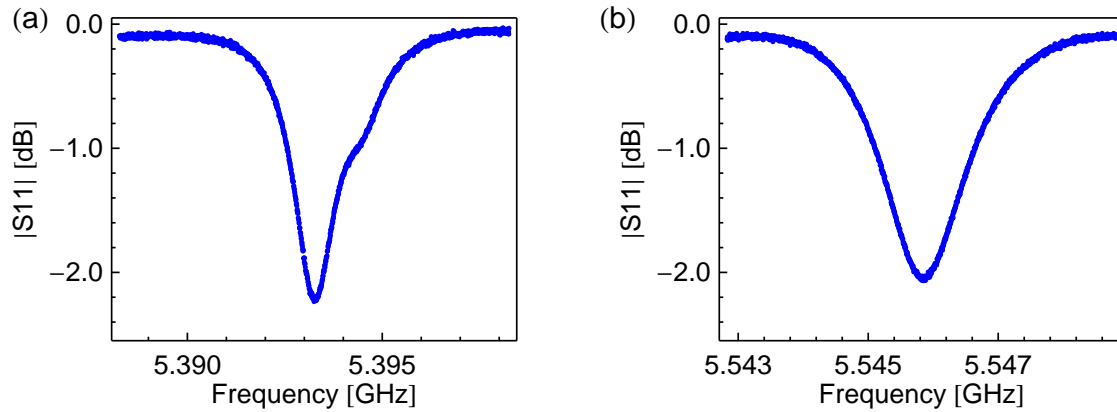
Figure 5.18: Reflection spectra of device C66 (a) without bonds and (b) with bonds.

RF Characterization of a Clean Break-Junction

By controllably electromigrating a clean break-junction, we implement a variable load, which allows for a complete characterization of a stub tuning circuit. We demonstrate the changing microwave properties of the impedance transformer as the load is increased and show that the measured response is well described by an equivalent electric circuit.

The device presented in the following was designed for a matched load of G_0 at 6 GHz and was measured using the dipstick setup described in Section 4.5. Before starting the migration, a reference spectrum was taken at a break-junction resistance of 15.6 Ω and used to calibrate the subsequent data by extracting a background and removing it from the measurements as described in Section 2.3.8. The break-junction was then migrated using the fixed resistance window feedback method (see Section 2.2.2). At a number of resistances, the bias was reduced to 10 mV, a value at which no migration occurs, and a microwave reflection spectrum of the device was taken using a vector network analyzer.

A set of reflection spectra taken at different DC resistances R_{BJ} of the break-junction is shown in Fig. 5.19. As expected, the matching circuit is out of resonance at low R_{BJ} reflecting most of the incoming wave, with a resonance forming as R_{BJ} increases. Furthermore, the minimum reflection coefficient decreases as the matched load is approached. At 12 kΩ, the maximum possible load for a continuous wire, a bandwidth of 45.2 MHz is extracted.

Three parameters characterize a stub tuner, the loss factor α and the electrical lengths d and l. Parasitic inductances and capacitances can be modeled as a change in electric length and can therefore be included in d and l (see Section 2.3.6). We fit d,l and α to the spectrum with the largest insertion loss (gray points and black line in Fig. 5.19), using equations (2.62) and (2.33) with $Z_{BJ} = R_{BJ}$. For all remaining
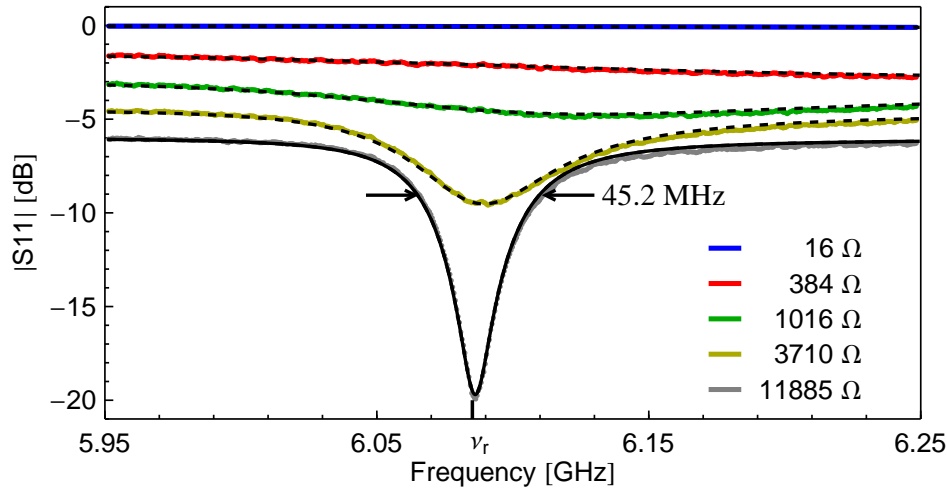
Figure 5.19: Reflectance spectra $|S_{11}|$ taken at different resistances of the break junc-
tion, the spectra are offset by 1.5 dB each for better visibility. The fit
extracting the electrical parameters of the circuit is shown by the solid
line, the fits for determining the RF impedance of the break junction
are shown as dashed lines.

measurements at other values of R_{BJ} we determine the RF impedance Z_{BJ} of the break
junction for each measured spectrum from a fit using the obtained set of parameters
(dashed lines).

For the presented device, the electrical lengths were determined to be $l = 5300.8 \pm$
0.2 μm and $d = 4853.4 \pm 0.2$ μm, close to the design values of $l = 5268.4$ μm and $d =$
4852.4 μm. The value of the extracted attenuation constant is $\alpha = 0.050$ 1/m, which
is within a factor of 2 of $\alpha = 0.023$ 1/m, determined from an independent resonator
measurement. The deviation in electric lengths between the design and extracted values
is partly due to the influence of the parasitic elements and partly due to the calibration
routine, which does not account for impedance mismatches in the experimental setup.
We can further use the extracted lengths to determine the device matched load and
resonance frequency, 29.3 kΩ at 6.085 GHz, as well as a bandwidth of 37.5 MHz on
resonance. Although the extracted electrical lengths are close to the expected values,
the extracted matched load differs significantly from the design matched load of G_0
due to the difference between the design and actual transmission line parameters ($\alpha =$
0.05, $\beta_0 = 50.84$ instead of $\alpha = 0.02$, $\beta_0 = 51$).

The calculated responses and measured data show good agreement as shown in
Fig. 5.19, both in case of the parameter extraction fit (solid line) and for the RF
impedance Z_{BJ} extraction fits(dashed lines). Furthermore, as shown in Fig. 5.20(a),
the reflection coefficient (blue points) on resonance shows good agreement with the

expected values calculated using the extracted parameters (dashed line).
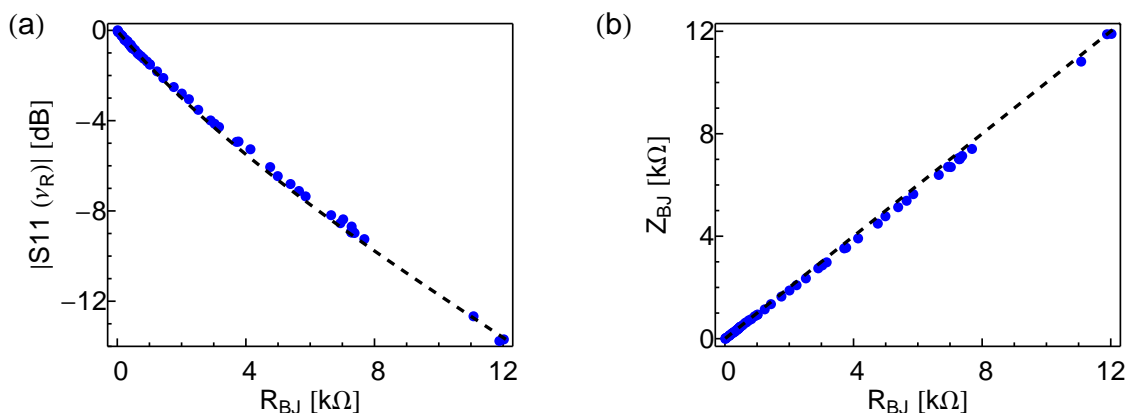
Figure 5.20: (a) The measured reflection coefficient (blue dots) versus the measured DC resistance R_{BJ} at ν_{r}=6.085 GHz, the dashed line indicates the expected behavior. (b) The extracted RF impedance Z_{BJ} plotted versus the measured DC resistance R_{BJ}, where the dashed line indicates $Z_{\mathrm{BJ}} = R_{\mathrm{BJ}}$

By plotting the fitted RF impedance Z_{BJ} against the measured DC resistance R_{BJ}, as done in Fig. 5.20(b), the validity of the model describing the tuner characteristics can be further tested. As expected for a metal junction with a linear $I - V$ curve, the RF impedance and the DC resistance show good quantitative agreement, the small deviations in the 4 kΩ to 8 kΩ range is attributed to the inaccuracies in the calibration. This type of measurement can be extended to allow for both the quantitative comparison between the low frequency and RF properties of nano-scale object devices as well as for time-resolved measurements of changes in the RF properties on a 10-100 ns timescale.

RF Measurements of Molecular Devices

Once the electric lengths of a stub tuner are known we can proceed to characterize the RF properties of single-molecule devices using equation (2.62). We expect the RF measurement to be similar to a lock-in measurement, which leads to a correspondence between the RF admittance and the DOS of the device under investigation. Differences are expected to arise from a different coupling, as coupling capacitances as small as attofarad significantly modify the total admittance at GHz frequencies. In addition, we may expect to see capacitive or inductive shifts due to quantum effects [Prêtre96, Gabelli06, Wang07, Frey12]. As a step toward understanding RF measurements of molecular devices, the measurement results of a NbTiN stub tuner with

a molecular junction are presented in the following.

The presented device, S63 06 04, was designed for a matched load of 3 kΩ at 5 GHz and was fabricated using NbTiN coplanar waveguides. In analogy to the previously discussed device, a background spectrum was extracted from an RF sweep with a closed break-junction and subsequently removed from the following datasets. The device was measured in the Arctic cryostat using the heterodyne measurement setup presented in Section 4.3.

We again observe the formation of a resonance with increasing load in the spectrum, plotted in Fig. 5.21(a) for several values of R_{BJ}. As a consequence of the applied calibration method, the reflection coefficient is larger than 0 dB for loads above 1 kΩ and frequencies larger than 5.1 GHz, see also Section 2.3.8. This limits the accuracy of the extracted parameters obtained from a fit (black dashed line) to the spectrum with the largest insertion loss (yellow points). We therefore also observe a deviation between the expected and measured reflection coefficient as a function of R_{BJ}, shown in Fig. 5.21(b).
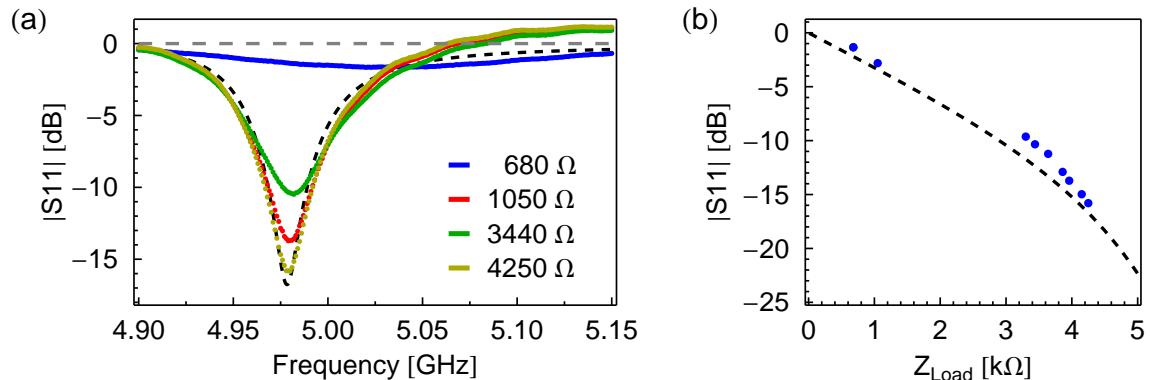
Figure 5.21: (a) Reflectance spectra taken at different break-junction resistances. The fit extracting the tuner parameters is indicated by the dashed line. (b) The measured reflection coefficient (blue dots) versus R_{BJ}, at f = 4.979 GHz, as well as the expected behavior (dashed line).

In contrast to the sample discussed in Section 5.3.3, non-linear $I - V$ curves were measured at resistances smaller than 12.9 kΩ, which is most likely due to transport through remaining residue from the chip fabrication. To explore the RF characteristics of such a non-linear response, we apply a train of square DC pulses with varying amplitude using the Keithley Source-Measure Unit, while simultaneously measuring the reflection coefficient at resonance with a 1 μs time resolution. The pulse train is an arbitrary pattern consisting of a linear increase in pulse amplitude, followed by a $1/n$ decay and is shown in Fig. 5.22(a). During each pulse, we also measure the current

through the device, allowing for the extraction of an $I - V$ curve, shown in Fig. 5.22(b) and showing a significant non-linearity.
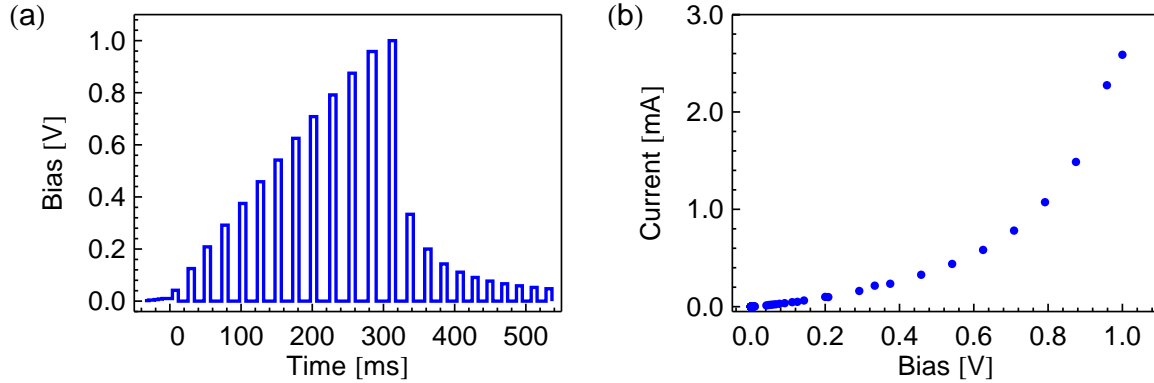
Figure 5.22: (a) Voltage pulse pattern as a function of time. (b) Measured $I - V$ characteristics.

We combined the data to plot the amplitude and phase of the reflection coefficient as a function of bias, as shown in Fig. 5.23. Here, the amplitude of the reflection coefficient is observed to decrease for increasing bias (a), while the phase increases (b). Comparing the RF response to the numerically extracted differential conductance shown in Fig. 5.24(a), we see that the reflection coefficient decreases for increasing differential conductance, while the phase increases with increasing differential conductance. Since we expect Z_{BJ} to be different from R_{BJ} for a molecular junction, this behavior can be explained either by a value Z_{BJ} larger than the matched load, which decreases for increasing bias, or a value of Z_{BJ} smaller than the matched load, which increases with bias. The two cases can be distinguished using an absolute value of the phase, which was not available in the performed measurement.

In the following, we assume that the RF impedance decreases with increasing bias, similar to the DC behavior, and extract Z_{BJ} from the measured points. We further add a shunt capacitance to the break-junction in the electrical model, as sketched in Fig. 5.24(b), as the observed phase shift is larger than expected for a real-valued load. The resulting data is shown in Fig. 5.24(c) and (d). The admittance shows a similar dependence on the bias as the differential conductance. In contrast, the extracted capacitance displays a similar behavior only up to a bias of 800 mV, after which it decreases again. Furthermore, for subsequent points measured on the downward sweep, the extracted capacitance is 20 aF larger than on the upward sweep. To a small degree, this hysteresis is mirrored in differential conductance and admittance data. As the electric field gradients at 1 V bias are large (1 GV/m), the observed changes are most likely caused by a physical change in the molecular junction, which has also been observed in other measurements, leading to a change in capacitance and conductance. At this
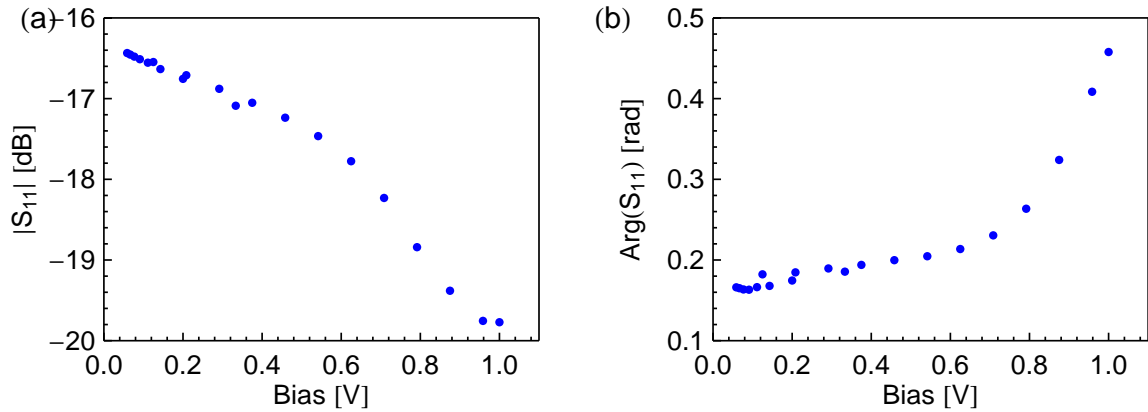
Figure 5.23: The measured (a) magnitude and (b) phase of the reflection coefficient versus bias.

point, the complete lack of knowledge about the molecules in the gap, the error introduced by the background calibration and the uncertainty in the parameter extraction fit preclude quantitative statements about the RF impedance and shunt capacitance. Nevertheless, the presented analysis demonstrates the feasibility of determining the RF impedance of single-molecule devices at frequencies in the GHz range.

5.3.4 Impedance Transformers with Single Carbon Nanotubes

Investigations of the RF properties of break-junction based single nano-scale object devices are impeded by two main issues, the low device yield and the uncertainty about the object in the gap. Single-walled carbon-nanotubes, in contrast, offer the advantage of deterministic device fabrication with a known object, as the electrodes can be fabricated independently and the tube of μm length integrated in the last fabrication step. In the following, DC, low-frequency and RF properties of a single single-walled CNT device are presented.

We first fabricate the required electrodes for an RF CNT device on an impedance transformer with an design matched load of 160 kΩ at 4.85 GHz and subsequently place a CNT on the chip using the process described in Section 3.2.5. At room-temperature and ambient pressure, we obtain a device resistance of 440 kΩ, which increased to 1 MΩ in vacuum, most likely due to the desorption of foreign molecules on the CNT or at the contacts, as adsorbed molecules at the contact interface can significantly alter the contact resistance [Javey03].

After cooling to 3 K, the $I - V$ characteristics were measured, showing a small gap on the order of 20 meV, see Fig. 5.25(a). We further simultaneously measure the
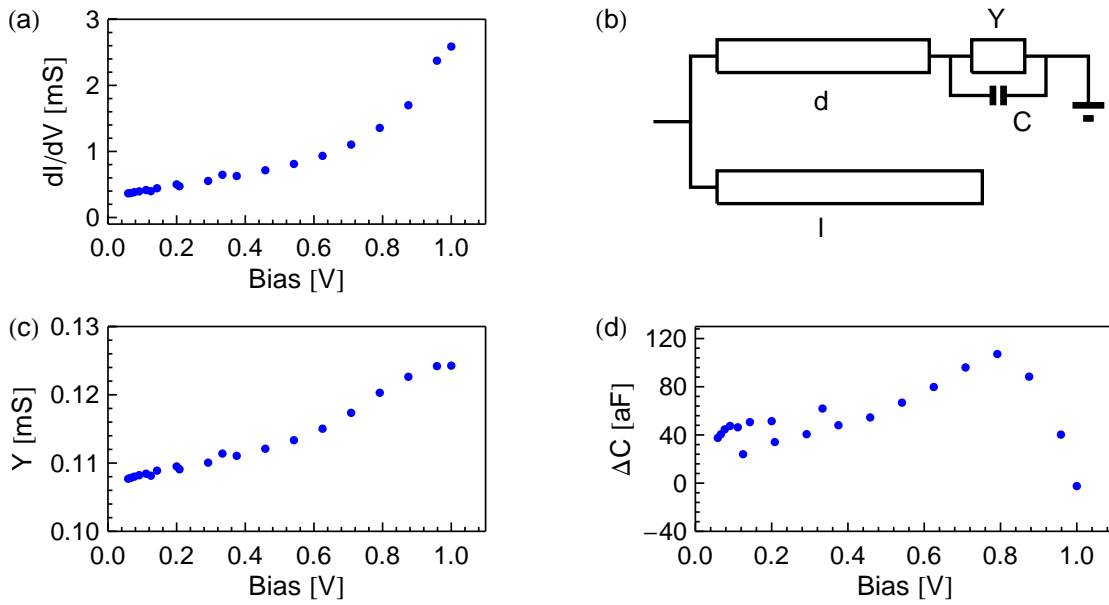
Figure 5.24: (a) dI/dV versus bias, extracted from the DC measurement. (b) Equivalent circuit model. (c) Admittance and (d) capacitance change versus bias.

dI/dV curve using a 2 mV, 71.23 Hz sinusoidal excitation, shown in Fig. 5.25(b). From the fact that the diameter distribution of the CNT growth process is less than 0.3 nm [Durrer09] and that it is optimized for 2 nm diameter CNTs, we conclude that the tube is metallic, with a small bandgap opened by strain or twist [Biercuk08]. The suspension length of the CNT, approximated from post measurement SEM image and scanning photo-current microscopy, is 2.7 μm, which, in an SET configuration, should lead to a charging energy of 1.8-8 meV [Ilani10]. Nevertheless, we did not observe an SET-like behavior in this device. Furthermore, it was not possible to observe changes in the $I-V$ characteristics by applying a gate voltage, most likely due to a broken gate line.

To investigate the RF impedance of the CNT, reflection spectra were additionally measured for each bias point in the presented $I-V$/dI/dV sweep, several such spectra are plotted in Fig. 5.26(a). We observe both a change in the insertion loss and in the resonance frequency. The data was calibrated by removing a constant background, which, for the presented 3 MHz bandwidth device, does not introduce visible errors. The background is obtained by heating the cryostat to 5 K, shifting the resonance by several line widths due to the kinetic inductance of the superconductor.

We extract the parameters d, l and α from the zero bias reflection spectrum (dashed lines in Fig. 5.26), which indicate a matched load of 420 kΩ. These parameters are then
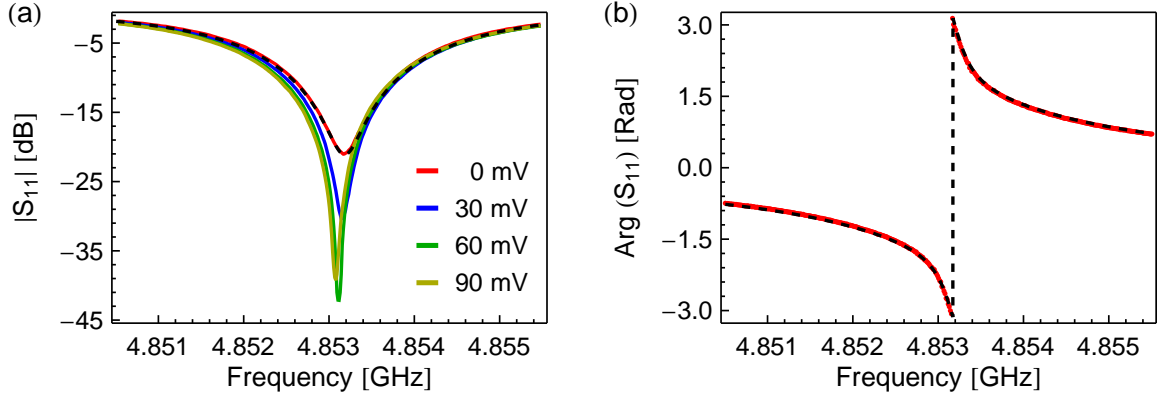
Figure 5.25: (a) $I-V$ curve of the CNT device. (b) $\mathrm{d}I/\mathrm{d}V$ curve, measured at 71.23 Hz with an excitation amplitude of 2 mV.
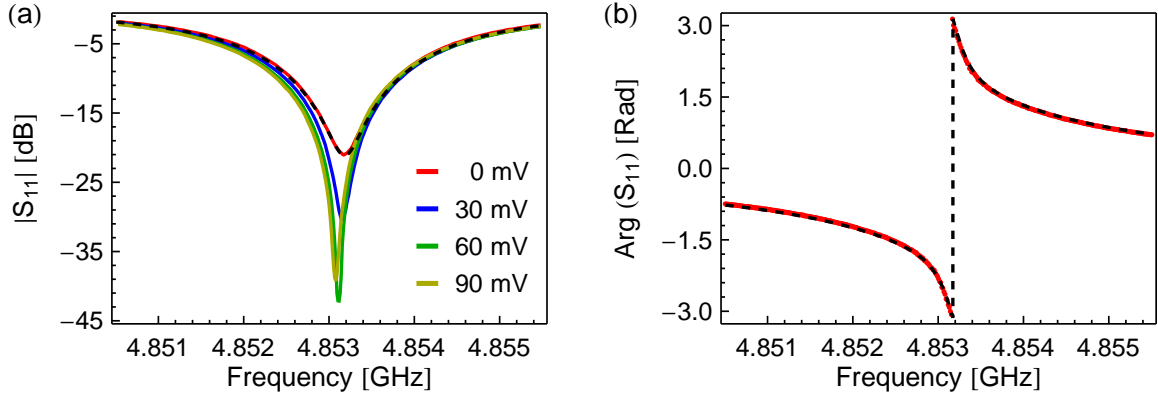
Figure 5.26: (a) Reflection spectra taken at different biases. (b) Phase spectrum at 0 mV bias. The dashed line indicates the parameter extraction fit.

used to determine the real valued admittance and shunt capacitance C of the device, similar to the molecular junction device, the equivalent electric circuit model is shown in Fig. 5.24(b). In this model, the shunt capacitance accounts for the frequency shifts observed in the spectra. The resulting values are plotted in Fig. 5.27. As the DOS in a metallic tube does not drop to zero, as indicated by the $\mathrm{d}I/\mathrm{d}V$ measurement, and $R_{\mathrm{CNT}} \neq Z_{\mathrm{CNT}}$, the extracted value of α has an error on the order of 1%, resulting in a 10% uncertainty for the extracted admittance and capacitance.

The extracted admittance is close to an order of magnitude larger than the low-frequency differential conductance. This increase can be explained by the Schottky barriers at the nanotube/electrode interface [Svensson11], which can be modeled as a parallel combination of a resistor R_{S} and capacitor C_{S}. We investigate the RF impedance of a CNT contacted by two Schottky barriers in a separate qualitative
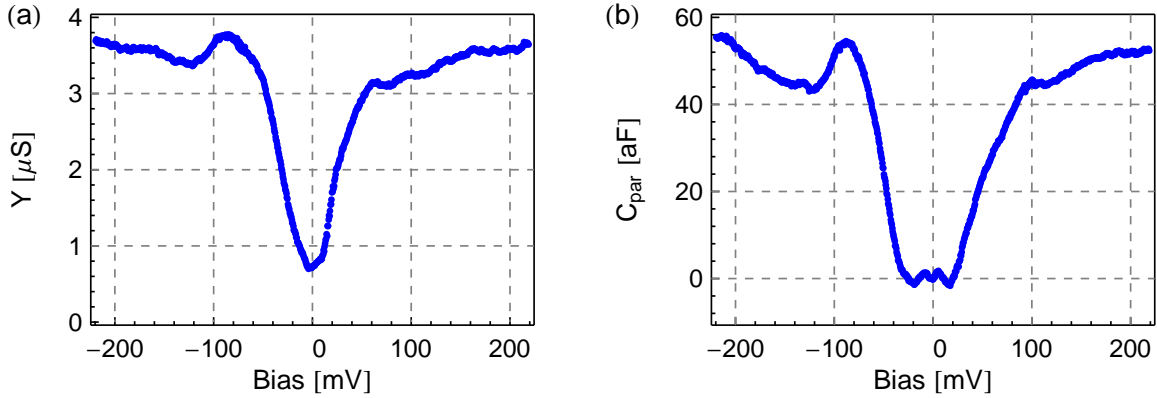
Figure 5.27: (a) Admittance and (b) capacitance of the CNT device as a function of applied bias, extracted from measured reflectance spectra taken at each bias point.

model, schematically shown in Fig. 5.28(a), a similar model was used to characterize single CNT devices in Ref. [Nougaret10]. For simplicity, we remove the shunt capacitance C shown in Fig. 5.24. The CNT itself is expected to have an impedance Z_{CNT} in the range of 6 kΩ to 15 kΩ. Assuming that the observed DC resistance of 2.5 MΩ at 200 mV is due to the resistors, a value of $R_S = 1.2$ MΩ is chosen. We further choose a value of 70 aF for each capacitor, and subsequently calculate the admittance as a function of frequency, the result is shown in Fig. 5.28(a). Using this simple model, we obtain an increase in the device admittance from DC to 5 GHz similar to the observed difference in the measured admittance at 71.23 Hz and 4.85 GHz. We conclude that the observed admittance at GHz frequencies significantly depends on the shunt capacitance of the contact barriers. Note that this model was not used to extract any parameters from a measurement.

We now turn our attention to the observed shift in resonance frequency at different biases. This shift is accounted for by a shunt capacitance C, as shown in Fig. 5.24(b), which is simultaneously extracted from the reflection spectra together with the RF impedance. The total capacitance of the device consists of a geometric part C_{geom}, which is bias independent and compensated for in the in extracted lengths of the stub tuner. A second contribution is due to the finite DOS in the CNT or other nanoscale object, which requires additional energy for rearranging the electron distribution to minimize the electrostatic energy and leads to an additional capacitance C_q, the so called quantum capacitance [Luryi88], which is proportional to the DOS [Ilani06]. We attribute the observed change in the device capacitance as a function of bias, plotted in Fig. 5.27(b), to this quantum capacitance C_q. A comparison with previous investigations of the quantum capacitance in semi-conducting CNTs [Ilani06] yields
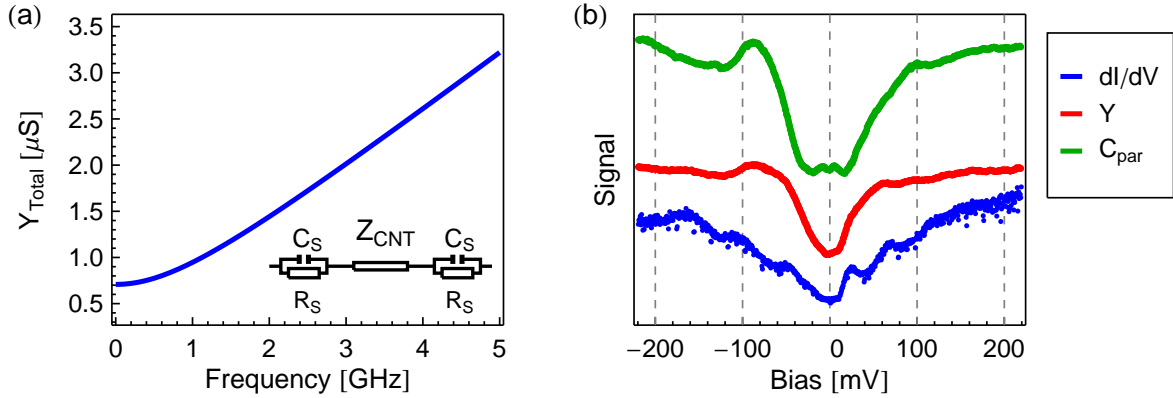
Figure 5.28: (a) The admittance of the equivalent circuit show in the inset as a function of frequency, the used values are $R_{\mathrm{S}} = 1.2$ MΩ, $C_{\mathrm{S}} = 70$ aF and $R_{\mathrm{CNT}} = 12$ kΩ. (b) The low frequency differential conductance, the RF admittance and the extracted capacitance as a function of bias.

similar values when taking the quasi-metallic behavior into account.

In principle, the low-frequency differential conductance, the RF admittance and the quantum capacitance should show the same type of behavior, as they are all related to the DOS. To qualitatively compare these three quantities, they are plotted without units in the same graph as a function bias voltage in Fig. 5.28(b). Two main differences in the behavior are visible, one is that the region of low admittance is smaller than the region of small capacitance, the other that the differential conductance shows several staircase-like steps not present in the RF measurements. To explain these differences, the dependence of each measurement on the different device parameters will be examined. The stray capacitance is expected to only depend on the DOS, being independent of the carrier type [Ilani06]. In contrast, the RF admittance is sensitive to changes in the capacitances associated with the Schottky barriers, while the differential conductance is dependent on the resistances associated with these barriers. Both of these measurements are expected to show only a weak dependence on the DOS due to the large contact barriers. In combination with the finite DOS in the gap, we therefore expect the RF admittance to mirror the step-like response of the barrier capacitance to the increase in bias [Tseng10], explaining the observed behavior. The differential conductance depends on the tunnel barrier formed by the Schottky contact [Svensson11], with only a weak dependence on the DOS. This explains the different response of dI/dV to a change in bias. Our model, however, does not explain the step like features observed in the dI/dV curve.

The presented results show a number of interesting features to explore in future experiments. In particular, a working gate in combination with a semi-conducting CNT

would greatly facilitate issues such as background calibration and parameter extraction, allowing for the exploration of the RF properties of CNTs, a subject of great interest, but where comparatively little research has been performed. By realizing a CNT SET, the coupling capacitances can be extracted from Coloumb diamond measurements, enabling a more precise characterization of the RF impedance. A further research direction are time-resolved measurements of the mechanical motion, as transport and vibrations are coupled in nanotubes [Steele09, Lassagne09], which should allow ring-down measurements of CNT-based mechanical resonators.

5.4 Optical measurements

The versatility of the implemented measurement setup allows for a number of different optical measurements to be performed, ranging from simple imaging, over fluorescence detection to microwave mode-mapping [Gross94, Zhuravel06, Hoffmann10] and photo-current measurements. In this section, the results of photo-current measurements on bare break-junctions, molecular devices and CNT devices are presented.

5.4.1 Confocal Microscope Properties

The most basic application of a confocal microscope (CFM) is imaging. By scanning the objective over the sample and measuring the intensity of the reflected light at each point, a reflection image can be assembled. The scanning is necessary, as a CFM only provides information about the point in focus. In the presented setup, two types of scanning modes are possible, a step scanning mode utilizing the coarse stepping positioners and a fine scanning mode using the scanning stage. In step scanning mode, a feedback loop ensures that a minimum increment in position has been achieved before acquiring a new point, allowing for scans up to 5 x 5 mm^2 with a smallest increment of 1 μm. An example reflection image of a chip with bondwires acquired in step scaning mode is shown in Fig. 5.29(a). Images with finer resolution can be obtained by utilizing the piezo scanning stage, allowing for a maximal range of 40 x 40 μm^6 at 3 K. The electronic design of the controller maps a 16 bit resolution to the scan range, allowing for sub-nm scan steps. An example scan image is shown in Fig. 5.29(b), where three break-junctions with leads are visible, as well as the number of the site "1" (horizontal arrow0, and two alignment marks, one indicated by the vertical arrow.

One of the principal advantages of using a CFM setup is that the sample is illuminated only at a single point, enabling an investigation of the spatial dependence of a photo-effect. A primary characteristic of the microscope is the spot-size, defined as
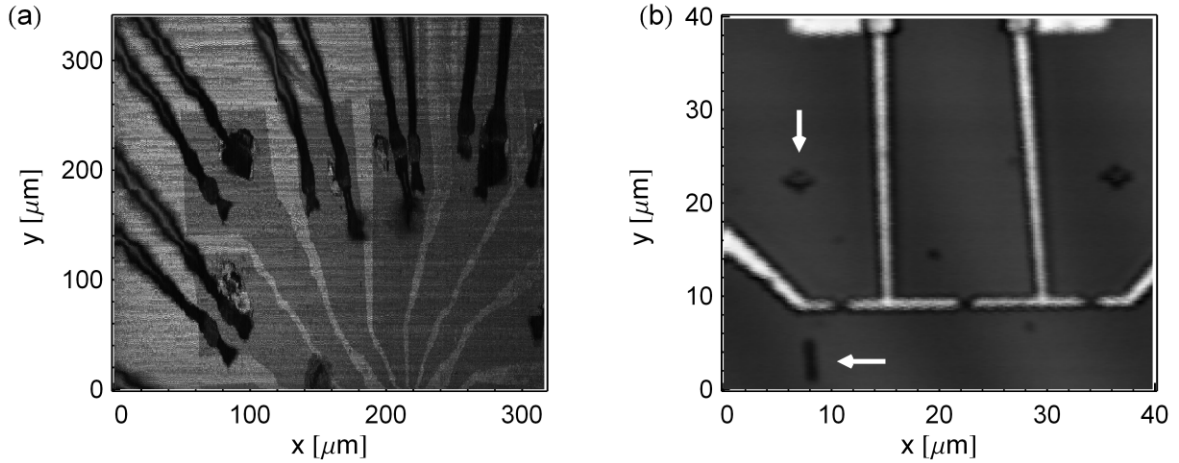
Figure 5.29: (a) Large area step scan of a sample. (b) CFM scan of a break-junction, the horizontal arrow indicates the junction numbering "1", the vertical one an alignment mark.

the full-width half-maximum of the gaussian spatial intensity distribution [Hogele08]. We extract the spotsize d by measuring the spatial dependence of the reflection signal when scanning over an object with sharp edges, for example the coplanar waveguide used in the impedance transformers. This dependence is given by the convolution of a gaussian intensity distribution with two step edges due to the non-vertical sidewalls of the utilized sample:

$$\Gamma(x) = a_1 \left(1 + Erf \left(\frac{x - x_0}{d} \right) \right) + a_2 \left(1 - Erf \left(\frac{x - x_0 + w}{d} \right) \right)$$

where a_1 and a_2 are complex numbers due to the coherent illumination, x_0 is the position of the step and w is the width of the non vertical sidewall. A fit of a linescan was performed for all three available wavelengths, the results are plotted in Fig. 5.30.

Spotsizes within 10 % of the diffraction limit $d_{dl} = \lambda/(2\ NA)$ are obtained using the specified NA of 0.6. The actual spotsize may be 10 % larger, as the reflected light also passes through the objective, enhancing the resolution. A further decrease in the spotsize is possible by the use of a solid immersion lens.

The illumination spot of the CFM is not only well confined in the $x - y$ plane, but also in the z direction, also leading to a gaussian intensity profile when scanning the z axis. An example measurement is shown in Fig. 5.31(a). The focus of the objective is observed at a z value of 4.2 μm with two additional peaks close to 8 μm and 10 μm. The latter are likely part of the Airy pattern formed by the tight focus of the beam. The observed higher frequency oscillations are due to the formation of a cavity between the fiber and sample [Hogele08], showing a period of $\lambda/2$. These periods can be used
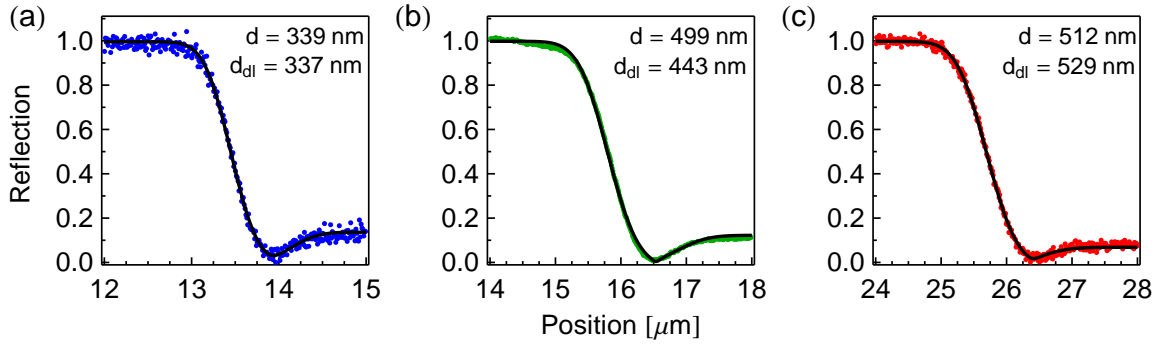
Figure 5.30: Line scans of a transmission line gap and extracted spotsize d using (a) 405 nm (b) 532 nm and (c) 635 nm light.
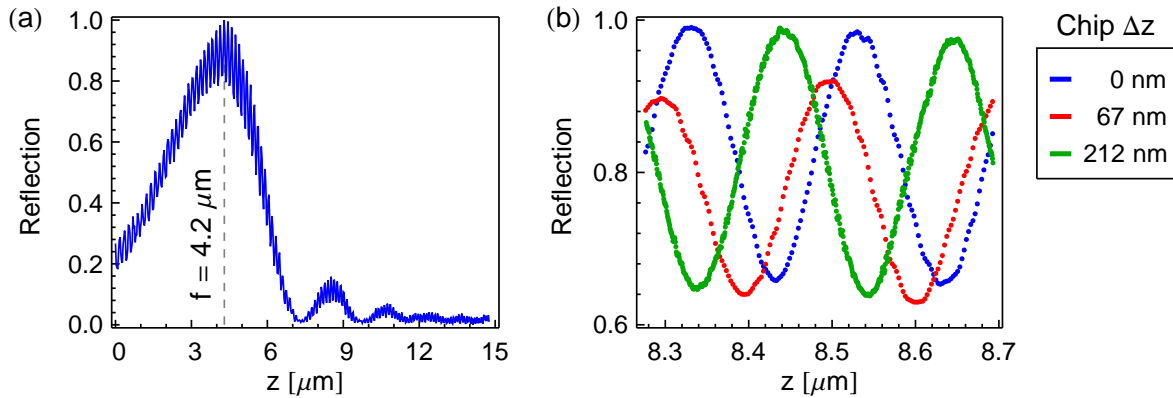
Figure 5.31: (a) z axis scan of the objective. (b) z-axis scans with different chip displacement Δz.

to determine the z-position of the chip with regard to the microscope housing when bending the chip in the MCBJ setup. This is demonstrated in Fig. 5.31, where three focus scans are shown, an initial scan (red), a scan after two steps of the stepper motor (blue) and a scan after six steps of the step motor (green). The extracted change in chip position corresponds to the expected values of 66 nm and 198 nm, the reduced amplitude for the second scan is due to drift in the optical setup. For large scans, the small focal depth of the objective can be an issue, requiring tilt compensation.

5.4.2 Photo-Induced Conductivity Changes in a Gold APC

On the path toward photo-current spectroscopy of single nano-scale object device, the optical response generated by the electrodes needs to be taken into account. Experiments on Raman spectroscopy of molecules in break-junctions [Ward07, Ward08] and photo-assisted tunneling in nanometer-sized gaps [Ward10], have indicated that

break-junctions can act as plasmon "antennas", which can create field enhancements in the gap up to a factor of 1000. Furthermore, illumination of APCs in break-junction-experiments has indicated a photo-induced enhancement of the conductivity [Guhr07,Ittah09], which can be explored in the presented setup, with the advantage of a high-resolution microscope operating at low temperatures.

In the following experiments, the laser amplitude is modulated sinusoidally with frequency on the order of 200 Hz and scanned over the sample. The target break-junction is voltage biased at 10 mV to 40 mV and the resulting current is measured using an $I-V$ converter, allowing for a simultaneous measurement of the junction resistance and the photo-current, extracted from a lock-in measurement at the modulation frequency of the laser. Furthermore, a reflection image is generated, allowing for a spatial correlation between the measured signal and device position. This results in four values per pixel, the reflection, the current, as well as amplitude and phase of the photo-current from the lock-in measurement.

We present measurements of two devices, each measured using a different wavelength. In case of Site #04l Chip #180, the 532 nm laser was used, modulated at 227.23 Hz with a maximum amplitude of 180 μW, while the junction was biased at 40 mV. The resulting data is shown in Fig. 5.32, where the outline of the device, taken from the EBL design, is matched to the reflection image. Due to its sub-wavelength dimensions, the break-junction cannot be resolved in the optical image. During the measurement, the conductance of the device changed by 0.002 G_0, which is shown in the conductance map in (b), the jump coincides with a scan close to the junction. This jump did not influence the photo-current amplitude (c) or phase (d). As expected, the photo-current is centered on the break-junction within the accuracy of determining the actual position. The added ring-like structures map out an Airy pattern indicating a well focused spot and sensitive measurement. The phase shows a shift of π as expected for a conductance enhancement in combination with an inverting amplifier.

Even though the signal is located at the expected point and shows the expected enhancement of the conductance, it is unclear whether the change in conductance is due to photo-assisted transport or due to thermal expansion. To address this issue, the same measurement should be repeated using blue light, where a photo-suppression of the conductance is expected, see also Section 2.1.4. Unfortunately, this was not performed in the presented devices, which where measured using either green or blue light.

We measured Site #14l of the same chip but with a different layout using blue 405 nm light. The resulting data is plotted in Fig. 5.33 and was acquired using a bias of 10 mV and a maximum laser intensity of 1.1 mW. Several differences to the measurement using 532 nm light are visible. The photo current signal is now located on the electrodes
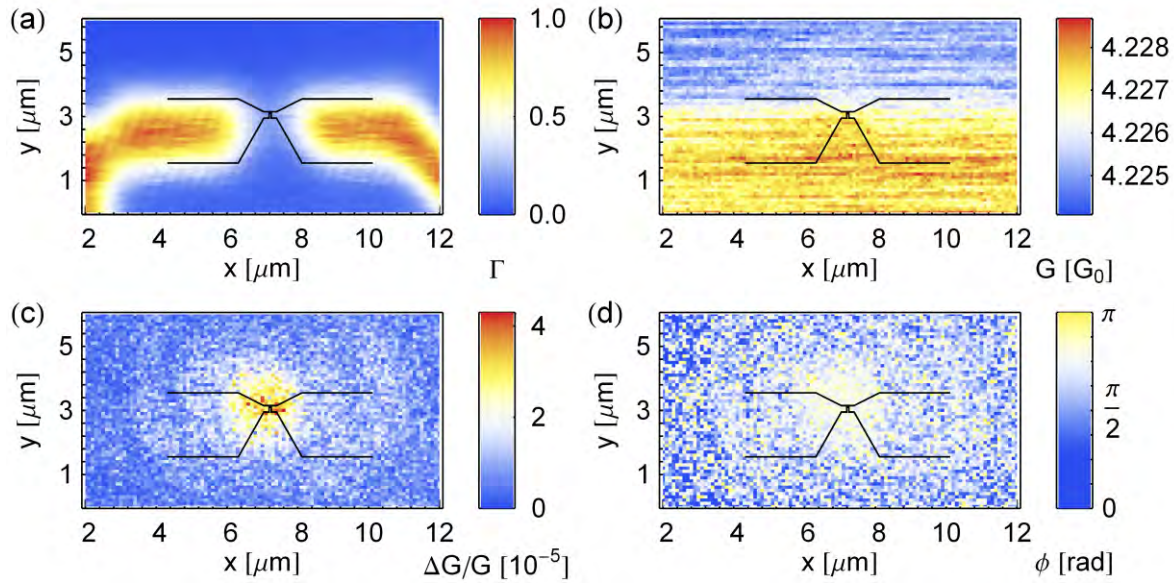
Figure 5.32: Measurement of Site #04l, Chip 1#80: (a) Reflection, (b) conductance (c) photo-current amplitude and (d) phase as a function of position.

themselves, instead of centered at the break-junction, both for amplitude and phase. Furthermore, the phase changes by π across the junction. The most likely explanation for the observed behavior is an asymmetrically formed break-junction, where the APC is situated at the left side of the bridge. In this case, heating dominates the signal on the right electrode, corresponding to a π phase shift, as the bridge expands. In contrast, the small mechanical lever on the right side leads to a signal dominated by photo suppression, indicated by a phase shift of zero.

Further investigations are clearly necessary to prove conclusively that the measured changes in conductance are not due to thermal expansion. Apart from characterizing the wavelength dependence, time-resolved measurements using laser-pluses should allow for a clearer picture. Moreover, APCs can be utilized to investigate the field enhancement caused by plasmon resonances.

5.4.3 Wavelength-dependent Photo Current in a Molecular Device

When illuminating a single-molecule device with different wavelengths, we expect to observe a different photo current, dependent on the type of molecule used. In the following, we present such a wavelength-dependent photo-current measurement of a molecular device.
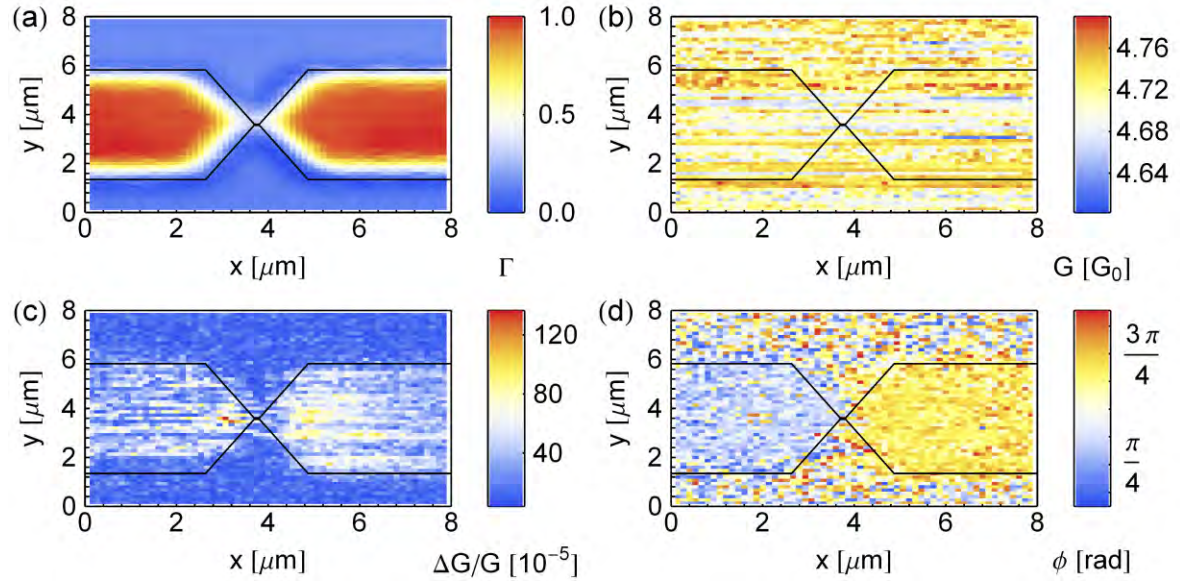
Figure 5.33: Measurement of Site #14l, Chip #180: (a) Reflection, (b) conductance (c) photo-current amplitude and (d) phase as a function of position.

We investigated one device (site #03 l) formed on the previously discussed chip #210 (Section 5.2.1), which was treated with C_{60} molecules. The resulting molecular device was weakly coupled, but did not show signs of Coulomb blockade. Position dependent photo-current measurements were performed at 405 nm, 532 nm and 635 nm laser wavelengths, sinusoidally modulated with a frequency of 272.35 Hz, using an illumination intensity of 1 μW, 2 μW and 10 μW respectively. These different values correspond to constant optical heating power, compensating for the wavelength dependence of the reflectivity of gold (36% at 405 nm, 70% at 535 nm, 95% at 635 nm). In case of 635 nm, the value represents the maximum power available instead of the required 30 μW. We applied a voltage bias of 40 mV (405 nm and 532 nm) and 50 mV (635 nm) to the device, the increase in bias for red was chosen to allow for a better signal-to-noise ratio.

The resulting data is shown in Fig. 5.34, where a reflection image is shown in (a) and the detected photo-currents are shown in (b) to (d) for 405 nm, 532 nm and 635 nm respectively. The plots show a clear photo-induced signal at 532 nm, which is not present when using either the blue or the red laser. Due to the fact that no signal was detected using blue light even though a similar amount of heat was generated, we deduct that the observed signal indeed originates from a laser-induced transport process. The different pixel sizes are due to the required shift in focus for each wavelength, the increased noise level for the red and blue wavelengths due to an increased sensitivity of the lock-in amplifier.
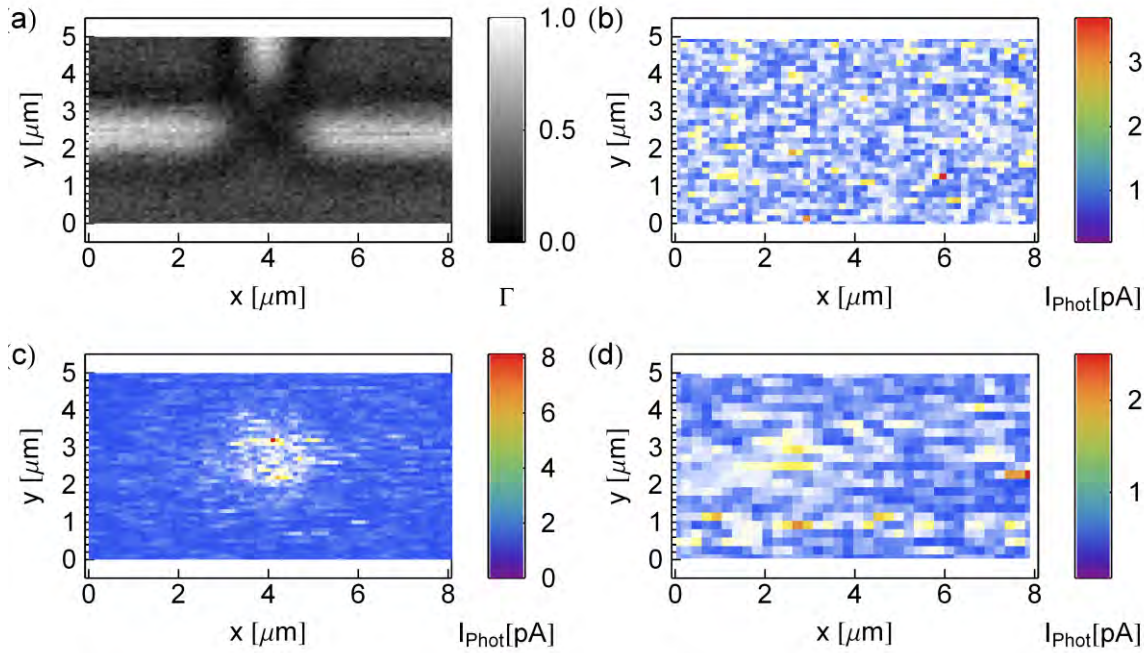
Figure 5.34: Photo-current measurements of a molecular device (site #03l, chip #210). (a) Reflection image and photo-current for (b) 405 nm, (c) 532 nm and (d) 635 nm laser light.

The observed wavelength dependence can have two origins: one is the probing of the molecular DOS at different levels in a photo-assisted tunneling picture, the second a difference in the field enhancement. FEM simulations for a one nanometer gap state a field enhancement of 6 for 405 nm light, 7-8 for 532 nm light and 30 for 635 nm light [García-Martín11]. This implies that the DOS plays a larger role in the photo current wavelength dependence than resonant field enhancement effects, although experimental investigations are necessary to validate the simulations.

To further investigate the optical response of the molecular device, the photo-current was measured as a function of bias and applied laser intensity at 532 nm, the results are plotted in Fig. 5.35. Panel (a) shows a negligible response of the numerically calculated $\mathrm{d}I/\mathrm{d}V$ curve to the applied laser intensity, indicating that the applied laser does not cause significant conformational changes in the device. The measured photo-current at different laser intensities is plotted versus bias in panel (b), showing an increasing photo-current for increasing bias, the absolute value of the photo current is about 0.3% of the total current.

For molecules with weak conductance variations at the voltage scale of $\hbar\omega/e$, where ω is the frequency of the applied optical field, the photo-current is expected to be proportional to $\mathrm{d}I^2/\mathrm{d}V^2$ [Arielly11, Ward10]. We do not expect this relation to hold
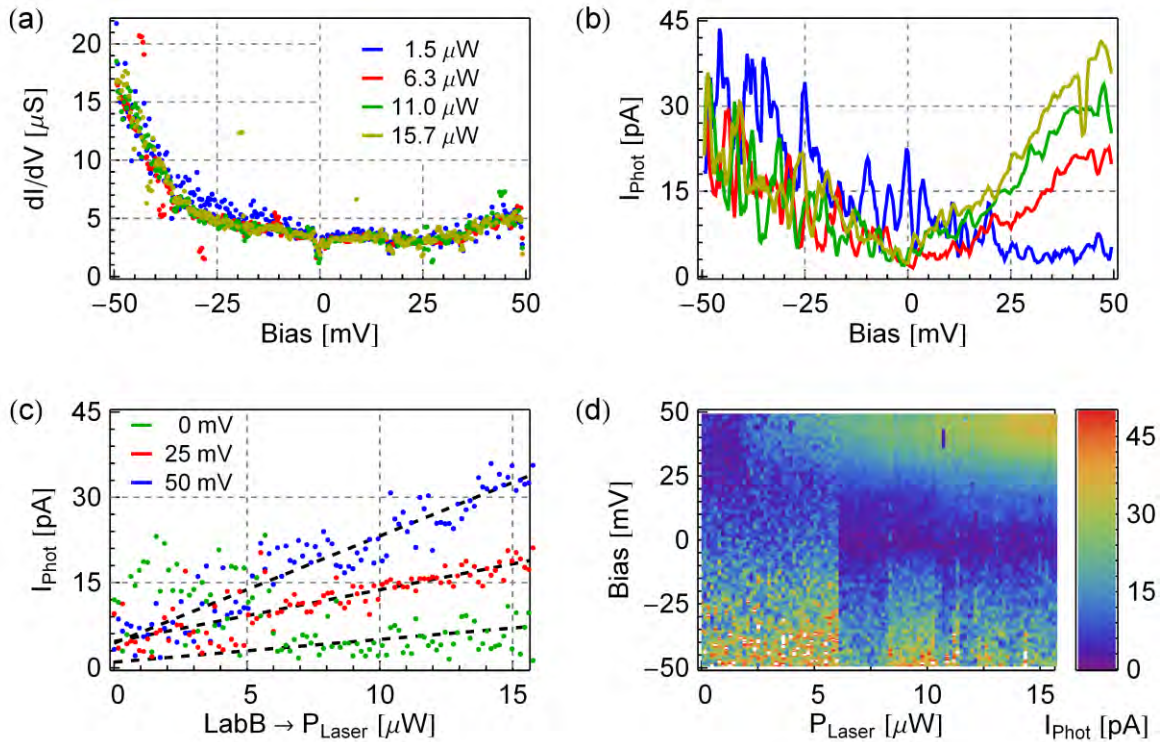
Figure 5.35: Photo-current measurements of a molecular device (site 03l, chip 210). (a) dI/dV versus bias and (b) I_{Phot} versus bias at different intensities. (c) I_{Phot} versus laser intensity at different biases. (d) I_{Phot} versus bias and laser intensity.

for our device due to the large changes in the DOS in C_{60} in the voltage range of 2 to 3 V [Lu03]. We indeed observe a photo current that is not proportional to dI^2/dV^2, for example being smaller at negative bias, although the non-linearity is larger.

We additionally measured the photo-current as a function of power, plotted in Fig. 5.35(c) for different biases, exhibiting a linear behavior (dashed lines), as expected for small applied powers. The density plot of I_{Phot} versus both intensity and bias reveals several configuration changes, indicating a non-stable device. A quantitative analysis was not performed due to the uncertainty about the number and type of molecules forming the device and further research on the expected behavior is necessary for future experiments. This experiment nonetheless demonstrates the viability of wavelength and intensity dependent measurements on nano-scale object devices.

5.4.4 Photo-Current Microscopy of a Carbon Nanotube

The localization of the photo-current by scanning the laser spot over the sample, also called scanning photo-current microscopy (SPCM), can also be used to investigate the spatial extent of a CNT and, given a suitable device, the localization of, for example, a $p - n$ junction formed in the tube [Buchs11]. It is also a useful tool to localize the object of interest for optical measurements.

In case of the CNT sample investigated in Section 5.3.4, we utilize SPCM to localize the CNT on the electrodes. Similar to photo-response measurements of APCs, the CNT device was biased with a voltage of 5 mV, while the laser, sinusoidally modulated at 66 Hz with a peak amplitude of 900 nW, was scanned across the sample.

The resulting reflection and photo-current images can be superimposed to facilitate the localization of the object of interest, as shown in Fig. 5.36(a). The position of the nanotube is clearly indicated by the photocurrent. For comparison, we also present an SEM image taken after the measurement, shown in Fig. 5.36(b), where one remaining part of the CNT is indicated by the white arrow. The position of the nanotube extracted from the photo current measurement corresponds to the position indicated by the SEM image. We explain the large extent of the signal compared to the spot size by a shifted focus and reflections of the laser light on the metal electrodes.
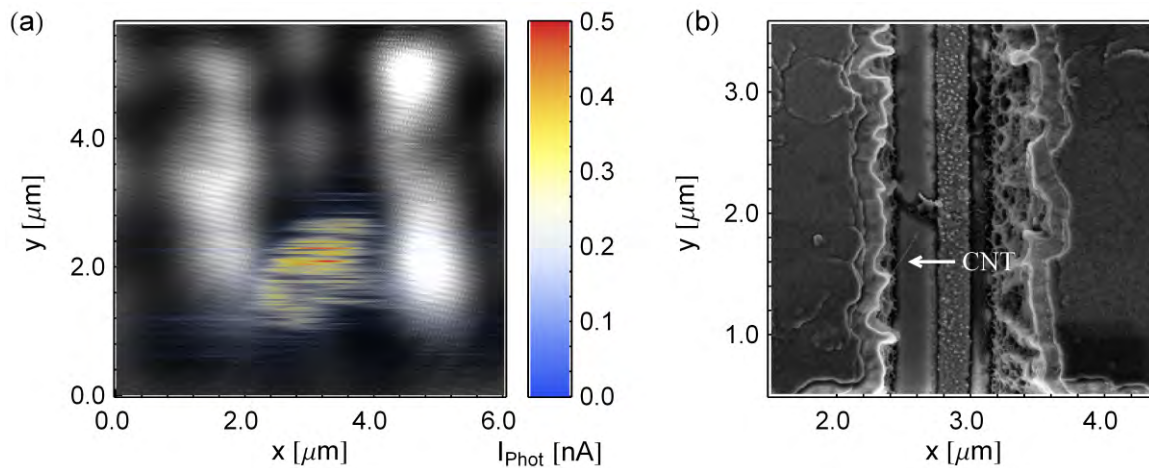
Figure 5.36: (a) SPCM scan of a CNT device, the photo-current is superimposed in color on the gray-scale reflection image. (b) Post-measurement SEM image of the same device, the remaining part of the CNT is indicated by the arrow.
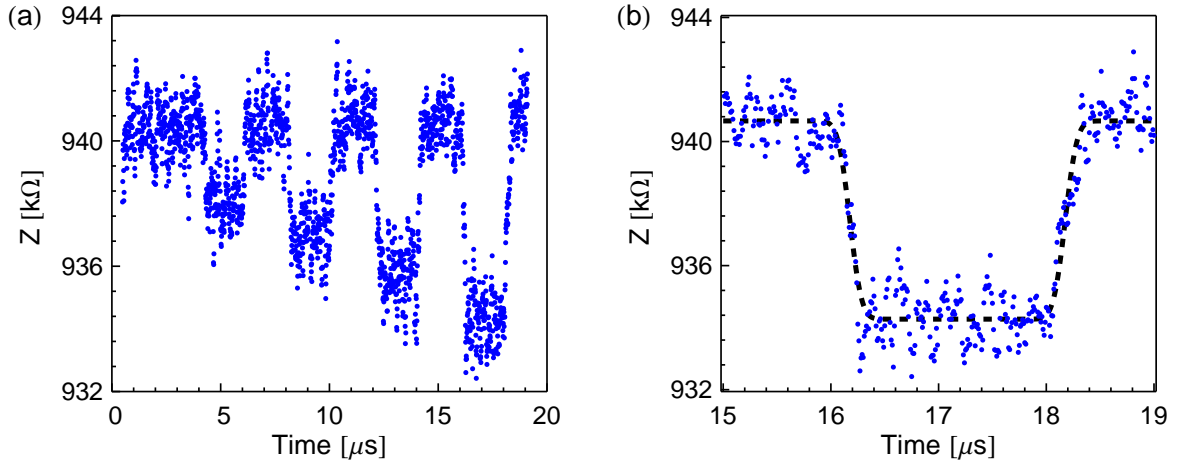
Figure 5.37: Time-resolved measurements of the photo-induced impedance change in a CNT device. (a) The entire pattern. (b) A zoom in on the last laser pulse, the determined rise time is 214 ns.

5.4.5 Time-Resolved Photo-Current in a Carbon Nanotube

In a final experiment, the developed optical and RF techniques are combined to perform time-resolved photo-response measurements on a singe CNT. In a first step we center the objective over the CNT, localized by SPCM, and set the bias to 0 mV. We then utilize an arbitrary waveform generator directly connected to the AOM to create a pulse sequence of four 2 μs long pulses with rising amplitudes of 1.5 μW to 2.1 μW in steps of 0.2 μW. Using the trigger scheme explained in Section 4.3.2, the RF reflection coefficient is measured at a single frequency (4.8305 GHz) during the duration of the pulse sequence with a time-resolution of 10 ns and an input power at the tuner of -80 dBm. To obtain a good signal-to-noise ratio at these low powers, we average 25 million times. The corresponding impedance response is then extracted using parameters calculated from a frequency sweep at 0 mV bias prior to the measurement. The resulting data is plotted in Fig. 5.37, panel (a) shows the response to the entire sequence, while panel (b) shows only the last pulse. The four laser pulses can be clearly resolved in the impedance response of the stub matching circuit, even at the low measurement power used for the RF measurement and using a room-temperature amplifier. We find a rise-time of $t_{rise} = 218$ ns for the impedance change, extracted from the response to the largest pulse. The expected rise time is a combination of the stub tuner rise time $tr_{st} = 163$ ns, extracted from the measured bandwidth of 2.14 MHz, and the rise time of the laser pulse $tr_{ls} = 150$ ns. We therefore expect a total rise time [Engelberg04] of $tr_{tot} = \sqrt{t_{st}^2 + t_{ls}^2} = 221$ ns, in agreement with the measured rise time.

The presented measurement demonstrates the feasibility of achieving a time-resolution

limited by the matching circuit in case of repeatable measurements, with a signal-to-noise ratio dependent on the amount of averaging. In this measurement, the time-resolution is limited by the circuit bandwidth and the laser pulse-rise-time. Using a better coupled CNT and corresponding circuit as well as a pulsed laser, a response time of 10 ns can be implemented in this type of setup. We expect to apply this type of measurement to the time-resolved investigation of the photo-response in APCs and single molecule devices, and to extend the stimulus from laser pulses to DC and RF pulses using the gate line.

6 Conclusion and Outlook

Two significant steps in the investigation of transport in single nano-scale object devices were presented in this thesis. One is the development of transmission line based impedance matching circuits with integrated break-junctions. These circuits enable both a determination of the RF impedance of such devices as well as time-resolved measurements with a resolution on the 10 to 100 ns scale and were demonstrated both using break-junctions and a single carbon nanotube device. The second was the implementation of a cryogenic setup combining a fiber-based confocal microscope with the circuitry for both DC and RF based transport measurements. Utilizing this setup, the wavelength-dependence of the photo-current in a molecule device was demonstrated, opening the path toward photo current spectroscopy. We further demonstrated that these two measurement techniques can be combined to enable low-power optical measurements with high signal-to-noise ratio, allowing for time-resolved measurements of photo-induced processes.

A number of technical developments were necessary to achieve these result such as the process development for the required micro- and nanofabricated samples and the design and implementation of a dedicated cryostat, combining an MCBJ setup with RF components and a confocal microscope. To enable investigations of three-terminal break-junction-based devices, we first developed an optimized electron beam lithography process which yields break-junctions with a cross-section of 20 x 20 nm^2 and allows for side gates within 30 to 40 nm of the break-junction. A second process was then developed integrating these break-junctions into transmission line based impedance transformers while maintaining mechanical control of the electrode spacing.

We further implemented a custom designed optical/RF cryogenic setup to investigate these samples, featuring a vibrationally decoupled pulse-tube cooler. It achieves a base-temperature of 2.9 K and a cooldown time to 4 K of less than 8 hours. The optical investigations are enabled by a fiber-based confocal microscope at base temperature, offering close to diffraction limited performance over the 400-700 nm wavelength range and a 5 x 5 mm^2 field of view.

Devices based on single or few molecules and single colloidal dot devices, created by electromigrating break-junctions, were first demonstrated in DC transport type measurements. The breaking process was investigated in both a two- and a four-point

measurement topology and we presented an algorithm capable of controllably electro-migrating a break-junction with a wiring/lead resistance of several 100 Ω. The presented devices are based on C_{60} molecules and 5 nm CdSe nanocrystals and our results are comparable to previous work. In case of the nanocrystals, the device resistance is reduced from typically 100 MΩ to the 100 kΩ range by use of benzene-edithiol as a linker molecule, allowing for future RF reflectometry measurements on nanocrystal devices.

The good control over the electromigration process was then utilized to investigate superconducting impedance matching circuits, first with clean break-junctions, where the break-junction is used as a variable load. Here we attain good agreement between the measured microwave reflection spectra and an equivalent electrical circuit. This approach was subsequently extended to a molecular junction and a carbon nanotube device. We extracted the RF impedance of the device from measured spectra, which, in case of the carbon nanotube, is reduced by a factor of five compared to the DC resistance and can be explained by a model based on Schottky barriers. A further effect we observe is a shift in the device capacitance on the order of 10-100 aF, which we attributed to the quantum capacitance.

In a further set of experiments, we explored the influence of light on transport in nano-scale object devices. Using clean break-junctions, gold atomic point contacts were formed and illuminated with both blue and green light, showing a qualitative difference in the observed photo-induced conductance enhancement between the two wavelengths. We then perform a similar experiment on a molecular junction most likely consisting of C_{60} molecules, where a strong wavelength dependence is observed: a photo current was only measured for green but not for blue nor for red illumination. Finally, we validated the time-resolution of our measurement setup by detecting the photo-induced change in the RF impedance of a single CNT device. By measuring a pulse sequence with a 10 ns time resolution, we extracted a rise time consistent with the combination of the device and optical pulse bandwidth.

In summary, a measurement setup was implemented which allows for a large range of optical and RF measurements when utilizing the developed RF circuits and fabrication processes. A number of characterization experiments have proven the basic concepts, which can now be applied to a set of interesting problems, discussed in the following.

So far, the RF properties of single molecule-devices have not been investigated, but which will have a significant relevance for actual devices. The presented methods allow a systematic study of these properties for different molecules and can also be applied to investigate the RF properties of single nanocrystal devices. In case of single carbon nanotube devices, a small number of investigations have been performed, in which case the presented measurement techniques can improve on and extend existing

measurements. Furthermore, the presented time-resolved measurement technique can be applied to investigate carbon nanotube based mechanical resonators, for example enabling ring-down measurements.

The implemented impedance transformers may also be utilized to investigate nuclear spins in molecules [Grose08, Vincent12], a possible resource for quantum computing, in which the nuclear spin is read out via the electrical characteristics of the molecule. The gain in time-resolution may enable fast read-out with better a signal-to-noise ratio, a significant step toward the coherent control of such a nuclear spin.

A third area now accessible is the investigation of photo-induced transport in APCs and single molecule/colloidal quantum dot devices. Due to photo-assisted tunneling, it may be possible to probe energy levels in molecular devices beyond the range of the bias voltage, which allows for both an identification of the molecule in the gap and further investigations of the energy-level structure of such devices. Additionally, the combination of optical excitation with the large bandwidth of the RF devices enables low optical power investigations, circumventing conductance changes caused by thermal expansion and allowing for time-resolved measurements.

As the formation of a single molecule devices typically requires several break-junctions to be broken, future measurements would profit from an increased number of RF devices per cooldown run. This could be attained by moving to different topology, where a number of impedance transformers are capacitively coupled and frequency multiplexed, similar to frequency-multiplexed resonators in cQED experiments [Jerger11]. This will also enable the use of a single low-noise HEMT amplifier for all devices, significantly reducing the noise temperature of the system and allowing for investigations at the 10 photon level, which may be even further improved by the introduction of a parametric amplifier.

Last, the setup would profit from a tunable laser source [Toptica] in combination with a chromatically corrected objective, allowing for photo current spectroscopy. This would allow for an accurate characterization of the field enhancement observed in nanogaps as well photo-induced transport in single-molecule devices.

A Fabrication Recipes

A.1 Substrates

Depending on the intended measurement, either silicon or sapphire substrates are used. Both are available as two inch wafers, with a typical substrate thickness of 275 μm for the silicon substrates and 500 μm for sapphire, although other thicknesses can be utilized. The silicon wafers are purchased with a layer of thermal oxide, ranging in thickness between 50 nm and 300 nm, depending on availability. Sapphire wafers are bought c-cut with one side polished and for RF devices are commercially coated with niobium or niobium-titanium-nitride.

A.2 DC Devices

Fabrication of DC break junctions requires two fabrication steps, one using optical lithography and one using electron beam lithography. Two fabrication processes have been developed, one for silicon substrates and one for sapphire.
In case of silicon, the sacrificial layer of silicon oxide is already deposited by the vendor. For sapphire substrates, the sacrificial layer is deposited using PECVD. Furthermore, the isolating properties of sapphire require a shorting layer to avoid ESD destruction of the break-junctions during fabrication, which is etched away in the release step. A flow chart of the fabrication is shown in Fig. A.1.

A.2.1 Sapphire wafer preparation

The silicon oxide deposited using PECVD on sapphire wafers is not as wet etch resistant as the thermal oxide grown on the silicon oxide. The etch resistance can be increased by O_2 plasma ashing after deposition, which also reduces chemical reactions between the unsaturated oxide and titanium shorting layer.
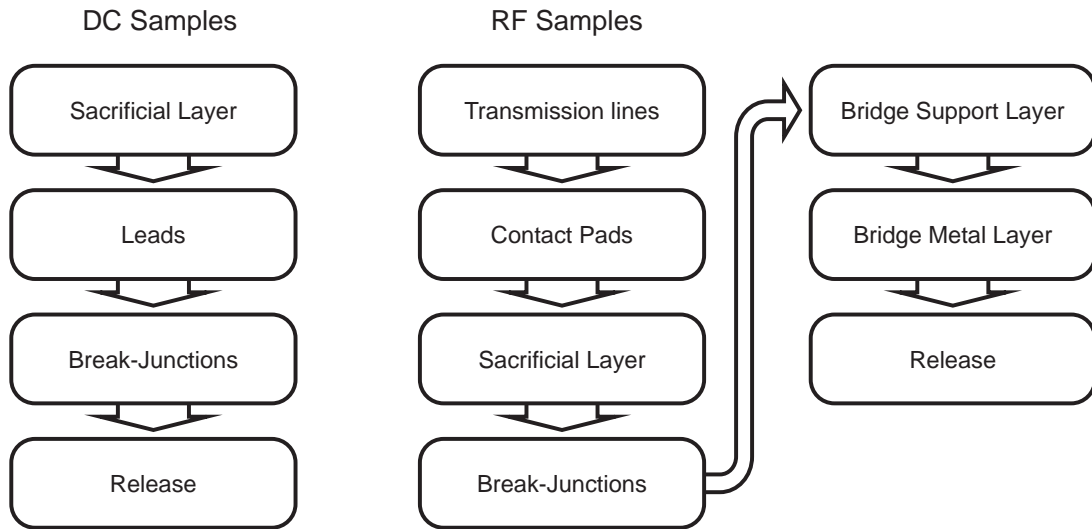
Figure A.1: Fabrication flow chart for DC and RF samples.

Silicon Oxide Sacrificial Layer and Titanium Shorting Layer Process		
Process Step	Description	Comments
Silicon Oxide deposition	Place sample in PECD	
	Precondition 10 minutes with standard program	Can be skipped if machine has not been used that day
	Deposition: 120 s (25 nm/min)	Program 'Puebla SiOx 120'
Oxidation	O$_2$ plasma Ash 5 min, 200 W	Plasma Asher
Shorting layer	Load into Plassys	
	Deposit 7 nm Titanium	Rate: 0.1 nm/s

A.2.2 Photolithography

LOR5B/AZ1505 Positive Resist Process for Lift-off		
Process Step	Description	Comments
Wafer cleaning	Sonicate in Acetone for 120 s at power 1 in 40 kHz in ultrasonic bath	Preferrably at 50°
	Sonicate in Isopropanol for 120 s at power 1 in 40 kHz in ultrasonic bath	Preferrably at 50°
	Blow dry with nitrogen	
IPA bake out	Bake wafer for 30 s at 100° C	
	Let wafer cool for 120 s	
Resist spinning and softbake	Spin LOR5B resist: ramp 6 s , 6000 rpm for 45 s	Clean pipette, use ≈ 1 mL resist
	Remove edgebead with MIF 726	Best done on chuck
	Remove resist on backside	
	Hardbake at 200° C for 300 s	
	Spin AZ1505 resist: Ramp 6 s, 6000 rpm for 45 s	Clean pipette, use ≈ 1 mL resist
	Remove edgebead/resist on backside with Acetone	
	Softbake at 100° C for 60 s	

LOR5B/AZ1505 Positive Resist Process for Lift-off		
Process Step	Description	Comments
UV Exposure using Karl Suss MA 6	Warm up mask aligner	Wait at least 20 minutes to stabilize
	Measure UV intensity at 405 nm	Usually between 8 and 12 mW/cm^2
	Load Program 1 (VAC)	Check if Multiple Exposure is activated
	Calculate time for 110 mJ/cm^2 dose	
	Load Mask	Remove possible dust with nitrogen gun
	Load wafer	Remove possible dust with nitrogen gun
	Align wafer flat to cut pattern	Minimizes broken chips during dicing
	Align wafer	Check critical structures for dust particles
	Expose	
	Clean mask in mask cleaner	
Development	Devolop in MIF 726 for 17 s	Time very critical.
	Check undercut in microscope Should be ≈ 1 μm	≈ 200 nm/s undercut rate using MIF 726
	Stop developer in water for 30 s	Use flowing water
	Blow dry with nitrogen	

A.2.3 Metal Deposition

Electrode Deposition and Lift-off		
Process Step	Description	Comments
Descum	O$_2$ plasma Ash 100 W, 30 s	Plasma Asher
Deposition	Load into Plassys MEB550S	
	Ar-ion etch 3 minutes, 15° tilt, 20°/s rotation	Use recipe
	5 nm Ti, 8° tilt, 20°/s rotation	not necessary for sapphire wafers
	50 nm Au, 7° tilt, 20°/s rotation	
Lift-off	Acetone $\approx$ 1 hour	Best at 50°, help with pipette
	Remove LOR with DMSO or MIF 726	TMAH (MIF 726) will attack aluminium

A.2.4 Electron Beam Lithography

PMMA 50K/950K EBL Process for Lift-off		
Process Step	Description	Comments
Wafer cleaning	O$_2$ plasma 200 W, 120 s	Plasma Asher
Resist spinning and softbake	Spin PMMA 50K CB: ramp 5 s, 5000 rpm for 60 s Bake at 180° C for 180 s Spin PMMA 950K 1:1 EL: ramp 5 s, 5000 rpm for 60 s Bake at 180° C for 180 s	Clean pipette, use $\approx$ 1 mL resist Postcool 60 s Clean pipette, use $\approx$ 1 mL resist
Charging Layer	7 nm Aluminium	Only sapphire wafers without shorting layer
EBL (Raith Two)	Load into machine Setup: 30 kV, 10 μm aperture, 150 μm write field, 3.5 nm raster, doses: 300 μC/cm^2, 300 μC/cm, UV, focal plane, write field adjustment Start exposure, $\approx$ 3.5 hours per wafer Unload	 Check design and position list, DF: 2.5/4.2 Use fully automatic exposure Check that first marker is found

PMMA 50K/950K EBL Process for Lift-off		
Process Step	Description	Comments
Development	Place IPA and MIBK:IPA 1:3 in ice-bath	Requires 20 minutes to stabilize temperature
	Develop 60 s MIBK:IPA 1:3 at 0°	
	Stop 30 s IPA at 0°	
	Blow dry N2 30 s	Avoids moisture
Descum	UV Ozone clean 2 minutes	UVOCS
Deposition	Load into Plassys MEB550S	Cover with aluminium mask
	Ar Ion etch 5 s	Use recipe
	1 nm Ti	not necessary for sapphire wafers
	40-80 nm Au	maximum $\approx$ 100 nm
Lift-off	Acetone $\approx$ 3 hours	Best at 50°

A.2.5 Release

Dry Release Process for Sapphire MCBJ		
Process Step	Description	Comments
RIE Etch	Load into RIE 76 Run Nb etch, 1 minute 20 sccm SF6, 10 sccm Ar 100 W, 130 μBar	Does not require post-cleaning

Wet Release Process for Silicon MCBJ		
Process Step	Description	Comments
Etch	BHF 60 s Rinse DI 30 s	
Clean	Acetone 20 min, 50° DMSO 40 min, 80° Acetone 5 min. IPA 1 min Blow dry N2	Do not use US!
Ash	Load into RIE 76 5 minutes, 100 sccm O_2 100 W, 150 μBar	

A.3 RF Devices

Fabrication of superconducting stub tuners with integrated MCBJs combines the fabrication process of the DC devices with a number of fabrication steps necessary for the microwave device. The process is as follows: transmission line patterning, followed by the deposition of contact pads and sacrificial pads. The break-junctions are then written using EBL, the airbridges are added in a last step before dicing and cleaning.

A.3.1 Niobium Patterning

AZ1505 Positive Resist Process for RIE Etching		
Process Step	Description	Comments
Wafer cleaning	Sonicate in Acetone for 120 s at power 1 in 40 kHz in ultrasonic bath	Preferrably at 50°
	Sonicate in Isopropanol for 120 s at power 1 in 40 kHz in ultrasonic bath	Preferrably at 50°
	Blow dry with nitrogen	
IPA bake out	Bake wafer for 30 s at 100° C	
	Let wafer cool for 120 s	
Resist spinning and softbake	Spin AZ1505 resist: ramp 6 s, 6000 rpm for 45 s	Clean pipette, use ≈ 1 mL resist
	Remove edgebead (acetone)	Best done on chuck
	Remove resist on backside	
	Softbake at 100° C for 60 s	

AZ1505 Positive Resist Process for RIE Etching		
Process Step	Description	Comments
UV Exposure using Karl Süss MA6	Warm up mask aligner	Wait at least 20 minutes to stabilize
	Measure UV intensity at 405 nm	Usually between 8 and 12 mW/cm^2
	Load Program 1 (VAC)	Check if Multiple Exposure is activated
	Calculate time for 110 mJ/cm^2 dose	Exposure dose uncritical
	Load Mask	Remove possible dust with nitrogen gun
	Load wafer	Remove possible dust with nitrogen gun
	Align wafer flat to cut pattern	Minimizes broken chips during dicing
	Align wafer	Check critical structures for dust particles and scratches
	Expose	
	Clean mask in mask cleaner	
Development	Devolop in MIF 726 for 17 s	Time very critical.
	Stop in DI for 30 s	Use flowing water
	Blow dry with nitrogen	

PMMA Positive Resist Process for RIE Etching		
Process Step	**Description**	**Comments**
Wafer cleaning	Sonicate in Acetone for 120 s at power 1 in 40 kHz in ultrasonic bath	Preferrably at 50°
	Sonicate in Isopropanol for 120 s at power 1 in 40 kHz in ultrasonic bath	Preferrably at 50°
	Blow dry with nitrogen	
IPA bake out	Bake wafer for 30 s at 100° C	
	Let wafer cool for 120 s	
Resist spinning and softbake	Spin PMMA 950K Pure in EL: ramp 2 s,2000 rpm for 90 s	Clean pipette, use ≈ 1 mL
	Wait 60 s for uniform layer	Can be judged by color
	Remove edgebead (acetone)	Best done on chuck
	Remove resist on backside	
	Softbake at 180° C for 180 s	
UV Exposure using ABM DUV aligner	Warm up mask aligner	Wait at least 20 minutes to stabilize
	Measure UV intensity at 220 nm	Usually 20 mW/cm^2
	Calculate time for 7.5 J/cm^2 dose	Dose uncritical

PMMA Positive Resist Process for RIE Etching		
Process Step	Description	Comments
	Load Mask	Remove possible dust with nitrogen gun
	Load wafer	Remove possible dust with nitrogen gun
	Perform wafer wedge error compensation	
	Align wafer flat to cut pattern	Minimizes broken chips during dicing
	Align wafer	Check critical structures for dust particles
	Expose	
	Clean mask in mask cleaner	
Development	Devolop in MIBK:IPA 1:1 for 60s	Time uncritical
	Stop developer in IPA for 30 s	
	Blow dry with nitrogen	

Niobium/Niobium-Titanium-Nitride RIE etch process		
Process Step	Description	Comments
Descum	O_2 plasma Ash 100 W, 30 s	Plasma Asher
Etching	Load into RIE 76 Run Nb etching process 20 sccm SF6, 10 sccm Ar 130μBar, 150 W	 60 nm/min Nb 40 nm/min NbTiN
Mask removal	Sonicate in Acetone for 300 s at power 1 in 40 kHz in ultrasonic bath Sonicate in Isopropanol for 120 s at power 1 in 40 kHz in ultrasonic bath Blow dry with nitrogen O_2 plasma Ash 200 W, 60 s	Preferrably at 50° Preferrably at 50° Plasma Asher

A.3.2 Contact Pads and Sacrificial Pad

Contact pad deposition process		
Process Step	Description	Comments
Photolithography	Use LOR5B/AZ1505 process A.2.2	
Pad Deposition	Use Deposition recipe A.2.3 180 s Ar Ion etch 1 nm Ti, 30-50 nm Au	

Sacrificial pad deposition process		
Process Step	Description	Comments
Photolithography	Use LOR5B/AZ1505 process A.2.2	$> 2~\mu$m undercut
Pad Deposition	50 nm SiOx, process A.2.1 O_2 plasma 100 W, 30 s 7 nm Ti	Plasma Asher
Lift-off	Acetone $\approx$ 3 hours Remove LOR 5B, DMSO/MIF726	Best at 50°
Post clean	O_2 plasma Ash 200 W, 60 s	Plasma Asher

Break Junctions via EBL		
Process Step	Description	Comments
EBL	Use EBL process A.2.4	

A.3.3 Airbridges

Airbridge process		
Process Step	Description	Comments
Resist spinning and softbake, repeat 3 times	Spin PMMA 950K Pure in EL: ramp 2 s,2000 rpm for 90 s	Clean pipette, use ≈ 1 mL
	Wait 60 s for resist stabilize	Uniformity can be seen by color of wafer
	Remove edgebead (acetone)	Best done on chuck
	Remove resist on backside	
	Softbake at 180° C for 180 s	
UV Exposure using ABM DUV aligner	Warm up mask aligner	Wait at least 20 minutes to stabilize
	Measure UV intensity at 220 nm	Usually 20 mW/cm^2
	Calculate time for 7.5 J/cm^2 dose	
	Load Mask	Remove possible dust with nitrogen gun
	Load wafer	Remove possible dust with nitrogen gun
	Perform wafer wedge error compensation	
	Align wafer to markers	Check with contact vacuum before exposure

Airbridge process		
Process Step	Description	Comments
	Expose Clean mask in mask cleaner	
Development	Devolop in MIBK:IPA 1:1 for 60s Stop developer in IPA for 30 s Blow dry with nitrogen	Time uncritical
Reflow	Bake Wafer at 180° C for 600 s Optical inspection	rounded edges are visible as coloured lines
Resist spinning and softbake	Spin AZ5214E resist: ramp 3 s, 3000 rpm for 45 s Remove edgebead (acetone) Remove resist on backside Softbake at 100° C for 60 s	Clean pipette, use $\approx$ 1 mL resist Best done on chuck
UV Exposure using Karl Süss MA6	Warm up mask aligner Measure UV intensity at 365 nm Load Program 1 (VAC)	Wait at least 20 minutes to stabilize Usually between 4 and 8 mW/cm² Check if Multiple Exposure is activated

Airbridge process		
Process Step	Description	Comments
	Calculate time for 50 mJ/cm^2 dose	Dose uncritical
	Load Mask	Remove possible dust with nitrogen gun
	Load wafer	Remove possible dust with nitrogen gun
	Align wafer to markers	Check with contact vacuum before exposure
	Expose	
	Clean mask in mask cleaner	
Reversal bake	50 s at 117°	Time and temperature are critical
Flood exposure	200 mJ dose at 405 nm	Typically 20-30 s
	Wait 300 s	
Development	Devolop in MIF 726 for 60 s	
	Stop in DI for 30 s	Use flowing water
	Blow dry with nitrogen	

Airbridge process		
Process Step	Description	Comments
Deposition	Load into Plassys MEB550S Ar Ion etch 3 minutes, 15° tilt, 20°/s rotation 20 nm Au, 15° tilt, 20°/s rotation 250 nm Al, 0° tilt, 20°/s rotation 230 nm Ti, 0° tilt, 20°/s rotation 80 nm Au, 15° tilt, 20°/s rotation	Use recipe
Lift-off	Acetone ≈ 1 hour Remove LOR with DMSO/MIF 726	Best at 50°, help with pipette

Dry Release		
Process Step	Description	Comments
Photolithography	Use LOR5B/AZ1505 process A.2.2 Strip AZ1505 with acetone	
Release	Use RIE release process A.2.5	
Clean	Remove LOR 5B with DMSO or MIF726 RIE O_2 plasma 300 s 80 W	

B Airbridge Design

To suppress mode conversion in coplanar waveguides at ground plane discontinuities, an electrical connection between the two ground planes on each side of the center conductor is necessary. This can be achieved by miniature metal bridges over the center conductor, called airbridges. Typical dimensions of these bridges are a length of 20-40μm, a width of 10-20μm and a height of .5-2.5μm.

The fabrication of these bridges requires two photo lithography steps, one step for the support underneath the bridge and a second to define the outline. As the support layer needs to be inert to the second photo lithography step, two different processes are required. In our case the first layer is PMMA patterned with DUV (220 nm) and developed with MIBK/IPA. To achieve the bridge-like vertical profile, the vertical edges of the PMMA layer are rounded off by heating the wafer, causing the PMMA to reflow. The second layer uses AZ5214E reversal bake photo resist, is patterned with UV (365-405 nm) and developed in water-based developer (MIF726).

B.1 General

The process requires the use of two different masks with different polarization as PMMA is a positive resist, AZ5214E a negative one. Each mask requires alignment between mask and substrate, a process which is only possible to a certain degree of precision. A good design should therefore allow misalignment on the order of 1-2 μm.

As the thickness of each resist layer is on the order of 1-1.5μm, the minimum feature size on the metalization mask is several microns, and on the bridge mask more than 5 micron due to reflow.

B.2 Support layer

The length of the bridge is a trade off between the shortest ground plane connection and added parasitic capacitance. This is influenced by the fact that the PMMA layer needs 3-7μm to achieve full height after reflow. Adding 2μm for misalignment yields a minimum of 5-10μm of distance between the end of the waveguide gap and the foot of

the bridge. Note that the maximum bridge length is on the order of 50 μm.

As the bridge support mask is positive, it should have as little clear areas as possible. An optimal mask would only expose the bridge feet, but a small set of windows in uncritical places facilitates alignment. Furthermore, the edges of the chip/wafer should be exposed to remove the edge bead, which allows for better resolution and easier alignment in the next lithography step.

B.3 Metalization layer

The main design considerations governing the length and width of the bridge are mechanical stability, resistance and parasitic capacitance. As the capacitance is typically in the 1-2 fF range it may be necessary to include it length calculations. To ensure good electrical and mechanical contact to the ground plane, a larger bridge foot can be incorporated into the design. This foot should be have the maximum possible distance from the waveguide, as stray capacitance from the foot to the center conductor can introduce further stray capacitance. Furthermore the metalization footprint should fit into the bridge support footprint with ample clearance both for misalignment and reflow. We suggest a minimum border of 2μm for misalignment and additional 3μm to allow for PMMA flow.

The metalization mask has a negative polarization, therefore exposed resist will stay. To minimize the influence of stray light, the mask should have as little clear area as possible, but lift-off is facilitated if the top layer is photo resist. Additionally, the chance of unwanted metalization is minimized with a photo resist top layer. A compromise is a shaded area around critical structures to minimize stray light from the vicinity and a clear field for the rest of the mask.

B.4 Alignment Markers

At each photo lithography step, the chip/wafer and mask need to be precisely aligned. As the desired features seldom overlap in fashion that allows good alignment, separate alignment markers on each mask and the sample itself are necessary. In principle, alignment markers are only necessary between two consecutive steps, but in practice alignment markers between the sample and the metalization mask are necessary. One reason is that the alignment markers in the PMMA layer are severely degraded after reflow, the other is that the misalignment of the PMMA layer can affect the alignment of the metalization mask.

To minimize the impact of bad lithography, alignment markers should always have a

number of redundant copies, ideally placed at different positions of the chip. 5 x 5 arrays at the corners are an example. Placement should be such that these arrays are as far apart as possible to maximize alignment, but far enough from the borders of the chip, that edge removal procedures and stray light do not imperil the markers. Obviously, the markers should not be placed near critical structures of the sample.

As the depth of field on the mask aligner is limited, alignment markers have a certain minimum size. There are several ways to increase alignment precision without having to use more resolution on the mask aligner. One is based on our ability to discriminate symmetry, for example requiring the alignment of a wide line to a thinner line as the middle. Another way is to use overlapping periodic patterns which create a Moire pattern.

Two possible designs are shown in Fig. B.2. The standard design is a thick short cross on top of a longer thinner one, which works very well. The second design incorporates a Moire pattern, but the minimum feature size of 2 μm makes fabrication hard. Additionally, the pattern is too small for good discrimination on a pattern basis.

Note that a "window" around the specific alignment markers used to align the mask itself is necessary if it is a dark field mask. Alignment markers which are patterned in the current layer for successive steps of alignment do not need a window.

B.5 Check list

- Polarization of Masks correct (PMMA positive, AZ5214E negative)?
- No unwanted deposition of metal through "holes" in both resists?
- Are the relative positions correct?
- Are alignment markers between all possible pairs of masks?
- Is there enough clear field around the alignment markers to allow for alignment?
- Is there enough tolerance for misalignment?
- Is PMMA removed in unwanted places (edge bead) with the support mask?
- Can the chip/wafer be moved to the desired position using the limited range of the mask aligner?

B.6 Notes on recipe

The entire fabrication procedure can be performed in a single day. The most critical step is exposure of the AZ5214E, as backscattered light tends to develop the photo resist underneath the mask in the gap areas, leading to resist bridges over the gaps

and subsequent failure of bridge definition. Should bridges be visible during inspection, fabrication failed, the samples should be cleaned very thoroughly, including DUV exposure, and one can start over again.

B.7 Illustration
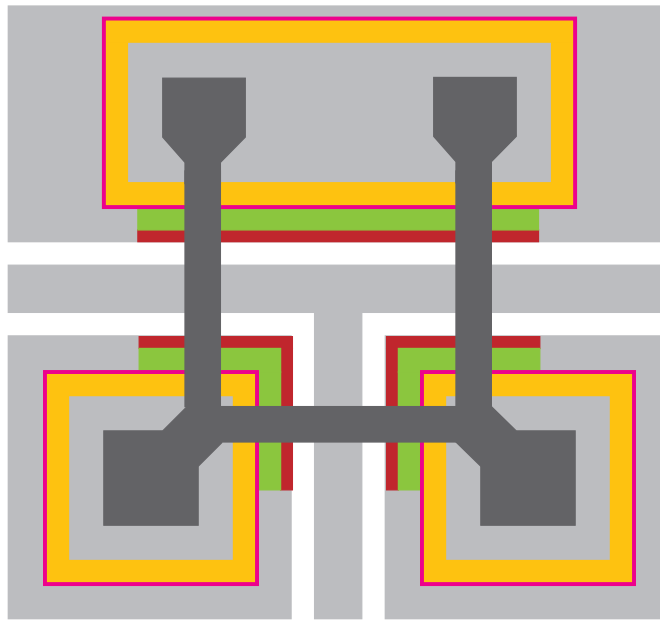
Figure B.1: Sample design of Airbridges for a T-Junction. The T-Junction is a coplanar waveguide (grey). Alignment Tolerance (red), Arc (green) and Reflow Tolerance (yellow) define a minimum distance between the waveguide gap and bridge foot. The bridges (dark grey) have a schematic anchor added, with additional tolerance added. The boxes for the holes in the support layer are pink.
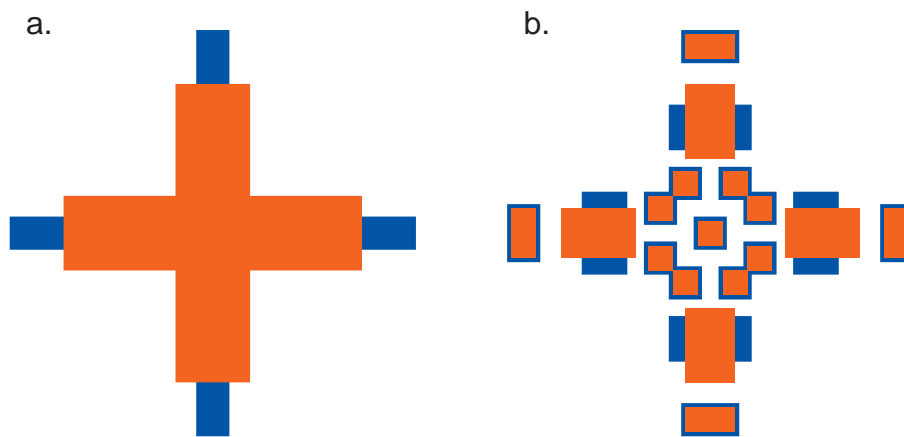
Figure B.2: Possible alignment mark designs. a. Standard thin/thick cross. b. Used design.

C Data Sheets
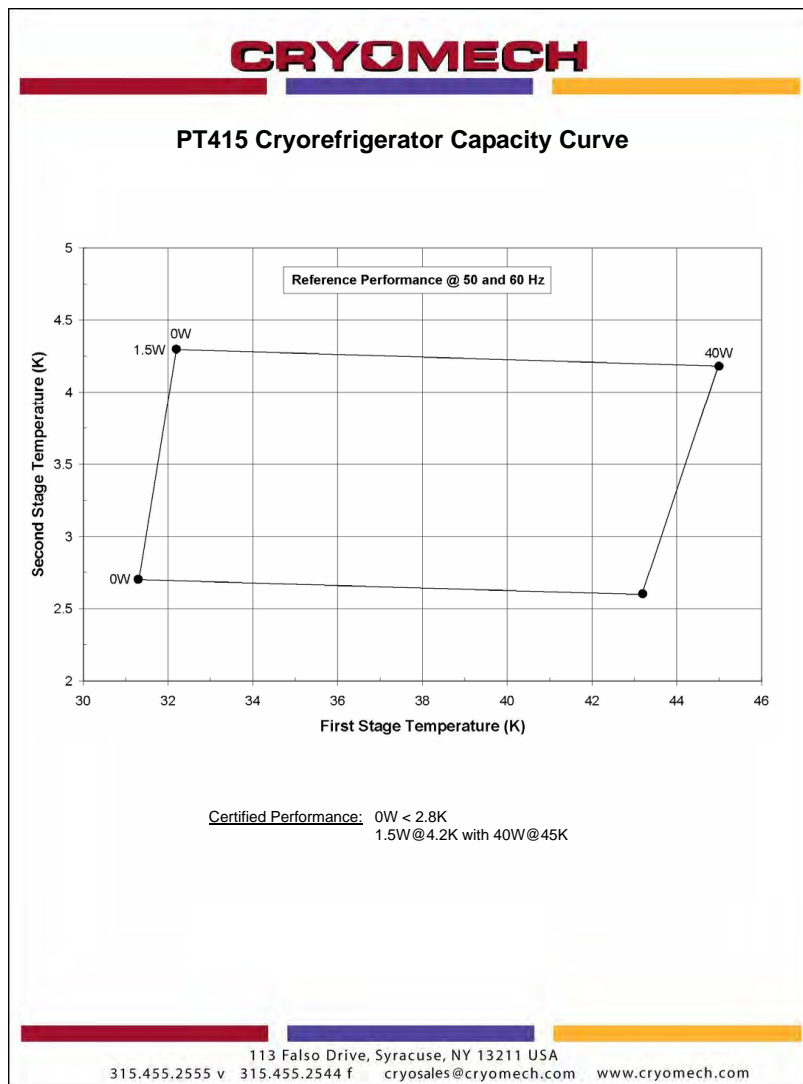
Figure C.1: Capacity curve of the PT 150 pulse tube cooler.

Bibliography

[Agraït93] N. Agraït, J. G. Rodrigo, and S. Vieira. "Conductance steps and quantization in atomic-size contacts." *Phys. Rev. B*, **47**, 12345–12348 (1993).

[Agrait03] N. Agrait, A. L. Yeyati, and J. M. van Ruitenbeek. "Quantum properties of atomic-sized conductors." *Physics Reports*, **377**, 81 – 279 (2003).

[Alivisatos96] A. P. Alivisatos. "Perspectives on the physical chemistry of semiconductor nanocrystals." *The Journal of Physical Chemistry*, **100**, 13226–13239 (1996).

[ANSYS] ANSYS. "Maxwell."

[Arielly11] R. Arielly, A. Ofarim, G. Noy, and Y. Selzer. "Accurate determination of plasmonic fields in molecular junctions by current rectification at optical frequencies." *ACS Nano Lett.*, **11**, 2968–2972 (2011).

[Arnero] Arnero. "Carbon nanotube armchair povray." en.wikipedia.org.

[Aström95] K. J. Aström and T. Hägglund. *The Control Handbook*. IEEE/CRC Press (1995).

[attocube GmbHa] attocube GmbH. "Anpx101."

[attocube GmbHb] attocube GmbH. "Anpz101."

[attocube GmbHc] attocube GmbH. "Ansxyz100."

[attocube GmbHd] attocube GmbH. "Asc 350."

[attocube GmbHe] attocube GmbH. "Asc 500."

[Averin91] D. Averin and K. Likharev. *Mesoscopic Phenomena in Solids*. North-Holland (1991).

[Aviram74] A. Aviram and M. A. Ratner. "Molecular rectifiers." *Chemical Physics Letters*, **29**, 277–283 (1974).

[Bakkers00] E. P. A. M. Bakkers and D. Vanmaekelbergh. "Resonant electron tunneling through semiconducting nanocrystals in a symmetrical and an asymmetrical junction." *Phys. Rev. B*, **62**, R7743–R7746 (2000).

[Balshaw96] N. H. Balshaw. *Practical Cryogenics*. Oxford Instruments Superconductivity Limited (1996).

[Banin03] U. Banin and O. Millo. "Tunneling and optical spectroscopy of semiconductor nanocrystals." *Annual Review of Physical Chemistry*, **54**, 465–492 (2003).

[Barthel10] C. Barthel, M. Kjærgaard, J. Medford, M. Stopa, C. M. Marcus, M. P. Hanson, and A. C. Gossard. "Fast sensing of double-dot charge arrangement and spin state with a radio-frequency sensor quantum dot." *Phys. Rev. B*, **81**, 161308 (2010).

[Biercuk08] M. Biercuk, S. Ilani, C. Marcus, and P. McEuen. "Electrical transport inǎsingle-wallǎcarbonǎnanotubes." In "Carbon Nanotubes," volume 111 of *Topics in Applied Physics*, 455–493. Springer Berlin / Heidelberg (2008).

[Binnig82] G. Binnig, H. Rohrer, C. Gerber, and E. Weibel. "Tunneling through a controllable vacuum gap." *App. Phys. Lett.*, **40**, 178–180 (1982).

[Birks97] T. A. Birks, J. C. Knight, and P. S. Russell. "Endlessly single-mode photonic crystal fiber." *Opt. Lett.*, **22**, 961–963 (1997).

[Black67] J. R. Black. "Mass transport of aluminium by momentum exchnage with conducting electrons." *Proceedings of the 1967 IEEE International Reliability Physics Symposium*, 148 (1967).

[Blum05] A. S. Blum, J. G. Kushmerick, D. P. Long, C. H. Patterson, J. C. Yang, J. C. Henderson, Y. Yao, J. M. Tour, R. Shashidhar, and B. R. Ratna. "Molecularly inherent voltage-controlled conductance switching." *Nature Materials*, **4**, 167–172 (2005).

[Bode45] H. W. Bode. *Network Analysis and Feedback Amplifier Design.* Van Sonstrand (1945).

[Böhler04] T. Böhler, J. Grebing, A. Mayer-Gindner, H. v Löhneysen, and E. Scheer. "Mechanically controllable break-junctions for use as electrodes for molecular electronics." *Nanotechnology*, **15**, S465 (2004).

[Bohler07] T. Bohler, A. Edtbauer, and E. Scheer. "Conductance of individual C_{60} molecules measured with controllable gold electrodes." *Phys. Rev. B*, **76**, 125432 (2007).

[Bolotin04] K. I. Bolotin, F. Kuemmeth, A. N. Pasupathy, and D. C. Ralph. "Metal-nanoparticle single-electron transistors fabricated using electromigration." *App. Phys. Lett.*, **84**, 3154 (2004).

[Booth99] J. C. Booth and C. L. Holloway. "Conductor loss in superconducting planar structures: Calculations and measurements." *IEEE Transactions on Microwave Theory and Techniques*, **47**, 769–774 (1999).

[Buchs11] G. Buchs, M. Barkelid, S. Bagiante, G. A. Steele, and V. Zwiller. "Imaging the formation of a p-n junction in a suspended carbon nanotube with scanning

photocurrent microscopy." *J. App. Phys.*, **110**, 074308 (2011).

[Bumm99] L. A. Bumm, J. J. Arnold, T. D. Dunbar, D. L. Allara, and P. S. Weiss. "Electron transfer through organic molecules." *The Journal of Physical Chemistry B*, **103**, 8122–8127 (1999).

[Burch09] S. Burch. *Electromigrated Mechanically Controllable Break-Junctions*. Master's thesis, ETH Zurich (2009).

[Cao12] J. Cao and A. M. Ionescu. "Self-aligned lateral dual-gate suspended-body single-walled carbon nanotube field-effect transistors." *App. Phys. Lett.*, **100**, 063103 (2012).

[Cassidy07] M. C. Cassidy, A. S. Dzurak, R. G. Clark, K. D. Petersson, I. Farrer, D. A. Ritchie, and C. G. Smith. "Single shot charge detection using a radio-frequency quantum point contact." *App. Phys. Lett.*, **91**, 222104 (2007).

[Champagne05] A. R. Champagne, A. N. Pasupathy, and D. C. Ralph. "Mechanically adjustable and electrically gated single-molecule transistors." *ACS Nano Lett.*, **5**, 305–308 (2005).

[Chaste08] J. Chaste, L. Lechner, P. Morfin, G. Feve, T. Kontos, J.-M. Berroir, D. C. Glattli, H. Happy, P. Hakonen, and B. Placais. "Single carbon nanotube transistor at GHz frequency." *ACS Nano Lett.*, **8**, 525–528 (2008).

[Chaste11] J. Chaste, M. Sledzinska, M. Zdrojek, J. Moser, and A. Bachtold. "High-frequency nanotube mechanical resonators." *App. Phys. Lett.*, **99**, 213502 (2011).

[Chaste12] J. Chaste, A. Eichler, J. Moser, G. Ceballos, R. Rurali, and A. Bachtold. "A nanomechanical mass sensor with yoctogram resolution." *Nature Nanotechnoloy*, **7**, 301–304 (2012).

[Clark70] A. Clark, G. Childs, and G. Wallace. "Electrical resistivity of some engineering alloys at low temperatures." *Cryogenics*, **10**, 295 – 305 (1970).

[Colvin94] V. L. Colvin, M. C. Schlamp, and A. P. Alivisatos. "Light-emitting diodes made from cadmium selenide nanocrystals and a semiconducting polymer." *Nature*, **370**, 354–357 (1994).

[Cord07] B. Cord, J. Lutkenhaus, and K. K. Berggren. "Optimal temperature for development of poly(methylmethacrylate)." In "PAPERS FROM THE 51st INTERNATIONAL CONFERENCE ON ELECTRON, ION, AND PHOTON BEAM TECHNOLOGY AND NANOFABRICATION," volume 25, 2013–2016. AVS (2007).

[Cuevas98] J. C. Cuevas, A. L. Yeyati, and A. Martin-Rodero. "Microscopic origin of conducting channels in metallic atomic-size contacts." *Phys. Rev. Lett.*, **80**,

1066–1069 (1998).

[Cuniberti05] G. Cuniberti, G. Fagas, and K. Richter. *Introducing Molecular Electronics.* Springer (2005).

[Dabbousi95] B. O. Dabbousi, M. G. Bawendi, O. Onitsuka, and M. F. Rubner. "Electroluminescence from CdSe quantum-dot/polymer composites." *App. Phys. Lett.*, **66**, 1316–1318 (1995).

[Dadosh05] T. Dadosh, Y. Gordin, R. Krahne, I. Khivrich, D. Mahalu, V. Frydman, J. Sperling, A. Yacoby, and I. Bar-Joseph. "Measurement of the conductance of single conjugated molecules." *Nature*, **436**, 677–680 (2005).

[Dai09] J. Dai, J. Li, H. Zeng, and X. Cui. "Measurements on quantum capacitance of individual single walled carbon nanotubes." *App. Phys. Lett.*, **94**, 093114 (2009).

[Datta09] S. S. Datta, D. R. Strachan, and A. T. C. Johnson. "Gate coupling to nanoscale electronics." *Phys. Rev. B*, **79**, 205404 (2009).

[Donhauser01] Z. J. Donhauser, B. A. Mantooth, K. F. Kelly, L. A. Bumm, J. D. Monnell, J. J. Stapleton, D. W. Price, A. M. Rawlett, D. L. Allara, J. M. Tour, and P. S. Weiss. "Conductance switching in single molecules through conformational changes." *Science*, **292**, 2303–2307 (2001).

[Dulić03] D. Dulić, S. J. van der Molen, T. Kudernac, H. T. Jonkman, J. J. D. de Jong, T. N. Bowden, J. van Esch, B. L. Feringa, and B. J. van Wees. "One-way optoelectronic switching of photochromic molecules on gold." *Phys. Rev. Lett.*, **91**, 207402 (2003).

[Durrer09] L. Durrer, J. Greenwald, T. Helbling, M. Muoth, R. Riek, and C. Hierold. "Narrowing SWNT diameter distribution using size-separated ferritin-based Fe catalysts." *Nanotechnology*, **20**, 355601 (2009).

[Eigler90] D. M. Eigler and E. K. Schweizer. "Positioning single atoms with a scanning tunnelling microscope." *Nature*, **344**, 524–526 (1990).

[Engelberg04] S. Engelberg. "The central limit theorem and low-pass filters." In "Electronics, Circuits and Systems, 2004. ICECS 2004. Proceedings of the 2004 11th IEEE International Conference on," 65 – 68 (2004).

[Esen05] G. Esen and M. S. Fuhrer. "Temperature control of electromigration to form gold nanogap junctions." *App. Phys. Lett.*, **87**, 263101 (2005).

[Fano50] R. Fano. "Theoretical limitations on the broadband matching of arbitrary impedances." *Journal of the Franklin Institute*, **249**, 57 – 83 (1950).

[Flowers-Jacobs07] N. E. Flowers-Jacobs, D. R. Schmidt, and K. W. Lehnert. "Intrinsic noise properties of atomic point contact displacement detectors." *Phys. Rev.*

Lett., **98**, 096804 (2007).

[Fong12] K. Fong and K. Schwab. "Ultra-sensitive and wide bandwidth thermal measurements of graphene at low temperatures." arXiv:1202.5737 (2012).

[Frey12] T. Frey, P. J. Leek, M. Beck, J. Faist, M. Büttiker, A. Wallraff, K. Ensslin, and T. Ihn. "Quantum dot admittance probed at microwave frequencies with an on-chip resonator." arXiv:1207.0945v1 (2012).

[Frunzio05] L. Frunzio, A. Wallraff, D. Schuster, J. Majer, and R. Schoelkopf. "Fabrication and characterization of superconducting circuit qed devices for quantum computation." *IEEE Transactions on Applied Superconductivity*, **15**, 860 – 863 (2005).

[Fu04] L. Fu, Lingchao, Y. Liu, and D. Zhu. "Molecular and nanoscale materials and devices in electronics." *Colloid and Interface Science*, **111**, 133–157 (2004).

[Gabelli06] J. Gabelli, G. FÃÍve, J.-M. Berroir, B. PlaÃğais, A. Cavanna, B. Etienne, Y. Jin, and D. C. Glattli. "Violation of Kirchhoff's laws for a coherent RC circuit." *Science*, **313**, 499–502 (2006).

[García-Martín11] A. García-Martín, D. R. Ward, D. Natelson, and J. C. Cuevas. "Field enhancement in subnanometer metallic gaps." *Phys. Rev. B*, **83**, 193404 (2011).

[Geerlings12] K. Geerlings, S. Shankar, E. Edwards, L. Frunzio, R. J. Schoelkopf, and M. H. Devoret. "Improving the quality factor of microwave compact resonators by optimizing their geometrical parameters." *App. Phys. Lett.*, **100**, 192601 (2012).

[Gerardin61] M. Gerardin. *Compt. Rend.*, **53**, 727 (1861).

[Ginger99] D. S. Ginger and N. C. Greenham. "Photoinduced electron transfer from conjugated polymers to CdSe nanocrystals." *Phys. Rev. B*, **59**, 10622–10629 (1999).

[Goppl08] M. Goppl, A. Fragner, M. Baur, R. Bianchetti, S. Filipp, J. M. Fink, P. J. Leek, G. Puebla, L. Steffen, and A. Wallraff. "Coplanar waveguide resonators for circuit quantum electrodynamics." *J. App. Phys.*, **104**, 113904 (2008).

[Gouttenoire10] V. Gouttenoire, T. Barois, S. Perisanu, J.-L. Leclercq, S. T. Purcell, P. Vincent, and A. Ayari. "Digital and fm demodulation of a doubly clamped single-walled carbon-nanotube oscillator: Towards a nanotube cell phone." *Small*, **6**, 1060–1065 (2010).

[Grose08] J. E. Grose, E. S. Tam, C. Timm, M. Scheloske, B. Ulgut, J. J. Parks, H. D. Abruna, W. Harneit, and D. C. Ralph. "Tunnelling spectra of individual magnetic endofullerene molecules." *Nature Materials*, **7**, 884–889 (2008).

[Gross94] R. Gross and D. Koelle. "Low temperature scanning electron microscopy of superconducting thin films and josephson junctions." *Reports on Progress in Physics*, **57**, 651 (1994).

[Grüter05] L. Grüter, F. Cheng, T. T. Heikkilä, M. T. Gonzalez, F. Diederich, C. Schönenberger, and M. Calame. "Resonant tunnelling through a C_{60} molecular junction in a liquid environment." *Nanotechnology*, **16**, 2143–2148 (2005).

[Guhr07] D. C. Guhr, D. Rettinger, J. Boneberg, A. Erbe, P. Leiderer, and E. Scheer. "Influence of laser light on electronic transport through atomic-size contacts." *Phys. Rev. Lett.*, **99**, 086801 (2007).

[Gustavsson06] S. Gustavsson, R. Leturcq, B. Simovič, R. Schleser, T. Ihn, P. Studerus, K. Ensslin, D. C. Driscoll, and A. C. Gossard. "Counting statistics of single electron transport in a quantum dot." *Phys. Rev. Lett.*, **96**, 076605 (2006).

[Hare91] J. Hare, H. Kroto, and R. Taylor. "Preparation and UV / visible spectra of fullerenes C_{60} and C_{70}." *Chem. Phys. Lett.*, **177**, 394 – 398 (1991).

[Hayashi08] T. Hayashi and T. Fujisawa. "Voltage-pulse-induced electromigration." *Nanotechnology*, **19**, 145709 (2008).

[He05] J. He, F. Chen, P. A. Liddell, J. Andreasson, S. D. Straight, D. Gust, T. A. Moore, A. L. Moore, J. Li, O. F. Sankey, and S. M. Lindsay. "Switching of a photochromic molecule on gold electrodes: single-molecule measurements." *Nanotechnology*, **16**, 695 (2005).

[Hellmüller12] S. Hellmüller, M. Pikulski, T. Müller, B. Küng, G. Puebla-Hellmann, A. Wallraff, M. Beck, K. Ensslin, and T. Ihn. "Optimization of sample chip design for stub-matched radio-frequency reflectometry measurements." *App. Phys. Lett.*, **101**, 042112 (2012).

[Hipps02] K. Hipps and U. Mazur. *Handbook of Vibrational Spectroscopy.* Wiley & Sons (2002).

[Hoffmann08] R. Hoffmann, D. Weissenberger, J. Hawecker, and D. Stoffler. "Conductance of gold nanojunctions thinned by electromigration." *App. Phys. Lett.*, **93**, 043118 (2008).

[Hoffmann10] E. Hoffmann, F. Deppe, T. Niemczyk, T. Wirth, E. P. Menzel, G. Wild, H. Huebl, M. Mariantoni, T. Weissl, A. Lukashenko, A. P. Zhuravel, A. V. Ustinov, A. Marx, and R. Gross. "A superconducting 180[degree] hybrid ring coupler for circuit quantum electrodynamics." *App. Phys. Lett.*, **97**, 222508 (2010).

[Hogele08] A. Hogele, S. Seidl, M. Kroner, K. Karrai, C. Schulhauser, O. Sqalli, J. Scrimgeour, and R. J. Warburton. "Fiber-based confocal microscope for

cryogenic spectroscopy." *Rev. Sci. Inst.*, **79**, 023709 (2008).

[Houck04] A. A. Houck, J. Labaziewicz, E. K. Chan, J. A. Folk, and I. L. Chuang. "Kondo effect in electromigrated gold break junctions." *ACS Nano Lett.*, **5**, 1685–1688 (2004).

[Hüttel09] A. K. Hüttel, G. A. Steele, B. Witkamp, M. Poot, L. P. Kouwenhoven, and H. S. J. van der Zant. "Carbon nanotubes as ultrahigh quality factor mechanical resonators." *ACS Nano Lett.*, **9**, 2547–2552 (2009).

[Huynh02] W. U. Huynh, J. J. Dittmer, and A. P. Alivisatos. "Hybrid nanorod-polymer solar cells." *Science*, **295**, 2425–2427 (2002).

[Ibach01] H. Ibach and H. Lüth. *Festkörperphysik*. Springer (2001).

[Ihn10] T. Ihn. *Semiconductor Nanostructures*. Oxford University Press, New Yord (2010).

[Ilani06] S. Ilani, L. A. K. Donev, M. Kindermann, and P. L. McEuen. "Measurement of the quantum capacitance of interacting electrons in carbon nanotubes." *Nature Physics*, **2**, 687–691 (2006).

[Ilani10] S. Ilani and P. L. McEuen. "Electron transport in carbon nanotubes." *Annu. Rev. Condens. Matter Phys.*, **1**, 1–25 (2010).

[Ittah08] N. Ittah, I. Yutsis, and Y. Selzer. "Fabrication of highly stable configurable metal quantum point contacts." *ACS Nano Lett.*, **8**, 3922–3927 (2008). PMID: 18954127.

[Ittah09] N. Ittah, G. Noy, I. Yutsis, and Y. Selzer. "Measurement of electronic transport through 1g0 gold contacts under laser irradiation." *ACS Nano Lett.*, **9**, 1615–1620 (2009).

[Javey03] A. Javey, J. Guo, Q. Wang, M. Lundstrom, and H. Dai. "Ballistic carbon nanotube field-effect transistors." *Nature*, **424**, 654–657 (2003).

[Jerger11] M. Jerger, S. Poletto, P. Macha, U. Hãijbner, A. Lukashenko, E. Il'ichev, and A. V. Ustinov. "Readout of a qubit array via a single transmission line." *EPL (Europhysics Letters)*, **96**, 40012 (2011).

[Joachim95] C. Joachim, J. K. Gimzewski, R. R. Schlittler, and C. Chavy. "Electronic transparence of a single C_{60} molecule." *Phys. Rev. Lett.*, **74**, 2102–2105 (1995).

[Joachim97] C. Joachim and J. Gimzewski. "An electromechanical amplifier using a single molecule." *Chem. Phys. Lett.*, **265**, 353–357 (1997).

[Joachim05] C. Joachim and M. A. Ratner. "Molecular electronics special feature: Molecular electronics: Some views on transport junctions and beyond." *Pro-*

ceedings of the National Academy of Sciences, **102**, 8801–8808 (2005).

[Josephson62] B. D. Josephson. "Possible new effects in superconductive tunnelling." *Physics Letters*, **1**, 251–253 (1962).

[Katsonis06] N. Katsonis, T. Kudernac, M. Walko, S. van der Molen, B. van Wees, and B. Feringa. "Reversible conductance switching of single diarylethenes on a gold surface." *Advanced Materials*, **18**, 1397–1400 (2006).

[Keithley] Keithley. "2602 system sourcemeter."

[Kergueris99] C. Kergueris, J.-P. Bourgoin, S. Palacin, D. Esteve, C. Urbina, M. Magoga, and C. Joachim. "Electron transport through a metal-molecule-metal junction." *Phys. Rev. B*, **59**, 12505–12513 (1999).

[Khalil12] M. S. Khalil, M. J. A. Stoutimore, F. C. Wellstood, and K. D. Osborn. "An analysis method for asymmetric resonator transmission applied to superconducting devices." *J. App. Phys.*, **111**, 054510 (2012).

[Kiguchi08] M. Kiguchi and K. Murakoshi. "Conductance of single C_{60} molecule bridging metal electrodes." *J. Phys. Chem. C*, **112**, 8140–8143 (2008).

[Kim11] Y. Kim, T. Pietsch, A. Erbe, W. Belzig, and E. Scheer. "Benzenedithiol: A broad-range single-channel molecular conductor." *ACS Nano Lett.*, **11**, 3734–3738 (2011).

[Klein96] D. L. Klein, P. L. McEuen, J. E. B. Katari, R. Roth, and A. P. Alivisatos. "An approach to electrical studies of single nanocrystals." *App. Phys. Lett.*, **68**, 2574–2576 (1996).

[Klein97] D. L. Klein, B J, R. Roth, A. K. L. Lim, A. P. Alivisatos, and P. L. McEuen. "A single-electron transistor made from a cadmium selenide nanocrystal." *Nature*, **389**, 699–+ (1997).

[Kolesnychenko99a] O. Y. Kolesnychenko, O. I. Shklyarevskii, and H. van Kempen. "Calibration of the distance between electrodes of mechanically controlled break junctions using field emission resonance." *Rev. Sci. Inst.*, **70**, 1442–1446 (1999).

[Kolesnychenko99b] O. Y. Kolesnychenko, O. I. Shklyarevskii, and H. van Kempen. "Giant influence of adsorbed helium on field emission resonance measurements." *Phys. Rev. Lett.*, **83**, 2242–2245 (1999).

[Krans96] J. Krans, J. van Ruitenbeek, and L. de Jongh. "Atomic structure and quantized conductance in metal point contacts." *Physica B: Condensed Matter*, **218**, 228 – 233 (1996).

[Krytar] Krytar. "Model number 102008010."

[Kushmerick02] J. G. Kushmerick, D. B. Holt, J. C. Yang, J. Naciri, M. H. Moore, and R. Shashidhar. "Metal-molecule contacts and charge transport across monomolecular layers: Measurement and theory." *Phys. Rev. Lett.*, **89**, 086802 (2002).

[Laser Components GmbH] Laser Components GmbH. "Count blue."

[Lassagne09] B. Lassagne, Y. Tarakanov, J. Kinaret, D. Garcia-Sanchez, and A. Bach-told. "Coupling mechanics to charge transport in carbon nanotube mechanical resonators." *Science*, **325**, 1107–1110 (2009).

[Leach92] S. Leach, M. Vervloet, A. Despres, E. Breheret, J. P. Hare, T. J. Dennis, H. W. Kroto, R. Taylor, and D. R. Walton. "Electronic spectra and transitions of the fullerene c60." *Chemical Physics*, **160**, 451 – 466 (1992).

[Lechner10] L. G. Lechner, F. Wu, R. Danneau, S. E. Andresen, and P. Hakonen. "RF-electrometer using a carbon nanotube resonant tunneling transistor." *J. App. Phys.*, **107**, 084316 (2010).

[Lee03] J.-O. Lee, G. Lientschnig, F. Wiertz, M. Struijk, R. A. J. Janssen, R. Eg-berink, D. N. Reinhoudt, P. Hadley, and C. Dekker. "Absence of strong gate effects in electrical measurements on phenylene-based conjugated molecules." *Nano Lett.*, **3**, 113–117 (2003).

[Levinson97] H. J. Levinson, M. A. McCord, F. Cerrina, R. D. Allen, J. G. Skinner, A. R. Neureuther, M. C. Peckerar, F. K. Perkins, and M. J. Rooks. *Handbook of Microlithography, Micromachining and Microfabrication.* Society of Photo-Optical Instrumentation Engineers (1997).

[Li04] S. Li, Z. Yu, S.-F. Yen, W. C. Tang, and P. J. Burke. "Carbon nanotube transistor operation at 2.6 ghz." *ACS Nano Lett.*, **4**, 753–756 (2004).

[Liang02] W. Liang, M. P. Shores, M. Bockrath, J. R. Long, and H. Park. "Kondo resonance in a single-molecule transistor." *Nature*, **417**, 725–729 (2002).

[Lu03] X. Lu, M. Grobis, K. H. Khoo, S. G. Louie, and M. F. Crommie. "Spatially mapping the spectral density of a single c$_{60}$ molecule." *Phys. Rev. Lett.*, **90**, 096802 (2003).

[Luber05] S. M. Luber, S. Strobel, H.-P. Tranitz, W. Wegscheider, D. Schuh, and M. Tornow. "Nanometre spaced electrodes on a cleaved AlGaAs surface." *Nanotechnology*, **16**, 1182– (2005).

[Luryi88] S. Luryi. "Quantum capacitance devices." *App. Phys. Lett.*, **52**, 501–503 (1988).

[Maxfield65] B. W. Maxfield and W. L. McLean. "Superconducting penetration depth of niobium." *Phys. Rev.*, **139**, A1515–A1522 (1965).

[Megrant12] A. Megrant, C. Neill, R. Barends, B. Chiaro, Y. Chen, L. Feigl, J. Kelly, E. Lucero, M. Mariantoni, P. J. J. O'Malley, D. Sank, A. Vainsencher, J. Wenner, T. C. White, Y. Yin, J. Zhao, C. J. Palmstrom, J. M. Martinis, and A. N. Cleland. "Planar superconducting resonators with internal quality factors above one million." *App. Phys. Lett.*, **100**, 113510 (2012).

[Meyer07] C. Meyer, J. M. Elzerman, and L. P. Kouwenhoven. "Photon-assisted tunneling in a carbon nanotube quantum dot." *ACS Nano Lett.*, **7**, 295–299 (2007).

[Mini Circuits] Mini Circuits. "Zx85-12g-s+."

[Moore65] G. E. Moore. "Cramming more components onto integrated circuits." *Electronics*, **38**, 4 (1965).

[Moreland85] J. Moreland and J. W. Ekin. "Electron tunneling experiments using nb-sn "break" junctions." *J. App. Phys.*, **58**, 3888–3895 (1985).

[Muller92a] C. Muller, J. van Ruitenbeek, and L. de Jongh. "Experimental observation of the transition from weak link to tunnel junction." *Physica C: Superconductivity*, **191**, 485 – 504 (1992).

[Muller92b] C. J. Muller, J. M. van Ruitenbeek, and L. J. de Jongh. "Conductance and supercurrent discontinuities in atomic-scale metallic constrictions of variable width." *Phys. Rev. Lett.*, **69**, 140–143 (1992).

[Muller10] T. Muller, B. Kung, S. Hellmuller, P. Studerus, K. Ensslin, T. Ihn, M. Reinwald, and W. Wegscheider. "An in situ tunable radio-frequency quantum point contact." *App. Phys. Lett.*, **97**, 202104 (2010).

[Muoth12] M. Muoth and C. Hierold. "Transfer of carbon nanotubes onto microactuators for hysteresis-free transistors at low thermal budget." In "2012 IEEE 25th International Conference on Micro Electro Mechanical Systems (MEMS)," 1352 –1355 (2012).

[Natelson12] D. Natelson. "Mechanical break junctions: Enormous information in a nanoscale package." *ACS Nano*, **6**, 2871–2876 (2012).

[Nougaret10] L. Nougaret, G. Dambrine, S. Lepilliet, H. Happy, N. Chimot, V. Derycke, and J.-P. Bourgoin. "Gigahertz characterization of a single carbon nanotube." *App. Phys. Lett.*, **96**, 042109 (2010).

[Park99] H. Park, A. K. L. Lim, A. P. Alivisatos, J. Park, and P. L. McEuen. "Fabrication of metallic electrodes with nanometer separation by electromigration." *App. Phys. Lett.*, **75**, 301–+ (1999).

[Park00] H. Park, J. Park, A. K. L. Lim, E. H. Anderson, A. P. Alivisatos, and P. L. McEuen. "Nanomechanical oscillations in a single-C_{60} transistor." *Nature,*

407, 57–60 (2000).

[Park02]   J. Park, A. N. Pasupathy, J. I. Goldsmith, C. Chang, Y. Yaish, J. R. Petta, M. Rinkoski, J. P. Sethna, H. D. Abruna, P. L. McEuen, and D. C. Ralph. "Coulomb blockade and the kondo effect in single-atom transistors." *Nature,* **417**, 722–725 (2002).

[Parks06]   J. J. Parks, A. R. Champagne, G. R. Hutchison, S. Flores-Torres, H. D. Abruna, and D. C. Ralph. "Tuning the kondo effect with a mechanically controllable break junction." *Phys. Rev. Lett.,* **99**, 026601 (2006).

[Pierce97]   D. Pierce and P. Brusius. "Electromigration: A review." *Microelectronics Reliability,* **37**, 1053 – 1072 (1997).

[Pozar05]   D. M. Pozar. *Microwave Engineering.* John Wiley & Sons Inc., New York, 3rd edition (2005).

[Prêtre96]   A. Prêtre, H. Thomas, and M. Büttiker. "Dynamic admittance of mesoscopic conductors: Discrete-potential model." *Phys. Rev. B,* **54**, 8130–8143 (1996).

[Prins11]   F. Prins, A. Barreiro, J. W. Ruitenberg, J. S. Seldenthuis, N. Aliaga-Alcalde, L. M. K. Vandersypen, and H. S. J. van der Zant. "Room-temperature gating of molecular junctions using few-layer graphene nanogap electrodes." *ACS Nano Lett.,* **11**, 4607–4611 (2011).

[Puebla-Hellmann12]   G. Puebla-Hellmann and A. Wallraff. "Realization of gigahertz-frequency impedance matching circuits for nano-scale devices." *App. Phys. Lett.,* **101**, 053108 (2012).

[Qin06]   H. Qin and D. A. Williams. "Radio-frequency point-contact electrometer." *App. Phys. Lett.,* **88**, 203506 (2006).

[R.98]   S. R., D. G., and D. M. S. *Physical Properties of Carbon Nanotubes.* Imperal College Press, London (1998).

[Reed97]   M. A. Reed, C. Zhou, C. J. Muller, T. P. Burgin, and J. M. Tour. "Conductance of a molecular junction." *Science,* **278**, 252–254 (1997).

[Reichert02]   J. Reichert, R. Ochs, D. Beckmann, H. B. Weber, M. Mayor, and H. v. Löhneysen. "Driving current through single organic molecules." *Phys. Rev. Lett.,* **88**, 176804 (2002).

[Reilly07]   D. J. Reilly, C. M. Marcus, M. P. Hanson, and A. C. Gossard. "Fast single-charge sensing with a RF quantum point contact." *App. Phys. Lett.,* **91**, 162101 (2007).

[Roch08]   N. Roch, S. Florens, V. Bouchiat, W. Wernsdorfer, and F. Balestro. "Quantum phase transition in a single-molecule quantum dot." *Nature,* **453**, 633–637 (2008).

[Roschier04] L. Roschier, M. Sillanpää, W. Taihong, M. Ahlskog, S. Iijima, and P. Hakonen. "Carbon nanotube radio-frequency single-electron transistor." *Journal of Low Temperature Physics*, **136**, 465–480 (2004).

[Rubio96] G. Rubio, N. Agraï, and S. Vieira. "Atomic-sized metallic contacts: Mechanical properties and electronic transport." *Phys. Rev. Lett.*, **76**, 2302–2305 (1996).

[Saha11] S. Saha, G. Qian, and K. M. Lewis. "Fabrication of nanogaps by a progressive electromigration technique using wires of various thicknesses." *Journal of Vacuum Science & Technology B: Microelectronics and Nanometer Structures*, **29**, 061802 (2011).

[Scheer97] E. Scheer, P. Joyez, D. Esteve, C. Urbina, and M. H. Devoret. "Conduction channel transmissions of atomic-size aluminum contacts." *Phys. Rev. Lett.*, **78**, 3535–3538 (1997).

[Scheer98] E. Scheer, N. Agrait, J. C. Cuevas, A. L. Yeyati, B. Ludoph, A. Martin-Rodero, G. R. Bollinger, J. M. van Ruitenbeek, and C. Urbina. "The signature of chemical valence in the electrical conduction through a single-atom contact." *Nature*, **394**, 154–157 (1998).

[Schoelkopf98] R. J. Schoelkopf, P. Wahlgren, A. A. Kozhevnikov, P. Delsing, and D. E. Prober. "The radio-frequency single-electron transistor (RF-SET): A fast and ultrasensitive electrometer." *Science*, **280**, 1238–1242 (1998).

[Schoon93] M. Schoon. "A semi-automatic 3-port network analyzer." *Microwave Theory and Techniques, IEEE Transactions on*, **41**, 974 –978 (1993).

[Schuster07] D. I. Schuster. *Circuit Quantum Electrodynamics*. Ph.D. thesis, Yale University (2007).

[Sheen91] D. Sheen, S. Ali, D. Oates, R. Withers, and J. Kong. "Current distribution, resistance, and inductance for superconducting strip transmission lines." *Applied Superconductivity, IEEE Transactions on*, **1**, 108 –115 (1991).

[Simons01] R. N. Simons. *Coplanar waveguide circuits, components and systems*. Wiley Series in Microwave and Optical Engineerging. John Wiley & Sons, Inc., New York (2001).

[Song09] H. Song, Y. Kim, Y. H. Jang, H. Jeong, M. A. Reed, and T. Lee. "Observation of molecular orbital gating." *Nature*, **462**, 1039–1043 (2009).

[Steele09] G. A. Steele, A. K. Hüttel, B. Witkamp, M. Poot, H. B. Meerwaldt, L. P. Kouwenhoven, and H. S. J. van der Zant. "Strong coupling between single-electron tunneling and nanomechanical motion." *Science*, **325**, 1103–1107 (2009).

[Strachan05] D. R. Strachan, D. E. Smith, D. E. Johnston, T.-H. Park, M. J. Therien, D. A. Bonnell, and A. T. Johnson. "Controlled fabrication of nanogaps in ambient environment for molecular electronics." *App. Phys. Lett.*, **86**, 3109–+ (2005).

[Strachan08] D. R. Strachan, D. E. Johnston, B. S. Guiton, S. S. Datta, P. K. Davies, D. A. Bonnell, and A. T. C. Johnson. "Real-time tem imaging of the formation of crystalline nanoscale gaps." *Phys. Rev. Lett.*, **100**, 056805 (2008).

[Svensson11] J. Svensson and E. E. B. Campbell. "Schottky barriers in carbon nanotube-metal contacts." *Journal of Applied Physics*, **110**, 111101 (2011).

[Taber90] R. C. Taber. "A parallel plate resonator technique for microwave loss measurements on superconductors." *Review of Scientific Instruments*, **61**, 2200–2206 (1990).

[Tang07] Y. Tang, I. Amlani, A. O. Orlov, G. L. Snider, and P. J. Fay. "Operation of single-walled carbon nanotube as a radio-frequency single-electron transistor." *Nanotechnology*, **18**, 445203 (2007).

[Tao06] N. J. Tao. "Electron transport in molecular junctions." *Nature Nanotechnology*, **1**, 173–181 (2006).

[Tavazza11] F. Tavazza, D. T. Smith, L. E. Levine, J. R. Pratt, and A. M. Chaka. "Electron transport in gold nanowires: Stable 1-, 2- and 3-dimensional atomic structures and noninteger conduction states." *Phys. Rev. Lett.*, **107**, 126802 (2011).

[Teufel08] J. Teufel. *Superconducting Tunnel Junctions as Direct Detectors for Submillimeter Astronomy*. Ph.D. thesis, Yale University (2008).

[Thorlabs] Thorlabs. "Pdf10a femtowatt photoreceiver."

[Tien63] P. K. Tien and J. P. Gordon. "Multiphoton process observed in the interaction of microwave fields with the tunneling between superconductor films." *Phys. Rev.*, **129**, 647–651 (1963).

[Tipler99] P. A. Tipler and R. A. Llewellyn. *Modern Physics*. W. H. Freeman (1999).

[Topliuchao] Topliuchao. "Uv-vis absorption of C_{60} in toluene solution." http://en.wikipedia.org/wiki/File:UV-Vis_C60.jpg.

[Toptica] Toptica. "ichrome TVIS."

[Trouwborst06] M. L. Trouwborst, S. J. van der Molen, and B. J. van Wees. "The role of joule heating in the formation of nanogaps by electromigration." *J. App. Phys.*, **99**, 114316 (2006).

[Tseng10] Y.-C. Tseng and J. Bokor. "Characterization of the junction capacitance of

metal-semiconductor carbon nanotube schottky contacts." *App. Phys. Lett.*, **96**, 013103 (2010).

[Tsutsui10] M. Tsutsui, T. Ohshiro, K. Matsubara, M. Furuhashi, M. Taniguchi, and T. Kawai. "Atomically controlled fabrications of subnanometer scale electrode gaps." *J. App. Phys.*, **108**, 064312 (2010).

[T.V.81] D. T.V. and T. C.W. *Principles of Superconductive Devices and Circuits.* Esevier North Holland, New York (1981).

[Van Hove53] L. Van Hove. "The occurrence of singularities in the elastic frequency distribution of a crystal." *Phys. Rev.*, **89**, 1189–1193 (1953).

[vanderMolen06] S. J. van der Molen, H. van der Vegte, T. Kudernac, I. Amin, B. L. Feringa, and B. J. van Wees. "Stochastic and photochromic switching of diarylethenes studied by scanning tunnelling microscopy." *Nanotechnology*, **17**, 310 (2006).

[vanRuitenbeek96] J. M. van Ruitenbeek, A. Alvarez, I. Pineyro, C. Grahmann, P. Joyez, M. H. Devoret, D. Esteve, and C. Urbina. "Adjustable nanofabricated atomic size contacts." *Rev. Sci. Inst.*, **67**, 108–111 (1996).

[vanWees88] B. J. van Wees, H. van Houten, C. W. J. Beenakker, J. G. Williamson, L. P. Kouwenhoven, D. van der Marel, and C. T. Foxon. "Quantized conductance of point contacts in a two-dimensional electron gas." *Phys. Rev. Lett.*, **60**, 848–850 (1988).

[Viljas07] J. K. Viljas and J. C. Cuevas. "Role of electronic structure in photoassisted transport through atomic-sized contacts." *Phys. Rev. B*, **75**, 075406 (2007).

[Vincent12] R. Vincent, S. Klyatskaya, M. Ruben, W. Wernsdorfer, and F. Balestro. "Electronic read-out of a single nuclear spin using a molecular spin transistor." *Nature*, **488**, 357–360 (2012).

[Vink07] I. T. Vink, T. Nooitgedagt, R. N. Schouten, L. M. K. Vandersypen, and W. Wegscheider. "Cryogenic amplifier for fast real-time detection of single-electron tunneling." *App. Phys. Lett.*, **91**, 123512 (2007).

[Waissman06] J. Waissman. "Impedance transformers for high frequency molecular electronics." QuDev Server (2006). Summer Report.

[Wang04] W. Wang, T. Lee, I. Kretzschmar, and M. A. Reed. "Inelastic electron tunneling spectroscopy of an alkanedithiol self-assembled monolayer." *ACS Nano Lett.*, **4**, 643–646 (2004).

[Wang07] J. Wang, B. Wang, and H. Guo. "Quantum inductance and negative electrochemical capacitance at finite frequency in a two-plate quantum capacitor." *Phys. Rev. B*, **75**, 155336 (2007).

[Ward07]   D. R. Ward, N. K. Grady, C. S. Levin, N. J. Halas, Y. Wu, P. Nordlander, and D. Natelson. "Electromigrated nanoscale gaps for surface-enhanced raman spectroscopy." *ACS Nano Lett.*, **7**, 1396–1400 (2007).

[Ward08]   D. R. Ward, N. J. Halas, J. W. Ciszek, J. M. Tour, Y. Wu, P. Nordlander, and D. Natelson. "Simultaneous measurements of electronic conduction and raman response in molecular junctions." *ACS Nano Letters*, **8**, 919–924 (2008).

[Ward10]   D. R. Ward, F. Huser, F. Pauly, J. C. Cuevas, and D. Natelson. "Optical rectification and field enhancement in a plasmonic nanogap." *Nature Nanotechnology*, **5**, 732–736 (2010).

[Ward11]   D. R. Ward, D. A. Corley, J. M. Tour, and D. Natelson. "Vibrational and electronic heating in nanoscale junctions." *Nature Nanotechnology*, **6**, 33–38 (2011).

[Watanabe94]   K. Watanabe, K. Yoshida, T. Aoki, and S. Kohjiro. "Kinetic inductance of superconducting coplanar waveguides." *Jpn. J. App. Phys.*, **33**, 5708–5712 (1994).

[Wen69]   C. Wen. "Coplanar waveguide, a surface strip transmission line suitable for nonreciprocal gyromagnetic device applications." In "Microwave Symposium, 1969 G-MTT International," 110 –115 (1969).

[Wenner11]   J. Wenner, R. Barends, R. C. Bialczak, Y. Chen, J. Kelly, E. Lucero, M. Mariantoni, A. Megrant, P. J. J. O'Malley, D. Sank, A. Vainsencher, H. Wang, T. C. White, Y. Yin, J. Zhao, A. N. Cleland, and J. M. Martinis. "Surface loss simulations of superconducting coplanar waveguide resonators." *Appl. Phys. Lett.*, **99**, 113513 (2011).

[Wharam88]   D. A. Wharam, T. J. Thornton, R. Newbury, M. Pepper, H. Ahmed, J. E. F. Frost, D. G. Hasko, D. C. Peacock, D. A. Ritchie, and G. A. C. Jones. "One-dimensional transport and the quantisation of the ballistic resistance." *Journal of Physics C: Solid State Physics*, **21**, L209 (1988).

[Williams03]   K. Williams, K. Gupta, and M. Wasilik. "Etch rates for micromachining processing-part II." *Journal of Microelectromechanical Systems*, **12**, 761 – 778 (2003).

[Wilson00]   N. Wilson. *The structure and dynamics of noble metal clusters.* Ph.D. thesis, University of Birmingham (2000).

[Wolff06]   I. Wolff. *Coplanar Microwave Integrated Circuits.* Wiley (2006).

[Wood09]   V. Wood, J. E. Halpert, M. J. Panzer, M. G. Bawendi, and V. Bulović? "Alternating current driven electroluminescence from znse/zns:mn/zns

nanocrystals." *ACS Nano Lett.*, **9**, 2367–2371 (2009). PMID: 19397294.

[Wu07]   Z. M. Wu, M. Steinacher, R. Huber, M. Calame, S. J. van der Molen, and C. Schonenberger. "Feedback controlled electromigration in four-terminal nanojunctions." *App. Phys. Lett.*, **91**, 053118 (2007).

[Wu10]   C. C. Wu, C. H. Liu, and Z. Zhong. "One-step direct transfer of pristine single-walled carbon nanotubes for functional nanoelectronics." *ACS Nano Lett.*, **10**, 1032–1036 (2010).

[Würfel05]   J. U. Würfel. *Molecular Break-Junctions: Interaction with Light and Conductance Switching*. Ph.D. thesis, Forschungszentrum Karlsruhe (2005).

[Xue07]   W. W. Xue, B. Davis, F. Pan, J. Stettenheim, T. J. Gilheart, A. J. Rimberg, and Z. Ji. "On-chip matching networks for radio-frequency single-electron transistors." *Applied Physics Letters*, **91**, 093511 (2007).

[Yang99]   F.-R. Yang, K.-P. Ma, Y. Qian, and T. Itoh. "A uniplanar compact photonic-bandgap (uc-pbg) structure and its applications for microwave circuit." *Microwave Theory and Techniques, IEEE Transactions on*, **47**, 1509 –1514 (1999).

[Yarema]   O. Yarema. Private Communications.

[Yoshida95]   K. Yoshida, K. Watanabe, T. Kisu, and K. Enpuku. "Evaluation of magnetic penetration depth and surface resistance of superconductiong thin films using coplanar waveguides." *IEEE Transactions on Applied Superconductivity*, **5**, 1979–1982 (1995).

[Yu04]   L. H. Yu and D. Natelson. "The Kondo Effect in C_{60} single-molecule transistors." *ACS Nano Lett.*, **4**, 79–83 (2004).

[Yu05a]   L. Yu, R. Singh, H. Liu, S. Wu, R. Hu, D. Durand, J. Bulman, J. Rowell, and N. Newman. "Fabrication of niobium titanium nitride thin films with high superconducting transition temperatures and short penetration lengths." *IEEE Transactions on Applied Superconductivity*, **15**, 44 – 48 (2005).

[Yu05b]   Z. Yu and P. J. Burke. "Microwave transport in metallic single-walled carbon nanotubes." *ACS Nano Lett.*, **5**, 1403–1406 (2005).

[Yu06]   Z. Yu, C. Rutherglen, and P. J. Burke. "Microwave nanotube transistor operation at high bias." *App. Phys. Lett.*, **88**, 233115 (2006).

[Zhitenev02]   N. B. Zhitenev, H. Meng, and Z. Bao. "Conductance of small molecular junctions." *Phys. Rev. Lett.*, **88**, 226801 (2002).

[Zhou95]   C. Zhou, C. J. Muller, M. R. Deshpande, J. W. Sleight, and M. A. Reed. "Microfabrication of a mechanically controllable break junction in silicon." *App. Phys. Lett.*, **67**, 1160–1162 (1995).

[Zhuravel06] A. Zhuravel, A. Sivakov, O. Turutanov, S. Anlage, A. Lukashenko, A. Ustinov, and D. Abraimov. "Laser scanning microscopy of hts films and devices." *Fizika Nizkikh Temperatur*, **32**, 775–794 (2006).

[Zlateva07] G. Zlateva, Z. Zhelev, R. Bakalova, and I. Kanno. "Precise size control and synchronized synthesis of six colors of cdse quantum dots in a slow-increasing temperature gradient." *Inorg. Chem.*, **46**, 6212–6214 (2007).

[Zurich Instruments] Zurich Instruments. "Hf2li lock-in amplifier."

Acknowledgments

I am deeply grateful to a number of people who have made this thesis possible, which, without their contribution, would have never reached its final state.

First, I would like to thank my advisor, Prof. Andreas Wallraff, who not only gave me the opportunity to work on such a fascinating subject. Starting a new project is a great experience and his support, mentoring and encouragement were essential to making it all happen. I would also like to thank my co-examiner, Prof. Christian Schönenberger, not only for reading and commenting my thesis, but also his enthusiasm about the project and the many constructive questions.

The entire QuDev lab has my gratitude, for being a fun lab to work in, for providing interesting discussions, for always helping one another. I would especially like to thank Romeo Bianchetti for helping me with all the small things in the lab and for being a great office buddy; Peter Leek for teaching me fabrication and helping me get started in the beginning; Janis Lütolf for all his contributions in actually setting up the Artic Cryostat; Farruh Abdumalikov for great discussions and proof-reading parts of the thesis and Jonas Mlynek for great skiing and proof-reading. I would also like to thank my semester/master thesis students Francois, Silvan, Andreas and Anna.

As nano-fabrication is a large part of this work, I would like to thank the FIRST Team, especially Otte Homan, for continued support and for answering all my fab questions. Many thanks also go to Andreas Alt for teaching me EBL and how to make airbridges as well as Matthias Muoth for the great collaboration on the nanotube project.

It was great to be able to draw on the expertise of a number of people at ETH who worked with optics, in particular Martin Kroner and Emre Ilgünsatiroglu, who enabled the confocal microscope setup, as well as the Quantum Optics group next door.

Last I would like to thank my family and my friends, for all the understanding and support during this sometimes very frustrating time. Thank you Mom and Dad, for all the love, for making it all possible. Thank you Marcus, for being a really great friend and for always being interested in my crazy nanoworld. Thank you Melanie, for so many things, for reading this thesis, for support, for understanding, for making these past years precious.

List of Publications

1. G. Puebla-Hellmann and A. Wallraff. "Realization of gigahertz-frequency impedance matching circuits for nano-scale devices" *Appl. Phys. Lett.*, **101**, 053108 (2012)

2. S. Hellmüller, M. Pikulski, T. Müller, B. Küng, G. Puebla-Hellmann, A. Wallraff, M. Beck, K. Ensslin and T. Ihn. "Optimization of sample chip design for stub-matched radio-frequency reflectometry measurements" *Appl. Phys. Lett.*, **101**, 042112 (2012)

3. M. Göppl, A. Fragner, M. Baur, R. Bianchetti, S. Filipp, J. M. Fink, P. J. Leek, G. Puebla-Hellmann, L. Steffen, and A. Wallraff. "Coplanar Waveguide Resonators for Circuit Quantum Electrodynamics." *J. Appl. Phys.*, **104**, 113904 (2008)

Curriculum Vitae

Gabriel F. Puebla-Hellmann
born December 30th, 1980 in Kaiserslautern, Germany.

2007 – 2012	Doctorate at the Quantum Device Lab, ETH Zürich, Switzerland (Dr. sc. ETH Zürich)
2006	Diploma Thesis at the Quantum Optics Group, ETH Zürich, Switzerland
2001 – 2006	Undergraduate studies in Physics , ETH Zürich, Switzerland (Dipl. Phys. ETH Zürich)
1992 – 2001	Lise-Meitner-Gymnasium, Grenzach-Wyhlen, Germany (High-School, Abitur)